



UiT The Arctic
University of Norway

UNIVERSITY OF
COPENHAGEN



Faculty of Science and Technology
Department of Mathematics and Statistics

Modelling the Earth System

From Tipping Elements to Reconstructions

Nils Bochow

A dissertation for the degree of Philosophiae Doctor, February 2024

This thesis has been submitted to the PhD School of The Faculty of Science, University of Copenhagen in collaboration with UiT - The Arctic University of Norway.

Abstract

Climate change can trigger climate tipping points, which are among the major threats to human society. Tipping points are thresholds beyond which a system undergoes abrupt, often irreversible, changes even if the external forcing is brought to a halt. Several large-scale elements in the Earth system are considered tipping elements with global consequences once critical thresholds are crossed and self-reinforcing changes are triggered. However, there is a large uncertainty as to whether some Earth system components should be considered tipping elements. The precise values of the critical thresholds remain uncertain, and it is unclear whether these can be temporarily exceeded without triggering a tipping point. Moreover, incomplete historical records complicate the inference of past dynamics of these components and current reconstruction methods introduce biases into higher-order statistics that are used to assess their stability. On the other hand, with the increasing availability of data and advancements in computational power, deep learning (DL) offers new advances in climate science, ranging from reconstructions to hybrid climate models.

This thesis presents an in-depth study of two distinct tipping elements: the Greenland ice sheet (GrIS) and the coupled system of the South American Monsoon and the Amazon rainforest (SAMS). Furthermore, we introduce a novel deep learning-based method to reconstruct spatiotemporal climate fields. By combining model- and observation-based analyses, we show that the SAMS is approaching a critical transition in response to deforestation, potentially leading to a large-scale reduction in precipitation rates in large parts of South America. We associate the critical transition with a weakening of the oceanic moisture inflow due to forest degradation.

Subsequently, we use two independent ice-sheet models and show for the first time that the GrIS's critical threshold can be temporarily exceeded without prompting a transition to an alternative state. Timely reversal of surface temperatures can prevent a complete retreat of the ice sheet due to the slow timescale of the ice loss. Lastly, we present a new deep learning-based reconstruction method. The model learns the underlying spatial relationships from climate model output and can inpaint observation-based datasets. Our method outperforms previous reconstruction methods and can realistically reconstruct known historical events, highlighting the potential of DL.

Abstract (DK)

Klimaændringer kan udløse klimatippepunkter, som er blandt de største trusler mod samfundet. Tippepunkter, eller tipping points, er tærskler, hvor et system gennemgår pludselige, ofte irreversible ændringer, selv hvis den eksterne påvirkning bringes til ophør. Flere stor-skala elementer i klimasystemet betragtes som tippeelementer med globale konsekvenser, når kritiske tærskler krydses, og selvforstærkende ændringer udløses. Der er dog stor usikkerhed omkring, hvorvidt nogle komponenter i klimasystemet bør betragtes som tippingelementer. De præcise værdier af de kritiske tærskler forbliver usikre, og det er uklart, om disse kan overskrides midlertidigt uden at systemet tipper. Desuden komplicerer ufuldstændigheden i historiske optegnelser den inferens der kan drages om tidligere tiders dynamik i disse komponenter. Derudover kan nuværende rekonstruktionsmetoder introducere bias i den højere ordens statistik, der bruges til at vurdere klimatelementernes stabilitet. På den anden side, med stigende tilgængelighed af data og fremskridt inden for beregningskraft, tilbyder dyb læring (deep learning, DL) nye fremskridt inden for klimavidenskab, lige fra rekonstruktioner til hybrid klimamodeller.

Denne afhandling præsenterer en dybdegående undersøgelse af to distinkte tippingelementer: Grønlands indlandsis (GrIS) og det koblede system af den sydamerikanske monsun og Amazonas regnskov (SAMS). Desuden introducerer vi en ny dyb læring-baseret metode til at rekonstruere klimaet i rum og tid. Ved at kombinere model- og observationsbaserede analyser viser vi, at SAMS nærmer sig en kritisk overgang som reaktion på afskovning, hvilket potentielt kan føre til en storstilet reduktion i nedbørsmængder i store dele af Sydamerika. Vi forbinder den kritiske overgang med en svækkelse af den oceaniske fugtighedsindstrømning på grund af skovdegradering.

Derefter viser vi for første gang, med brug af to uafhængige iskappemodeller, at GrIS's kritiske tærskel kan overskrides midlertidigt uden at fremkalde en overgang til en alternativ tilstand. Rettidig nedbringelse af overfladetemperaturer kan forhindre en komplet tilbagetrækning af iskappen på grund af den langsomme tidsskala for istabet. Endelig præsenterer vi en ny DL-baseret rekonstruktionsmetode. Modellen lærer de underliggende rumlige relationer fra klimamodeloutput og kan inkorporere observationsbaserede datasæt. Vores metode overgår tidligere rekonstruktionsmetoder og kan realistisk rekonstruere kendte historiske begivenheder, hvilket fremhæver DL's potentiale.

Acknowledgements

First and foremost, I want to thank all my supervisors. I would like to express my sincerest thanks to my main supervisor Martin Rypdal for the valuable feedback, giving me the freedom to research what interests me, the opportunities to travel, and all the support throughout my PhD journey. Furthermore, I want to thank my main supervisor at the University of Copenhagen, Peter Ditlevsen, for all the useful discussions and always being available. A special thank you goes to my co-supervisor Niklas Boers. I am immensely grateful for the useful discussions, the guidance throughout the years, and for always making time for me and believing in me. I also want to thank Rune Graversen for allowing me to use their computing time when I ran out of mine.

My thanks go to the Potsdam Institute for Climate Impact Research and all my colleagues there for having me as guest researcher, preparing excellent press releases, and providing me with storage and computing time over many years. Furthermore, I want to thank all the people from the Earth System Modeling group at TUM that always gave me very useful feedback and ideas. I also want to thank the Physics department at UiT for providing me with coffee for the last two years. Thanks to the students I taught for the funny moments and the much-needed breaks from research. I want to thank all my colleagues at UiT and especially my group, with special thanks to my colleague Anna Poltronieri. I am thankful for the countless and often useless conversations, the horrible travel experiences, the shared suffering (and Covid), the tears and laughter throughout the last three years. I am also grateful for all the amazing and smart people I have got to know through these years, with special thanks to the TiPES and CriticalEarth community as well as the CHES research school for great discussions and organising many great conferences, summer schools and workshops.

I want to thank all my friends both in and outside of Germany. A big thank you goes to my family and especially my brother Paul and my grandparents Sigrid and Werner for all the support and for always welcoming me back in Germany. Finally, I want to thank my significant other, Eleonora Qvist, and her family. I am grateful for all the support, patience, love and food throughout the years.

Contents

Abstract	i
Abstract (DK)	iii
Acknowledgements	v
List of Figures	ix
1 Introduction	1
2 Tipping Points and Elements	5
2.1 Underlying Theoretical Concepts	5
2.1.1 Bifurcations and Beyond	5
2.1.2 Early-Warning Signals	13
2.2 Overview of Potential Tipping Elements	17
2.3 Greenland Ice Sheet	19
2.3.1 Mass Balance	19
2.3.2 Surface Mass Balance Components	20
2.3.3 Feedback Mechanisms	22
2.4 South American Monsoon System	24
2.4.1 Climatic Background	25
2.4.2 Feedback Mechanisms	27
2.5 The Cryosphere	30
2.5.1 Antarctic Ice Sheet	30
2.5.2 Arctic Sea Ice	32
2.5.3 Permafrost	33
2.5.4 Mountain Glaciers	34
2.6 Atmospheric and Ocean Circulations	34
2.6.1 Atlantic Meridional Overturning Circulation	34
2.6.2 Southern Ocean Circulation	36
2.6.3 Monsoon Systems	36
3 Climate and Earth System Models	39
3.1 Simple Models	41

3.1.1	Energy Balance models	41
3.1.2	Box Models	43
3.2	Earth System Models of Intermediate Complexity	45
3.3	Comprehensive Climate and Earth System Models	46
3.4	Ice-Sheet Models	48
3.4.1	Ice Flow	49
3.4.2	Surface Melt	51
3.4.3	Alternative Modelling Choices	52
4	Deep Learning	55
4.1	Overview	55
4.1.1	Parameterisations, Emulation & Neural GCM	55
4.1.2	Physics-informed ML	57
4.1.3	Other Applications	58
4.2	LaMa	59
4.2.1	Network architecture	59
4.2.2	Loss functions	61
5	Summary of Publications	63
5.1	Paper I	63
5.2	Paper II	65
5.3	Paper III	67
6	Conclusion and Outlook	71
6.1	Summary and Conclusion	71
6.2	Outlook and Future Research	73
	Bibliography	77
7	Paper I: The South American Monsoon System Approaches a Critical Transition	103
8	Paper II: Overshooting the Critical Threshold for the Greenland Ice Sheet	129
9	Paper III: Reconstruction of Climate Fields Using Deep Learning	153

List of Figures

2.1	Visualisation of different tipping types. Three types of tipping are depicted; bifurcation-induced tipping (B-tipping), noise-induced (N-tipping) and rate-induced tipping (R-tipping). The top row corresponds to the stability landscape (potential U_p), where minima correspond to stable equilibria (solid lines, bottom row) and the maximum corresponds to the unstable equilibrium (dashed line). The red circle denotes the system state. Black arrows indicate changes in the system state, while dark blue arrows indicate changes in the potential. In realistic models, all three types of tipping can occur simultaneously, making it challenging to separate them. Adapted from Brunetti and Ragon (2022) ⁸	6
2.2	Schematic bifurcation diagram of a double-fold bifurcation. The system has either one stable equilibrium or two stable equilibria (solid lines) and one unstable equilibrium (dashed line). The top row corresponds to the potential U_p for given p . Either the potential has one local minimum (filled red circle) that corresponds to a stable equilibrium or two stable equilibria and one unstable equilibrium (empty red circle).	8
2.3	Phase diagram in the (λ, x)-plane of system 2.14. (a) For $0 < r < p$, (b) for $r = p$ and (c) for $r > p$. The blue lines correspond to the invariant lines A and B , while the dashed lines denote the quasi-static equilibria \bar{x}_s and \bar{x}_u . Adapted from Ashwin et al. (2012) ¹¹ and reprinted with permission from Bochow (2020) ²⁰	12

- 2.4 **Rate-induced tipping in a potential landscape without multistability.** (a) Potential landscape with one stable state. The state of the system is denoted by the black ball. (b) A slow rate of change leads to a small excursion of the system state (green line) in the potential landscape. Rather than the ball moving, it is the potential landscape itself that moves. Eventually, the system returns to the initial state. (c) In contrast, a fast rate of change leads to a substantial excursion of the system's state in the potential landscape (purple line). Adapted from Feudel (2023)¹⁵. Artwork courtesy of Silas Vagts. . . . 13
- 2.5 **Exemplary potential and trajectories of a double-fold bifurcation with varying forcing.** (a) Potential well for a typical double-fold bifurcation with different trajectories (black lines) with varying noise levels. More transparent trajectories correspond to greater noise level. The red line denotes the noise-free solution (quasi-static equilibrium) of the system. When the critical point is approached the fluctuations around the equilibrium increase. For high noise levels, the transition can occur earlier since the potential well can be crossed sooner. The pink lines show the widening of the potential well towards the critical point. (b) Same as a but for a different perspective. The variance and autocorrelation at lag-one (inset) increase when the critical point is approached. The trajectories and potentials are offset and scaled for clarity. 15
- 2.6 **Map of selection of key tipping elements.** A selection of major tipping elements is depicted. This map does not aim to give a complete picture. Acronyms are as follows; Greenland ice sheet (GrIS), (West) Antarctic ice sheet ((W)AIS), Atlantic Meridional Overturning Circulation (AMOC), South-American Monsoon system-Amazon rainforest (SAMS-AMZ). Adapted from PIK. 18
- 2.7 **Schematic diagram of important feedback mechanisms associated with a critical transition of the coupled SAMS-Amazon rainforest system.** Red arrows depict positive feedbacks that destabilise the coupled system. Green arrows depict effects that potentially stabilise the system, while blue arrows have uncertain impact on the stability of the system. 29

3.1 **Schematic diagram of climate model hierarchy.** (a) Pyramid of different climate models with increasing complexity towards the top. The simplest models are at the bottom of the pyramid, while comprehensive climate models form the top. Some seminal climate models are denoted on the respective levels of the pyramid. The models can be categorised based on the complexity of four components: (i) surface processes, (ii) chemistry, (iii) dynamics and resolution, and (iv) radiation. (b) Same as a but for the model resolution. The respective papers that introduce the models in a are denoted. Adapted with permission from McGuffie and Henderson-Sellers (2014)²⁴⁸. 40

3.2 **Schematic bifurcation diagram in simple EBM.** Bifurcation diagram of an EBM showing two stable branches (solid blue lines) and one unstable branch (dotted red line). The lower branch corresponds to the ice covered snowball Earth, while the upper branch corresponds to present day climatic conditions. For the present day solar constant S , three states are possible, two of which are stable (yellow and purple dots). The bifurcation gives rise to hysteresis (A,B,C). Adapted with permission from McGuffie and Henderson-Sellers (2014)²⁴⁸. 43

4.1 **LaMa network architecture.** The mask m and image x are concatenated into one input tensor x' and fed into the network. Subsequently, x' is down-scaled, several FFC blocks are applied and the tensor is up-scaled again to give the initial resolution. The concept behind the FFC block is depicted. The input tensor gets split into two interconnected local and global branches. Eventually, the multi-component loss \mathcal{L} is optimised to give a realistic inpainted image \hat{x} . Adapted from Suvorov et al. (2021)³⁴⁵. 61



Introduction

Climate change is one of the most serious threats to human society in the near future, manifesting itself across various temporal and spatial scales. Most prominently, there has been a steady increase in global mean temperatures (GMT) since the industrial revolution¹. There is unequivocal agreement that anthropogenic activities, primarily greenhouse gas emissions, are causing global warming, with current global mean temperatures having exceeded 1.1°C (2011-2020) above pre-industrial levels (1850-1900) (ref.¹). Besides the trend in the GMT, the impacts of human-made climate change are already evident today, manifesting as, for example, rising sea levels or an increased frequency of extreme events, with vulnerable communities being disproportionately affected by it¹. Continued greenhouse gas emissions will further exacerbate climate change with projected GMTs ranging from 1.4°C (very low emission scenario) to 4.4°C (very high emission scenario) above pre-industrial by the end of this century¹. At the same time, changes on a regional and local scale are expected to be even more severe with local precipitation changes of up to 40% or temperature changes of more than 7°C (ref.¹).

While international initiatives to mitigate climate change have made progress over the last decade, current agreements make it likely that the GMT will exceed 1.5°C and potentially 2°C by the end of the 21st century¹. According to the Intergovernmental Panel on Climate Change (IPCC), the window of opportunity to ensure a sustainable and habitable planet is rapidly closing and immediate action is needed to limit global warming². Considering the current efforts to reduce greenhouse gas emissions, the question arises regarding

the extent to which current warming levels may already lead to irreversible, unavoidable, and abrupt changes, or if an overshoot is acceptable under certain circumstances. In this context, the concept of tipping elements and tipping points have received considerable scientific and public attention in recent years. The IPCC defines a tipping point as a critical threshold beyond which a system reorganises, potentially irreversibly². Once the critical threshold is crossed, feedback loops lead to self-perpetuating changes in the system even if external forcing, i.e. global warming, would be brought to a halt.

Especially large-scale components of the Earth system are of interest due to their potentially global impact. Indeed, paleoclimatic evidence suggests abrupt, large-scale Earth system changes in the past³. According to the IPCC, there is high confidence in a threshold behaviour of several Earth system components such as the Greenland ice sheet². While there is relatively low agreement on the exact values of many tipping point thresholds, many estimated thresholds lie within the temperature projections for the end of this century. In other words, crossing estimated thresholds becomes likely under current warming rates and hence every additional increment in the temperature increases the risk of irreversible changes. While increasing computational power over the past decades allowed for extensive computer simulations of the whole Earth system and its components, there is still a considerable knowledge gap about many tipping elements.

First, many processes on a small scale still cannot be explicitly resolved in climate models and need parameterisation due to limited computing resources, leading to uncertainty in projections, particularly on long time scales. Second, it is difficult to detect characteristic changes associated with tipping points in observational data, especially due to the sparsity of records. Observational datasets are optimised to capture long-term mean trends rather than to preserve higher-order statistics that are often used as indicators to assess the stability of a system⁴. This can lead to biases in these early-warning indicators and can give false impressions of the stability of tipping elements. However, recent developments in artificial intelligence hold the potential for substantial progress in the field of climate science. Artificial intelligence-based methods have been shown to realistically reconstruct historical records^{5,6}. They can potentially overcome the shortcomings of conventional methods and yield new insights, for example, into the past dynamics of tipping elements. This could reduce biases in early-warning indicators, allowing for better assessments of the stability of tipping elements. Additionally, several new Earth system models that leverage the advantages of classical physics-based models and data-driven methods are being developed. The first coupled neural climate model has recently been proposed, potentially introducing a new era of climate modelling⁷.

The main contributions of this thesis are the three distinct yet related pa-

pers. Each paper explores a different research question, all connected by the overarching theme of climate modelling. First, we explore the potential of the coupled South American monsoon-Amazon rainforest system to exhibit tipping behaviour by combining results from both models and observations. Second, we investigate the long-term consequences of overshooting the critical threshold of the Greenland ice sheet using two state-of-the-art ice-sheet models. Lastly, we introduce a new deep learning-based method for reconstructing spatiotemporal climate fields.

Outline

This thesis comprises two thematically distinct but interconnected parts. The first and main part of the thesis focuses on tipping elements, while the second part discusses different climate modelling approaches. First, we briefly lay out the theoretical foundation of tipping points, including the different types of bifurcations and early warning signals (Section 2.1), followed by a comprehensive, though not exhaustive, overview of important tipping elements in the Earth system (Section 2.2). We then provide detailed overviews of the climatic conditions and potential feedback mechanisms relevant for the Greenland ice sheet (GrIS) (Section 2.3) and the South American Monsoon System (SAMS) (Section 2.4). The remainder of Chapter 2 concludes with a succinct overview of feedback mechanisms for other relevant tipping elements. The second part discusses the hierarchy of models, ranging from the simplest energy balance models to comprehensive climate models (Chapter 3). Special emphasis is given to ice-sheet models, including the governing equations for ice flow and other modelling choices (Section 3.4). Chapter 4 gives an overview of machine learning (ML) applications in climate science and a description of the machine learning-based model (LaMa) used in this thesis (Section 4.2). Summaries of the three papers constituting this thesis are presented in Chapter 5. Finally, Chapter 6 concludes the thesis, offering an outlook for future research. The three papers written for this thesis are included in Chapters 7 to 9.

/2

Tipping Points and Elements

2.1 Underlying Theoretical Concepts

The concept of tipping points and their underlying theory have been steadily developed in recent years. Three types of tipping can be differentiated: (1) bifurcation-induced tipping, (2) noise-induced tipping, and (3) rate-induced tipping. The idea behind the different types is illustrated in Fig. 2.1. Besides the ongoing research into theoretical mechanisms behind tipping points, considerable effort is being made to accurately predict and identify precursor signals of tipping points. The following sections provide an overview of the three different types of tipping and explain the concept behind the notion of early-warning signals (EWS).

2.1.1 Bifurcations and Beyond

Bifurcation Induced Tipping

The most studied mechanism for a sudden change in a nonlinear system is so-called bifurcation induced tipping. A (local) bifurcation occurs when a change in a control parameter p causes a stability change of the equilibrium of the system. The system passes a *bifurcation point* p_c that causes a sudden

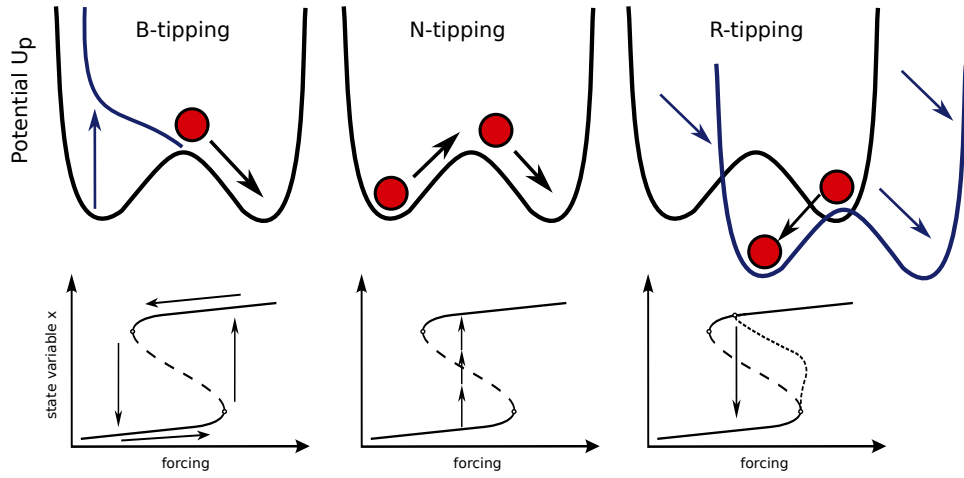


Figure 2.1: Visualisation of different tipping types. Three types of tipping are depicted; bifurcation-induced tipping (B-tipping), noise-induced (N-tipping) and rate-induced tipping (R-tipping). The top row corresponds to the stability landscape (potential U_p), where minima correspond to stable equilibria (solid lines, bottom row) and the maximum corresponds to the unstable equilibrium (dashed line). The red circle denotes the system state. Black arrows indicate changes in the system state, while dark blue arrows indicate changes in the potential. In realistic models, all three types of tipping can occur simultaneously, making it challenging to separate them. Adapted from Brunetti and Ragon (2022)⁸.

qualitative change of its behaviour⁹. In other words, a system has a bifurcation point at a critical value p_c if the value separates two regions of qualitatively different behaviour¹⁰. When speaking about tipping points or critical thresholds in climate science, it is often implied that the tipping point is a bifurcation point.

More technically we can consider the open system

$$\frac{dx}{dt} = -\partial_x U_p(x) = f(x, p(t)), \quad (2.1)$$

with the time-varying input $p(t)$ and the potential $U_p(x)$. We refer to the stable solution of the parameterised system, that is when p is constant, as quasi-static attractor¹¹. If $p(t)$ passes through a bifurcation point, the attractor loses stability and the system tips.

To exemplify a bifurcation-induced transition, consider the simple system

$$\frac{dx}{dt} = f(x, p) = p - x^2, \quad t > 0. \quad (2.2)$$

The equilibria of the system, that is where $f(\bar{x}, p) = 0$, correspond to

$$\bar{x}_1 = \sqrt{p}, \quad \bar{x}_2 = -\sqrt{p}.$$

Both equilibria are hyperbolic; that is the Jacobian matrix of the linearised system has no eigenvalues with zero real parts¹². At the bifurcation point $p_c = 0$, the two equilibria collide, form a saddle-node equilibrium, and then disappear. Since both equilibria are hyperbolic, their stability is determined by the sign of the real part of the eigenvalues of the Jacobian matrix. Therefore, \bar{x}_1 is stable, while \bar{x}_2 is unstable. This type of bifurcation is referred to as a saddle-node or fold bifurcation.

In climate science, the double-fold bifurcation, that is a fold bifurcation with two stable branches, is often used as a conceptual model for tipping elements (Fig. 2.2). Consider the following system

$$f(x) = ax(t) - bx^3(t) + p, \quad a, b, p \in \mathbb{R} \text{ and } a, b > 0. \quad (2.3)$$

$$U_p(x) = \frac{a}{2}x(t)^2 - \frac{b}{4}x^4(t) + px(t) \quad (2.4)$$

The parameter a determines the distance between the two stable branches, while b determines the nonlinearity in the system¹³. The system can have one to three equilibria and the number of equilibria can be determined by the discriminant of system 2.3 (ref.¹³). The discriminant is given by $D = (bp/2)^2 - b(a/3)^3$ (ref.¹³). For $D > 0$ there is one stable branch, while there are two stable branches for $D \leq 0$. The critical value p_c for given a, b and $D = 0$, where the system transitions from two stable branches to one, is given by¹³

$$p_c(a, b) = \pm 2\sqrt{\frac{1}{b} \left(\frac{a}{3}\right)^3}. \quad (2.5)$$

For $-p_c < p < p_c$ the system has two stable and one unstable equilibrium.

The potential U_p is useful to visualise the stability of the system for given p (top row Fig. 2.2). For $p < -p_c$ there is one local minimum which corresponds to the lower stable branch. When the control parameter p exceeds $-p_c$ but is still less than p_c , a new local minimum and a new local maximum emerge, corresponding to the alternative stable and the unstable branches, respectively. The parameter range with more than one stable equilibrium is called the multistability range or bistability range if there are exactly two stable equilibria. Assume the state variable x tracks the lower stable branch, then the system does not tip towards the upper stable branch before $p > p_c$. Once the bifurcation point p_c is exceeded, the system tips toward the only remaining stable equilibrium (upper branch). The local maximum and the other minimum vanish. However,

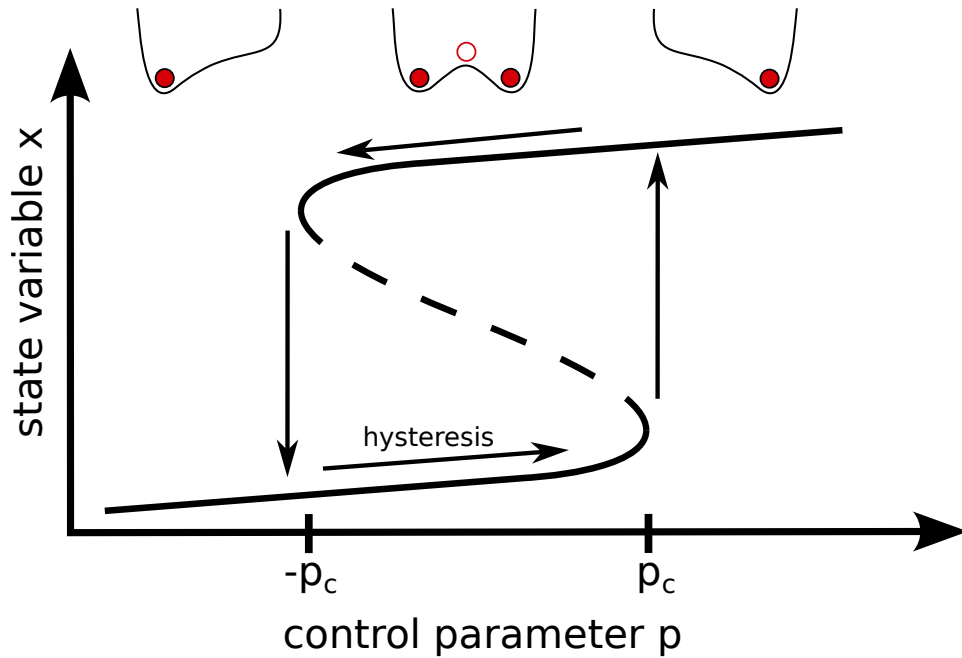


Figure 2.2: Schematic bifurcation diagram of a double-fold bifurcation. The system has either one stable equilibrium or two stable equilibria (solid lines) and one unstable equilibrium (dashed line). The top row corresponds to the potential U_p for given p . Either the potential has one local minimum (filled red circle) that corresponds to a stable equilibrium or two stable equilibria and one unstable equilibrium (empty red circle).

if the control parameter were to be reversed again, the system would still track the upper stable branch until $p < -p_c$. This phenomenon is called hysteresis. The state of the system depends on its history. In climate science, this is of special interest since hysteresis can potentially give rise to a range of (quasi-)irreversibility of a tipping element. Once the critical threshold is crossed, there might be no practical way to reverse the change of the system's state.

There are many other types of bifurcations such as the pitchfork, transcritical or Hopf bifurcation¹⁴. While extensively studied in the mathematical literature, these types of bifurcation have been less explored in the context of climate tipping points and we do not consider them here¹⁵.

Noise Induced Tipping

A natural system usually experiences high-frequency forcing due to external and internal fluctuations such as weather variability. These stochastic perturbations potentially give rise to noise-induced tipping, where a transition can

occur without crossing a bifurcation point. Aswhin et al.¹¹ define noise-induced tipping as an escape of a system from the neighbourhood of a quasistatic attractor as the result of noisy fluctuations. In the picture of the potential landscape, the ball can jiggle in the minimum, but a large enough perturbation or sufficient consecutive perturbations (the noise) can push the system across the basin boundary (the maximum) toward the alternative equilibrium without ever crossing the bifurcation point (Fig. 2.1). Alternatively, one can define a noise-induced transition as a qualitative change in the probability distribution of the system's state, with the noise intensity as the bifurcation parameter^{15,16}.

To exemplify the effect of noise on a system, consider the following pitchfork bifurcation,

$$f(x, p) = \frac{dx_t}{dt} = px_t - x_t^3 + \sigma\xi_t. \quad (2.6)$$

with the white noise term $\sigma\xi_t$. The deterministic system has one stable solution $\bar{x}_1 = 0$ for $p < 0$ that loses stability when $p > 0$ and two new stable equilibria bifurcate $\bar{x}_{1,2} = \pm\sqrt{p}$. This system corresponds to a Langevin equation $f(x, t) = h(x) + \eta_t g(x) + \Gamma_t$ which describes a diffusion process with additive noise Γ_t and multiplicative noise $\eta_t g(x)$. For the system 2.6 only additive noise is considered, that is, $g(x) = \text{const}$. In other words, the influence of the environmental fluctuations does not depend on the system state¹⁶. The first term in the Langevin equation $h(x)$ describes the deterministic dynamics of the system. In the following, we assume $\langle \Gamma_t \Gamma_{t+\tau} \rangle = 2d_1 \delta(\tau)$ and $\langle \eta_t \eta_{t+\tau} \rangle = 2d_2 \delta(\tau)$.

An alternative, useful way to describe a diffusion process is the Fokker-Planck equation^{16,17}. Later on, the probability distribution $P(x, t)$ governed by the Fokker-Planck equation allows us to draw conclusions about noise-induced transition. The equation is given by

$$\begin{aligned} \partial_t P(x, t) = & -\partial_x [(f(x) + d_2 g(x) g'(x)) P(x, t)] \\ & + 2\partial_x^2 [(d_1 + d_2 g(x)^2) P(x, t)]. \end{aligned} \quad (2.7)$$

This equation describes the time evolution of the probability distribution $P(x, t)$ of the state variable x with additive and multiplicative noise. The solution is given by¹⁷

$$P(x) = \frac{N}{\sqrt{d_2 g(x)^2 + d_1}} \exp \left[\int^x \frac{f(u) du}{d_2 g(u)^2 + d_1} \right], \quad (2.8)$$

with the normalisation constant N . We can rewrite the solution as

$$P(x) = N e^{-\mathcal{V}(x)} \quad (2.9)$$

where $\mathcal{V}(x)$ is the probabilistic or stochastic potential of the dynamics, analogously to the deterministic potential $V(x)$. The potential $\mathcal{V}(x)$ is then given by

$$\mathcal{V}(x) = \frac{1}{2} \ln [d_2(g(x))^2 + d_1] - \int^x \frac{f(u)du}{d_2(g(u))^2 + d_1}. \quad (2.10)$$

For the system 2.6 with only additive noise $g(x) = 0$ and $\Gamma_t = \sigma \xi_t$, the solution and the stochastic potential $\mathcal{V}(x)$ simplify to¹⁶

$$P(x) = N \exp \left[\frac{2}{\sigma^2} \left(p \frac{x^2}{2} - \frac{x^4}{4} \right) \right] \quad (2.11)$$

$$\begin{aligned} \mathcal{V}(x) &= \frac{1}{4} \ln \sigma^2 - \frac{2}{\sigma^2} \int^x f(u)du \\ &= \frac{1}{4} \ln \sigma^2 - \frac{2}{\sigma^2} \left(p \frac{x^2}{2} - \frac{x^4}{4} \right). \end{aligned} \quad (2.12)$$

The deterministic potential $V(x) = -\int^x f(u)du$ is known from earlier. It is now obvious that in the case of purely additive noise, the minima (stable equilibrium) and maxima (unstable) of the stochastic and deterministic potential coincide modulo a constant. They correspond to the equilibria found earlier. Additive noise does not qualitatively modify the stationary behaviour of the system. It just “jiggles” the ball around in the potential but does not change the potential itself¹⁶. Additive noise just smears out $P(x)$ around the deterministic steady states. However, this does not exclude the possibility of transitioning between the alternative states when the noise intensity is large enough. The frequency of jumps between the maxima of the probability distribution (corresponding to the minima of potential) is proportional to the noise intensity d and the height of the potential $\Delta \mathcal{V}(x)$ (ref.¹⁸). For the considered example the frequency is proportional to $\exp(-p^2/2\sigma^2)$. It is obvious, that the transition frequency increases with increasing noise intensity σ .

However, we also see that multiplicative noise changes this picture. If the environmental fluctuations depend on the state of the system, the potential itself changes. For small noise intensities $d_2 \ll 1$ the first term in equation 2.10 does not change the position and number of maxima and minima¹⁶. The external noise is not strong enough to qualitatively change the extrema of the potential. However, the relative heights and depths of the extrema might change even for small noise intensities¹⁶. For large noise the position and number of extrema of $P(x)$ might be substantially different from the deterministic equilibria. The multiplicative noise can create new potential wells that correspond to new system states. In other words, when the noise intensity d_2 exceeds a certain threshold, the shape of $P(x)$ might change drastically, which corresponds to a purely noise-induced transition.

Sometimes, a special case of noise-induced tipping with a one-time large-amplitude perturbation is called shock-induced tipping¹⁵. Here, we do not consider shock-induced tipping separately.

Rate Induced Tipping

In the third type of tipping, the system's state depends on the rate of change of the environment. R-tipping differs from the previous two tipping types in three substantial ways¹⁵: (1) the intrinsic timescale and the timescale of the environmental change are important, (2) no existence of alternative stable states is necessary, (3) the critical threshold is defined by the rate of change of a parameter rather than a parameter itself. In contrast to bifurcation-induced tipping, the potential landscape does not qualitatively change but its position is shifted (Fig. 2.1). If the threshold (the maximum of the potential) moves past the initial position of the system's state for a new forcing level, the system's state is said to be threshold unstable¹⁹. The ball in the potential moves toward an alternative state when the ball is on the other side of the maximum after a sufficiently fast shift, i.e. when the rate threshold is exceeded. However, if the rate of change is slow, the ball can track the initial potential minimum and no tipping occurs.

We consider the simple non-autonomous system, following Ashwin et al. (2012)¹¹

$$\begin{aligned} \frac{dx}{dt} &= (x + \lambda)^2 - p, \quad t > 0 \\ \frac{d\lambda}{dt} &= r. \end{aligned} \quad (2.13)$$

This corresponds to the previously introduced fold bifurcation with an additional parameter $\lambda(t) \in \mathbb{R}$ that drifts with the rate r . The system has two λ -dependent quasi-stationary equilibria ($dx/dt = 0$):

$$\begin{aligned} \bar{x}_s(p) &= \{(x, \lambda) \in \mathbb{R}^2 : \lambda = -\sqrt{p} - x\} \\ \bar{x}_u(p) &= \{(x, \lambda) \in \mathbb{R}^2 : \lambda = \sqrt{p} - x\}, \end{aligned}$$

with the stable node \bar{x}_s and the unstable saddle \bar{x}_u . They correspond to straight lines in the (λ, x) plane (Fig. 2.3). If $p > r$, there are two invariant lines

$$\begin{aligned} A(r, p) &= \{(x, \lambda) \in \mathbb{R}^2 : \lambda = -\sqrt{p-r} - x\} \\ B(r, p) &= \{(x, \lambda) \in \mathbb{R}^2 : \lambda = \sqrt{p-r} - x\}, \end{aligned}$$

with $A(r, p)$ attracting and $B(r, p)$ repelling (Fig. 2.3). For constant λ , i.e. $r = 0$, the quasi-stationary equilibria coincide with the invariant lines. If $0 < r < p$ the invariant line $B(r, p)$ defines a tipping threshold above which initial conditions

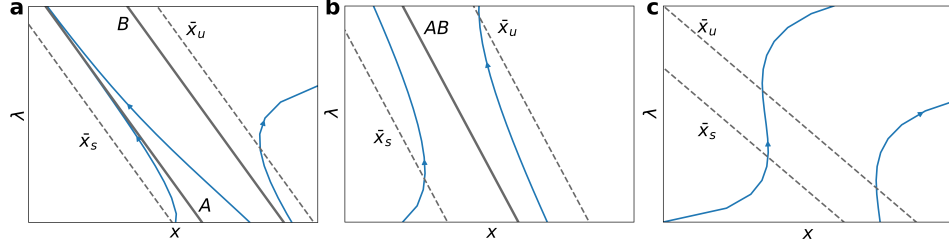


Figure 2.3: Phase diagram in the (λ, x) -plane of system 2.14. (a) For $0 < r < p$, **(b)** for $r = p$ and **(c)** for $r > p$. The blue lines correspond to the invariant lines A and B , while the dashed lines denote the quasi-static equilibria \bar{x}_s and \bar{x}_u . Adapted from Ashwin et al. (2012)¹¹ and reprinted with permission from Bochow (2020)²⁰.

diverge $x(t) \rightarrow \infty$ as $t \rightarrow \infty$, while initial conditions below $B(r, p)$ converge toward $A(r, p)$ (Fig. 2.3). When $r = p$, both invariant lines coalesce into a neutrally stable line AB (Fig. 2.3b). For $r > p$, the line AB disappears and every trajectory becomes unbounded $x(t) \rightarrow \infty$ as $t \rightarrow \infty$ (Fig. 2.3c). The threshold for rate-induced tipping is now the value of r at which the trajectory becomes unbounded, that is when $B(r, p)$ crosses the initial value. Assume an initial condition (x_0, λ_0) at $t = 0$ between $\lambda = -x$ and $\bar{x}_s(p)$, i.e. $-x_0 < \lambda_0 < -x_0 + \sqrt{p}$, then $B(r, p)$ crosses the initial point (x_0, λ_0) when

$$\begin{aligned}\lambda_0 &= \sqrt{p-r} - x_0 \\ r &= p - (\lambda_0 + x_0)^2.\end{aligned}$$

For any other initial values (x_0, λ_0) the critical rate r_c is the rate at which $B(r, p)$ and $A(r, p)$ coalesce and disappear. Therefore

$$r_c = \begin{cases} p - (\lambda_0 + x_0)^2 & \text{if } -x_0 < \lambda_0 < -x_0 + \sqrt{p} \\ p & \text{if } \lambda_0 \leq -x_0. \end{cases}$$

Since the drift is steady in the system 2.14, the problem can be simplified to a saddle-node bifurcation problem via an appropriate coordinate transformation¹¹. However, this is generally not the case. In contrast to bifurcation-induced tipping, it is rather the ability of the system to track the quasi-stable equilibrium than the parameter itself that bifurcates¹¹.

Earlier, we stated that the existence of an alternative stable state is not necessary for rate-induced tipping. Even without an alternative stable state, the system's state can deviate substantially from the quasi-stationary equilibrium if the rate of change is sufficiently fast. This is visualised in Fig. 2.4.

Closely related to rate-induced tipping is the phenomenon of overshooting the critical threshold of a system. Generally, the critical threshold of a system can

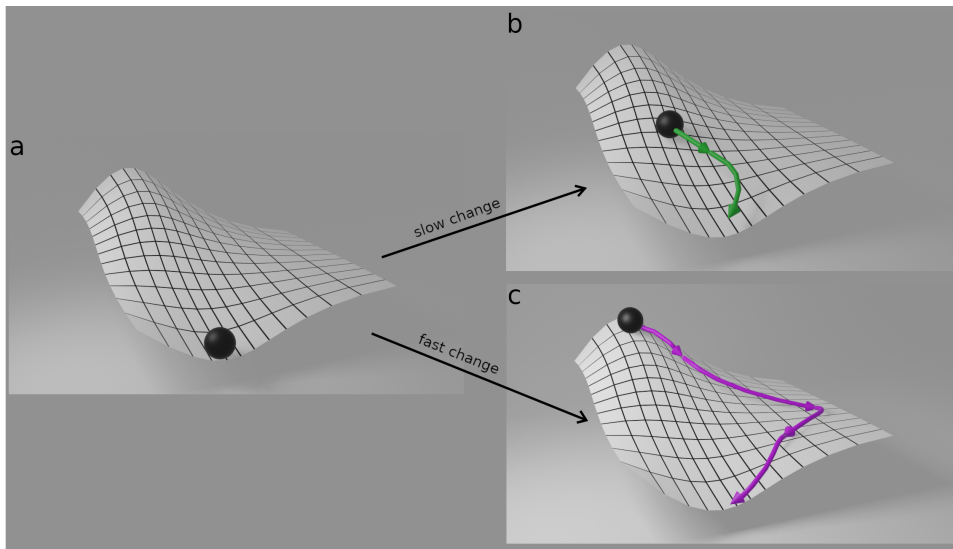


Figure 2.4: Rate-induced tipping in a potential landscape without multistability. (a) Potential landscape with one stable state. The state of the system is denoted by the black ball. (b) A slow rate of change leads to a small excursion of the system state (green line) in the potential landscape. Rather than the ball moving, it is the potential landscape itself that moves. Eventually, the system returns to the initial state. (c) In contrast, a fast rate of change leads to a substantial excursion of the system's state in the potential landscape (purple line). Adapted from Feudel (2023)¹⁵. Artwork courtesy of Silas Vagts.

be overshoot without prompting a transition to an alternative system state if the system reacts slowly compared to the forcing and the forcing is subsequently reversed below the critical value. The tipping behaviour of a system depends on the effective timescale of the system τ , the time above the threshold t_e and the distance above the threshold $\tilde{\chi}$ (ref.^{21,22}). The effective timescale is the time needed to recover from a perturbation in the equilibrium state. For simple dynamical systems, it has been shown that for symmetric overshoots, a system does not tip if the stabilisation level $\chi < 16\tau^2 \tilde{\chi}/t_e^2$ (ref.²¹). This means that there is a time window in which a reversal of the forcing below the critical threshold can prevent a tipping of the system.

2.1.2 Early-Warning Signals

The possibly disastrous consequences of an abrupt transition, especially in the climate system, raise the question if a tipping point can be predicted. In the last years, several methods have been proposed to predict a forthcoming critical transition. A recent metastudy identifies more than 30 different so-called

early-warning signals (EWS)²³. The majority of EWS assumes that the system gradually approaches a bifurcation point which leads to a loss of stability of the system (critical slowing down (CSD)). However, there have also been methods proposed to predict rate-induced and noise-induced tipping^{23,24}. In the following we will follow the classification by Dakos et al. (2023)²³ and distinguish between CSD-based and not-CSD based early-warning signals.

CSD-based EWS

When a dynamical system approaches a tipping point, the system generally needs more time to recover from small perturbations. The restoring forces of the system, that pull the system back to the equilibrium after a perturbation, become weaker and make the system more sluggish²³. In other words, as the system approaches the bifurcation point, the potential V widens and the ball needs more time to return to the minimum. This critical slowing down of the system leaves distinct signatures in the temporal or spatial dynamics of the system that theoretically can be observed²³. The concept of critical slowing down is depicted in Fig. 2.5.

The rate of recovery back to the equilibrium after a perturbation can be approximated by the leading real eigenvalue, i.e. maximum eigenvalue, of the equilibrium solution²⁵. To exemplify this, assume the following simple system²⁶

$$\frac{dx}{dt} = \gamma(x - a)(x - b). \quad (2.14)$$

with the parameters a and b and the scaling factor γ . The system has one stable and one unstable equilibrium at $\bar{x}_1 = a$ and $\bar{x}_2 = b$. We assume \bar{x}_1 is the stable equilibrium in the following. A linearisation using a Taylor-expansion after small perturbation $f(\bar{x}_1 + \varepsilon)$ around \bar{x}_1 gives

$$\frac{d(\bar{x}_1 + \varepsilon)}{dt} = f(\bar{x}_1) + \frac{d\varepsilon}{dt} = f(\bar{x}_1 + \varepsilon) \approx f(\bar{x}_1) + \partial_x f|_{\bar{x}_1} \varepsilon \quad (2.15)$$

and hence

$$f(\bar{x}_1) + \frac{d\varepsilon}{dt} = f(\bar{x}_1) + \partial_x f|_{\bar{x}_1} \varepsilon \Rightarrow \frac{d\varepsilon}{dt} = \lambda_1 \varepsilon. \quad (2.16)$$

The eigenvalues are then given by

$$\lambda_{1,2} = \partial_x f|_{a,b} = \mp \gamma(b - a).$$

For $b > a$, λ_1 is negative and hence \bar{x}_1 is stable. The eigenvalue λ_1 approaches 0 from below toward the bifurcation point, indicating the diminishing of the

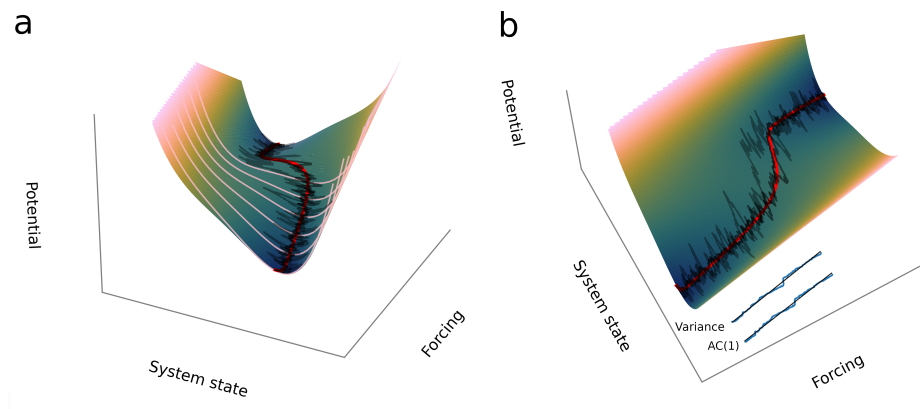


Figure 2.5: Exemplary potential and trajectories of a double-fold bifurcation with varying forcing. (a) Potential well for a typical double-fold bifurcation with different trajectories (black lines) with varying noise levels. More transparent trajectories correspond to greater noise level. The red line denotes the noise-free solution (quasi-static equilibrium) of the system. When the critical point is approached the fluctuations around the equilibrium increase. For high noise levels, the transition can occur earlier since the potential well can be crossed sooner. The pink lines show the widening of the potential well towards the critical point. (b) Same as a but for a different perspective. The variance and autocorrelation at lag-one (inset) increase when the critical point is approached. The trajectories and potentials are offset and scaled for clarity.

restoring forces. The rate of recovery of the linearised system scales exponentially with the eigenvalue $\exp(\lambda\Delta t)$ (ref.^{26,27}). At the critical point $\lambda_{1,2} = 0$, and the system does not recover from a perturbation anymore. In many real-world systems, the exact governing equations and hence the eigenvalues are not known. However, the CSD is visible in the statistical properties of the system.

Given a time series with a fixed small time step Δt , the slowing down of the recovery rate is visible as an increase of the variance and autocorrelation at lag-one (AC(1) or AR(1)) of the time series^{25,26,28} (Fig. 2.5b). It can be shown that the autocorrelation tends toward one and the variance toward infinity when the bifurcation point is approached^{26,28}. In simple terms, when the system approaches the critical point, the state of the system x_t resembles more and more its past states x_{t-1} since the restoring forces decrease, leading to an increase of the autocorrelation at lag-one. At the same time, perturbations lead to larger fluctuations around the equilibrium measurable as increase in the variance. Since other factors, such as a change in the variability of the forcing, can also lead to an increase in variance, detecting both an increase in AC(1) and variance is necessary for a robust early-warning signal²⁸.

There exist spatial analogues of the temporal variance and autocorrelation. It is expected that spatial autocorrelation and variance increase as the tipping point is approached^{23,29}. Other methods based on CSD similarly aim to detect changes in statistical properties associated with CSD²³.

Non-CSD-based EWS

Early-warning signals based on the notion of critical slowing down assume that the noise-to-signal ratio is small and therefore they break down with strong stochasticity²³. Besides the previously discussed EWS, there have been several other methods proposed that are not directly based on critical slowing down, that we will discuss in the following.

In the presence of strong noise, a phenomenon called flickering can occur (Fig. 2.5)³⁰. The system gets pushed into the basin of attraction of the alternative state and subsequently returns to the original state long before the bifurcation. The closer the bifurcation point, the more likely the flickering becomes. While flickering is directly captured by an increase in the variance and is also easily visually detectable, other more advanced methods exist to detect flickering³¹.

A change in the skewness and kurtosis of the probability distribution of the system states close to the bifurcation point is expected^{32,33}. When the system loses stability, a transition to an alternative state becomes more likely and the temporal distribution is expected to become skewed. Depending on the position of the alternative equilibria, the skewness either increases or decreases²³.

Several ecosystems have a clear self-organised spatial structure³⁴. These systems tend to show distinct spatial patterns prior to a critical transition, that are thought to increase their resilience or even allow them to evade tipping³⁵. For example, in dryland ecosystems, the vegetation fragments into smaller patches when the stress on the system is increased²⁹. The forming of spatial patterns in ecosystems as a potential early warning for a forthcoming transition has been studied extensively^{35–38}.

Recently, network-based methods have been proposed to detect critical transitions^{23,39}. They avoid the problem that classical EWS have to detect changes in multivariate systems²³. Changes in the network structure (e.g. connectivity, node centrality) can indicate an approaching tipping point. Alternatively, dimension reduction techniques, such as Principal Component Analysis, can be used to detect changes in multivariate systems²³.

In recent years, machine learning (ML) methods have been used to infer the

proximity of a critical threshold^{40,41}. For example, one can train the ML models on synthetic data with different kinds of critical and non-critical transitions and then apply it to observational data to predict the critical threshold and even the type of transition. It has been shown that these methods outperform classical CSD-based methods and can even be used for spatial systems⁴⁰⁻⁴².

Straightforwardly, one can fit a threshold model, usually a simple dynamical model with a bifurcation, to existing observational data to infer the proximity to a tipping point²³. Another notable method is potential analysis, where spatial or temporal data samples can be used to reconstruct the potential landscape and hence possible thresholds and alternative stable states²³.

There are several other methods that will not be discussed here further. However, it should be noted that all early-warning signals have limitations. First, to use EWS appropriately, it is important to have prior knowledge about the stability of the system in question and that it actually exhibits tipping behaviour⁴³. Furthermore, most EWS requires high-quality and a sufficiently long time series of the system to capture the long-term dynamics of the system. Interpolation or infilling techniques of incomplete time series as well as varying external noise can lead to false-positive or false-negative EWS.

2.2 Overview of Potential Tipping Elements

In recent years, tipping elements emerged as growing and highly policy-relevant research area. More than 25 tipping elements (TE) have been identified so far that could be crossed as global temperatures increase further⁴⁴⁻⁴⁶. At least five tipping elements have been identified in the cryosphere, including the two major ice sheets in Greenland and Antarctica, the Arctic sea ice, local glacier meltdown, and permafrost thaw. More than 10 tipping points in the biosphere, such as large-scale dieback of tropical and boreal forests, die-off of corals, and fishery collapse have been proposed. Furthermore, several large-scale tipping points in oceanic and atmospheric circulations, such as the Atlantic Meridional Overturning Circulation (AMOC), the North Atlantic Subpolar Gyre (SPG), and several monsoon systems, are expected to exhibit tipping behaviour once critical temperature thresholds are crossed. However, there is considerable disagreement about the classification of tipping elements and different studies come to different conclusions⁴⁵.

While definitions of tipping elements vary across the literature, we follow the definition of Lenton et al. (2008)⁴⁴ and Armstrong McKay et al. (2022)⁴⁵, closely related to the notion of a bifurcation-induced transition.

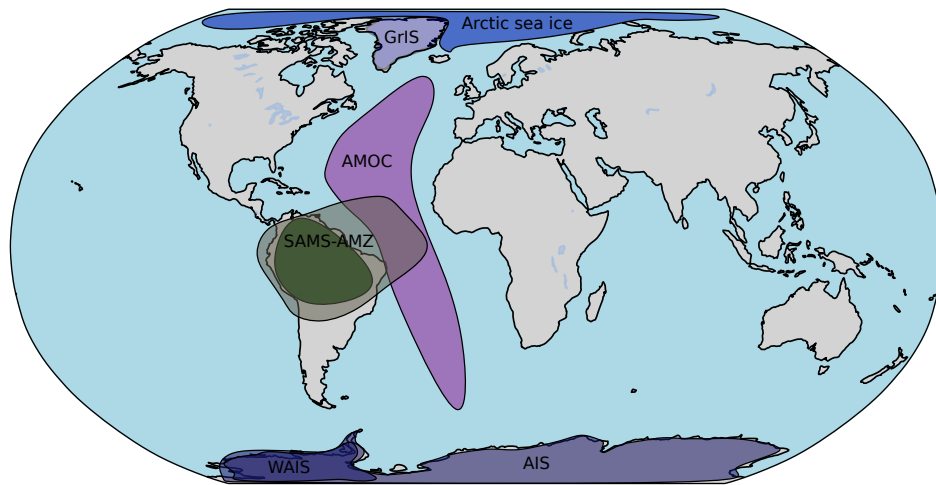


Figure 2.6: Map of selection of key tipping elements. A selection of major tipping elements is depicted. This map does not aim to give a complete picture. Acronyms are as follows; Greenland ice sheet (GrIS), (West) Antarctic ice sheet ((W)AIS), Atlantic Meridional Overturning Circulation (AMOC), South-American Monsoon system-Amazon rainforest (SAMS-AMZ). Adapted from PIK.

Definition. *Tipping elements are components in the Earth system that are suspected to undergo nonlinear, abrupt and self-perpetuating changes once the tipping point is crossed. A tipping point is a critical point (p_c) in a control parameter p (forcing) beyond which a small perturbation (δp) causes a qualitative change (\hat{F}) in the future state of a system after some system-specific observation time ($t > 0$):*

$$|F(p \leq p_c + \delta p | t) - F(p_c | t)| \geq \hat{F} > 0.$$

Tipping elements are generally thought to have implications for the global climate system, while some tipping elements mostly have a local or regional impact⁴⁵. For example, some tipping elements might induce additional radiative forcing or greenhouse gas emissions, thereby potentially intensifying global warming, once they transition to a new state⁴⁶. Some studies propose that dynamic interactions between tipping elements, so-called tipping cascades, could potentially reinforce positive feedbacks and even commit the climate system to several degrees of additional warming^{47–51}. Some of the TEs, such as the large ice sheets, are anticipated to respond on time scales of centuries or millennia to temperature changes. This potentially delayed response of tipping elements can lead to additional warming that is not captured by metrics, such as climate sensitivity, that are widely used to assess the climate response⁵². However, a slow response also implies that there is a window of opportunity where a change in the control parameter could be reversed without triggering

a transition of the system to a new state^{21,53}.

In the following sections, we provide an overview of important potential tipping elements in the Earth system with a focus on cryospheric and atmospheric-oceanic tipping elements, particularly the South American monsoon system and the Greenland ice sheet due to their relevance for this thesis. Due to the complexity of the topic, we do not aim to give a comprehensive overview of all tipping elements in this chapter. Other tipping elements that are not discussed here include tipping elements in the biosphere, i.e. boreal forest dieback, desertification, lake eutrophication, fishery collapse and coral reef die-off as well as more specific tipping elements such as methane release from destabilisation of marine methane hydrate deposits or breakup of stratocumulus cloud decks^{45,46}.

2.3 Greenland Ice Sheet

The Greenland ice sheet (GrIS) is the Earth's second largest ice body with a total ice volume of around 3 million km³, corresponding to a potential global sea level rise of 7.42 m (ref.⁵⁴). Only the Antarctic ice sheet is larger with a sea level rise potential of 58 m (ref.⁵⁵). The GrIS has been hypothesised to exhibit several stable states with a potential for abrupt transitions between them if global temperatures exceed a critical threshold^{45,56–58}. Recent studies show that the GrIS is shrinking at an accelerated rate due to current warming trends^{59–61} and early-warning signals consistent with an approaching critical transition have been found⁶². In the following, we give an overview of the most important processes and feedbacks that govern the stability of the Greenland ice sheet.

2.3.1 Mass Balance

The health of an ice sheet is generally expressed as the mass balance (MB)⁶³. The ice sheet mass balance is the total difference between ablation (A) and accumulation (C)

$$MB = C - A, \quad (2.17)$$

where both terms are positive. Generally, the mass balance is given in units of mass change (Gt per year). The accumulation term is the sum of the surface, internal and basal accumulation. The ablation has an additional frontal ablation (D) contribution due to calving and frontal melting. The sum of surface ablation and accumulation is known as surface mass balance (SMB). The sum of internal balance and SMB are often referred to as climatic balance⁶³. Often the internal

accumulation and ablation, that is the re-freezing and melting in the firn zone, is implicitly included in the surface mass balance⁶³. In the following, we will follow this convention and include the internal balance in the SMB. Thus, the total mass balance can be rewritten as

$$MB = SMB - BMB - D, \quad (2.18)$$

with the basal mass balance BMB and the ice discharge or frontal ablation D (sometimes also called marine mass balance).

In contrast to the Antarctic ice sheet, where an increased ice discharge due to glacier acceleration is causing a decrease in the MB^{61,64–67}, the changes in the mass balance of the Greenland ice sheet are mostly determined by changes in the SMB^{61,68}. However, it is estimated that ice discharge in Greenland will contribute an equal amount to the total mass loss until the end of this century⁶⁹. Since we are mostly interested in the Greenland ice sheet, we will concentrate on the surface mass balance in the following.

The SMB is ultimately linked to the liquid water balance and energy balance at the surface and in the firn layer and can be written as⁶¹

$$SMB = \text{Precipitation} - \text{Runoff} - \text{Sublimation/Evaporation} - \text{Wind erosion}. \quad (2.19)$$

The runoff is the sum of melt, rainfall, condensation and refreezing and retention of water. The melt at the surface is determined by the surface energy balance^{61,70}

$$\text{Melt Energy} = SW_{\text{net}} + LW_{\text{net}} + SHF + LHF + G_S, \quad (2.20)$$

with the net shortwave radiation SW_{net} , net longwave radiation LW_{net} , the turbulent sensible heat flux SHF, latent heat flux LHF and the subsurface conductive heat flux G_S (ref.⁶¹). The terms are defined as positive when directed toward the surface.

2.3.2 Surface Mass Balance Components

The mass gain of the ice sheet is mostly determined by precipitation, that is, rain and snow^{61,71,72}. To a minor extent, the ice sheet can gain mass by water vapour deposition⁷¹. Since the atmospheric temperatures over the ice sheet are usually below the freezing point of water, most precipitation falls as snow⁶¹. However, if temperatures in the atmospheric layers sufficiently exceed the freezing point, precipitation can fall as rain on the surface. Over the last decades the precipitation remained relatively constant with slight increases in parts of

the interior of the ice sheet^{72–76}. However, it is expected that precipitation rates over the GrIS increase with continued warming, especially on the eastern side of the ice sheet^{72,77}.

In the coastal regions, the precipitation is mainly driven by orographic precipitation⁷⁸. The topography of the interior GrIS is relatively flat, while the margins show a complex and steep topography. This leads to high snowfall amounts up to several meters where the topography is steepest, e.g. in southeast Greenland⁶¹. The topography also determines the near-surface winds. Since the net radiation is generally negative at the ice sheet surface⁶¹, the wind regime is mostly katabatic leading to snow redistribution⁷⁹.

The decrease of the SMB is mostly driven by an increasing surface melt due to rising atmospheric temperatures. Melting occurs when excess energy is available at the ice sheet surface and the surface temperatures exceed the melting point⁶¹. Subsurface melt (<10 cm) is also possible if the solar radiation penetrates below the surface^{61,70}. The energy available for melt is determined by the surface energy balance (equation 2.20). There are different pathways for the meltwater at the surface: (1) it can form supraglacial lakes at the surface⁸⁰; (2) it runs off the ice sheet supraglacially⁸¹; (3) it percolates into the snowpack and runs off englacially or subglacially⁸²; (4) it percolates into the snowpack and is stored in liquid form, e.g. as subsurface lakes or in the firn⁸³ or (5) it percolates into the snowpack and is stored in frozen form⁸³. The meltwater retention and refreezing are estimated to be substantial, that is around 45% of the total annual meltwater⁸⁴. Hence, the runoff leaving the ice sheet is generally less than the total surface meltwater.

Evaporation from standing water, e.g. supraglacial lakes on the ice sheet and sublimation of snow particles and the surface contribute further to a mass loss but play a minor role in the total surface mass balance⁶¹. Wind erosion can lead to redeposition of snow from areas where the air flow diverges to areas where the air flow converges⁶¹. This leads to net snow erosion in the former regions and net snow deposition in the latter regions, contributing to changes in the local SMB.

The SMB of the GrIS is strongly influenced by synoptic and large-scale atmospheric circulations. Approximately 80% of the accumulation on the GrIS can be explained by large-scale atmospheric dynamics and its interaction with the topography of the GrIS⁸⁵. Precipitation on the ice sheet is mostly caused by advection of moist and mild air by low-pressure systems branching off the North Atlantic storm track⁶¹. In the winter, cyclonic activity is concentrated around Iceland, reaching regularly to the southern and southeastern parts of the GrIS⁶¹. This induces high precipitation rates in these parts during the winter. During the summer season, the atmospheric flow is mostly blocked by the ice

sheet, causing a north-south atmospheric flow and resulting in precipitation on the west coast of the GrIS. This leads to a pronounced seasonality in the spatial distribution of precipitation over Greenland.

Surface melt on the GrIS is strongly linked to the North Atlantic Oscillation (NAO), a large-scale atmospheric circulation in the North Atlantic^{86,87}. The strength of the NAO is usually characterised by the NAO index, that is the normalised sea level pressure difference between the Azores and Iceland⁶¹. A positive NAO index indicates a zonally directed North Atlantic large-scale circulation while a negative NAO is characterised by a weak or wavy jet stream⁶¹. While the precipitation in Greenland does not significantly correlate with the NAO⁸⁸, negative phases of the NAO favour warmer and drier summers on the GrIS than normal^{86,87}. This led to anomalously high surface melt rates in Greenland in recent decades with a peak in the year 2012 (ref.^{86,87}). The SMB has subsequently returned to previous levels.

2.3.3 Feedback Mechanisms

For the GrIS to be classified as a tipping element, nonlinear positive feedbacks are necessary that lead to an accelerated loss once a critical threshold is crossed. The most important feedback mechanisms for the GrIS are the melt-elevation feedback⁸⁹, melt-albedo feedback^{90–93}, the glacial isostatic adjustment (GIA) feedback⁹⁴, and the precipitation-temperature feedback^{95,96}. In contrast, for marine-terminating ice sheets like the Antarctic ice sheet, feedbacks such as the marine ice cliff instability (MICI)⁹⁷ and marine ice sheet instability (MISI)⁹⁸ are also relevant, but they do not play a major role for the GrIS.

The melt-elevation feedback is thought to be the strongest feedback mechanism for the GrIS. It is caused by the vertical temperature change in the atmosphere. Generally, atmospheric temperature decreases with altitude, a phenomenon measured by the atmospheric temperature lapse rate. When the local surface temperatures increase in Greenland due to, for example, global warming, this leads to increased surface melting. This causes a decrease of the ice sheet surface height, assuming a static bedrock. The lowered elevation exposes the ice to warmer temperatures due to the atmospheric lapse rate, thereby accelerating surface melting and perpetuating a positive feedback loop.

Commonly, the temperature lapse rate is equated with the moist adiabatic lapse rate and considered constant across the ice sheet. The moist adiabatic lapse rate can be derived from thermodynamic relations and is usually assumed to be 5–7°C per km for the GrIS^{99–101}. However, observational studies showed that the lapse rate has a seasonal and spatial variability over the GrIS^{102,103}.

A previous idealised study has found that the melt-elevation feedback alone might be sufficient to cause an irreversible tipping behaviour of the GrIS when a critical temperature is exceeded⁸⁹. Early-warning signals consistent with an approaching critical transition have been found in time series of the melt rates in the southwestern GrIS⁶². This suggests that these parts of the ice sheet are already in the process of tipping, mainly driven by the melt-elevation feedback⁶².

The second important positive feedback mechanism is the melt-albedo feedback^{92,93,104,105}. Darker surfaces absorb more solar radiation than bright surfaces. This leads to more energy being available for melt, increasing the surface melt. Already small changes in the surface albedo can double the amount of absorbed solar radiation^{106,107}. Fresh snow has a high albedo, reflecting most of the incoming solar radiation. Melting decreases the albedo of the snowpack even without removing the snow due to increasing snow grain size¹⁰⁸. As the albedo decreases, more energy is available for melt. Eventually, darker firn or bare ice gets exposed once the fresh snow cover is completely melted, causing even more melt and closing the feedback loop. It has been shown that the albedo induced increase in absorbed solar radiation is the major driver for surface ablation during the summer season of the GrIS¹⁰⁶.

The albedo on the GrIS has a strong seasonal and spatial dependency, with up to 65% difference between months¹⁰⁶. Formation of deep melt ponds¹⁰⁹, surface roughening¹¹⁰, snowline fluctuation¹¹¹, dust deposition¹⁰⁷ or algae growth^{112–114} contribute to seasonal variations in the surface albedo¹¹⁰. In the winter and sometimes during the summer, fresh snowfall interrupts the feedback reducing the surface melt¹¹⁵. In recent years, changes in the albedo caused locally up to 51% of the surface melting when the bare ice is exposed⁹³. A warming climate will likely reduce the albedo in the ablation zone further due to changes in the snow lines, increased meltwater, and algal growth^{110,111}. However, most present-day melt models do not directly represent these processes, potentially underestimating future melt^{111,114}.

In contrast to the previous two feedbacks, the glacial isostatic adjustment feedback is a negative feedback. Changes in the ice load lead to responses of the solid Earth beneath the ice sheet. If the ice load is reduced, the ground beneath the ice sheet lifts up and increases the ice sheet height again. While the ice thickness decreases when ice is lost, the ice surface height does not necessarily decrease. In a first approximation, based on Archimedes' principle, the GIA would compensate approximately one third of the ice sheet thinning⁹⁴. Therefore, the GIA counteracts the positive melt-elevation feedback to some extent⁹⁴.

The response of the viscous bedrock is believed to occur on the timescale of

millennia to decamillennia and therefore generally lags behind changes in the ice load^{94,116}. However, previous studies indicate that the response of the solid Earth might be faster than previously thought¹¹⁷. Currently, the bedrock beneath the GrIS is depressed due to the massive load of the ice. However, the Earth is still not in isostatic equilibrium after the deglaciation of the Pleistocene ice sheets¹¹⁸. Modelling studies have shown that the GIA can even overcompensate the ice loss due to increased temperatures in long-term scenarios⁹⁴.

In addition to the GIA feedback, there is a negative precipitation-temperature feedback^{95,96}. According to the Clausius-Clapeyron relationship, the moisture holding capacity of air increases with increasing temperatures which in turn leads to increasing precipitation rates. This assumes that precipitation is solely driven by the atmospheric temperature and the available atmospheric moisture content. A simple estimate using the Clausius-Clapeyron relationship gives a global scaling factor of 8% precipitation increase per K of warming⁹⁶. For Greenland, the precipitation sensitivity is often estimated to be around 7.3%/K (ref.¹¹⁹). However, the future precipitation sensitivity predicted by climate models varies significantly across models⁵³. While this negative feedback dampens the decreasing surface mass balance with increasing temperatures, it most likely only minimally counteracts the increase in temperature driven surface melt. Additionally, topographic changes of the ice sheet lead to increases of precipitation at the margins of the retreating ice sheet¹²⁰. In coupled ice sheet-atmospheric circulation model simulations, an increase of the cloudiness in the interior of the ice sheet has been observed¹²⁰. This reduces incoming solar radiation and hence surface melt, giving rise to a substantial negative feedback¹²⁰. Furthermore, circulation changes are expected with a retreating GrIS, potentially dampening the ice loss¹²⁰.

2.4 South American Monsoon System

The South American Monsoon System (SAMS) has, until present-day, not been classified as tipping element^{45,46}. However, the Amazon rainforest is generally accepted as a global tipping element with the potential of an abrupt transition to a savanna-like state^{44,121}. The SAMS and rainforest experience pressure from changing temperatures but also from human-made large-scale deforestation of the rainforest that eventually could lead to a dieback of substantial parts of the rainforest⁴⁵. The Amazon rainforest is the world's largest tropical rainforest with rich biodiversity and importance for the local climate. Since the rainforest is a critical component in the global carbon cycle as a major carbon sink¹²² and storage of carbon¹²³, a dieback of substantial parts of the rainforest could accelerate climate change. Our recent study (cf. chapter 7 and 5.1) shows that the SAMS and rainforest are inherently coupled and puts the coupled system

on the map of potential tipping elements for the first time¹²⁴. In the following we will give an overview of the climatic background in South America and Amazonia and summarise possible feedback mechanisms that could lead to a critical transition.

2.4.1 Climatic Background

The South American Monsoon determines the climate in most parts of South America (SA)¹²⁵. A monsoon is most commonly defined as a seasonal reversal of the surface winds¹²⁶. However, it was not until the late 20th century that the SAMS was recognised as a monsoon system since easterly winds dominate the wind regime in South America and the tropical Atlantic all year round¹²⁷. The reversal in the low-level circulation becomes apparent only when examining the monthly wind anomalies. In South America, the monsoon manifests as a pronounced seasonality in the precipitation patterns (wet and dry seasons), trade winds, surface pressure and atmospheric moisture transport¹²⁵. In the southern hemisphere, the wet season in SA is marked by high precipitation rates 2 to 3 months before the Intertropical Convergence Zone (ITCZ) migrates southward¹²⁸. The wet season coincides with the austral summer (boreal winter) (December to February, DJF) and is preceded by a relatively rapid increase in precipitation rates during the spring (September to November, SON) and the dry season in winter (June to August, JJA). In fall (March to May, MMA) the precipitation rates decrease again. North of the equator, the seasons are reversed meaning that the wet season is in austral winter (JJA)¹²⁹. The climatic conditions in the Amazon Basin are therefore largely determined by the SAMS.

The seasonal cycle is primarily driven by the differential heating between the South American land mass and the Atlantic Ocean¹²⁵. Several mechanisms have been proposed that are associated with the wet season onset in SA^{130–133}. During the initiation phase (90 to 50 days before the wet season onset), the atmospheric moisture content begins to increase. The main contributor of increasing water vapour during this phase is an increase in the evapotranspiration¹³⁰. This is caused by an increasing surface latent heat flux due to an increase of the downward solar radiation¹³⁰. While the rainfall increases slightly towards the end of the initiation phase, the cross-equatorial flow remains mostly the same as in the dry season.

During the developing phase (50 to 0 days before wet season onset), dynamic processes become more important. The net moisture flux changes from divergence to convergence due to moist air transported from the Caribbean Sea to Amazonia¹³⁴. While the evapotranspiration rates remain at a similar level as in the initiation phase, the moisture convergence becomes an important water

vapour source¹³⁰. Precipitation rates increase steadily during this phase with a rapid increase towards the onset. At the same time cold air fronts periodically enter the Amazon basin from the extratropics¹³². These cold intrusions can cause sharp temperature drops in large parts of SA¹³⁵. The cold fronts are followed by intense rainfall events at the boundaries of these fronts east of the Andes (northwest-southeastern orientation)¹³². When these fronts enter the Amazon basin, northerly or northwesterly winds transport warm and moist air from western Amazonia to southeastern Brazil, intensifying moisture convergence and setting up wet season conditions^{132,136}. Rainy events caused by these cold fronts heat the atmosphere through diabatic heating and drive a reversal of the cross equatorial flow, enhancing the moisture inflow from the Atlantic ocean¹³⁶. This can trigger the wet season onset if the atmospheric and land surface conditions are sufficient, i.e. when the atmosphere is humid and unstable enough¹³². Eventually, moisture convergence becomes a greater source of water vapour than evapotranspiration and the enhanced response of the moisture convergence to increased rainfall drives the wet season¹³⁰. It has been shown that the wet season onset is further accelerated or potentially initiated by rainforest transpiration during the transition season¹²⁸.

Other important features of the SAMS, besides the strong seasonal cycle, are the South Atlantic Convergence Zone (SACZ), the Bolivian High, the Northeast Trough, the low-level Gran-Chaco Low and the northerly low-level jet¹²⁵. The SACZ is characterised by northwest-southeast orientated precipitation and persistent cloudiness and determines large parts of the climate in southeastern South America.

The SAMS exhibits strong interaction with the land surface, ocean and biosphere, leading to variability in the strength and extent of the SAMS. Intraseasonal variations are modulated by the Madden-Julian oscillation¹³⁷ and other tropical-extratropical interactions¹³⁸. Variations on the interannual timescale in the precipitation rates in SA can mostly be explained by the El Niño Southern Oscillation (ENSO)¹³³, land surface processes¹³⁹ and sea surface temperature anomalies in the tropical Atlantic ocean¹⁴⁰. Multi-annual and interdecadal variability has been linked to the Atlantic Multidecadal Oscillation (AMO) and the Pacific Decadal Oscillation (PDO)¹²⁵.

Modelling studies indicate a spatial expansion of the SAMS westward and eastward over the oceans with continued global warming¹²⁵. Furthermore, the seasonal differences between wet and dry season are expected to intensify with a strong spatial dependency. The average precipitation during the wet season is expected to increase. At the same time, a lengthening of the consecutive dry days is anticipated¹⁴¹. However, there is still high uncertainty about the effect of climate change on the SAMS¹²⁵.

Besides the changing climate, the SAMS-rainforest system is threatened by anthropogenic deforestation. Land-use change in Amazonia affects the local and regional climate through changes in the surface energy and hydrological balance¹⁴². Intensive deforestation and global warming threaten the rainforest and have turned it into a net carbon source in the recent years¹⁴³. Around 20% of the Brazilian rainforest has already been cleared¹⁴⁴ with accelerated deforestation rates in the last years⁴⁵. Deforested areas have higher albedo than forest which leads to reduction in the absorbed solar radiation and evapotranspiration¹⁴⁵. Large-scale deforestation is expected to increase local temperatures by several degrees and change precipitation patterns^{146,147}. A meta-analysis of modelling results showed that deforestation leads to an average reduction of precipitation of more than 10% in the Amazon basin with a more severe reduction during the dry season^{147,148}. This projected drying trend would increase the fire pressure on the rainforest and human-induced fires could further increase the vulnerability of the rainforest¹⁴⁹.

2.4.2 Feedback Mechanisms

Observational and modelling studies suggest that a large fraction of the vegetation in the Amazon basin exhibits several stable states with critical thresholds in the deforestation, precipitation and warming rates^{45,147}. Large-scale deforestation, changes in the precipitation patterns or substantial warming could push large parts of the rainforest beyond these thresholds and initiate self-reinforced drying, tipping it into a degraded or savanna-like state⁴⁵. Several feedback mechanisms have been hypothesised that could lead to this critical transition (Fig. 2.7). However, there is considerable uncertainty in their extent.

The rainforest is inherently coupled to the SAMS via its interaction with the moisture transport across SA. Generally, the Amazon rainforest receives substantial amounts of precipitation with an annual mean of 2,200 mm (ref.⁴⁶). However, it has been shown that there is a limit of approximately 1,600 mm of yearly precipitation below which a closed-canopy rainforest in South America could not be sustained, making the rainforest a potentially bistable system^{150,151}. A substantial fraction (between 25% and 35%) of the precipitation over large parts of the rainforest is recycled by the rainforest itself through evapotranspiration with a strong east to west gradient^{152,153}. During the dry season, the recycled moisture is the main source of precipitation⁴⁶. If forest is lost due to deforestation, droughts and fires, the regional moisture recycling gets perturbed. Reduced forest cover means less water recycling via evapotranspiration, leading to decreasing rainfall in remote parts of the rainforest during wet and dry season. The increased water stress leads to an increase in the large tree mortality¹⁵⁴ and reduces forest cover. This contributes further to climate change

due to the release of stored biomass carbon. The overall rainforest area shrinks and is replaced by more fire prone vegetation, inhibiting rainforest regrowth further⁴⁶.

In addition to the changes in the regional moisture recycling, it is hypothesised that large-scale deforestation of the rainforest changes the atmospheric circulation of the SAMS itself, ultimately leading to a large-scale reduction in precipitation rates in SA and eventually causing dieback of substantial parts of the rainforest^{124,155}. Increased forest loss reduces the atmospheric moisture content and hence the average latent heat over Amazonia due to decreasing evapotranspiration. The heating gradient between the ocean and continent, i.e. the major driver of the seasonal cycle of the SAMS, weakens and impedes the yearly transition into the wet season. The shortened wet season and longer dry season increase the water stress on the trees via reduced precipitation rates and depletion of the soil, which acts as a buffer during the dry season. This increases the tree mortality and eventually causes dieback of large parts of the remaining rainforest when the atmospheric moisture content and thus the latent heating does not suffice anymore to switch the system back into the yearly wet season. This would push the coupled system into a permanent dry season state with reduced precipitation rates in large parts of SA.

However, there is still uncertainty if deforestation actually leads to a decreased moisture inflow¹⁵⁶. Some models simulate an increasing moisture inflow into the continent from the Atlantic ocean with increasing deforestation^{157,158}. This is most likely due to a decreased surface roughness that increases the surface wind acceleration and subsequently the precipitation rates in intact regions of the rainforest¹²⁴. It is unclear to what extent this effect outweighs the aforementioned positive moisture feedbacks.

Furthermore, a positive deforestation-drought feedback has been proposed¹⁵⁹. More intense droughts are accompanied by increased human-induced deforestation. This occurs mostly because clear-cut deforestation is facilitated by increased dry-season intensity and forest fires spread more easily with drier conditions¹⁵⁹. Additionally, reduced precipitation in deforested agricultural areas might force agricultural activity further into deeper rainforest areas. Although this feedback currently appears to be weak, it could become increasingly important as water stress in the Amazon basin intensifies.

Besides a possible deforestation-induced transition, a critical local temperature threshold of 3-4 °C has been proposed beyond which a rainforest dieback would be likely^{45,147}. While modelling results generally concur that the temperatures in the Amazon basin will increase over the 21st century, there is considerable variability in the projected precipitation trends⁴⁶. The direct effects of rising CO₂ levels on the plant physiology remain uncertain as well. While increased

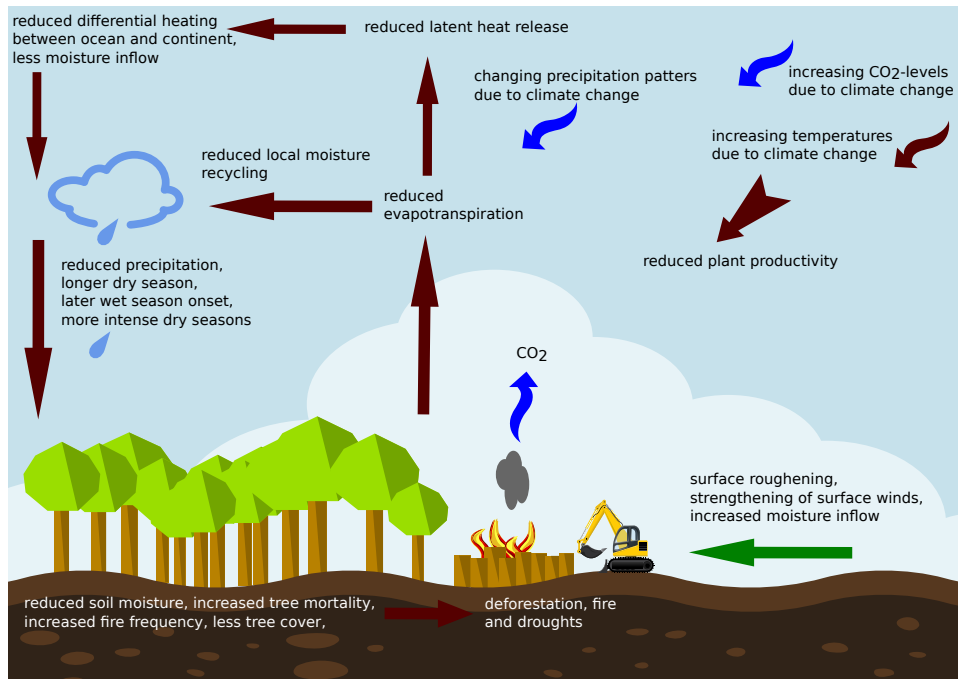


Figure 2.7: Schematic diagram of important feedback mechanisms associated with a critical transition of the coupled SAMS-Amazon rainforest system. Red arrows depict positive feedbacks that destabilise the coupled system. Green arrows depict effects that potentially stabilise the system, while blue arrows have uncertain impact on the stability of the system.

CO₂-levels are thought to increase the biomass production of plants due to the so-called CO₂-fertilisation effect, the Amazon rainforest biomass growth is likely strongly limited by other factors such as the availability of phosphorus in the soil^{160,161}. Elevated CO₂ levels might also reduce the rate of stomatal leaf opening and hence reduce the evapotranspiration and precipitation recycling rate⁴⁶.

Statistically significant changes in the hydrological budget have been observed over recent decades in SA, particularly in the Amazon basin, which are consistent with an approaching critical transition¹²⁴. The dry season has lengthened in large parts of the Amazon rainforest^{162,163} and is associated with a delayed onset of the wet season^{143,164,165}. Southeastern Amazonia shows a declining trend in precipitation rates¹⁶⁶ and there has been an increase in the cumulative water deficit over recent decades¹⁶⁷. Additionally, extreme droughts have become more frequent, driving increasing tree mortality^{154,166,167}. Evidence suggests that tropical forests are nearing the critical temperature beyond which photosynthesis fails¹⁶⁸ and seasonal temperatures have already increased by 1.6 to 2.5°C in some parts of the Amazon basin¹⁴³. Recently, statistical early-

warning signals consistent with an approaching transition have been detected in the precipitation rates across South America (cf. Section 5.1)¹²⁴. Moreover, studies indicate a loss of resilience in large parts of the Amazon rainforest since the 2000s¹⁶⁹. This evidence collectively suggests that the coupled system is undergoing change and may be nearing a critical transition in response to anthropogenic forcing.

2.5 The Cryosphere

The cryosphere encompasses all elements in the Earth system that are in the form of ice or snow, for example the two major ice sheets in Greenland and Antarctica, glaciers, permafrost and the sea ice. This section provides a brief overview of the major cryospheric tipping elements, besides the Greenland ice sheet which has been discussed in Section 2.3.

2.5.1 Antarctic Ice Sheet

Ice sheets are generally considered to be major tipping elements. The Earth system's two major ice sheets, located in Greenland and Antarctica (AIS), have a potential of more than 60 meters of global sea level rise when completely melted^{54,55}. In recent decades, the sea-level rise contribution from the GrIS and AIS has accelerated by more than 700% compared to the period 1992-2001⁴⁶. Currently, both ice sheets together contribute between 1.2 mm and 1.9 mm to global sea-level rise each year^{170,171}. Continued global warming is expected to initiate a potentially irreversible large-scale loss of the GrIS and western Antarctic ice sheet (WAIS) followed by a retreat of the eastern Antarctic ice sheet with higher warming levels^{45,46}.

Paleoclimatic evidence shows that the global sea level may have been several meters higher during the Eemian (ca. 1°C warmer than today) and Pliocene (2-3°C warmer than today) compared to present-day^{172,173}. However, the magnitude of sea level rise during the Eemian remains uncertain, ranging from 1 to 9 m (ref.¹⁷³⁻¹⁷⁵). The sea level during the Pliocene epoch is estimated to have been 22±10 m higher than present-day level, with a contribution of 3 to 10 m solely from the eastern Antarctic ice sheet¹⁷².

Feedback Mechanisms

The feedback mechanisms governing the stability of the ice sheets are remarkably different between the GrIS and the AIS. The ice loss in Greenland is mostly

driven by increasing surface temperatures (cf. Section 2.3) while the AIS ice loss is mostly driven by marine warming. Large parts of the AIS, especially the WAIS, are marine-based, i.e. grounded below sea level and lie on retrograde bedrock (reverse slope) forming ice shelves and marine terminating ice streams at the margins^{46,176}. There are two dominant feedback mechanisms for marine-terminating ice sheets, i.e. the Marine Ice Shelf Instability and the Marine Ice Cliff Instability, that can lead to an abrupt and irreversible loss.

The first mechanism, known as the Marine Ice Shelf Instability (MISI), can lead to a self-sustaining retreat of marine ice sheets^{98,177–179}. When the grounding lines, that are the boundaries between grounded and floating ice, in marine ice sheet basins retreat as a result of warming, it can lead to a self-sustaining retreat of the ice sheet. The ice flux across the grounding line is proportional to the thickness of the glacier at the grounding line⁴⁶. As the grounding line retreats, the ice thickness of the ice at the grounding line increases due to the reverse sloping of the bedrock⁴⁶. Subsurface ocean warming leads to increasing melt beneath the ice shelves, causing a retreating grounding line. This leads to accelerated ice flow into the sea, pushing the grounding line even further back and ultimately leads to a collapse of the ice sheet^{45,46}. Several basins in the WAIS are currently retreating in accordance with MISI dynamics^{180–182}. For example, the Thwaites glacier grounding line retreated more than 14 km between the years 1996 and 2011¹⁸². The Thwaites Glacier is considered a critical component for the stability of the entire WAIS, and its collapse could trigger a wider disintegration of the WAIS¹⁸³. Parts of the East Antarctic subglacial basin are also suspected to be affected by the MISI^{184–186}.

When the ice shelves themselves shrink and eventually disappear completely due to warmer oceanic and atmospheric temperatures, a second positive feedback called Marine Ice Cliff Instability (MICI) can be triggered^{46,97}. The buttressing effect of the ice shelf vanishes and can cause an abrupt loss of the ice cliff when the glaciostatic stress exceeds the yield strength of ice¹⁸⁷. In other words, the shear strength of the ice cannot withstand the longitudinal stress at the cliff face any longer and would cause abrupt loss via calving⁴⁶. This threshold is exceeded for cliff heights of approximately 100 m (ref.¹⁸⁷). However, the MICI hypothesis remains highly uncertain and there is no evidence of present-day MICI on the Antarctic ice sheet^{46,185}.

A recent study concludes that current warming rates suggest an unavoidable increase in ocean temperatures during the 21st century, even under the most ambitious mitigation scenarios¹⁸⁸. This could ultimately lead to a collapse of the WAIS¹⁸⁸. While other studies support the notion of an inevitable collapse of the WAIS^{181,189}, a recent study finds no indication of marine ice sheet instability in the WAIS that would imply an irreversible loss^{190,191}. In contrast to the WAIS, the East Antarctic ice sheet is expected to remain stable with high CO₂ levels,

even beyond 650 ppm (ref.⁴⁵). However, CO₂ levels exceeding 1,000 ppm might ultimately trigger self-reinforcing large-scale ice loss⁴⁵.

2.5.2 Arctic Sea Ice

The Arctic sea ice is sometimes considered a tipping element. However, there is considerable disagreement about the extent to which the Arctic sea ice can be considered as such^{45,46}. While McKay et al. (2022)⁴⁵ classify the Arctic winter sea ice (AWSI) as a global core tipping element but not the loss of Arctic summer sea ice (ASSI), Wang et al. (2023)⁴⁶ classify ASSI as a regional tipping element but not AWSI.

In the last decades the Arctic sea ice area has significantly decreased throughout all regions and months^{192–195} and is statistically attributable to anthropogenic emissions¹⁹⁶. The fraction of multiyear sea ice (at least 5 years old) in the Arctic has declined from 30% of the total ice coverage to 2% between 1984 and 2019 (ref.¹⁹⁷). Furthermore, the multiyear sea ice thickness has almost halved over the last three decades¹⁹⁸. This observed rapid decline of the sea ice area regularly outpaces climate model predictions¹⁹².

Feedback Mechanisms

Several positive feedbacks potentially lead to an accelerated loss of the Arctic sea ice. The most prominent feedback is the ice-albedo feedback¹⁹⁴. The bright sea ice is highly reflective while the dark sea surface is highly absorptive. Increased atmospheric and ocean temperatures lead to a decline of the reflective sea ice, increasing the area with open water. The open water absorbs more solar radiation, leading to further warming of the ocean and the lower atmospheric layers. Subsequently, more sea ice melts, closing the feedback loop. The initial thinning of multiyear ice also enhances the melt-albedo feedback, as seasonal sea ice is more susceptible to melting¹⁹⁹. Together with other feedbacks such as the lapse-rate feedback²⁰⁰, the melt-albedo feedback contributes strongly to Arctic amplification, i.e. temperatures in the Arctic increase faster than the global average.

Some negative feedbacks might mitigate the rapid sea ice loss. Seasonal ice regrows faster than multiyear ice while open water loses heat faster to the atmosphere than ice, facilitating the regrowth of sea ice over large areas²⁰¹. The delay in sea ice regrowth further leads to reduced snow cover which usually prevents sea ice regrowth to some extent²⁰². However, these negative feedbacks do not suffice to prevent a further decline of the Arctic sea ice⁴⁶.

An ASSI free Arctic is expected by the middle of the current century, even if global temperatures are kept below 1.5°C above pre-industrial level^{195,203}. Currently, evidence suggests a linear decline of the summer sea ice rather than an abrupt transition to an ice free state with further warming, hinting that the ASSI is already transitioning to a new state⁴⁶. Due to the observed linear response of the ASSI, McKay et al. (2022)⁴⁵ classify the loss of ASSI as a threshold-free feedback. The loss of winter sea ice is expected to be more abrupt than the loss of the ASSI²⁰⁴. However, it is very likely that the AWSI will not be lost before the end of this century even in the most extreme scenarios^{204,205}. Therefore, a year-round ice-free Arctic remains unlikely in the near future. Furthermore, the loss of the AWSI is considered reversible under certain conditions, such as if winter sea temperatures fall below the freezing point again^{204,206,207}.

2.5.3 Permafrost

Permafrost, which covers around 23 million km² of Earth's surface, stores between 1,460 and 1,700 Gt of carbon just in the Northern Hemisphere — twice the amount currently present in the atmosphere⁴⁶. Permafrost is defined as any material that is below freezing temperatures for several consecutive years.

Rising global temperatures, largely attributed to anthropogenic emissions, are leading to widespread warming of the permafrost worldwide²⁰⁸. Additionally, changes in precipitation patterns, wildfires and albedo changes contribute to thawing of permafrost⁴⁶. Thawing permafrost and the subsequent release of stored carbon could significantly accelerate warming rates. However, the timescale on which such a thawing would happen is uncertain⁴⁶. Generally, thawing can be categorized as either gradual or abrupt. The majority of permafrost degradation will likely happen via gradual thaw on timescales of centuries⁴⁶. On local scales, abrupt so-called thermokarst events can be self-perpetuating and can happen on time scales of days to years²⁰⁹. Abrupt thawing has the potential to increase emissions by 50 to 100% compared to gradual thawing⁴⁵. Estimates of carbon released by the end of the year 2300 under the SSP585 scenario vary widely, ranging from a net absorption of 167 Gt C to a release of 641 Gt C (ref.²¹⁰) Currently, the thaw process is dominated by CO₂ release, however the contribution of CH₄ release is expected to increase in the future²¹¹. A collapse of regional permafrost, driven by internal heat production in carbon-rich permafrost, is hypothesised to occur with a GMT anomaly of 4°C over a timescale of 10 to 300 years, potentially contributing an additional 0.2 to 0.4°C to GMT warming^{45,212}.

2.5.4 Mountain Glaciers

Mountain glaciers generally show a similar response to warming as the glaciers in Greenland and Antarctica, albeit on smaller scales. Mountain glaciers are not considered global tipping elements due to their predominantly regional impact. Individual glaciers generally have different mass balance thresholds, i.e. temperature thresholds, for a potential loss. However, synchronous large-scale losses of most glaciers are expected if global warming reaches levels of 1.5–3°C, occurring over a timescale of centuries^{45,201,213–216}. On average, the response of glaciers to warming is expected to be relatively linear until the end of this century²¹⁶. However, on longer time scales, nonlinear effects might become more dominant²¹⁷. Glaciers can recover from mass loss but on a slower timescale than the melt. Furthermore, the recovery of the biophysical and social downstream effects may take a longer time.

2.6 Atmospheric and Ocean Circulations

Several atmospheric and oceanic circulations are classified as potential tipping elements. However, the existence and characteristics of these tipping elements are subject to considerable uncertainty and debate. For instance, the El Niño–Southern Oscillation (ENSO) was previously considered a potential tipping element, but it is now deemed unlikely to undergo abrupt transitions due to global warming²¹⁸. This section briefly reviews three potential examples of atmospheric and oceanic circulations that have been suggested as tipping elements: the Atlantic Meridional Overturning Circulation, the Southern Ocean Circulation and the monsoon systems.

2.6.1 Atlantic Meridional Overturning Circulation

The Atlantic Meridional Overturning Circulation (AMOC) is a self-sustained ocean circulation across the Atlantic Ocean. Warm, saline waters flow northward towards the northern North Atlantic in the upper ocean layer from the tip of South Africa. These waters cool down, sink, and subsequently return southwards in the deeper ocean layers²¹⁸. The AMOC significantly influences the climate and weather of the Northern Hemisphere due to the redistribution of heat between the tropics and the high latitudes. Interannual variability of the AMOC is mostly driven by large-scale wind patterns in the North Atlantic²¹⁹, while salinity and temperature anomalies are driving decadal variability²²⁰.

Increasing temperatures, freshwater runoff from the GrIS, and changes in sea surface temperatures, and sea ice cover as well as enhanced poleward atmo-

spheric moisture transport due to climate change have raised concerns of a slowing down or complete shutdown of the AMOC^{45,46}. Several numerical simulations and paleoclimatic observations suggest the existence of alternative stable states of the AMOC, driven by the salt-advection feedback^{221–223}. The transition between on- and off-states of the AMOC is hypothesised to be one of the main mechanisms of Heinrich events and substantial changes in the AMOC strength are thought to have happened during Dansgaard-Oeschger events^{46,224}. A weakening or collapse of the AMOC would lead to cooling over large parts of the Northern hemisphere, impact monsoon systems, change Arctic sea ice distribution, disrupt marine ecosystems and influence sea level rise²¹⁸. Several studies predict a future slowing or collapse of the AMOC under continued anthropogenic forcing, with a best estimate of a 4°C increase in global temperatures (ranging from 1.4 to 8°C)^{45,225–227}. However, there is a large spread in the model response and the best estimate might rather indicate the uncertainty in the AMOC response^{218,228}. Additionally, there is an ongoing debate about a possibly overestimated stability of the AMOC in climate models^{229,230}. Several studies have shown indications of a slowing down of the AMOC and early-warning signals linked to a critical transition^{62,227,231–233}. However, it has been argued that the currently available observational time series are too short to detect trends in the AMOC stability²³⁴.

Feedback Mechanisms

Due to anthropogenic warming, the freshening of the upper ocean layers from melt water and increased precipitation rates will cause surface waters in the North Atlantic to become less dense²¹⁸. The freshening is primarily caused by accelerated melt from the GrIS (cf. Section 2.3), as well as increasing Arctic river discharge and decreasing Arctic sea ice extent²¹⁸. Subsequently, the sinking process that drives the North Atlantic deep water (NADW) formation is inhibited by the less saline water⁴⁶. A positive advective-convective feedback associated with the subpolar gyre might further inhibit the NADW formation²³⁵. Sometimes, the North Atlantic subpolar gyre itself is classified as a tipping element²¹⁸. A weakening of the NADW formation results in a weaker baroclinic gyre circulation which causes a salt divergence at the convective site, further inhibiting the formation of the NADW⁴⁶. These effects collectively weaken the AMOC and less saline water is brought to the Northern Atlantic, closing the salt-advection feedback loop²²¹. However, the strength and timescale of this feedback are relatively uncertain²¹⁸. Furthermore, other feedbacks related to evaporation and precipitation patterns might temporally mask or even overcome the salt-advection feedback²¹⁸.

Even without additional freshwater influx, the coupling between the AMOC and the subpolar gyre could trigger events similar to Dansgaard-Oeschger events²³⁶.

Climate model simulations have demonstrated that adding freshwater to the AMOC can cause a collapse⁴⁶. However, the freshwater fluxes used in these simulations are often unrealistically large²³⁷. Additionally, studies suggest that the AMOC's response might depend on the rate of freshwater flux, not solely on the magnitude of the influx²³⁸.

2.6.2 Southern Ocean Circulation

The Southern Ocean has potentially two tipping points with global impacts: (1) the Antarctic Overturning Circulation and (2) an abrupt change in the circulation around the Antarctic shelf leading to sudden warming of the ocean temperatures near the ice shelves²¹⁸. The Antarctic Overturning Circulation is the second branch of the global ocean overturning circulation and has been shown to be a key regulator of the global energy balance²¹⁸. A change or even collapse would have global implications, including changes of global precipitation patterns and global ocean heat storage^{239,240}.

Brine rejection is a key mechanism in the Antarctic Overturning Circulation²¹⁸. The salt of the saline water is rejected during the freezing process, creating salty brine that drains into the surrounding sea water, making it heavier and causing it to sink. Compared to the AMOC, projections and understanding of the processes of the Antarctic Overturning Circulation are not very well defined^{218,241}. In recent years, observational and modelling studies have raised concerns about an ongoing decline of the ocean circulation^{240,242,243}. Climate models consistently indicate a potential slowing or collapse of the Antarctic Overturning Circulation, however there is a high uncertainty due to the aforementioned gaps in the process understanding²¹⁸. In West Antarctica, ice cavities are exposed to relatively warm water, driving the ice shelf melt¹⁸⁸. An abrupt warming of these cavities, as simulated by some models, would substantially increase basal melting and ultimately have consequences for the stability of the whole WAIS^{218,244}.

2.6.3 Monsoon Systems

In addition to the South American Monsoon system (cf. Section 2.4), there are two other major seasonal monsoon systems: the West African monsoon (WAM) and the Indian Summer monsoon (ISM)⁴⁶. Monsoon systems play a crucial role in the global hydrological cycle, contributing to around 30% of the global precipitation²¹⁸. Several idealised studies suggest the possibility of abrupt changes in monsoon circulations, however most comprehensive climate models predict more gradual changes with continued climate change^{46,124,245–247}. The possibility of abrupt changes in monsoon circulations is supported by several

paleoclimatic records⁴⁶. Notably, the WAM is thought to have experienced a sudden emergence 6,000 to 15,000 years ago⁴⁶. However, radiative forcing rates during these periods were large compared to current forcing levels⁴⁶.

The mechanisms underlying an abrupt change of the monsoon systems are similar to the one discussed before (cf. Section 2.4). Differential heating between the ocean and the land masses strengthens moisture inflow into the continent, leading to self-reinforcing dynamics. Anthropogenic forcing changes the temperature gradient between ocean and land due to changes in albedo, precipitation, and vegetation, disrupting the moisture-advection feedback. Changes in other Earth system components, e.g. a slowing of the AMOC could further disrupt monsoon circulations⁴⁶. The likelihood of a potential transition of the ISM or WAM toward an alternative state due to ongoing climate change remains uncertain^{45,218}. These changes are generally projected to occur over timescales spanning decades to centuries²¹⁸.

/ 3

Climate and Earth System Models

Climate and Earth system modelling is inherently complex. The 1960s are generally marked as the beginning of modern climate modelling with the introduction of simple energy balance models²⁴⁸. Over recent decades, model complexity has increased in proportion to available computing power, allowing us to resolve more and more processes in the Earth system. However, this increase in complexity often comes at the cost of reduced understanding. The current near-continuous spectrum of climate models in terms of their complexity (Fig. 3.1) allows us to investigate a wide range of different problems, ranging from the paleoclimatic climate to near-past and far-future climate scenarios. In the following chapter, we give a brief overview of different modelling approaches ranging from simple climate models to comprehensive Earth system models with a particular emphasis on the most relevant models, namely, simple models and ice-sheet models.

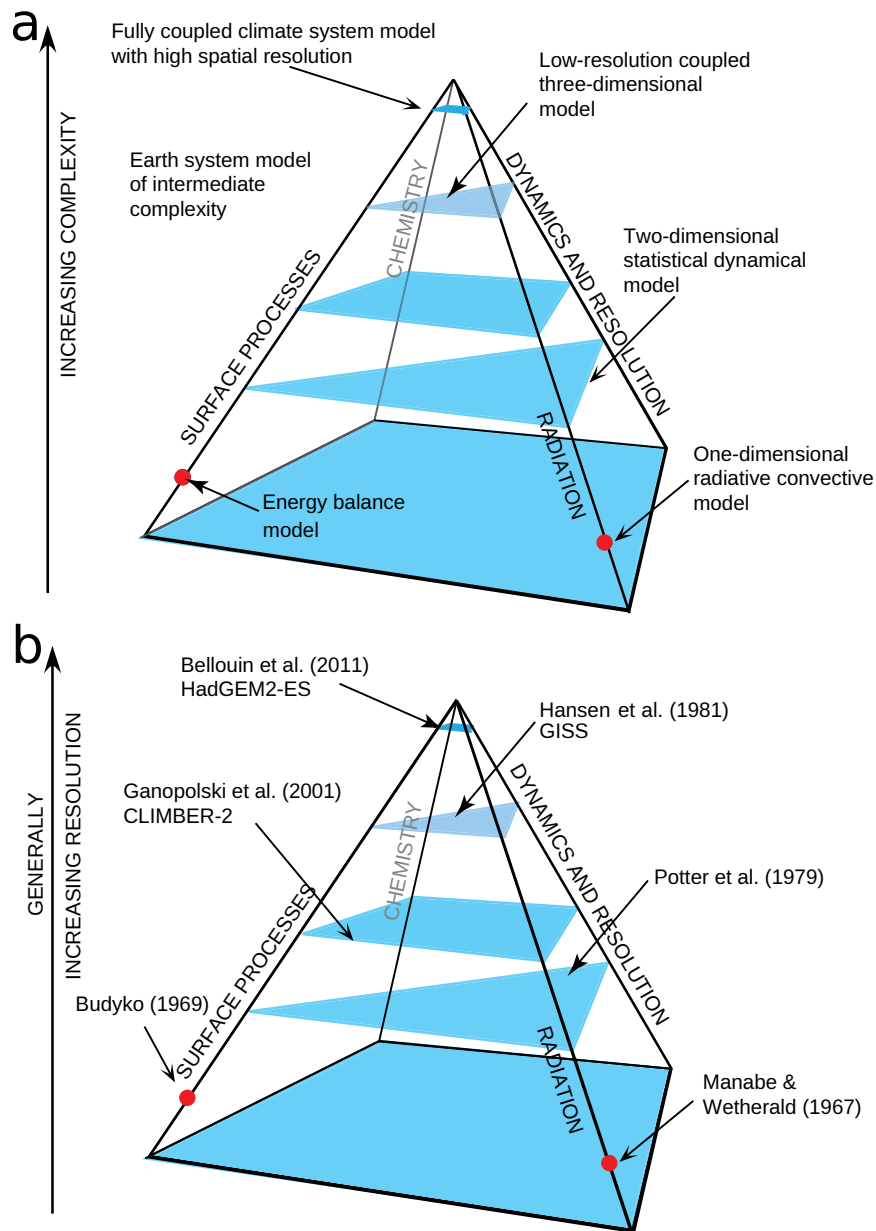


Figure 3.1: Schematic diagram of climate model hierarchy. (a) Pyramid of different climate models with increasing complexity towards the top. The simplest models are at the bottom of the pyramid, while comprehensive climate models form the top. Some seminal climate models are denoted on the respective levels of the pyramid. The models can be categorised based on the complexity of four components: (i) surface processes, (ii) chemistry, (iii) dynamics and resolution, and (iv) radiation. **(b)** Same as **a** but for the model resolution. The respective papers that introduce the models in **a** are denoted. Adapted with permission from McGuffie and Henderson-Sellers (2014)²⁴⁸.

3.1 Simple Models

Simple climate models are at the bottom of the model hierarchy (Fig. 3.1). They include energy-balance models^{249,250}, radiative-convective models and box models. In the following section, we also categorise simple models of single Earth system components or other conceptual models into this category. Simple models are especially useful for initial studies and to inform more complex models, while keeping an understanding of underlying mechanisms.

3.1.1 Energy Balance models

The principle behind energy balance models (EBM) is the planetary radiation budget of incoming and outgoing radiation and the equator-pole energy transport. EBMs allow, therefore, a first approximation of the Earth's climate. Budyko²⁵⁰ and Sellers²⁴⁹ formulated independently the first energy balance models in 1969.

In the simplest form, the energy balance of the Earth is given as

$$E_{\text{in}} = E_{\text{out}}.$$

In a zero-dimensional approach, the time averaged incoming energy over the whole Earth is given by $Q = S/4$ with the solar constant $S = 1370 \text{ W/m}^2$ (ref.²⁴⁸). If we approximate the Earth as a black body and take into account the infrared transmissivity $\varepsilon\tau_a = 0.62$, the outgoing radiation is governed by the Stefan-Boltzmann law and hence we get

$$C \frac{dT}{dt} = (1 - \alpha)Q - \sigma\varepsilon\tau_a T^4,$$

with the albedo α , the heat capacity C , the Stefan-Boltzmann constant $\sigma = 5.67 \cdot 10^{-8} \text{ Wm}^{-2}\text{K}^{-4}$, the atmospheric transmissivity τ_a , the surface temperature T and the emissivity ε . The effective emissivity $\varepsilon\tau_a \approx 0.62$ describes the effectiveness of the Earth in emitting energy as thermal radiation and is used to mimic the effect of greenhouse gases on the energy balance. This equation describes the time-dependent global temperature for a generic planet. In the equilibrium case the equation reduces to

$$\begin{aligned} (1 - \alpha)Q &= \sigma\varepsilon\tau_a T^4 \\ \Rightarrow \bar{T} &= \left(\frac{(1 - \alpha)Q}{\sigma\varepsilon\tau_a} \right)^{\frac{1}{4}} \end{aligned}$$

For Earth this gives an equilibrium surface temperature of $T = 287 \text{ K}$ if we assume an albedo of $\alpha = 0.3$ (ref.²⁴⁸). However, this simple EBM has a lot of simplifications.

A straightforward expansion of the EBM is by assuming a temperature dependence of the albedo $\alpha(T)$. This effectively accounts for the freezing of water. In the simplest form we can assume a step function for the albedo, a more general and often used dependence of the albedo is as following²⁵¹

$$\alpha(T) = 0.5 - 0.2 \tanh\left(\frac{T - 265}{10}\right).$$

However, the resulting EBM has no analytical solution anymore. Solving the EBM numerical yields two stable equilibria at $\bar{T}_1 = 288$ K and $\bar{T}_3 = 233$ K and one unstable equilibrium at $\bar{T}_2 = 265$ K (ref.²⁵¹). This equation gives rise to solution \bar{T}_3 , which corresponds to the so-called snowball Earth, a fully glaciated Earth. Indeed, there is geological evidence that the Earth might have been in such state several hundred million years ago with subsequent rapid warming events due to reduced CO₂ uptake²⁵¹. Interestingly, the temperature-dependence of the albedo also gives rise to a bifurcation in the system with respect to the parameter Q (Fig. 3.2). This bifurcation indicates the presence of hysteresis between the warm and cold equilibria. Once the system is tipped into the snowball Earth, the temperature would need to increase past the critical point of glaciation.

It is straightforward to extend the model to one dimension by considering each latitude zone i independently, giving rise to

$$S_i(1 - \alpha(T_i)) = E_{\text{out}}(T_i) + F(T_i) \quad (3.1)$$

where F is the latitudinal energy transport. Budyko (1969)²⁵⁰ and Seller (1969)²⁴⁹ proposed two different functions for the energy transport F . Budyko (1969) proposed Newtonian cooling, represented by $F(T_i) = k(T_i - \bar{T})$, where k is an empirical constant, whereas Sellers proposed a diffusion term $\text{div}\{k(\phi) \cdot \nabla T(\phi)\}$ that varies with latitude ϕ . Additionally, a correction term in the outgoing energy $E_{\text{out}} = A + BT$ due to cloudiness is assumed with the empirical constants A and B (ref.²⁵¹). Ultimately, the 1D-EBM can be expressed as

$$C \frac{dT_i}{dt} + F(T_i) = (1 - \alpha_i)S_i - A - BT_i \quad (3.2)$$

In the simplest case C and α are time- and temperature-independent and one assumes Newtonian cooling for $F(T_i)$. A temperature-dependent albedo $\alpha(T)$ in the 1D-EBM corresponds to the simplest form of a glacier model, giving rise to ice caps at the northern and southern poles. The previously mentioned bifurcation persists in the one dimensional case and is known as the small ice-cap instability in the time-dependent case, which has been extensively studied in the literature^{252,253}.

EBMs can be extended as desired, e.g. by expanding into more dimensions, by adding seasonality or coupling with other models. In mathematical fields, EBMs

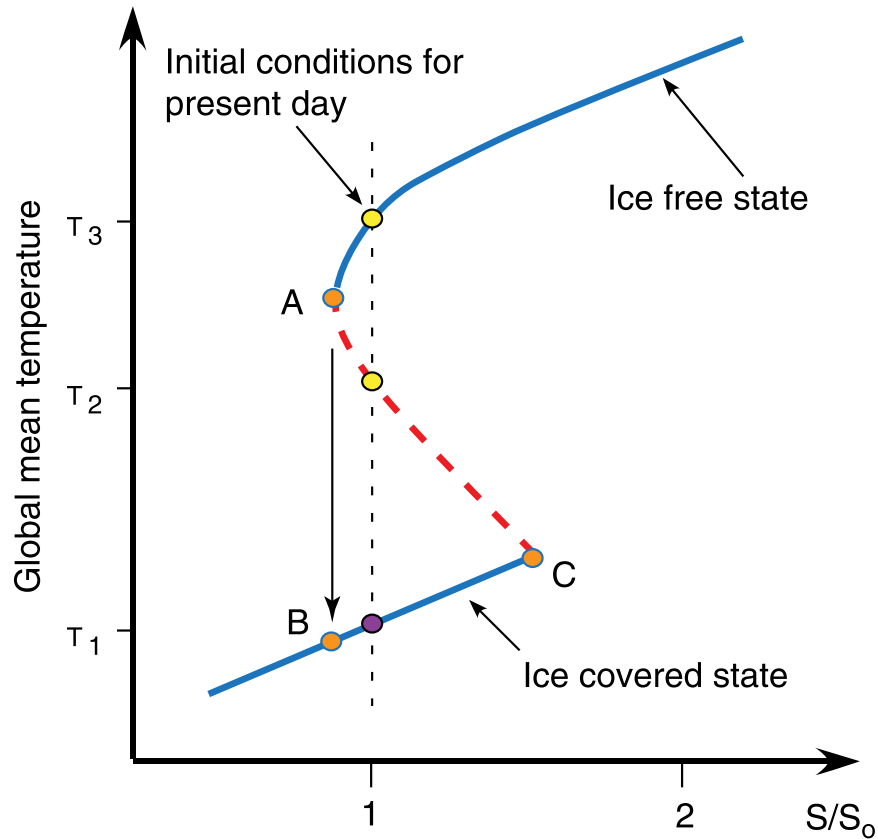


Figure 3.2: Schematic bifurcation diagram in simple EBM. Bifurcation diagram of an EBM showing two stable branches (solid blue lines) and one unstable branch (dotted red line). The lower branch corresponds to the ice covered snowball Earth, while the upper branch corresponds to present day climatic conditions. For the present day solar constant S , three states are possible, two of which are stable (yellow and purple dots). The bifurcation gives rise to hysteresis (A,B,C). Adapted with permission from McGuffie and Henderson-Sellers (2014)²⁴⁸.

remain of interest because they permit the application of analytical methods. Furthermore, modified EBMs are sometimes incorporated as submodel within more complex models, for instance, to calculate the surface mass balance of ice sheets²⁵⁴.

3.1.2 Box Models

Box models are reduced versions of complex systems, simplified to interconnected boxes through fluxes. Their simplicity and easy extensibility make them useful for a variety of problems. Exemplary applications include box models for

ocean circulation, such as the AMOC^{221,226,255}, for vegetation or ecosystems^{256,257} and for the entire climate system²⁵⁸.

To illustrate box models, consider the simple ocean-atmosphere model with four boxes introduced by Wigley and Schlesinger (1985)²⁵⁸. The model consists of two atmospheric boxes, one oceanic mixed layer and a deeper diffusive ocean, given by the equations:

$$\Delta T_{aL} = \frac{f\lambda\Delta T_i + k\Delta T_{aO}}{f\lambda + k} \quad (3.3)$$

$$\Delta T_{aO} = \frac{(f(1-f)\lambda + k)\lambda\Delta T_i + k_{as}(1-f)(f\lambda + k)\Delta T}{(f(1-f)\lambda + k)\lambda + k_{as}(1-f)(f\lambda + k)} \quad (3.4)$$

$$C_m \frac{d\Delta T}{dt} = \Delta Q - \lambda\Delta T - \Delta M \quad (3.5)$$

$$\frac{\partial\Delta T_0}{\partial t} = \kappa \frac{\partial^2\Delta T_0}{\partial z^2}. \quad (3.6)$$

The first two equations describe the air temperature change over land ΔT_{aL} and ocean ΔT_{aO} . The third and fourth describe the temperature change in the mixed ocean layer and deep ocean, respectively. The parameter f is the fraction of the globe covered by land ($f \approx 0.29$), $\Delta Q(t)$ is a change of thermal forcing, k and k_{as} are land-ocean and land-air heat transfer coefficients, $\Delta T_i(t) = \Delta Q/\lambda$ is the instantaneous equilibrium temperature change, λ is the climate feedback parameter, κ is the turbulent diffusion coefficient, C_m is the total heat capacity, z is the depth of the ocean and ΔM is the leakage of energy from the mixed layer into deeper waters. With appropriate boundary conditions and assuming an infinitely deep ocean, one can derive the following equation²⁴⁸

$$\gamma \frac{d\Delta T}{dt} + \Delta T \left[\frac{1}{\tau_f} + \frac{\mu\gamma}{(\tau_d t)^{\frac{1}{2}}} \right] = \frac{\Delta Q}{\rho_w c_w h} \quad (3.7)$$

with $\tau_f = \rho_w c_w h/\lambda$, the density of water ρ_w , the specific heat capacity of water c_w , the mixed layer depth h , a characteristic time for heat exchange between the mixed and ocean layers τ_d and the parameters γ and μ .

This ordinary differential equation can be analytically solved for a given ΔQ . This simple box model is also known under the acronym MAGICC²⁴⁸. The IPCC extensively used it to provide homogenised projections of future GMT change by tuning this model to match projections of comprehensive models. Despite its simplicity, the MAGICC model effectively replicates global and annual mean temperature variations²⁴⁸.

3.2 Earth System Models of Intermediate Complexity

Earth system models of intermediate complexity (EMICs) serve as a bridge between conceptual simple models and complex GCMs or ESMs. They have been extensively utilised for climate change assessment by the IPCC, especially for long-term projections². The spectrum of EMICs is broad and many different modelling approaches exist from statistical-dynamical atmosphere models or energy balance moisture balance models to simplified versions of GCMs²⁴⁸. Typically, EMICs feature lower spatial resolution, and compared to comprehensive models, more processes are parameterised rather than explicitly resolved. Reflecting the heterogeneity of EMICs, the applications and use cases of EMICs are extensive with individual models being more suitable for specific problems².

EMICs typically comprise several coupled submodels for the different subsystems such as atmosphere, ocean, sea ice, land ice and vegetation. This coupling involves the exchange of various fields including heat, moisture or vegetation cover, between the submodels. Often, the atmospheric model is used to characterise and distinguish EMICs since the atmosphere generally exhibits the fastest timescale and is the computationally most demanding component²⁵⁹. Therefore, we summarise some atmospheric modelling choices in EMICs in the following section. While the implementation of the other subsystems also varies considerably, often state-of-the-art models are used to model them.

One approach involves the use of radiative-convective models that simulate the vertical temperature profile within a vertical atmospheric column on Earth, consisting of different layers. The radiative scheme is typically detailed, constituting the majority of computational time, whereas the convective scheme is often a simple adjustment to allow for vertical motion and the formation of clouds²⁴⁸. In the simplest case of an isolated column, this results in a one-dimensional model. However, this concept can be extended to multicolumn models with fluxes between the single columns²⁶⁰. These models include parameterisation of the radiation scattering and absorption due to, e.g. cloud cover and are computationally very efficient. Single column models, which represent a single column from a more complex model, are also used to systematically investigate the behaviour of GCMs or ESMs. In these cases, the advective fluxes are prescribed by the complex models, allowing for the analysis of mechanisms in GCMs that are otherwise difficult to quantify²⁴⁸. Simple radiative-convective models are strictly speaking not necessarily climate models of intermediate complexity but are rather placed between the very simple models and EMICs.

A widely used approach is statistical dynamical modelling, which assumes that the atmosphere is governed by large-scale, long-term dynamics^{261–263}. These models solve the two or three dimensional atmospheric equations, that is, the equations of zonal momentum, meridional momentum, hydrostatic and thermodynamic balance and continuity²⁴⁸. These equations are similar to the ones solved in comprehensive models, however with lower resolution and considerably more parameterisation. The typical length scale of newer statistical dynamical models is 500–1,000 km (ref.²⁶³). While older models were often limited to two dimensions, accounting for vertical and latitudinal variations, newer EMICs solve equations in three dimensions. However, these technically three-dimensional models often simplify the complexities of radiative processes, leading to their designation as two-and-a-half-dimensional (2.5D) models²⁴⁸. To solve these equations numerically, prescriptions of the eddy fluxes are necessary, which is linked to considerable uncertainty²⁴⁸. Additionally, model parameters and parameterisation are often tuned to fit present-day observations²⁶³. Some employed approximations in EMICs such as the geostrophic approximation used in CLIMBER-X lead to deficiencies close to the equator²⁶³.

Direct extensions of the simple energy balance models are EBMs that either include some dynamics or include a moisture balance^{248,264–266}. The hydrological cycle is parameterised by an eddy-diffusive approximation of the water vapour balance equation in the atmosphere²⁶⁴. In contrast to other approaches, this thermodynamical approach does not allow for internal variability²⁶⁵. Other approaches include truncation of spectral general circulation models, effectively corresponding to a reduction of resolution, solving the three dimensional spectral primitive equations²⁶⁷ or solving the quasi-geostrophic equations²⁵⁹.

3.3 Comprehensive Climate and Earth System Models

Comprehensive climate models include General Circulation Models (GCM)^I and Earth System Models (ESM). Both model types simulate the global climate system by solving the fundamental laws that govern the behaviour of the atmosphere, ocean, land, sea ice, land ice, vegetation and other components on a three-dimensional finite grid. ESMs can be considered as extensions of GCMs, encompassing all the dynamics present in a GCM and additionally incorporating the elements of biogeochemical cycling²⁶⁸. These models build, to a large extent, the basis for the IPCC reports².

I. Sometimes the abbreviation GCM is used as an acronym for Global Climate Model²⁴⁸.

Present-day comprehensive climate models usually have spatial resolutions on the order of 100 km and are run on simulation time scales of decades to centuries^{269,270}. Running these simulations requires weeks or months of wall-clock time²⁷¹. On these relatively coarse resolutions, many important processes are not explicitly resolved but instead are parameterised. However, there is an ongoing effort to increase model resolution, which substantially increases computational demands^{271–273}. A doubling of the horizontal resolution increases the computational cost by a factor of approximately 16 and the benefit of continuously increasing resolution in climate models is debated²⁷¹.

The atmospheric dynamics on a rotating sphere are generally governed by the Navier-Stokes equation²⁷⁴. However, closed-form solutions to these equations are generally unavailable, necessitating numerical solutions. These equations are solved in the spectral space or in the grid space with a time step of 10–30 min by the dynamical core (DyCore) of the climate model²⁴⁸. The unresolved processes, i.e. processes on a subgrid scale that need to be parameterised, are called model physics. They typically include radiation schemes, boundary layer schemes, surface parameterisation, convection schemes (including cloud parameterisation) and large scale precipitation schemes²⁴⁸. Additionally, basic atmospheric chemistry models that simulate the distribution of non-CO₂ radiatively active gases and aerosols are included in ESMs²⁷⁵.

The ocean is, similarly to the atmosphere, governed by the fluid dynamical equations. The horizontal resolutions in the most recent generation of ESMs are on the scale of 50–100 km and therefore do not allow the explicit resolution of mesoscale eddies²⁷⁶. However, increasing resolutions of ocean models in recent years allow to partially resolve eddies and can be expected in the next generation of ESMs²⁷⁶. Additionally, absorption of solar radiation, density changes due to precipitation, river influx and melting sea ice as well as CO₂ absorption are often taken into account²⁴⁸.

Sea ice is a critical, rapidly responding component of the Earth system, interacting with both the ocean and atmosphere. While the earliest models were restricted to purely thermodynamic formulation, current ESMs include also dynamical processes, that is the movement of sea ice²⁴⁸. State-of-the-art sea ice models also include parameterisation of, e.g. the anisotropy of sea ice, melt ponds or ridging. Furthermore, they often consist of several vertical layers and include explicit snow models²⁷⁷. The sea ice model naturally has the same grid configuration and hence the same horizontal resolution as the ocean model. However, current ESMs still struggle with accurately simulating the evolution and distribution of sea ice. For example, the observed rapid decrease in the sea ice in the last years was not predicted by the last generation of ESMs²⁷⁸.

The land component models all surface processes, which include, among oth-

ers, vegetation, anthropogenic land use activities, soil hydrology, groundwater schemes, and the snowpack. Most processes in the land models are parameterised and based on empirical relationships²⁷⁹. However, a detailed descriptions of the land model schemes is beyond the scope of this thesis. For a description of the land ice component, we refer to Section 3.4.

All the subcomponents are coupled through a coupler that periodically exchanges data among the individual, isolated components. However, that does not imply that all submodules necessarily interact in a sophisticated way with each other. The coupling is highly nontrivial due to the different time scales of the single components. Usually, the ocean runs in parallel to the other components with daily exchange between atmosphere and ocean²⁴⁸. Effective coupling must consider the respective computer architecture to achieve optimal parallelisation. The complexity of the models can be reduced by using simplified modelling choices such as slab oceans or reducing the resolution of single components or of the whole model. Additionally, many ESMs permit the inclusion of non-interactive, temporally fixed components, known as data components.

While these models are extensively used in climate science, there is a considerable debate about the role of comprehensive climate models in climate science²⁷⁴. Many ESMs share submodels or derive from the same model family; therefore, they are not statistically independent, yet they yield considerably different results. For example, the equilibrium climate sensitivity between the NorESM2 and the CESM2 model varies by a factor of two even though both models share the majority of code besides the ocean models²⁸⁰. Another major criticism concerns the tuning or calibration of model parameters to match historical or present day climate²⁷⁴. Relying on expert opinions for the current tuning process can introduce subjectivity and bias into the model²⁸¹. This also raises the question of whether climate models are overly constrained or stable, thereby limiting their ability to replicate certain phenomena^{281,282}. However, automated parameter optimisation algorithms could help mitigate this issue²⁷⁴. Besides these concerns, comprehensive climate models remain an indispensable tool to investigate the climate of the past, present and future at the top of the model hierarchy.

3.4 Ice-Sheet Models

Understanding the future and past behaviour of ice sheets is crucial, given their significant impact on the global climate as previously discussed. In the following section, we will discuss (1) the governing equations for ice flow and (2) the primary processes integrated within ice-sheet models.

3.4.1 Ice Flow

The ice flow is modelled using the equations of continuum dynamics, e.g. conservation of mass, energy and momentum as well as some description of the ice rheology. In the following section, we will follow Schoof and Hewitt (2013)²⁸³. We let $\mathbf{u} = (u_1, u_2, u_3) = (u, v, w)$ be the velocity field in the ice relative to a Cartesian coordinate system $(x_1, x_2, x_3) = (x, y, z)$. We use the Einstein sum convention, i.e. we imply summation over duplicate indices $\sum_i a_{ij}b_i = a_{ij}b_i$. Ice is usually considered as a nonlinear viscous incompressible material, i.e.

$$\nabla \mathbf{u} = 0. \quad (3.8)$$

Most ice flow models assume a simple rheology with a strain-rate dependent viscosity η of the following form²⁸³

$$\begin{aligned} \tau_{ij} &= 2\eta D_{ij} \\ D_{ij} &= \frac{1}{2} \left(\frac{\partial u_i}{\partial x_j} + \frac{\partial u_j}{\partial x_i} \right), \end{aligned}$$

where D_{ij} (also $\dot{\epsilon}_{ij}$) is the strain rate and τ_{ij} is the deviatoric stress tensor linked through $\sigma_{ij} = \tau_{ij} - p\delta_{ij}$ to the stress tensor σ_{ij} with $p = -\sigma_{kk}/3$.

The most widely used rheology based on an empirical relationship derived by Glen (1958)²⁸⁴ is a power law

$$\eta = \frac{1}{2} B D^{-1+1/n},$$

with $D = \sqrt{D_{ij}D_{ij}/2}$, the constant n and the strain rate-independent factor B . This equation is also often written in the form

$$D_{ij} = A \tau^{n-1} \tau_{ij}$$

with $\tau = \sqrt{\tau_{ij}\tau_{ij}/2}$ and $A = B^{-1/n}$. Glen's work indicates an exponent $n \approx 3$. Many other, more complex flow relations have been proposed, however Glen's law is still widely used due to its simplicity.

The viscosity is usually dependent on other factors such as temperature T or impurities. In Glen's law these dependencies are usually absorbed into the factor $B = B(T)$ via an Arrhenius-type relationship

$$B = B_0 \exp(E_0/RT),$$

with the parameter B_0 , the activation energy E_0 , the gas constant R and the temperature T .

The motion of the ice sheet behaves like a Stokes flow under the action of gravity

$$\frac{\partial \tau_{ij}}{\partial x_j} - \frac{\partial p}{\partial x_i} + \rho g_i = 0, \quad (3.9)$$

with the density of ice ρ and the i -th component of gravity g_i .

The ice surface $z = s(x, y, t)$ is treated as a free boundary without stress

$$\sigma_{ij} n_j = 0 \quad \text{and} \quad \frac{\partial s}{\partial t} + u \frac{\partial s}{\partial x} + v \frac{\partial s}{\partial y} = w + a$$

with the accumulation or ablation rate a and the normal vector \mathbf{n} .

Basal sliding is often a dominant component of the ice flow in temperate glaciers and it is necessary to use a friction law $f(u_b)$ that relates the shear stress τ_b at the bed surface $z = b(x, y)$ with the sliding velocity u_b . Early glacier sliding laws were mostly described by some power law of the form $f(u_b) = Cu_b^n$ (ref.²⁸³). Today, there are more complicated friction laws dependent on, for example, temperature and the effective pressure.

Shallow Ice Approximation

Solving the whole Stokes-flow equations is computationally expensive. Therefore, several approximations have been developed. One of the most used lubrication approximations is the shallow ice approximation (SIA), where only the bed-parallel shear stress is considered.

The SIA requires that the prescribed friction law $\tau_b = f(u_b)$ is invertible, i.e. $u_b = F(\tau_b)$. Assuming Glen's sliding law, the governing equations 3.9 reduce to

$$\frac{\partial \tau}{\partial z} = -\nabla_x p, \quad \frac{\partial p}{\partial z} = -\rho g, \quad \frac{\partial U}{\partial z} = 2A|\tau|^{n-1}\tau \quad \text{for } b < z < s, \quad (3.10)$$

$$\tau = 0, \quad p = 0 \quad \text{on } z = s, \quad U = F(|\tau|)\tau/|\tau| \quad \text{on } z = b, \quad (3.11)$$

with $\tau = (\tau_{xz}, \tau_{yz})$, $U = (u, v)$ and $\nabla_x = (\partial_x, \partial_y)$. Integrating Equation 3.8 from the bottom b to the surface s of the ice yields

$$\frac{\partial s}{\partial t} + \nabla_x \mathbf{q} = a, \quad \mathbf{q} = \int_b^s U dz.$$

Together with Equation 3.11 this ultimately gives the shallow ice velocity

$$\begin{aligned} U = & -2(\rho g)^n \left[\int_b^{dz} A(dz')(s - dz')^n dz' \right] |\nabla_x s|^{n-1} \nabla_x s \\ & - F(\rho g(s - b)|\nabla_x s|) \frac{\nabla_x s}{|\nabla_x s|}. \end{aligned} \quad (3.12)$$

For no slip, i.e. $F = 0$, this equation simplifies to

$$\frac{\partial s}{\partial t} - \nabla_{\mathbf{x}} \cdot \left[\frac{2A}{n+2} (s-b)^{n+2} |\nabla_{\mathbf{x}} s|^{n-1} \nabla_{\mathbf{x}} s \right] = a.$$

Equation 3.12 is a highly nonlinear diffusion problem but computationally much easier to solve than the full Stokes equations. In ice-sheet models there is often an additional enhancement factor E_{SIA} in the first term in Equation 3.12 to account for the non-isotropic nature of the ice or other unresolved processes²⁸⁵.

The SIA is used for grounded parts of the ice sheets where sliding is minimal or non-existent. However, SIA becomes inappropriate for regions with fast sliding such as ice streams, and different approximation approaches are needed²⁸³. Similar to SIA, the shallow shelf approximation (SSA) is widely used for ice shelves or sliding ice streams, instead of solving the full Stokes equations. A hybrid approach superposes the SIA and the SSA as a sliding law (SIA+SSA). This allows for modelling higher ice velocities than in a pure SIA approach.

3.4.2 Surface Melt

The surface melt is a boundary condition for the ice sheet model, which determines the surface mass balance. There are several approaches to model the surface energy balance or surface melt, ranging from coupled ESM⁵⁸ or regional climate model simulations^{76,286,287} to simpler parameterisation^{56,92,100,288,289}.

A straightforward way is to integrate the ice sheet model into a coupled ESM such that the surface mass balance is provided by the atmospheric model component. Alternatively, the ESM can provide the surface mass balance for the ice sheet model to operate in standalone or offline mode. In this case, feedback between the evolving ice sheet geometry and the surface mass balance is generally not considered. Hence, the offline approach is suitable only for short time scales without large changes in the ice sheet geometry. However, these two approaches are computationally expensive and only feasible for submillennial time scales.

For longer time scales, parameterised approaches are necessary. One of the most used simple melt parameterisation is the positive degree day (PDD) model^{100,288,290}. The PDD model calculates the number of days with temperatures above freezing in a year, known as melt days, based on daily temperatures according to the following equation¹⁰⁰,

$$\text{PDD} = \frac{1}{\sigma_{\text{PDD}} \sqrt{2\pi}} \int_0^A dt \int_0^\infty dT T \exp \left[-\frac{[T - T_a(t)]^2}{2\sigma_{\text{PDD}}^2} \right].$$

Here, the equation is integrated over a time period of one year A , with the annual near-surface temperature T_a that varies sinusoidally over time and the standard deviation of the mean monthly temperatures σ_{PDD} . Subsequently, the melt is computed by multiplying the number of positive degree days PDD with some latitude- and surface-cover-dependent PDD-factors β . Generally, the annual precipitation cycle and the refreezing rate are assumed to be constant over time in the PDD model. While the PDD model can produce results for present-day ice sheets similar to those from regional climate models, its simplicity may limit its reliability for simulating far future projections^{53,76,291,292}.

Several extensions and alternatives to the PDD model have been proposed, accounting for factors such as seasonal changes in solar radiation^{92,289,293,294}. In this thesis, we employ a simplified version of the diurnal Energy Balance Model (dEBM-simple) incorporated into the Parallel Ice Sheet Model (PISM)^{92,254,294}. The governing equation of the melt M is given by⁹²

$$M = \frac{\Delta t_\phi}{\Delta t \rho_w L_m} \left(\tau_A (1 - \alpha_s) \overline{S_\phi} + c_1 T_{\text{eff}} + c_2 \right),$$

with the freshwater density ρ_w , the latent heat of fusion L_m , the length of a day Δt , the surface albedo α_s , the incoming radiation $\overline{S_\phi}$, the empirical parameters c_1 and c_2 , the parameterised transmissivity τ_A , the effective temperature T_{eff} and the time Δt_ϕ during which the sun's elevation angle exceeds the threshold for melting. The first term in the equation describes the insolation driven melt, the second term describes the directly temperature driven melt, while the last term describes a constant offset related to outgoing longwave radiation. Similar to the PDD model, the effective temperature T_{eff} is a function of the cumulative temperature exceeding the melting point in a given month⁹². In contrast to the PDD model, this melt scheme directly includes radiation induced melting and changing day length.

3.4.3 Alternative Modelling Choices

Besides the ice flow and surface melt, several other modelling choices must be made such as the Earth deformation model, the ocean model or changes in precipitation and temperature. We summarise some common parameterisation used in ice sheet modelling in the following section. We do not consider ocean modelling here, as it is not a major factor for the GrIS.

Earth Deformation Model

Changes in the ice load lead to a response of the solid Earth. Usually, this response is very slow, occurring over millennia. While fully process-based Earth

deformation models exist, they are computationally demanding and are therefore typically not coupled with ice-sheet models^{117,295}. Simpler models, often incorporated into ice-sheet models, include the flat Earth Elastic Lithosphere Relaxing Asthenosphere (ELRA) model²⁹⁶ or the Lingle-Clark model, which generalises the ELRA model^{297,298}. The Lingle-Clark model conceptualises the solid Earth as consisting of two layers: a viscous mantle with viscosity η and density ρ , and an elastic layer with flexural rigidity D , which represents the lithosphere⁹⁴. The response of the lithosphere is instantaneous, while the response of the mantle is on the timescale of decades to millennia. This approximation is valid when there is no spatial variability in viscosity or load, specifically for regions of limited spatial extent. The governing differential equation for the vertical displacement of the bedrock u in the Lingle-Clark model is given by

$$2\eta|\nabla|\frac{\partial u}{\partial t} + \rho g u + D\nabla^4 u = \sigma_{zz}$$

where g is the gravitational acceleration and σ_{zz} is the ice load force per unit area⁹⁴. This equation can be solved quickly using a computationally efficient Fast Fourier transform-based method²⁹⁸. Although parameterised Earth deformation models give reasonable results, there is a considerable uncertainty in the parameters and hence in the response of the bedrock⁹⁴.

Temperature and Precipitation Scaling

The spatial annual surface temperature and precipitation fields are usually fixed as boundary conditions in standalone ice sheet modelling. However, several parameterisations exist to account for factors such as changing ice sheet geometry. The surface temperature is often directly scaled by a scalar or spatiotemporal temperature anomaly. To account for changes in the surface elevation, a simple lapse rate is applied to the surface temperature relative to the initial ice sheet geometry. The precipitation is subsequently scaled either directly via a precipitation lapse rate or through an exponential relationship

$$P = P_i \exp(C\Delta T),$$

where C is a scaling factor, P_i the initial precipitation and ΔT is the change of temperature due to elevation and/or the background climate¹¹⁹. This increases precipitation by $100(\exp(C) - 1)\%$ for each degree of warming. Additionally, orographic effects on precipitation are sometimes parameterised²⁹⁹.

/4

Deep Learning

Machine Learning (ML) and its applications in climate science have gained tremendous traction in recent years. ML focuses on making predictions by learning from data, which is highly relevant for climate science. In the following, we will also refer to deep learning (DL), a subfield of ML that uses multi-layered (deep) networks to extract higher-level features in the data. The notions of DL and ML will be used interchangeably in the following. Applications of ML and DL in climate science range from reconstructing climate fields and predicting time series to developing neural Earth System Models (ESMs). While providing a complete overview is beyond this thesis's scope, we provide a brief overview of potential applications of DL-based methods in climate science, particularly in the context of climate modeling. Subsequently, we will outline the network architecture of the model used in this thesis.

4.1 Overview

4.1.1 Parameterisations, Emulation & Neural GCM

As described earlier, climate models typically utilise parameterisations of many processes, especially on a subgrid scale, such as convection and radiation. These parameterisations often involve complex statistical methods and can be computationally demanding³⁰⁰. Machine learning methods can replace or emulate individual subcomponents of an existing parameterisation scheme, or

even replace or emulate several parameterisation schemes within a single ML model, potentially offering increased performance and reduced computational costs³⁰⁰. In this context, emulation refers to replicating the behaviour of an existing scheme using an ML method, which benefits from requiring no or only minimal re-tuning³⁰⁰. Alternatively, ML-based models are used to correct existing parameterisation schemes³⁰¹.

The first ML-based (based on neural networks) subgrid parameterisations and emulations of radiation schemes were developed in the end of the 1990s and early 2000s, offering considerable speed up over classical methods^{302,303}. Later, ML-based parameterisation schemes were introduced in aquaplanet GCM simulations using so-called coarse graining^{300,304–306}. The ML model is trained on high-resolution data that potentially resolves the desired process, and subsequently applies this knowledge to data on a coarser grid³⁰⁰. The models are either trained on model output or directly on observational data. Recently, parameterisation schemes and emulations have been applied beyond idealised aquaplanet GCMs to realistic land-ocean simulations^{307–310}. It has been demonstrated that these schemes can outperform classical parameterisations in some aspects. However, they can introduce instabilities and thus require careful implementation.

All the aforementioned studies do not run long-term simulations, which are linked to an inherent problem in machine learning; generic ML models do not conserve physical quantities³⁰⁰. However, it is possible to constrain neural networks, for example, through the loss function or directly within the architecture, to ensure the conservation of physical quantities³⁰⁰. It has been shown that even without constraining the networks, decade long simulations of hybrid ML-GCM models are possible³¹¹. While most emulation and parameterisation schemes are aimed at the atmospheric component of climate models due to the computational cost of it, ML-based methods also exist for the other components such as land, ocean, sea ice or ice sheets^{300,312,313}. Recently, a fully differentiable, fully coupled neural GCM has been introduced that is trained on reanalysis data and produces multi-decadal long, physically consistent climate forecasts⁷. The neural GCM consists of a classical dynamical core that solves the primitive equations and a machine learning component that parameterises all physical processes. Additionally, it can produce ensemble weather and climate projections using a stochastic loss function. Although ensemble simulations have previously been generated³¹⁴, creating them with ML-based methods remains a challenge³⁰⁰.

The growing availability of training data and computational resources has shifted the focus from single-component parameterisations towards replacing entire GCMs with ML-based methods. First proof-of-concept attempts employed ML models to generate global weather forecasts with single variables on very

coarse grids or convolutional neural networks to iteratively predict the next model state of simple GCMs or EMICs^{315–317}. These studies were limited to short time scales, spanning only a few days. Subsequent studies extended these forecasts by increasing the number of predicted variables, incorporating the spherical nature of the Earth, and extending the lead-time to a few weeks^{318–320}. These models demonstrated similar performance to traditional models for short-term forecasts.

Recently, graph neural networks have been used to predict realistic short-term forecasts with a tremendous increase in the performance, predicted variables and spatiotemporal resolution^{321,322}. The GraphCast model consistently outperforms state-of-the-art numerical weather models³²². GraphCast is trained on historical reanalysis data and can predict several hundred weather variables with a 0.25° resolution for the next 10 days in less than one minute³²².

Several other models and applications have been proposed and the field evolves rapidly^{323–325}. However, the use of ML-based methods for long-term climate prediction remains limited, primarily due to a lack of training data, a challenge that is likely to be overcome in the future³⁰⁰.

4.1.2 Physics-informed ML

Although machine learning (ML) methods can learn underlying physical relationships and principles, they typically do not preserve physical quantities like momentum or energy. Moreover, the results are frequently difficult to interpret and lack explainability, raising questions about their plausibility. A recently introduced method to address these problems is physics-constrained or physics-informed machine learning (PIML)^{326,327}. PIML incorporates knowledge of the underlying physical system that is to be modelled to build physically consistent models with increased data efficiency, interpretability, and generalisability as well as a faster training process³²⁶. PIMLs are not constrained to applications in climate science but have been applied to many other areas^{328,329}. There are several approaches to design PIML ranging from custom loss functions to custom network architectures³²⁶.

For example, constrained generative adversarial networks have been used to emulate complex physical processes, similar to those mentioned in the previous section^{330,331}. Regularisation or penalty terms are introduced into the loss function that help to preserve desired properties of the underlying data. The constrained networks have been shown to achieve greater accuracy compared to unconstrained networks. Constrained GANs have been used to super-resolve existing data³³² or to post-process numerical climate model output³³³. Furthermore, PIML has been used to solve the shallow-water equations on a rotating

sphere and hence can serve as alternative approach to solving differential equations³³⁴. However, it is important to note that PIMLs always require some knowledge of the underlying system and must be adapted to the individual problem.

4.1.3 Other Applications

The applications of ML-based methods in climate science extend well beyond the previously mentioned examples. We mention some other interesting applications in the following.

As briefly mentioned earlier, ML-based methods can be used to aid in solving or even completely solve partial differential equations. Early methods were mostly aimed at accelerating PDE solvers using ML-based preconditioning. Preconditioning is the transformation of parts of the problem making it more suitable for the numerical solver and leading to a reduced number of iterations³⁰⁰. Subsequently, parts of the numerical solver were completely replaced^{335,336}. Neural networks have enabled solving nonlinear PDEs on coarser grids while maintaining accuracy comparable to classical solvers, resulting in a speedup by several orders of magnitude³³⁷. An alternative approach is to learn the evolution of the operator of the underlying unknown PDE from data since neural networks can approximate any nonlinear continuous operator³³⁸. These approaches promise considerable speedup compared to classical numerical methods.

While most examples so far are concerned with forecasting, ML can improve historical records, which are important to quantify changes in a system. ML-based methods have been shown to outperform traditional reconstruction approaches, such as principal component analysis or kriging (Gaussian process regression), especially when data is very sparse⁵. The ML models learn the underlying physical relationships to some extent and are able to realistically fill in missing data. In this thesis, we introduce a novel ML method for the reconstruction of climate fields (cf. Section 4.2 and 5.3) that outperforms previous methods. Our reconstructions can lead to new insights into the climate system due to the enhanced plausibility of the spatiotemporal fields.

In contrast to emulation and parameterisation approaches, ML-based methods have also been employed to nudge climate models towards observations³³⁹. However, research in this direction has been limited so far³⁰⁰. Other approaches include classical time series forecasting of different variables³⁴⁰⁻³⁴², early-warning signals (cf. Section 2.1.2), uncertainty quantification³⁴³ and extreme event forecasting³⁴⁴.

4.2 LaMa

The third paper of this thesis focuses on the reconstruction of spatiotemporal climate fields using deep learning. Instrumental records of climate fields are typically limited to several decades at best and are often incomplete, presenting a serious challenge in assessing long-term system changes. In the context of tipping points, long time series are particularly important as short time series hinder the inference of long-term changes in system dynamics, which could potentially indicate an approaching critical transition. To generate long, spatiotemporally consistent time series, we employ the recently introduced Resolution-robust Large Mask Inpainting with Fourier Convolutions model (LaMa) that has been shown to outperform previous methods³⁴⁵. LaMa is a deterministic model; that is, the same combination of mask and image always yields the same reconstruction. In this thesis, deep learning is utilised as a tool, and we refrain from providing an extensive theoretical background on the network architecture and the various operators used in machine learning. However, we will briefly summarise the key features of the network (Fig. 4.1) following Suvorov et al. (2021)³⁴⁵.

4.2.1 Network architecture

The model's goal is to inpaint an image x masked by a binary mask m . The image is stacked with the mask $x \odot m$, resulting in a 4-channel input tensor $x' = \text{stack}(x \odot m, m)$. In our case of single-channel climate fields, we replicate the single channel, such as temperature, across the other two colour channels, creating a 3-channel grey scale image. The model is trained on image-mask pairs, where the training images with known ground truth are derived from sources such as reanalyses or climate model outputs. Training masks are either derived from the dataset of interest or randomly generated during the training, following the original mask generation algorithm³⁴⁵. The feed-forward network $f_{\Theta}(\cdot)$ produces the inpainted image $\hat{x} = f_{\Theta}(x')$. A feed-forward network describes the simplest form of a neural network where information only propagates forward through the network, from the input nodes through the hidden layers to the output nodes.

The core component of the model is the fast Fourier convolution (FFC) block, based on a channel-wise fast Fourier transform (FFT). The large advantage of FFC is that it enables global context in the early layers of the network, in contrast to conventional convolutions, which have a spatially limited receptive field³⁴⁶. The FFC comprises two interconnected branches; (i) a local branch in the spatial domain using conventional convolutions and (ii) a global branch in the spectral domain using real FFT. The input tensor x is split along the feature channels into the local branch x^l and the global branch x^g . The local part $x^l \in \mathbb{R}^{H \times W \times (1-\alpha)C}$

with the spatial dimension $H \times W$ and the channels C is designed to capture small scale information, while the global part $x^g \in \mathbb{R}^{H \times W \times \alpha C}$ targets large-scale context. The hyperparameter $\alpha \in [0, 1]$ represents the split ratio of the feature channels between the global and local branch. While the global branch can be sufficient for realistic inpainting, the local branch adds stability to the network³⁴⁷. Assume the output tensor of the FFC block is denoted by $y = \{y^l, y^g\}$ and has the same dimension and the same local and global split ratio as the input tensor $x = \{x^l, x^g\}$. Then the procedure in the FFC block can be described as³⁴⁶

$$\begin{aligned} y^l &= y^{l \rightarrow l} + y^{g \rightarrow l} = f_l(x^l) + f_{g \rightarrow l}(x^g), \\ y^g &= y^{g \rightarrow g} + y^{l \rightarrow g} = f_g(x^g) + f_{l \rightarrow g}(x^l). \end{aligned}$$

Here, f_l denotes the local operation via conventional convolutions, f_g denotes the global spectral transformer and $f_{g \rightarrow l}$ and $f_{l \rightarrow g}$ denote the inter-path transitions via conventional convolutions (Fig. 4.1). The spectral transform f_g in the global path is the component that ensures the global context in the early layers.

For simplicity, assume our global branch input tensor has the following form $x^g \in \mathbb{R}^{H \times W \times C}$, then the spectral transform f_g in the FFC block applies the following (Fig. 4.1):

- (i) a real two-dimensional FFT and concatenates the real and imaginary parts; $\mathbb{R}^{H \times W \times C} \rightarrow \mathbb{C}^{H \times \frac{W}{2} \times C} \rightarrow \mathbb{R}^{H \times \frac{W}{2} \times 2C}$,
- (ii) a convolutional block in the frequency domain consisting of an activation function (rectified linear unit, ReLU), batch normalisation (BN) and a 1×1 convolutional layer; $\mathbb{R}^{H \times \frac{W}{2} \times 2C} \rightarrow \mathbb{R}^{H \times \frac{W}{2} \times 2C}$,
- (iii) an inverse transform into the spatial domain; $\mathbb{R}^{H \times \frac{W}{2} \times 2C} \rightarrow \mathbb{C}^{H \times \frac{W}{2} \times C} \rightarrow \mathbb{R}^{H \times W \times C}$.

Here, the activation function calculates the output of an individual node based on its inputs and weights and is crucial for successful training of deep learning networks. The ReLU is easy to optimise and currently the most adopted activation function in deep learning³⁴⁸. It is defined as the positive part of its argument. Batch normalisation is used to make training more stable and efficient through re-scaling and re-centring of the layers' input³⁴⁹.

Eventually, the outputs of the local and global branch are fused together. In contrast to conventional convolutions, the FFC has an image-wide receptive field which allows for global context already in the early layers of the network. With conventional convolutions, the number of layers would need to be substantially

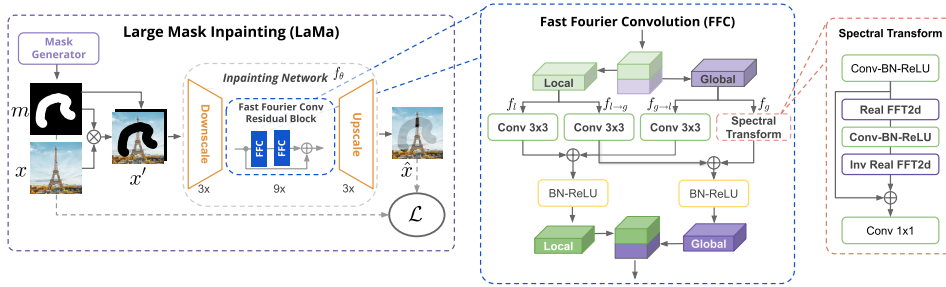


Figure 4.1: LaMa network architecture. The mask m and image x are concatenated into one input tensor x' and fed into the network. Subsequently, x' is down-scaled, several FFC blocks are applied and the tensor is up-scaled again to give the initial resolution. The concept behind the FFC block is depicted. The input tensor gets split into two interconnected local and global branches. Eventually, the multi-component loss \mathcal{L} is optimised to give a realistic inpainted image \hat{x} . Adapted from Suvorov et al. (2021)³⁴⁵.

greater to achieve a similar receptive field in later layers, leading to higher computational demands.

4.2.2 Loss functions

The second crucial component of the network, enabling the realistic inpainting of images, is a highly non-trivial multi-component loss function. The first component of this loss is the high receptive field perceptual loss $\mathcal{L}_{\text{HRFPL}}$, which evaluates the distance between the target and predicted image using a pre-trained network $\phi_{\text{HRF}}(\cdot)$ with a high receptive field. Unlike naive supervised loss, a perceptual loss allows for a non-exact reconstruction, thereby avoiding blurry results often caused by averaging multiple plausible reconstructions³⁴⁵. The loss function is defined as follows:

$$\mathcal{L}_{\text{HRFPL}}(x, \hat{x}) = \mathcal{M}([\phi_{\text{HRF}}(x) - \phi_{\text{HRF}}(\hat{x})]^2),$$

using the element-wise operation $[\cdot - \cdot]^2$ and the mean operator \mathcal{M} (interlayer mean of intralayer means). In other words, the perceptual distance of the inpainted image \hat{x} and the original image x is evaluated at each layer of the pre-trained network $\phi_{\text{HRF}}(\cdot)$. Here, $\phi_{\text{HRF}}(\cdot)$ is a segmentation model, specifically, a pre-trained ResNet50 network with dilated convolutions. Dilated convolutions in this model allow for global context, analogous to the FFC.

The second component of the loss function is an adversarial loss, ensuring that the inpainting network $f_{\Theta}(x')$ generates natural-looking local details. A discriminator $D_{\xi}(\cdot)$ is introduced, operating at a local level to differentiate between real and fake patches. The generator, namely the inpainting network,

quickly learns to replicate the unmasked parts of the ground truth, while only the masked parts are classified as fake. The generator aims to deceive the discriminator into classifying the masked generated patches (fakes) as real, essentially engaging in a two-player min-max game³⁵⁰. For the general concept and a derivation of adversarial losses we refer to Goodfellow et al. (2014)³⁵⁰. The resulting non-saturating adversarial loss L_{adv} that is to be optimised is given by

$$\begin{aligned}\mathcal{L}_D &= -\mathbb{E}_x [\log D_\xi(x)] - \mathbb{E}_{x,m} [\log D_\xi(\hat{x}) \odot m] \\ &\quad - \mathbb{E}_{x,m} [\log(1 - D_\xi(\hat{x})) \odot (1 - m)] \\ \mathcal{L}_G &= -\mathbb{E}_{x,m} [\log D_\xi(\hat{x})] \\ L_{\text{adv}} &= \min_{\Theta, \xi} [\text{sg}_\Theta(\mathcal{L}_D) + \text{sg}_\xi(\mathcal{L}_G)],\end{aligned}$$

with the expected value \mathbb{E}_x over all real data instances and the expected value $\mathbb{E}_{x,m}$ over all artificially masked instances (fake). $D_\xi(x)$ is the discriminator's estimate that the real image is real and $D_\xi(\hat{x})$ is the discriminator's estimate of the probability that the generated image is real. Analogously, $D_\xi(\hat{x}) \odot m$ is the discriminator's estimate of the generated image only for the artificially masked areas. Here, non-saturating loss means that the generator maximises the probability of the images being real rather than minimising the probability of the images being fake. The stop gradient operator $\text{sg}(\cdot)$ applied to the respective variable ensures consistent training.

The final loss is the sum of the aforementioned losses plus a regularisation term $R_1 = \mathbb{E}_x [|\nabla D_\xi(x)|^2]$ and a discriminator-based perceptual loss or feature-matching loss $\mathcal{L}_{\text{DiscPL}}$ that increases stability and performance³⁴⁵. The regularisation loss prevents overfitting by penalising the discriminator, which ensures better generalisation³⁵¹. The full loss function is given by

$$\mathcal{L} = \kappa L_{\text{adv}} + \alpha \mathcal{L}_{\text{HRFPL}} + \beta \mathcal{L}_{\text{DiscPL}} + \gamma R_1$$

with the weights $\kappa = 10$, $\alpha = 30$, $\beta = 100$ and $\gamma = 0.001$. Summarised, the terms L_{adv} and $\mathcal{L}_{\text{DiscPL}}$ ensure naturally looking local details, while $\mathcal{L}_{\text{HRFPL}}$ ensures the global structure.

/5

Summary of Publications

The three papers included in this thesis constitute its main scientific contribution. The first two papers are thematically closely related, whereas the third paper explores a distinct topic and is independent. The following chapter summarises each paper and attempts to establish a common framework.

5.1 Paper I

Bochow, N. & Boers, N., The South American monsoon approaches a critical transition in response to deforestation. *Sci. Adv.* **9**, eadd9973 (2023).
<https://doi.org/10.1126/sciadv.add9973>

This study aims to investigate and identify mechanisms behind the tipping behaviour of the coupled South American Monsoon - Amazon rainforest system. Our findings suggest that a critical transition in the coupled system could result in a pronounced, large-scale reduction of precipitation rates across South America, followed by a dieback of large parts of the Amazon rainforest. Additionally, we have identified precursor signals of this critical transition in response to deforestation.

The Amazon rainforest has long been hypothesised to exhibit tipping behaviour^{44,45,150,155,352-355}, however previous studies often ignore the interplay between the large-scale atmosphere and the vegetation system. This oversight

may lead to an underestimation of potential positive feedback mechanisms. Our approach combines observation- and model-based analyses to identify precursor signals and mechanisms that can lead to a critical transition in the coupled system. We use a nonlinear dynamical model of the moisture transport and recycling across South America coupled to the vegetation system and simulate deforestation scenarios. Upon crossing a specific deforestation threshold, we find an abrupt decline in the precipitation rates in non-deforested parts of the forest in our model. This results in an abrupt dieback of the remaining rainforest. Several statistical and physical precursor signals precede the critical transition, i.e. reduction of soil moisture, lengthening of the dry season, delayed onset of the wet season and statistically significant increases in variance and lag-one autocorrelation in the precipitation rates. Guided by our modelling results, we analyse various observational and reanalysis products.

Measuring observables in Amazonia is inherently difficult due to the dense tree cover and year-round cloudiness³⁵⁶. To avoid biases in our analysis, we analyse four different rainfall datasets ERA5³⁵⁷, GPCP³⁵⁸, GPCP³⁵⁹ and CHIRPS³⁶⁰. Consistent with our modelling results, we find both significant statistical and physical precursor signals in large parts of South America across the different datasets. We find a year-round decrease of the soil moisture in the Amazon basin, a lengthening of the dry season in southern Amazonia mostly due to a delayed wet season onset and increases in variance and lag-one autocorrelation of the precipitation rates in (southern) Amazonia. Interestingly, regions with high lag-one autocorrelation and variance closely correspond with the main atmospheric moisture transport routes in South America and particularly the aerial river across the Amazon to the subtropics^{361,362}.

We propose the following chain of mechanisms that leads to the deforestation-induced transition of the coupled system. The time needed to initiate the wet season is prolonged as the atmospheric moisture content decreases with ongoing deforestation. Indeed, over the past decades, large parts of the Amazon rainforest have shown a reduced moisture content³⁶³. The decreasing heating gradient between the Atlantic Ocean and Amazonia further impedes the wet season, leading to a reduction of the soil moisture while evaporation rates remain high. This results in a further reduction of soil moisture during the dry season. At the critical point, the atmospheric moisture content, and consequently the latent heating, is no longer sufficient anymore to switch the system back into the annual wet season. This leads to a permanent dry season state with reduced precipitation rates, ultimately leading to the dieback of large portions of the Amazon rainforest. This large-scale reduction in precipitation rates is not necessarily limited to the Amazon basin, given the importance of the rainforest for the hydrological cycle in South America³⁶⁴⁻³⁶⁶.

This study identifies the coupled system of the South American monsoon and Amazon rainforest as potential tipping elements. We demonstrate that forest loss could substantially contribute to climate change in South America, particularly in Amazonia, eventually driving the coupled system beyond the critical threshold.

5.2 Paper II

Bochow, N., Poltronieri, A., Robinson, A., Montoya, M., Rypdal, M. & Boers, N. Overshooting the critical threshold for the Greenland ice sheet. *Nature* **622**, 528–536 (2023). <https://doi.org/10.1038/s41586-023-06503-9>

This study investigates the reversibility of an overshoot of the critical threshold for the Greenland ice sheet. It is known from dynamical systems theory that a bifurcation point in a slow system can be exceeded without necessarily transitioning to an alternative equilibrium, provided the change in the control parameter is reversed sufficiently fast²¹. Unlike the previous paper, which investigated a relatively fast system, the GrIS reacts on much slower time scales than other components of the Earth system. The Greenland ice sheet has been hypothesised to exhibit several stable equilibria⁵⁶ and precursor signals for a critical transition have been found in observational data⁶². This study demonstrates for the first time that the critical threshold of the GrIS can be exceeded without necessarily committing to a full retreat of the ice sheet if the temperature is reversed sufficiently fast.

We use the two state-of-the-art ice-sheet models; the Parallel Ice Sheet Model (PISM)²⁸⁵ coupled to the recently introduced Simple Diurnal Energy Balance Model (dEBM-simple)⁹² and the ice sheet model Yelmo³⁶⁷ coupled to the Regional Energy-Moisture Balance Orographic model (REMBO)²⁸⁹. We initialise each model to match the present-day ice sheet configuration and climate. Subsequently, we conduct several hundred long-term overshoot scenarios with a simulation time of at least 100,000 years. In our simulations, the maximum overshoot temperature is reached after 100 years, in the year 2100. The overshoot temperature ranges from 0.5 to 6.5°C in terms of global mean temperature above pre-industrial levels. We then gradually reduce the temperatures over varying time windows from 100 to 10,000 years (referred to as convergence time) to different final temperatures (convergence temperature). To convert regional temperature changes into changes in global mean temperature, we use historical observational temperature records³⁶⁸ as well as results from the latest coupled model intercomparison project (CMIP6)²⁷⁰.

We find a critical threshold between 1.7 (Yelmo-REMBO) and 2.3°C (PISM-

dEBM-simple) above pre-industrial GMT, beyond which we observe a full retreat of the ice sheet in the long term. However, we also see that the critical threshold can be exceeded for some time without necessarily committing to irreversible ice loss or a full retreat of the ice sheet. For both models, this timescale spans centuries to millennia. However, overshooting the critical threshold is still linked to global sea-level rise on the magnitude of decimetres to meters, depending on the overshoot temperature and convergence time. In any case, the ice sheet is lost in the long term if the temperatures are not reversed below the critical threshold after the initial exceedance.

In general, the longer the overshoot, the more important the overshoot temperature and vice versa. This means that for short overshoots, the maximum temperature, i.e. the overshoot temperature, has little influence on the ice loss, whereas for long overshoots, it has a substantial influence on the ice loss. Given the slow timescale of an ice sheet, it is not surprising to find that a reversal of the temperature trend can prevent a large-scale loss of the ice sheet. Even with a constant temperature anomaly of 6.5°C , the ice sheet is not completely lost for several thousand years. Although the two ice-sheet models largely agree on both long- and short-term evolution, there are some differences in the response of the ice sheet. The GrIS simulated by PISM-dEBM-simple shows oscillatory behaviour under constant temperature anomalies below the critical threshold over decamillennial timescales. This is likely due to an interplay between the glacial isostatic adjustment (GIA) and the melt-elevation feedback⁹⁴ and has also been observed in other studies^{58,94,369,370}. While Yelmo-REMBO employs the same Earth deformation model, we do not find such oscillations in these simulations. We attribute these differences to a different balance between positive feedbacks (mostly at the surface) and the glacial isostatic adjustment. Furthermore, we find a temperature range of irreversibility below the critical threshold for longer convergence times in Yelmo-REMBO, which we do not observe in PISM-dEBM-simple, further emphasising the risk of irreversible ice loss.

In our study, we are limited to the use of standalone ice-sheet models. Due to computational constraints, it is not possible to run fully-coupled Earth system models on these time scales. Additionally, many state-of-the-art Earth system models do not yet natively support interactive ice-sheet models or are just in the process of incorporating them^{371,372}. However, almost all other sub-elements of the Earth system, e.g. atmospheric and ocean circulation patterns, react more quickly than ice sheets. This may affect the long-term stability of the GrIS. Recent advances in Earth system modelling⁷ might make it possible to run fully coupled long-term simulations of the whole Earth system, opening the door for necessary follow-up studies.

To our knowledge, we show for the first time with two state-of-the-art models,

that the critical threshold of the GrIS can be crossed for substantial time (on human times scales) without committing to a transition to an alternative ice sheet state. However, our findings also indicate that even without an irreversible transition, the sea level rise contribution from the GrIS alone can exceed several meters, depending on the overshoot temperature, convergence temperature and convergence time. The applicability of these findings to other tipping elements, such as the coupled SAMS-Amazon rainforest system, remains an open question given the shorter timescale of nearly every tipping element and similar studies are needed for other Earth system components.

5.3 Paper III

Bochow, N., Poltronieri, M., Rypdal, M., Boers, N. Reconstruction of Climate Fields Using Deep Learning.

The aim of this study is to reconstruct historical climate fields and to improve upon widely used reconstruction and infilling methods in geosciences. For this purpose, we apply a state-of-the-art deep learning method to reconstruct structurally different historical climate fields with highly irregular and large missing areas. Historical observations are crucial to infer knowledge of past and present changes in the Earth system. However, historical observations are often sparse in time and space before systematic observations were introduced in the 20th century. Precipitation and temperature records have the most complete spatiotemporal coverage of all climate fields and partially reach back until the 19th century. However, these datasets rely heavily on interpolation^{373,374}. Measurements of many other climate variables such as sea ice thickness or vegetation indices reach only back some decades or even years^{257,375,376}. This poses a problem since, generally, longer time series are needed to capture long-term dynamics of a system^{257,377}. This is particularly relevant for the concept of tipping points. Often, statistical indicators are used to infer the stability of a system or to estimate the approach of a critical point^{26,377,378}. However, short time series or interpolation can result in spurious signals³⁷⁸. In theory, advanced deep learning methods can alleviate this problem by learning the underlying dynamics of the system.

In this paper, we use the recently introduced image inpainting method Resolution-robust Large Mask Inpainting with Fourier Convolutions (LaMa) that is based on a feed-forward ResNet-like inpainting network with a multi-component loss³⁴⁵. First, we reconstruct the observation-based temperature dataset HadCRUT4³⁷³. Secondly, we show that LaMa generalises to higher resolutions than trained on and masks outside the training set. Lastly, we show that our model is also able to reconstruct Arctic sea ice concentration, a structurally

completely different climate field.

We train the deep learning model on monthly historical (1850-2012) surface temperature data from the fifth coupled model intercomparison project (CMIP5). During training, we used masks derived from the missing data in the HadCRUT4 dataset. The training and evaluation data were transformed into 72×72 pixel grey-scale images. This corresponds to a $5^\circ \times 2.5^\circ$ longitude-latitude grid. After training, we first evaluate the model on held-out CMIP5 data and in a second step on the HadCRUT4 temperatures. Since there is no ground truth available for the historical temperatures, we compare our inpainted dataset with known historical events as well as with reanalysis data. Furthermore, we compare our method with kriging and a previously introduced machine learning inpainting method based on partial convolutions (PConv)⁵.

The model successfully reproduces the spatiotemporal patterns of the CMIP5 data and outperforms kriging and the PConv method in terms of the spatial and site-wise root-mean-square error on the CMIP5 evaluation dataset. The infilling of the HadCRUT4 dataset yields reasonable results. We successfully reconstruct spatial patterns of known historical events, including strong El Niño and La Niña years. Our results generally agree with the 20CRv3.SI reanalysis³⁷⁹. However, especially the polar regions show differences across the different datasets and reconstructions, which is mostly due to the sparsity of measurements in these regions.

In a second step, we demonstrate LaMa's capability to reconstruct datasets using masks it has not encountered during training and with higher resolutions than trained on. The model, trained solely on masks derived from HadCRUT4, produces artefacts when evaluated on masks outside the training set. Therefore, we modify the mask generation process and use randomly generated masks during the training³⁴⁵. We reconstruct the Berkeley Earth Surface Temperatures (BEST) dataset with a 90×90 pixel resolution and show that the model realistically inpaints the missing areas.

Finally, we demonstrate the model's applicability to a structurally different climate field. We train our model on daily Arctic sea ice concentration data from 1979 to the present day^{380,381} with a resolution of 180×1440 pixel. Subsequently, we evaluate LaMa on artificially masked held-out days of the training set. The model learns the distribution of continents and realistically reconstructs the sea ice concentration. The Central Arctic exhibits the smallest errors, while the edges of the sea ice have the largest deviations from the ground truth.

In this paper, we present a novel and easy-to-use method to realistically reconstruct a variety of climate fields that outperforms current interpolation

methods. Our method and possible further developments in this direction provide a promising alternative to widely used reconstruction methods.

/6

Conclusion and Outlook

6.1 Summary and Conclusion

The primary goal of this work is to enhance the understanding of the climate system in the past, present, and future. This is achieved by employing various modelling approaches ranging from a conceptual dynamical model, to state-of-the-art ice-sheet models and deep learning-based methods. While all papers are linked by the aforementioned overarching goal and the methods used, this thesis is divided into two partially distinct parts. The first part of this thesis lays out the theoretical basis and gives an overview of tipping elements, needed to understand the first two papers. The second part summarises different modelling approaches that were employed in this thesis.

The main scientific contribution of this thesis consists of three papers. The first two papers specifically concern two distinct tipping elements, while the third paper introduces a novel method for climate field reconstruction. In more detail, the main findings of this thesis can be summarised as follows. In the first paper, we show for the first time, evidence for a deforestation-induced critical transition in the coupled SAMS-Amazon rainforest system. We show that the vegetation is a crucial component for the stability of the SAMS that has been neglected in previous studies. We combine model- and observation-based analyses and find statistically significant and consistent early-warning signals across model and observations. In addition to the well-established statistical early-warning signals, we observe physical early-warning signals related to changes in the hydrological cycle in response to the deforestation in Amazonia,

which offer additional evidence for an approaching critical transition. While the SAMS has been hypothesised to exhibit threshold behaviour¹⁵⁵, no early warning signals or similar signs in connection with a deforestation-induced tipping point have been reported before.

In the second paper, we investigate an overshoot of the critical temperature threshold of the GrIS using two independent state-of-the-art ice-sheet models. A previous conceptual study showed that critical thresholds can be temporally exceeded, under certain circumstances, without prompting a transition to an alternative state²¹. We show for the first time, that this is true for the GrIS, using two comprehensive ice-sheet models. The timescale of the ice melt is slow enough such that a timely reversal of the surface temperature can prevent a large-scale loss of the GrIS. Generally, the longer and the higher the exceedance, the greater the ice loss and hence the sea-level rise. In any case, the sea-level rise is generally greater for scenarios that overshoot the critical threshold than for scenarios where the temperature does not exceed the critical temperature at any point. However, we also show that long-term exceedance of the critical threshold leads to a complete meltdown of the GrIS and long-term overshoot can lead to partially irreversible ice loss. That means that even a reversal of the temperature below the critical threshold does not necessarily lead to a full regrowth of the GrIS.

In the third paper we introduce a new deep learning-based method to reconstruct arbitrary spatiotemporal climate fields. We utilise a recently introduced image inpainting method based on Fourier convolutions. We train our model on numerical climate model output and reanalysis data to reconstruct historical surface temperature and sea ice concentration data with large missing areas. Our method is able to realistically reconstruct known historical events and outperforms widely used methods in the geosciences such as kriging and previously introduced machine learning-based methods. This can potentially lead to new insights in a variety of fields based on new and better reconstructions. Particularly for tipping elements, long, spatiotemporally consistent time series are essential to assess past dynamics and hence the stability.

Combining the results from the first two papers, we corroborate previous estimates suggesting that current warming and deforestation rates likely lead to crossing the critical thresholds for the SAMS and GrIS. However, it should be noted that it is inherently difficult to quantify exact values for these thresholds. In the second paper, we address this issue by employing two independent models, allowing us to provide two independent estimates of the critical threshold for the GrIS. Additionally, we demonstrate that the inherent timescale of tipping elements is a crucial factor in assessing the urgency to implement mitigation measures. Tipping elements with slow responses, like the GrIS, may tolerate temporary temperature overshoots, whereas other tipping elements may react

more quickly than a potential reversal can take place. Our overshooting approach offers a new perspective on tipping elements by focusing on a more realistic concept of reversibility compared to earlier studies that focused on equilibrium responses. Applying similar approaches to other tipping elements could help constrain their potential tipping probabilities.

This thesis shows how the urgency of climate change calls for an interdisciplinary approach combining theoretical, modelling and observation-based methods. By adopting this strategy, we have successfully enhanced our understanding of two distinct tipping elements and have proposed a new reconstruction method for climate fields.

6.2 Outlook and Future Research

Future research directions and possibilities are vast. Although our understanding of tipping elements advanced considerably in the last years, a lot of uncertainty and numerous open questions remain. The emergence of artificial intelligence offers new opportunities for climate science and particularly for tipping elements. This section outlines several promising general and specific research directions.

To date, the representation of tipping elements in comprehensive climate models is strongly limited, mainly for two reasons. Firstly, it has been argued that the tuning process in climate model development often leads to an overestimation of the stability, rendering the observation of tipping behaviour in these models virtually impossible^{3,282}. Improved and standardised tuning and calibration processes that include paleoclimatic records can improve the representation of tipping phenomena in ESMs³⁸². A traceable model hierarchy²⁷⁴ is crucial to understand the mismatch in tipping phenomena between simpler models and state-of-the-art comprehensive climate models. Secondly, computational limitations currently prevent fully coupled simulation runs, let alone ensemble simulations over millennial or even decamillennial time scales. However, due to the slow timescale of many tipping elements, long runs are essential to assess their stability. Advances in machine learning, such as the improved parameterisation or emulation schemes previously discussed, might lead to substantial speed-ups, enabling coupled long-term simulations. At the same time, it is crucial to ensure physical plausibility, which requires extensive validation of these models. Furthermore, alternative computationally efficient approaches have been proposed that reduce the number of simulation years needed to assess tipping behaviour in comprehensive climate models³⁸³.

These advancements are especially relevant for the two major ice sheets as

the slowest tipping elements in the Earth system. Currently, the long timescale of the GrIS's response does not permit running long-term experiments with fully coupled ESMs. Furthermore, the ice sheet geometry is typically static in many state-of-the-art ESMs, meaning it does not evolve with a changing climate. Marine ice sheet processes are even less well-represented. However, there is increasing effort to bidirectionally couple ice sheets with other climate system components and to include marine processes³⁸⁴. The impact of potential changes in atmospheric and oceanic circulation on the evolution of the ice sheets is currently not well understood. Coupled simulations could help to reduce uncertainties related to the ice sheets' sensitivity to global warming, while simultaneously providing better constraints on past changes. Additionally, improved projections of ice sheet melt, and consequently the freshwater influx into the ocean, can help constrain the likelihood of a potential AMOC tipping point.

In contrast to other tipping elements, the literature on the SAMS-rainforest system is relatively sparse and its classification as a tipping element remains uncertain. The critical thresholds in terms of global warming and deforestation are not very well constrained¹²¹. Most studies on the Amazon rainforest do (i) only investigate either the impact of global warming or deforestation but not their combined effects and (ii) do not include bidirectional coupling between the monsoon and the vegetation or (iii) rely only on conceptual models. Given the relatively short timescale of the SAMS, coupled ESM simulations offer a feasible tool to investigate the combined effect of deforestation and global warming on the coupled system. Consequently, the SAMS is relatively unique, as many other tipping elements require substantially longer integration times. For example, spatiotemporally different deforestation scenarios could constrain the tipping point threshold and provide insights into particularly critical regions. Additionally, land and vegetation models depend heavily on parameterisation schemes, introducing considerable uncertainty. Especially in densely vegetated areas such as Amazonia, observations are sparse, leading to even greater parameter uncertainties. This calls for large-scale observational missions to constrain parameters better.

While there are numerous studies on the general concept of tipping elements, fewer studies address their potential for overshoot, or are limited to conceptual models^{21,385}. In light of current climate change mitigation efforts, more focus must be placed on overshoot scenarios using comprehensive climate models. Particularly, slower tipping elements such as the ice sheets⁵³ or potentially the AMOC may have the potential for a temporary temperature overshoot without triggering a critical transition. However, rapidly reacting elements such as coral reefs, monsoon circulations, or forests likely lack this overshoot potential. Concurrently, it has been demonstrated that even the most ambitious mitigation scenarios may not prevent changes in, for example, oceanic circulations by the

end of this century¹⁸⁸. In other words, the current greenhouse gas emissions lock in unavoidable changes that could trigger tipping points, even under the most extreme mitigation scenarios. In the same vein, reversing the GMT, for instance through carbon capture, does not guarantee a reversal of regional or local temperatures³⁸⁶. One would expect a spatial-dependent temperature decrease, similarly to the observed temperature increase, introducing another layer of uncertainty into future projections. Furthermore, even small, temporary overshoots can lead to irreversible changes, even without a transition to an alternative state⁵³. It should also be noted that each overshoot scenario implies the necessity of drastic measures to reverse the warming trend.

Studies investigating tipping elements often ignore structural, algorithmic and parameter uncertainties. Typically, a single set of best-estimate parameters is chosen and single runs are performed. Subsequently, rudimentary uncertainty estimations are performed by varying key parameters. Additionally, most studies are restricted to only one model ignoring any model-dependent structural uncertainties. We propose several approaches towards a more probabilistic treatment of tipping elements. First, a coordinated model intercomparison for tipping elements, utilising a standardised experimental protocol similar to that of other intercomparison projects, is required. This would enable the resolution of model dependency in tipping elements and potentially even provide insights into tipping mechanisms. Indeed, first initiatives for a tipping point modelling intercomparison project are underway¹. Secondly, methodologies allowing for efficient parameter uncertainty estimation are needed. Often, model parameters are not well constrained, leading to a huge number of plausible parameter combinations. Running simulations for each combination is computationally infeasible or even impossible. For example, Bayesian approaches that incorporate parameter uncertainty can help constrain the positions of tipping points³⁸⁷. Additionally, rare event algorithms, which have been successfully applied for other high impact, low likelihood climate events such as heat waves, could also help constrain tipping probabilities³⁸⁸.

The study of the impact of tipping elements often only focuses on the global scale. However, efficient mitigation strategies require to investigate regional and local impacts of tipping events. For example, dynamical downscaling of coarser models that exhibit tipping phenomena can be used to inform regional climate models via, for example, boundary conditions. This allows for the assessment of the impact of tipping events on smaller spatial scales.

In recent years, research on tipping points has shifted considerably from relying solely on simple conceptual models to incorporating more comprehensive models. Additionally, more and more observational data become freely available.

1. See for example TIPMIP at <https://tipmip.pik-potsdam.de/>. Accessed 16.01.2024.

While these developments offer new possibilities and insights, there is a risk that this increased complexity may come at the expense of understanding. Particularly with the growing application of machine learning in climate science, conceptual models and models of intermediate complexity will remain crucial for ensuring understanding throughout the entire model hierarchy, enabling an integrated assessment of tipping points in the Earth system.

Bibliography

1. Calvin, K. *et al.* IPCC, 2023: *Climate Change 2023: Synthesis Report. Contribution of Working Groups I, II and III to the Sixth Assessment Report of the Intergovernmental Panel on Climate Change [Core Writing Team, H. Lee and J. Romero (eds.)].* IPCC, Geneva, Switzerland. tech. rep. (Intergovernmental Panel on Climate Change (IPCC), 2023).
2. Intergovernmental Panel On Climate Change. *Climate Change 2021 – The Physical Science Basis: Working Group I Contribution to the Sixth Assessment Report of the Intergovernmental Panel on Climate Change* 1st ed. ISBN: 978-1-00-915789-6 (Cambridge University Press, 2023).
3. Boers, N., Ghil, M. & Stocker, T. F. Theoretical and paleoclimatic evidence for abrupt transitions in the Earth system. *Environmental Research Letters* **17**, 093006 (2022).
4. Ben-Yami, M., Skiba, V., Bathiany, S. & Boers, N. *Uncertainties in critical slowing down indicators of observation-based fingerprints of the Atlantic Overturning Circulation* 2023.
5. Kadow, C., Hall, D. M. & Ulbrich, U. Artificial intelligence reconstructs missing climate information. *Nature Geoscience* **13**, 408–413 (2020).
6. Bochow, N., Poltronieri, A., Rypdal, M. & Boers, N. *Reconstructing historical climate fields with deep learning* 2023.
7. Kochkov, D. *et al.* *Neural General Circulation Models* 2023.
8. Brunetti, M. & Ragon, C. Attractors and bifurcation diagrams in complex climate models. *Physical Review E* **107**, 054214 (2023).
9. Lenton, T. M. Environmental Tipping Points. *Annual Review of Environment and Resources* **38**, 1–29 (2013).
10. Alkhayuon, H. Rate-induced transitions for parameter shift systems (2018).
11. Ashwin, P., Wieczorek, S., Vitolo, R. & Cox, P. Tipping points in open systems: bifurcation, noise-induced and rate-dependent examples in the climate system. *Philosophical Transactions of the Royal Society A: Mathematical, Physical and Engineering Sciences* **370**, 1166–1184 (2012).
12. Guckenheimer, J. & Holmes, P. J. *Nonlinear Oscillations, Dynamical Systems, and Bifurcations of Vector Fields* ISBN: 978-0-387-90819-9 (1983).

13. Klose, A. K., Karle, V., Winkelmann, R. & Donges, J. F. Emergence of cascading dynamics in interacting tipping elements of ecology and climate. *Royal Society Open Science* **7**, 200599 (2020).
14. Thompson, J. M. T., Stewart, H. B. & Ueda, Y. Safe, explosive, and dangerous bifurcations in dissipative dynamical systems. *Physical Review E* **49**, 1019–1027 (1994).
15. Feudel, U. Rate-induced tipping in ecosystems and climate: the role of unstable states, basin boundaries and transient dynamics. *Nonlinear Processes in Geophysics* **30**, 481–502 (2023).
16. Horsthemke, W. & Lefever, R. *Noise-Induced Transitions* ISBN: 978-3-540-11359-1 (Springer, Berlin, Heidelberg, 2006).
17. Ghosh, S., Pal, A. K. & Bose, I. Noise-induced regime shifts: A quantitative characterization. *The European Physical Journal E* **36**, 123 (2013).
18. Toral, R. Noise-induced transitions vs. noise-induced phase transitions. *AIP Conference Proceedings* **1332**, 145–154 (2011).
19. Ritchie, P. D. L., Alkhayoun, H., Cox, P. M. & Wiczorek, S. Rate-induced tipping in natural and human systems. *Earth System Dynamics* **14**, 669–683 (2023).
20. Bochow, N. *A Conceptual Model Coupling the Amazon Rainforest with the South American Monsoon System* MA thesis (Humboldt-Universität zu Berlin, Berlin, 2020).
21. Ritchie, P. D. L., Clarke, J. J., Cox, P. M. & Huntingford, C. Overshooting tipping point thresholds in a changing climate. *Nature* **592**, 517–523 (2021).
22. Ritchie, P., Karabacak, Ö. & Sieber, J. Inverse-square law between time and amplitude for crossing tipping thresholds. *Proceedings of the Royal Society A: Mathematical, Physical and Engineering Sciences* **475**, 20180504 (2019).
23. Dakos, V. *et al.* *Tipping Point Detection and Early-Warnings in climate, ecological, and human systems* preprint (Biosphere and ecosystems/Human/Earth system interactions/Other methods, 2023).
24. Ritchie, P. & Sieber, J. Early-warning indicators for rate-induced tipping. *Chaos: An Interdisciplinary Journal of Nonlinear Science* **26**, 093116 (2016).
25. Van Nes, E. H. & Scheffer, M. Slow recovery from perturbations as a generic indicator of a nearby catastrophic shift. *The American Naturalist* **169**, 738–747 (2007).
26. Scheffer, M. *et al.* Early-warning signals for critical transitions. *Nature* **461**, 53–59 (2009).
27. Arnoldi, J.-F., Bideault, A., Loreau, M. & Haegeman, B. How ecosystems recover from pulse perturbations: A theory of short- to long-term responses. *Journal of theoretical biology* **436**, 79–92 (2018).
28. Ditlevsen, P. D. & Johnsen, S. J. Tipping points: Early warning and wishful thinking. *Geophysical Research Letters* **37** (2010).

29. Dakos, V. *et al.* Slowing Down in Spatially Patterned Ecosystems at the Brink of Collapse. *The American Naturalist* **177**, E153–E166 (2011).
30. Dakos, V., van Nes, E. H. & Scheffer, M. Flickering as an early warning signal. *Theoretical Ecology* (2013).
31. Carpenter, S. R., Brock, W. A., Cole, J. J. & Pace, M. L. A new approach for rapid detection of nearby thresholds in ecosystem time series. *Oikos* **123**, 290–297 (2014).
32. Guttal, V. & Jayaprakash, C. Changing skewness: an early warning signal of regime shifts in ecosystems. *Ecology Letters* **11**, 450–460 (2008).
33. Guttal, V. & Jayaprakash, C. Spatial variance and spatial skewness: leading indicators of regime shifts in spatial ecological systems. *Theoretical Ecology* **2**, 3–12 (2009).
34. Rietkerk, M. & van de Koppel, J. Regular pattern formation in real ecosystems. *Trends in Ecology & Evolution* **23**, 169–175 (2008).
35. Rietkerk, M. *et al.* Evasion of tipping in complex systems through spatial pattern formation. *Science* **374**, eabj0359 (2021).
36. Rietkerk, M., Dekker, S. C., de Ruiter, P. C. & van de Koppel, J. Self-Organized Patchiness and Catastrophic Shifts in Ecosystems. *Science* **305**, 1926–1929 (2004).
37. Kéfi, S. *et al.* Spatial vegetation patterns and imminent desertification in Mediterranean arid ecosystems. *Nature* **449**, 213–217 (2007).
38. Kéfi, S. *et al.* Early Warning Signals of Ecological Transitions: Methods for Spatial Patterns. *PLOS ONE* **9** (ed Solé, R. V.) e92097 (2014).
39. Lu, Z., Yuan, N., Yang, Q., Ma, Z. & Kurths, J. Early Warning of the Pacific Decadal Oscillation Phase Transition Using Complex Network Analysis. *Geophysical Research Letters* **48**, e2020GL091674 (2021).
40. Bury, T. M. *et al.* Deep learning for early warning signals of tipping points. *Proceedings of the National Academy of Sciences* **118**, e2106140118 (2021).
41. Deb, S., Sidheekh, S., Clements, C. F., Krishnan, N. C. & Dutta, P. S. Machine learning methods trained on simple models can predict critical transitions in complex natural systems. *Royal Society Open Science* **9**, 211475 (2022).
42. Dylewsky, D. *et al.* Universal early warning signals of phase transitions in climate systems. *Journal of The Royal Society Interface* **20**, 20220562 (2023).
43. Kéfi, S., Dakos, V., Scheffer, M., Nes, E. H. V. & Rietkerk, M. Early warning signals also precede non-catastrophic transitions. *Oikos* **122**, 641–648 (2013).
44. Lenton, T. M. *et al.* Tipping elements in the Earth's climate system. *Proceedings of the National Academy of Sciences* **105**, 1786–1793 (2008).
45. Armstrong McKay, D. I. *et al.* Exceeding 1.5°C global warming could trigger multiple climate tipping points. *Science* **377**, eabn7950 (2022).

46. Wang, S. *et al.* Mechanisms and Impacts of Earth System Tipping Elements. *Reviews of Geophysics* **61**, e2021RG000757 (2023).
47. Steffen, W. *et al.* Trajectories of the Earth System in the Anthropocene. *Proceedings of the National Academy of Sciences* **115**, 8252–8259 (2018).
48. Rocha, J. C., Peterson, G., Bodin, Ö. & Levin, S. Cascading regime shifts within and across scales. *Science* **362**, 1379–1383 (2018).
49. Dekker, M. M., von der Heydt, A. S. & Dijkstra, H. A. Cascading transitions in the climate system. *Earth System Dynamics* **9**, 1243–1260 (2018).
50. Lenton, T. M. *et al.* Climate tipping points — too risky to bet against. *Nature* **575**, 592–595 (2019).
51. Wunderling, N., Gelbrecht, M., Winkelmann, R., Kurths, J. & Donges, J. F. Basin stability and limit cycles in a conceptual model for climate tipping cascades. *New Journal of Physics* **22**, 123031 (2020).
52. Bastiaansen, R., Ashwin, P. & von der Heydt, A. S. Climate response and sensitivity: time scales and late tipping points. *Proceedings of the Royal Society A: Mathematical, Physical and Engineering Sciences* **479**, 20220483 (2023).
53. Bochow, N. *et al.* Overshooting the critical threshold for the Greenland ice sheet. *Nature* **622**, 528–536 (2023).
54. Morlighem, M. *et al.* BedMachine v3: Complete Bed Topography and Ocean Bathymetry Mapping of Greenland From Multibeam Echo Sounding Combined With Mass Conservation. *Geophysical Research Letters* **44**, 11, 051–11, 061 (2017).
55. Morlighem, M. *et al.* Deep glacial troughs and stabilizing ridges unveiled beneath the margins of the Antarctic ice sheet. *Nature Geoscience* **13**, 132–137 (2020).
56. Robinson, A., Calov, R. & Ganopolski, A. Multistability and critical thresholds of the Greenland ice sheet. *Nature Climate Change* **2**, 429–432 (2012).
57. Pattyn, F. *et al.* The Greenland and Antarctic ice sheets under 1.5 °C global warming. *Nature Climate Change* **8**, 1053–1061 (2018).
58. Petrini, M. *et al.* A topographically-controlled tipping point for complete Greenland ice-sheet melt. *The Cryosphere Discussions*, 1–28 (2023).
59. Shepherd, A. *et al.* Mass balance of the Greenland Ice Sheet from 1992 to 2018. *Nature* **579**, 233–239 (2020).
60. King, M. D. *et al.* Dynamic ice loss from the Greenland Ice Sheet driven by sustained glacier retreat. *Communications Earth & Environment* **1**, 1–7 (2020).
61. Otosaka, I. N. *et al.* Mass balance of the Greenland and Antarctic ice sheets from 1992 to 2020. *Earth System Science Data* **15**, 1597–1616 (2023).
62. Boers, N. & Rypdal, M. Critical slowing down suggests that the western Greenland Ice Sheet is close to a tipping point. *Proceedings of the National Academy of Sciences* **118** (2021).

63. Cogley, J. *et al.* *Glossary of glacier mass balance and related terms* programme and meeting document (International Association of Cryospheric Sciences, 2011).
64. Rignot, E., Velicogna, I., van den Broeke, M. R., Monaghan, A. & Lenaerts, J. T. M. Acceleration of the contribution of the Greenland and Antarctic ice sheets to sea level rise. *Geophysical Research Letters* **38** (2011).
65. Mougintot, J., Rignot, E. & Scheuchl, B. Sustained increase in ice discharge from the Amundsen Sea Embayment, West Antarctica, from 1973 to 2013. *Geophysical Research Letters* **41**, 1576–1584 (2014).
66. Rignot, E. *et al.* Four decades of Antarctic Ice Sheet mass balance from 1979–2017. *Proceedings of the National Academy of Sciences* **116**, 1095–1103 (2019).
67. Shepherd, A. *et al.* Mass balance of the Antarctic Ice Sheet from 1992 to 2017. *Nature* **558**, 219–222 (2018).
68. Lenaerts, J. T. M., Medley, B., van den Broeke, M. R. & Wouters, B. Observing and Modeling Ice Sheet Surface Mass Balance. *Reviews of Geophysics* **57**, 376–420 (2019).
69. Choi, Y., Morlighem, M., Rignot, E. & Wood, M. Ice dynamics will remain a primary driver of Greenland ice sheet mass loss over the next century. *Communications Earth & Environment* **2**, 1–9 (2021).
70. Van den Broeke, M. *et al.* Partitioning of melt energy and meltwater fluxes in the ablation zone of the west Greenland ice sheet. *The Cryosphere* **2**, 179–189 (2008).
71. Vernon, C. L. *et al.* Surface mass balance model intercomparison for the Greenland ice sheet. *The Cryosphere* **7**, 599–614 (2013).
72. Lenaerts, J. T. M., Camron, M. D., Wyburn-Powell, C. R. & Kay, J. E. Present-day and future Greenland Ice Sheet precipitation frequency from CloudSat observations and the Community Earth System Model. *The Cryosphere* **14**, 2253–2265 (2020).
73. Van den Broeke, M. R. *et al.* On the recent contribution of the Greenland ice sheet to sea level change. *The Cryosphere* **10**, 1933–1946 (2016).
74. Lewis, G. *et al.* Recent precipitation decrease across the western Greenland ice sheet percolation zone. *The Cryosphere* **13**, 2797–2815 (2019).
75. Montgomery, L., Koenig, L., Lenaerts, J. T. M. & Munneke, P. K. Accumulation rates (2009–2017) in Southeast Greenland derived from airborne snow radar and comparison with regional climate models. *Annals of Glaciology* **61**, 225–233 (2020).
76. Fettweis, X. *et al.* GrSMBMIP: intercomparison of the modelled 1980–2012 surface mass balance over the Greenland Ice Sheet. *The Cryosphere* **14**, 3935–3958 (2020).
77. Kiilsholm, S., Christensen, J. H., Dethloff, K. & Rinke, A. Net accumulation of the Greenland ice sheet: High resolution modeling of climate changes. *Geophysical Research Letters* **30** (2003).

78. Chen, Q.-s., Bromwich, D. H. & Bai, L. Precipitation over Greenland Retrieved by a Dynamic Method and Its Relation to Cyclonic Activity. *Journal of Climate* **10**, 839–870 (1997).
79. Broeke, M. R. v. d., Lipzig, N. P. M. v. & Meijgaard, E. v. Momentum Budget of the East Antarctic Atmospheric Boundary Layer: Results of a Regional Climate Model. *Journal of the Atmospheric Sciences* **59**, 3117–3129 (2002).
80. Koenig, L. S. *et al.* Wintertime storage of water in buried supraglacial lakes across the Greenland Ice Sheet. *The Cryosphere* **9**, 1333–1342 (2015).
81. Bell, R. E. *et al.* Antarctic ice shelf potentially stabilized by export of meltwater in surface river. *Nature* **544**, 344–348 (2017).
82. Chandler, D. M. *et al.* Evolution of the subglacial drainage system beneath the Greenland Ice Sheet revealed by tracers. *Nature Geoscience* **6**, 195–198 (2013).
83. Forster, R. R. *et al.* Extensive liquid meltwater storage in firn within the Greenland ice sheet. *Nature Geoscience* **7**, 95–98 (2014).
84. Rennermalm, A. K. *et al.* Understanding Greenland ice sheet hydrology using an integrated multi-scale approach. *Environmental Research Letters* **8**, 015017 (2013).
85. Van der Veen, C. J., Bromwich, D. H., Csatho, B. M. & Kim, C. Trend surface analysis of Greenland accumulation. *Journal of Geophysical Research: Atmospheres* **106**, 33909–33918 (2001).
86. Fettweis, X. *et al.* Brief communication "Important role of the mid-tropospheric atmospheric circulation in the recent surface melt increase over the Greenland ice sheet". *The Cryosphere* **7**, 241–248 (2013).
87. Hanna, E., Fettweis, X. & Hall, R. J. Brief communication: Recent changes in summer Greenland blocking captured by none of the CMIP5 models. *The Cryosphere* **12**, 3287–3292 (2018).
88. Hanna, E. *et al.* Greenland Ice Sheet surface mass balance 1870 to 2010 based on Twentieth Century Reanalysis, and links with global climate forcing. *Journal of Geophysical Research: Atmospheres* **116** (2011).
89. Levermann, A. & Winkelmann, R. A simple equation for the melt elevation feedback of ice sheets. *The Cryosphere* **10**, 1799–1807 (2016).
90. Qu, X. & Hall, A. What Controls the Strength of Snow-Albedo Feedback? *Journal of Climate* **20**, 3971–3981 (2007).
91. Flanner, M. G., Shell, K. M., Barlage, M., Perovich, D. K. & Tschudi, M. A. Radiative forcing and albedo feedback from the Northern Hemisphere cryosphere between 1979 and 2008. *Nature Geoscience* **4**, 151–155 (2011).
92. Zeitz, M., Reese, R., Beckmann, J., Krebs-Kanzow, U. & Winkelmann, R. Impact of the melt–albedo feedback on the future evolution of the Greenland Ice Sheet with PISM-dEBM-simple. *The Cryosphere* **15**, 5739–5764 (2021).

93. Box, J. E. *et al.* Greenland Ice Sheet Rainfall, Heat and Albedo Feedback Impacts From the Mid-August 2021 Atmospheric River. *Geophysical Research Letters* **49**, e2021GL097356 (2022).
94. Zeitz, M., Haacker, J. M., Donges, J. F., Albrecht, T. & Winkelmann, R. Dynamic regimes of the Greenland Ice Sheet emerging from interacting melt-elevation and glacial isostatic adjustment feedbacks. *Earth System Dynamics Discussions*, 1–25 (2021).
95. Ghil, M. Cryothermodynamics: the chaotic dynamics of paleoclimate. *Physica D: Nonlinear Phenomena. Special Issue Originating from the 13th Annual International Conference of the Center for Nonlinear Studies Los Alamos, NM, USA, 17–21 May 1993* **77**, 130–159 (1994).
96. Nicola, L., Notz, D. & Winkelmann, R. Revisiting temperature sensitivity: how does Antarctic precipitation change with temperature? *The Cryosphere* **17**, 2563–2583 (2023).
97. DeConto, R. M. & Pollard, D. Contribution of Antarctica to past and future sea-level rise. *Nature* **531**, 591–597 (2016).
98. Schoof, C. Ice sheet grounding line dynamics: Steady states, stability, and hysteresis. *Journal of Geophysical Research: Earth Surface* **112** (2007).
99. Gardner, A. S. *et al.* Near-Surface Temperature Lapse Rates over Arctic Glaciers and Their Implications for Temperature Downscaling. *Journal of Climate* **22**, 4281–4298 (2009).
100. Fausto, R. S., Ahlstrøm, A. P., As, D. V., Bøggild, C. E. & Johnsen, S. J. A new present-day temperature parameterization for Greenland. *Journal of Glaciology* **55**, 95–105 (2009).
101. Erokhina, O. *et al.* Dependence of slope lapse rate over the Greenland ice sheet on background climate. *Journal of Glaciology* **63**, 568–572 (2017).
102. Hanna, E. *et al.* Runoff and mass balance of the Greenland ice sheet: 1958–2003. *Journal of Geophysical Research: Atmospheres* **110** (2005).
103. Stone, E. J., Lunt, D. J., Rutt, I. C. & Hanna, E. Investigating the sensitivity of numerical model simulations of the modern state of the Greenland ice-sheet and its future response to climate change. *The Cryosphere* **4**, 397–417 (2010).
104. Le clec’h, S. *et al.* Assessment of the Greenland ice sheet–atmosphere feedbacks for the next century with a regional atmospheric model coupled to an ice sheet model. *The Cryosphere* **13**, 373–395 (2019).
105. Raoult, N. *et al.* Improving modelled albedo over the Greenland ice sheet through parameter optimisation and MODIS snow albedo retrievals. *The Cryosphere* **17**, 2705–2724 (2023).
106. Stroeve, J. Assessment of Greenland albedo variability from the advanced very high resolution radiometer Polar Pathfinder data set. *Journal of Geophysical Research: Atmospheres* **106**, 33989–34006 (2001).
107. Box, J. E., As, D. v. & Steffen, K. Greenland, Canadian and Icelandic land-ice albedo grids (2000–2016). *GEUS Bulletin* **38**, 53–56 (2017).

108. Box, J. E. *et al.* Greenland ice sheet albedo feedback: thermodynamics and atmospheric drivers. *The Cryosphere* **6**, 821–839 (2012).
109. Sneed, W. A. & Hamilton, G. S. Evolution of melt pond volume on the surface of the Greenland Ice Sheet. *Geophysical Research Letters* **34** (2007).
110. Ryan, J. C. *et al.* Decreasing surface albedo signifies a growing importance of clouds for Greenland Ice Sheet meltwater production. *Nature Communications* **13**, 4205 (2022).
111. Ryan, J. C. *et al.* Greenland Ice Sheet surface melt amplified by snowline migration and bare ice exposure. *Science Advances* **5**, eaav3738 (2019).
112. Tedstone, A. J. *et al.* Dark ice dynamics of the south-west Greenland Ice Sheet. *The Cryosphere* **11**, 2491–2506 (2017).
113. Tedstone, A. J. *et al.* Algal growth and weathering crust state drive variability in western Greenland Ice Sheet ice albedo. *The Cryosphere* **14**, 521–538 (2020).
114. Cook, J. M. *et al.* Glacier algae accelerate melt rates on the south-western Greenland Ice Sheet. *The Cryosphere* **14**, 309–330 (2020).
115. Noël, B. *et al.* Evaluation of the updated regional climate model RACMO2.3: summer snowfall impact on the Greenland Ice Sheet. *The Cryosphere* **9**, 1831–1844 (2015).
116. Barletta, V. R. *et al.* Observed rapid bedrock uplift in Amundsen Sea Embayment promotes ice-sheet stability. *Science* **360**, 1335–1339 (2018).
117. Whitehouse, P. L. Glacial isostatic adjustment modelling: historical perspectives, recent advances, and future directions. *Earth Surface Dynamics* **6**, 401–429 (2018).
118. Wake, L. M., Lecavalier, B. S. & Bevis, M. Glacial Isostatic Adjustment (GIA) in Greenland: a Review. *Current Climate Change Reports* **2**, 101–111 (2016).
119. Huybrechts, P. Sea-level changes at the LGM from ice-dynamic reconstructions of the Greenland and Antarctic ice sheets during the glacial cycles. *Quaternary Science Reviews* **21**, 203–231 (2002).
120. Gregory, J. M., George, S. E. & Smith, R. S. Large and irreversible future decline of the Greenland ice sheet. *The Cryosphere* **14**, 4299–4322 (2020).
121. Flores, B. M. *et al.* Critical transitions in the Amazon forest system. *Nature* **626**, 555–564 (2024).
122. Pan, Y. *et al.* A Large and Persistent Carbon Sink in the World's Forests. *Science* **333**, 988–993 (2011).
123. Saatchi, S. S. *et al.* Benchmark map of forest carbon stocks in tropical regions across three continents. *Proceedings of the National Academy of Sciences* **108**, 9899–9904 (2011).
124. Bochow, N. & Boers, N. The South American monsoon approaches a critical transition in response to deforestation. *Science Advances* **9**, eadd9973 (2023).

125. De Carvalho, L. M. V. & Cavalcanti, I. F. A. in *The Monsoons and Climate Change: Observations and Modeling* (eds de Carvalho, L. M. V. & Jones, C.) 121–148 (Springer International Publishing, Cham, 2016). ISBN: 978-3-319-21650-8.
126. Ramage, C. in *International Geophysics Series* 296–296 (Academic Press, New York, 1971). ISBN: 0-19-504254-9.
127. Zhou, J. & Lau, K.-M. Does a Monsoon Climate Exist over South America? *Journal of Climate* **11**, 1020–1040 (1998).
128. Wright, J. S. *et al.* Rainforest-initiated wet season onset over the southern Amazon. *Proceedings of the National Academy of Sciences* **114**, 8481–8486 (2017).
129. Liebmann, B. & Mechoso, C. R. in, 137–157 (2011). ISBN: 978-981-4343-41-1.
130. Li, W. & Fu, R. Transition of the Large-Scale Atmospheric and Land Surface Conditions from the Dry to the Wet Season over Amazonia as Diagnosed by the ECMWF Re-Analysis. *Journal of Climate* **17**, 2637–2651 (2004).
131. Fu, R. & Li, W. The influence of the land surface on the transition from dry to wet season in Amazonia. *Theoretical and Applied Climatology* **78** (2004).
132. Li, W. & Fu, R. Influence of Cold Air Intrusions on the Wet Season Onset over Amazonia. *Journal of Climate* **19**, 257–275 (2006).
133. Marengo, J. A. *et al.* Recent developments on the South American monsoon system. *International Journal of Climatology* **32**, 1–21 (2012).
134. Wang, H. & Fu, R. Cross-Equatorial Flow and Seasonal Cycle of Precipitation over South America. *Journal of Climate* **15**, 1591–1608 (2002).
135. Espinoza, J. C. *et al.* Revisiting wintertime cold air intrusions at the east of the Andes: propagating features from subtropical Argentina to Peruvian Amazon and relationship with large-scale circulation patterns. *Climate Dynamics* **41**, 1983–2002 (2013).
136. Sierra, J. P. *et al.* Impacts of land-surface heterogeneities and Amazonian deforestation on the wet season onset in southern Amazon. *Climate Dynamics* **61**, 4867–4898 (2023).
137. Madden, R. A. & Julian, P. R. Observations of the 40–50-Day Tropical Oscillation—A Review. *Monthly Weather Review* **122**, 814–837 (1994).
138. Carvalho, L. M. V. *et al.* Moisture transport and intraseasonal variability in the South America monsoon system. *Climate Dynamics* **36**, 1865–1880 (2011).
139. Ma, H.-Y., Ji, X., Neelin, J. D. & Mechoso, C. R. Mechanisms for Precipitation Variability of the Eastern Brazil/SACZ Convective Margin. *Journal of Climate* **24**, 3445–3456 (2011).
140. Bombardi, R. J., Carvalho, L. M. V., Jones, C. & Reboita, M. S. Precipitation over eastern South America and the South Atlantic Sea surface

- temperature during neutral ENSO periods. *Climate Dynamics* **42**, 1553–1568 (2014).
141. Kitoh, A. *et al.* Monsoons in a changing world: A regional perspective in a global context. *Journal of Geophysical Research: Atmospheres* **118**, 3053–3065 (2013).
 142. Lejeune, Q., Davin, E. L., Guillod, B. P. & Seneviratne, S. I. Influence of Amazonian deforestation on the future evolution of regional surface fluxes, circulation, surface temperature and precipitation. *Climate Dynamics* **44**, 2769–2786 (2015).
 143. Gatti, L. V. *et al.* Amazonia as a carbon source linked to deforestation and climate change. *Nature* **595**, 388–393 (2021).
 144. Da Cruz, D. C., Benayas, J. M. R., Ferreira, G. C., Santos, S. R. & Schwartz, G. An overview of forest loss and restoration in the Brazilian Amazon. *New Forests* **52**, 1–16 (2021).
 145. Von Randow, C. *et al.* Comparative measurements and seasonal variations in energy and carbon exchange over forest and pasture in South West Amazonia. *Theoretical and Applied Climatology* (2004).
 146. Lawrence, D. & Vandecar, K. Effects of tropical deforestation on climate and agriculture. *Nature Climate Change* **5**, 27–36 (2015).
 147. Nobre, C. A. *et al.* Land-use and climate change risks in the Amazon and the need of a novel sustainable development paradigm. *Proceedings of the National Academy of Sciences* **113**, 10759–10768 (2016).
 148. Spracklen, D. V. & Garcia-Carreras, L. The impact of Amazonian deforestation on Amazon basin rainfall. *Geophysical Research Letters* **42**, 9546–9552 (2015).
 149. Marengo, J. A., Nobre, C. A., Sampaio, G., Salazar, L. F. & Borma, L. S. in *Tropical Rainforest Responses to Climatic Change* 259–283 (Springer Berlin Heidelberg, Berlin, Heidelberg, 2011).
 150. Hirota, M., Holmgren, M., Van Nes, E. H. & Scheffer, M. Global Resilience of Tropical Forest and Savanna to Critical Transitions. *Science* **334**, 232–235 (2011).
 151. Staal, A. *et al.* Hysteresis of tropical forests in the 21st century. *Nature Communications* **11**, 4978 (2020).
 152. Zemp, D. C. *et al.* On the importance of cascading moisture recycling in South America. *Atmospheric Chemistry and Physics* **14**, 13337–13359 (2014).
 153. Dominguez, F. *et al.* Amazonian Moisture Recycling Revisited Using WRF With Water Vapor Tracers. *Journal of Geophysical Research: Atmospheres* **127**, e2021JD035259 (2022).
 154. Anderson, L. O. *et al.* Remote sensing detection of droughts in Amazonian forest canopies. *New Phytologist* **187**, 733–750 (2010).
 155. Boers, N., Marwan, N., Barbosa, H. M. & Kurths, J. A deforestation-induced tipping point for the South American monsoon system. *Scientific Reports* **7**, 99–104 (2017).

156. Spracklen, D. V. & Coelho, C. A. S. Modeling early warning signs of possible Amazon Forest dieback. *Science Advances* **9**, eadk5670 (2023).
157. Eiras-Barca, J. *et al.* Changes in South American hydroclimate under projected Amazonian deforestation. *Annals of the New York Academy of Sciences* **1472**, 104–122 (2020).
158. Luo, X. *et al.* The Biophysical Impacts of Deforestation on Precipitation: Results from the CMIP6 Model Intercomparison. *Journal of Climate* **35**, 3293–3311 (2022).
159. Staal, A. *et al.* Feedback between drought and deforestation in the Amazon. *Environmental Research Letters* **15**, 044024 (2020).
160. Fleischer, K. *et al.* Amazon forest response to CO₂ fertilization dependent on plant phosphorus acquisition. *Nature Geoscience* **12**, 736–741 (2019).
161. Cunha, H. F. V. *et al.* Direct evidence for phosphorus limitation on Amazon forest productivity. *Nature* **608**, 558–562 (2022).
162. Fu, R. *et al.* Increased dry-season length over southern Amazonia in recent decades and its implication for future climate projection. *Proceedings of the National Academy of Sciences* **110**, 18110–18115 (2013).
163. Espinoza, J. C., Ronchail, J., Marengo, J. A. & Segura, H. Contrasting North–South changes in Amazon wet-day and dry-day frequency and related atmospheric features (1981–2017). *Climate Dynamics* **52**, 5413–5430 (2019).
164. Leite-Filho, A. T., Sousa Pontes, V. Y. & Costa, M. H. Effects of Deforestation on the Onset of the Rainy Season and the Duration of Dry Spells in Southern Amazonia. *Journal of Geophysical Research: Atmospheres* **124**, 5268–5281 (2019).
165. Leite-Filho, A. T., Costa, M. H. & Fu, R. The southern Amazon rainy season: The role of deforestation and its interactions with large-scale mechanisms. *International Journal of Climatology* **40**, 2328–2341 (2020).
166. Li, W., Fu, R., Juárez, R. I. N. & Fernandes, K. Observed change of the standardized precipitation index, its potential cause and implications to future climate change in the Amazon region. *Philosophical Transactions of the Royal Society B: Biological Sciences* **363**, 1767–1772 (2008).
167. Anderson, L. O. *et al.* Vulnerability of Amazonian forests to repeated droughts. *Philosophical Transactions of the Royal Society B: Biological Sciences* **373**, 20170411 (2018).
168. Doughty, C. E. *et al.* Tropical forests are approaching critical temperature thresholds. *Nature* **621**, 105–111 (2023).
169. Boulton, C. A., Lenton, T. M. & Boers, N. Pronounced loss of Amazon rainforest resilience since the early 2000s. *Nature Climate Change* **12**:3 **12**, 271–278 (2022).
170. Bamber, J. L., Westaway, R. M., Marzeion, B. & Wouters, B. The land ice contribution to sea level during the satellite era. *Environmental Research Letters* **13**, 063008 (2018).

171. in. *The Ocean and Cryosphere in a Changing Climate: Special Report of the Intergovernmental Panel on Climate Change* (ed Intergovernmental Panel on Climate Change (IPCC)) 321–446 (Cambridge University Press, Cambridge, 2022). ISBN: 978-1-00-915796-4.
172. Cook, C. P. *et al.* Dynamic behaviour of the East Antarctic ice sheet during Pliocene warmth. *Nature Geoscience* **6**, 765–769 (2013).
173. Dutton, A. *et al.* Sea-level rise due to polar ice-sheet mass loss during past warm periods. *Science* **349**, aaa4019 (2015).
174. Austermann, J., Hoggard, M. J., Latychev, K., Richards, F. D. & Mitrovica, J. X. The effect of lateral variations in Earth structure on Last Interglacial sea level. *Geophysical Journal International* **227**, 1938–1960 (2021).
175. Dyer, B. *et al.* Sea-level trends across The Bahamas constrain peak last interglacial ice melt. *Proceedings of the National Academy of Sciences* **118**, e2026839118 (2021).
176. Le Brocq, A. M., Payne, A. J. & Vieli, A. An improved Antarctic dataset for high resolution numerical ice sheet models (ALBMAP v1). *Earth System Science Data* **2**, 247–260 (2010).
177. Weertman, J. Stability of the Junction of an Ice Sheet and an Ice Shelf. *Journal of Glaciology* **13**, 3–11 (1974).
178. Thomas, R. H. & Bentley, C. R. A Model for Holocene Retreat of the West Antarctic Ice Sheet. *Quaternary Research* **10**, 150–170 (1978).
179. Shepherd, A., Wingham, D. & Rignot, E. Warm ocean is eroding West Antarctic Ice Sheet. *Geophysical Research Letters* **31** (2004).
180. Favier, L. *et al.* Retreat of Pine Island Glacier controlled by marine ice-sheet instability. *Nature Climate Change* **4**, 117–121 (2014).
181. Joughin, I., Smith, B. E. & Medley, B. Marine Ice Sheet Collapse Potentially Under Way for the Thwaites Glacier Basin, West Antarctica. *Science* **344**, 735–738 (2014).
182. Rignot, E., Mouginot, J., Morlighem, M., Seroussi, H. & Scheuchl, B. Widespread, rapid grounding line retreat of Pine Island, Thwaites, Smith, and Kohler glaciers, West Antarctica, from 1992 to 2011. *Geophysical Research Letters* **41**, 3502–3509 (2014).
183. Yu, H., Rignot, E., Seroussi, H., Morlighem, M. & Choi, Y. Impact of Iceberg Calving on the Retreat of Thwaites Glacier, West Antarctica Over the Next Century With Different Calving Laws and Ocean Thermal Forcing. *Geophysical Research Letters* **46**, 14539–14547 (2019).
184. Garbe, J., Albrecht, T., Levermann, A., Donges, J. F. & Winkelmann, R. The hysteresis of the Antarctic Ice Sheet. *Nature* **585**, 538–544 (2020).
185. Edwards, T. L. *et al.* Revisiting Antarctic ice loss due to marine ice-cliff instability. *Nature* **566**, 58–64 (2019).
186. DeConto, R. M. *et al.* The Paris Climate Agreement and future sea-level rise from Antarctica. *Nature* **593**, 83–89 (2021).

187. Crawford, A. J. *et al.* Marine ice-cliff instability modeling shows mixed-mode ice-cliff failure and yields calving rate parameterization. *Nature Communications* **12**, 2701 (2021).
188. Naughten, K. A., Holland, P. R. & De Rydt, J. Unavoidable future increase in West Antarctic ice-shelf melting over the twenty-first century. *Nature Climate Change* **13**, 1222–1228 (2023).
189. Alley, R. B. *et al.* Oceanic Forcing of Ice-Sheet Retreat: West Antarctica and More. *Annual Review of Earth and Planetary Sciences* **43**, 207–231 (2015).
190. Hill, E. A. *et al.* The stability of present-day Antarctic grounding lines – Part 1: No indication of marine ice sheet instability in the current geometry. *The Cryosphere* **17**, 3739–3759 (2023).
191. Reese, R. *et al.* The stability of present-day Antarctic grounding lines – Part 2: Onset of irreversible retreat of Amundsen Sea glaciers under current climate on centennial timescales cannot be excluded. *The Cryosphere* **17**, 3761–3783 (2023).
192. Stroeve, J., Holland, M. M., Meier, W., Scambos, T. & Serreze, M. Arctic sea ice decline: Faster than forecast. *Geophysical Research Letters* **34** (2007).
193. Nghiem, S. V. *et al.* Rapid reduction of Arctic perennial sea ice. *Geophysical Research Letters* **34** (2007).
194. Stroeve, J. C. *et al.* Trends in Arctic sea ice extent from CMIP5, CMIP3 and observations. *Geophysical Research Letters* **39** (2012).
195. Notz, D. & Stroeve, J. The Trajectory Towards a Seasonally Ice-Free Arctic Ocean. *Current Climate Change Reports* **4**, 407–416 (2018).
196. Notz, D. & Marotzke, J. Observations reveal external driver for Arctic sea-ice retreat. *Geophysical Research Letters* **39** (2012).
197. Stroeve, J. & Notz, D. Changing state of Arctic sea ice across all seasons. *Environmental Research Letters* **13**, 103001 (2018).
198. Wadhams, P. Arctic Ice Cover, Ice Thickness and Tipping Points. *AMBIO* **41**, 23–33 (2012).
199. Haine, T. W. N. & Martin, T. The Arctic-Subarctic sea ice system is entering a seasonal regime: Implications for future Arctic amplification. *Scientific Reports* **7**, 4618 (2017).
200. Linke, O. *et al.* Constraints on simulated past Arctic amplification and lapse rate feedback from observations. *Atmospheric Chemistry and Physics* **23**, 9963–9992 (2023).
201. Levermann, A. *et al.* Potential climatic transitions with profound impact on Europe. *Climatic Change* **110**, 845–878 (2012).
202. Sturm, M. & Massom, R. A. in *Sea Ice* 65–109 (John Wiley & Sons, Ltd, 2017). ISBN: 978-1-118-77837-1.
203. Notz, D. & Community, S. Arctic Sea Ice in CMIP6. *Geophysical Research Letters* **47**, e2019GL086749 (2020).

204. Bathiany, S., Notz, D., Mauritsen, T., Raedel, G. & Brovkin, V. On the Potential for Abrupt Arctic Winter Sea Ice Loss. *Journal of Climate* **29**, 2703–2719 (2016).
205. in. *Climate Change 2021 – The Physical Science Basis: Working Group I Contribution to the Sixth Assessment Report of the Intergovernmental Panel on Climate Change* (ed Intergovernmental Panel on Climate Change (IPCC)) 1211–1362 (Cambridge University Press, Cambridge, 2023). ISBN: 978-1-00-915788-9.
206. Ridley, J. K., Lowe, J. A. & Hewitt, H. T. How reversible is sea ice loss? *The Cryosphere* **6**, 193–198 (2012).
207. Li, C., Notz, D., Tietsche, S. & Marotzke, J. The Transient versus the Equilibrium Response of Sea Ice to Global Warming. *Journal of Climate* **26**, 5624–5636 (2013).
208. Smith, S. L., O’Neill, H. B., Isaksen, K., Noetzli, J. & Romanovsky, V. E. The changing thermal state of permafrost. *Nature Reviews Earth & Environment* **3**, 10–23 (2022).
209. Abbott, B. W. & Jones, J. B. Permafrost collapse alters soil carbon stocks, respiration, CH₄, and N₂O in upland tundra. *Global Change Biology* **21**, 4570–4587 (2015).
210. McGuire, A. D. *et al.* Dependence of the evolution of carbon dynamics in the northern permafrost region on the trajectory of climate change. *Proceedings of the National Academy of Sciences* **115**, 3882–3887 (2018).
211. Turetsky, M. R. *et al.* Carbon release through abrupt permafrost thaw. *Nature Geoscience* **13**, 138–143 (2020).
212. Teufel, B. & Sushama, L. Abrupt changes across the Arctic permafrost region endanger northern development. *Nature Climate Change* **9**, 858–862 (2019).
213. Clark, P. U. *et al.* Consequences of twenty-first-century policy for multi-millennial climate and sea-level change. *Nature Climate Change* **6**, 360–369 (2016).
214. Huss, M. & Hock, R. Global-scale hydrological response to future glacier mass loss. *Nature Climate Change* **8**, 135–140 (2018).
215. Van Breedam, J., Goelzer, H. & Huybrechts, P. Semi-equilibrated global sea-level change projections for the next 10,000 years. *Earth System Dynamics* **11**, 953–976 (2020).
216. Rounce, D. R. *et al.* Global glacier change in the 21st century: Every increase in temperature matters. *Science (New York, N.Y.)* **379**, 78–83 (2023).
217. Marzeion, B. *et al.* Partitioning the Uncertainty of Ensemble Projections of Global Glacier Mass Change. *Earth’s Future* **8**, e2019EF001470 (2020).
218. Loriani, S. *et al.* *Tipping points in ocean and atmosphere circulations* preprint (Climate change/Human/Earth system interactions/Earth system and climate modeling, 2023).

219. Moat, B. I. *et al.* Pending recovery in the strength of the meridional overturning circulation at 26°N. *Ocean Science* **16**, 863–874 (2020).
220. Buckley, M. W. & Marshall, J. Observations, inferences, and mechanisms of the Atlantic Meridional Overturning Circulation: A review. *Reviews of Geophysics* **54**, 5–63 (2016).
221. Stommel, H. Thermohaline Convection with Two Stable Regimes of Flow. *Tellus* **13**, 224–230 (1961).
222. Rahmstorf, S. Ocean circulation and climate during the past 120,000 years. *Nature* **419**, 207–214 (2002).
223. Lynch-Stieglitz, J. The Atlantic Meridional Overturning Circulation and Abrupt Climate Change. *Annual Review of Marine Science* **9**, 83–104 (2017).
224. Vettoretti, G., Ditlevsen, P., Jochum, M. & Rasmussen, S. O. Atmospheric CO₂ control of spontaneous millennial-scale ice age climate oscillations. *Nature Geoscience* **15**, 300–306 (2022).
225. Hawkins, E. *et al.* Bistability of the Atlantic overturning circulation in a global climate model and links to ocean freshwater transport. *Geophysical Research Letters* **38** (2011).
226. Wood, R. A., Rodríguez, J. M., Smith, R. S., Jackson, L. C. & Hawkins, E. Observable, low-order dynamical controls on thresholds of the Atlantic meridional overturning circulation. *Climate Dynamics* **53**, 6815–6834 (2019).
227. Ditlevsen, P. & Ditlevsen, S. Warning of a forthcoming collapse of the Atlantic meridional overturning circulation. *Nature Communications* **14**, 4254 (2023).
228. Gong, X., Liu, H., Wang, F. & Heuzé, C. Of Atlantic Meridional Overturning Circulation in the CMIP6 Project. *Deep Sea Research Part II: Topical Studies in Oceanography* **206**, 105193 (2022).
229. Hofmann, M. & Rahmstorf, S. On the stability of the Atlantic meridional overturning circulation. *Proceedings of the National Academy of Sciences* **106**, 20584–20589 (2009).
230. Jackson, L. C. & Wood, R. A. Hysteresis and Resilience of the AMOC in an Eddy-Permitting GCM. *Geophysical Research Letters* **45**, 8547–8556 (2018).
231. Caesar, L., Rahmstorf, S., Robinson, A., Feulner, G. & Saba, V. Observed fingerprint of a weakening Atlantic Ocean overturning circulation. *Nature* **556**, 191–196 (2018).
232. Michel, S. L. L. *et al.* Early warning signal for a tipping point suggested by a millennial Atlantic Multidecadal Variability reconstruction. *Nature Communications* **13**, 5176 (2022).
233. Michel, S. *et al.* Deep learning reconstruction of Atlantic Meridional Overturning Circulation strength validates ongoing twenty-first century decline. preprint. 2023.

234. Lobelle, D., Beaulieu, C., Livina, V., Sévellec, F. & Frajka-Williams, E. Detectability of an AMOC Decline in Current and Projected Climate Changes. *Geophysical Research Letters* **47**, e2020GL089974 (2020).
235. Born, A., Stocker, T. F. & Sandø, A. B. Transport of salt and freshwater in the Atlantic Subpolar Gyre. *Ocean Dynamics* **66**, 1051–1064 (2016).
236. Klockmann, M., Mikolajewicz, U., Kleppin, H. & Marotzke, J. Coupling of the Subpolar Gyre and the Overturning Circulation During Abrupt Glacial Climate Transitions. *Geophysical Research Letters* **47**, e2020GL090361 (2020).
237. Jackson, L. C. *et al.* Understanding AMOC stability: the North Atlantic Hosing Model Intercomparison Project. *Geoscientific Model Development* **16**, 1975–1995 (2023).
238. Lohmann, J. & Ditlevsen, P. D. Risk of tipping the overturning circulation due to increasing rates of ice melt. *Proceedings of the National Academy of Sciences* **118**, e2017989118 (2021).
239. Bronselaer, B. *et al.* Change in future climate due to Antarctic meltwater. *Nature* **564**, 53–58 (2018).
240. Li, Q., England, M. H., Hogg, A. M., Rintoul, S. R. & Morrison, A. K. Abyssal ocean overturning slowdown and warming driven by Antarctic meltwater. *Nature* **615**, 841–847 (2023).
241. Purich, A. & England, M. H. Projected Impacts of Antarctic Meltwater Anomalies over the Twenty-First Century. *Journal of Climate* **36**, 2703–2719 (2023).
242. Gunn, K. L., Rintoul, S. R., England, M. H. & Bowen, M. M. Recent reduced abyssal overturning and ventilation in the Australian Antarctic Basin. *Nature Climate Change* **13**, 537–544 (2023).
243. Zhou, S. *et al.* Slowdown of Antarctic Bottom Water export driven by climatic wind and sea-ice changes. *Nature Climate Change* **13**, 701–709 (2023).
244. Siahayan, A. *et al.* The Antarctic contribution to 21st-century sea-level rise predicted by the UK Earth System Model with an interactive ice sheet. *The Cryosphere* **16**, 4053–4086 (2022).
245. Levermann, A., Schewe, J., Petoukhov, V. & Held, H. Basic mechanism for abrupt monsoon transitions. *Proceedings of the National Academy of Sciences* **106**, 20572–20577 (2009).
246. Boos, W. R. & Storelvmo, T. Near-linear response of mean monsoon strength to a broad range of radiative forcings. *Proceedings of the National Academy of Sciences* **113**, 1510–1515 (2016).
247. Bathiany, S., Scheffer, M., Van Nes, E. H., Williamson, M. S. & Lenton, T. M. Abrupt Climate Change in an Oscillating World. *Scientific Reports* **8** (2018).
248. McGuffie, K. & Henderson-Sellers, A. *The Climate Modelling Primer*, 4th Edition 4th edition. ISBN: 978-1-119-94337-2 (Wiley-Blackwell, Chichester, West Sussex, UK ; Hoboken, NJ, UK, 2014).

249. Sellers, W. D. A Global Climatic Model Based on the Energy Balance of the Earth-Atmosphere System. *Journal of Applied Meteorology and Climatology* **8**, 392–400 (1969).
250. Budyko, M. I. The effect of solar radiation variations on the climate of the Earth. *Tellus* **21**, 611–619 (1969).
251. Kaper, H. E. H. *Mathematics and Climate* ISBN: 978-1-61197-260-3 (Society for Industrial and Applied Mathematics, Philadelphia, 2013).
252. North, G. R. Analytical Solution to a Simple Climate Model with Diffusive Heat Transport. *Journal of the Atmospheric Sciences* **32**, 1301–1307 (1975).
253. North, G. R. The Small Ice Cap Instability in Diffusive Climate Models. *Journal of the Atmospheric Sciences* **41**, 3390–3395 (1984).
254. Krebs-Kanzow, U. *et al.* The diurnal Energy Balance Model (dEBM): a convenient surface mass balance solution for ice sheets in Earth system modeling. *The Cryosphere* **15**, 2295–2313 (2021).
255. Cessi, P. A Simple Box Model of Stochastically Forced Thermohaline Flow. *Journal of Physical Oceanography* **24**, 1911–1920 (1994).
256. Baudena, M., Boni, G., Ferraris, L., von Hardenberg, J. & Provenzale, A. Vegetation response to rainfall intermittency in drylands: Results from a simple ecohydrological box model. *Advances in Water Resources* **30**, 1320–1328 (2007).
257. Blaschke, L. L. *et al.* *Spatial correlation increase in single-sensor satellite data reveals loss of Amazon rainforest resilience* 2023.
258. Wigley, T. M. L. & Schlesinger, M. E. Analytical solution for the effect of increasing CO₂ on global mean temperature. *Nature* **315**, 649–652 (1985).
259. Goosse, H. *et al.* Description of the Earth system model of intermediate complexity LOVECLIM version 1.2. *Geoscientific Model Development* **3**, 603–633 (2010).
260. De Haan, B. J. *et al.* An atmosphere-ocean model for integrated assessment of global change. *Water, Air, and Soil Pollution* **76**, 283–318 (1994).
261. Ganopolski, A. *et al.* CLIMBER-2: a climate system model of intermediate complexity. Part II: model sensitivity. *Climate Dynamics* **17**, 735–751 (2001).
262. Montoya, M. *et al.* The earth system model of intermediate complexity CLIMBER-3 α . Part I: description and performance for present-day conditions. *Climate Dynamics* **25**, 237–263 (2005).
263. Willeit, M., Ganopolski, A., Robinson, A. & Edwards, N. R. The Earth system model CLIMBER-X v1.0 – Part 1: Climate model description and validation. *Geoscientific Model Development* **15**, 5905–5948 (2022).
264. Fanning, A. F. & Weaver, A. J. An atmospheric energy-moisture balance model: Climatology, interpentadal climate change, and coupling to an ocean general circulation model. *Journal of Geophysical Research: Atmospheres* **101**, 15111–15128 (1996).

265. Weaver, A. J. *et al.* The UVic earth system climate model: Model description, climatology, and applications to past, present and future climates. *Atmosphere-Ocean* **39**, 361–428 (2001).
266. Ritz, S. P., Stocker, T. F. & Joos, F. A Coupled Dynamical Ocean–Energy Balance Atmosphere Model for Paleoclimate Studies. *Journal of Climate* **24**, 349–375 (2011).
267. Lenton, T. M. *et al.* Effects of atmospheric dynamics and ocean resolution on bi-stability of the thermohaline circulation examined using the Grid ENabled Integrated Earth system modelling (GENIE) framework. *Climate Dynamics* **29**, 591–613 (2007).
268. Asch, R. G., Pilcher, D. J., Rivero-Calle, S. & M. Holding, J. Demystifying Models: Answers to Ten Common Questions That Ecologists Have About Earth System Models. *Limnology and Oceanography Bulletin* **25**, 65–70 (2016).
269. Palmer, T. Climate forecasting: Build high-resolution global climate models. *Nature* **515**, 338–339 (2014).
270. Eyring, V. *et al.* Overview of the Coupled Model Intercomparison Project Phase 6 (CMIP6) experimental design and organization. *Geoscientific Model Development* **9**, 1937–1958 (2016).
271. Flato, G. M. Earth system models: an overview. *WIREs Climate Change* **2**, 783–800 (2011).
272. *High Resolution Numerical Modelling of the Atmosphere and Ocean* (eds Hamilton, K. & Ohfuchi, W.) ISBN: 978-0-387-36671-5 (Springer, New York, NY, 2008).
273. Haarsma, R. J. *et al.* High Resolution Model Intercomparison Project (HighResMIP v1.0) for CMIP6. *Geoscientific Model Development* **9**, 4185–4208 (2016).
274. Balaji, V. *et al.* Are general circulation models obsolete? *Proceedings of the National Academy of Sciences* **119**, e2202075119 (2022).
275. Lamarque, J.-F. *et al.* CAM-chem: description and evaluation of interactive atmospheric chemistry in the Community Earth System Model. *Geoscientific Model Development* **5**, 369–411 (2012).
276. Hewitt, H. T. *et al.* Resolving and Parameterising the Ocean Mesoscale in Earth System Models. *Current Climate Change Reports* **6**, 137–152 (2020).
277. Danabasoglu, G. *et al.* The Community Earth System Model Version 2 (CESM2). *Journal of Advances in Modeling Earth Systems* **12**, e2019MS001916 (2020).
278. Poltronieri, A., Bochow, N., Boers, N., Jakobsen, P. K. & Rypdal, M. *Arctic summer sea ice loss will accelerate in coming decades* preprint. 2022.
279. Lawrence, D. M. *et al.* The Community Land Model Version 5: Description of New Features, Benchmarking, and Impact of Forcing Uncertainty. *Journal of Advances in Modeling Earth Systems* **11**, 4245–4287 (2019).

280. Scafetta, N. Advanced Testing of Low, Medium, and High ECS CMIP6 GCM Simulations Versus ERA5-T2m. *Geophysical Research Letters* **49**, e2022GL097716 (2022).
281. Hourdin, F. *et al.* The Art and Science of Climate Model Tuning. *Bulletin of the American Meteorological Society* **98**, 589–602 (2017).
282. Valdes, P. Built for stability. *Nature Geoscience* **4**, 414–416 (2011).
283. Schoof, C. & Hewitt, I. Ice-Sheet Dynamics. *Annual Review of Fluid Mechanics* **45**, 217–239 (2013).
284. Glen, J. W. The flow law of ice. A discussion of the assumptions made in glacier theory, their experimental foundations and consequences. *International Association of Scientific Hydrology* **47**, 171–183 (1958).
285. Winkelmann, R. *et al.* The Potsdam Parallel Ice Sheet Model (PISM-PIK) – Part 1: Model description. *The Cryosphere* **5**, 715–726 (2011).
286. Fettweis, X. *et al.* Reconstructions of the 1900–2015 Greenland ice sheet surface mass balance using the regional climate MAR model. *The Cryosphere* **11**, 1015–1033 (2017).
287. Niwano, M. *et al.* NHM–SMAP: spatially and temporally high-resolution nonhydrostatic atmospheric model coupled with detailed snow process model for Greenland Ice Sheet. *The Cryosphere* **12**, 635–655 (2018).
288. Reeh, N. Parameterization of Melt Rate and Surface Temperature in the Greenland Ice Sheet. *Polarforschung* (1991).
289. Robinson, A., Calov, R. & Ganopolski, A. An efficient regional energy-moisture balance model for simulation of the Greenland Ice Sheet response to climate change. *The Cryosphere* **4**, 129–144 (2010).
290. Aschwanden, A. *et al.* Contribution of the Greenland Ice Sheet to sea level over the next millennium. *Science Advances* (2019).
291. Noël, B. *et al.* Modelling the climate and surface mass balance of polar ice sheets using RACMO2 – Part 1: Greenland (1958–2016). *The Cryosphere* **12**, 811–831 (2018).
292. Garbe, J., Zeitz, M., Krebs-Kanzow, U. & Winkelmann, R. The evolution of future Antarctic surface melt using PISM-dEBM-simple. *The Cryosphere Discussions*, 1–39 (2023).
293. Van den Berg, J., van de Wal, R. & Oerlemans, H. A mass balance model for the Eurasian Ice Sheet for the last 120,000 years. *Global and Planetary Change* **61**, 194–208 (2008).
294. Krebs-Kanzow, U., Gierz, P. & Lohmann, G. Brief communication: An ice surface melt scheme including the diurnal cycle of solar radiation. *The Cryosphere* **12**, 3923–3930 (2018).
295. Whitehouse, P. L., Gomez, N., King, M. A. & Wiens, D. A. Solid Earth change and the evolution of the Antarctic Ice Sheet. *Nature Communications* **10**, 503 (2019).
296. Meur, E. L. & Huybrechts, P. A comparison of different ways of dealing with isostasy: examples from modelling the Antarctic ice sheet during the last glacial cycle. *Annals of Glaciology* **23**, 309–317 (1996).

297. Lingle, C. S. & Clark, J. A. A numerical model of interactions between a marine ice sheet and the solid earth: Application to a West Antarctic ice stream. *Journal of Geophysical Research: Oceans* **90**, 1100–1114 (1985).
298. Bueler, E., Lingle, C. S. & Brown, J. Fast computation of a viscoelastic deformable Earth model for ice-sheet simulations. *Annals of Glaciology* **46**, 97–105 (2007).
299. Smith, R. B. & Barstad, I. A Linear Theory of Orographic Precipitation. *Journal of the Atmospheric Sciences* **61**, 1377–1391 (2004).
300. De Burgh-Day, C. O. & Leeuwenburg, T. Machine learning for numerical weather and climate modelling: a review. *Geoscientific Model Development* **16**, 6433–6477 (2023).
301. Meyer, D., Hogan, R. J., Dueben, P. D. & Mason, S. L. Machine Learning Emulation of 3D Cloud Radiative Effects. *Journal of Advances in Modeling Earth Systems* **14**, e2021MS002550 (2022).
302. Chevallier, F., Chéruy, F., Scott, N. A. & Chédin, A. A Neural Network Approach for a Fast and Accurate Computation of a Longwave Radiative Budget. *Journal of Applied Meteorology and Climatology* **37**, 1385–1397 (1998).
303. Krasnopolsky, V. M., Fox-Rabinovitz, M. S. & Chalikov, D. V. New Approach to Calculation of Atmospheric Model Physics: Accurate and Fast Neural Network Emulation of Longwave Radiation in a Climate Model. *Monthly Weather Review* **133**, 1370–1383 (2005).
304. Brenowitz, N. D. & Bretherton, C. S. Prognostic Validation of a Neural Network Unified Physics Parameterization. *Geophysical Research Letters* **45**, 6289–6298 (2018).
305. Rasp, S., Pritchard, M. S. & Gentine, P. Deep learning to represent subgrid processes in climate models. *Proceedings of the National Academy of Sciences* **115**, 9684–9689 (2018).
306. Brenowitz, N. D. & Bretherton, C. S. Spatially Extended Tests of a Neural Network Parametrization Trained by Coarse-Graining. *Journal of Advances in Modeling Earth Systems* **11**, 2728–2744 (2019).
307. Han, Y., Zhang, G. J., Huang, X. & Wang, Y. A Moist Physics Parameterization Based on Deep Learning. *Journal of Advances in Modeling Earth Systems* **12**, e2020MS002076 (2020).
308. Mooers, G. *et al.* Assessing the Potential of Deep Learning for Emulating Cloud Superparameterization in Climate Models With Real-Geography Boundary Conditions. *Journal of Advances in Modeling Earth Systems* **13**, e2020MS002385 (2021).
309. Clark, S. K. *et al.* Correcting a 200 km Resolution Climate Model in Multiple Climates by Machine Learning From 25 km Resolution Simulations. *Journal of Advances in Modeling Earth Systems* **14**, e2022MS003219 (2022).
310. Bretherton, C. S. *et al.* Correcting Coarse-Grid Weather and Climate Models by Machine Learning From Global Storm-Resolving Simulations. *Journal of Advances in Modeling Earth Systems* **14**, e2021MS002794 (2022).

311. Wang, X., Han, Y., Xue, W., Yang, G. & Zhang, G. J. Stable climate simulations using a realistic general circulation model with neural network parameterizations for atmospheric moist physics and radiation processes. *Geoscientific Model Development* **15**, 3923–3940 (2022).
312. Jouvét, G. *et al.* Deep learning speeds up ice flow modelling by several orders of magnitude. *Journal of Glaciology* **68**, 651–664 (2022).
313. Andersson, T. R. *et al.* Seasonal Arctic sea ice forecasting with probabilistic deep learning. *Nature Communications* **12**, 5124 (2021).
314. Bi, K. *et al.* Accurate medium-range global weather forecasting with 3D neural networks. *Nature* **619**, 533–538 (2023).
315. Dueben, P. D. & Bauer, P. Challenges and design choices for global weather and climate models based on machine learning. *Geoscientific Model Development* **11**, 3999–4009 (2018).
316. Scher, S. Toward Data-Driven Weather and Climate Forecasting: Approximating a Simple General Circulation Model With Deep Learning. *Geophysical Research Letters* **45**, 12, 616–12, 622 (2018).
317. Scher, S. & Messori, G. Weather and climate forecasting with neural networks: using general circulation models (GCMs) with different complexity as a study ground. *Geoscientific Model Development* **12**, 2797–2809 (2019).
318. Weyn, J. A., Durran, D. R. & Caruana, R. Can Machines Learn to Predict Weather? Using Deep Learning to Predict Gridded 500-hPa Geopotential Height From Historical Weather Data. *Journal of Advances in Modeling Earth Systems* **11**, 2680–2693 (2019).
319. Weyn, J. A., Durran, D. R. & Caruana, R. Improving Data-Driven Global Weather Prediction Using Deep Convolutional Neural Networks on a Cubed Sphere. *Journal of Advances in Modeling Earth Systems* **12**, e2020MS002109 (2020).
320. Rasp, S. & Thuerey, N. Data-Driven Medium-Range Weather Prediction With a Resnet Pretrained on Climate Simulations: A New Model for WeatherBench. *Journal of Advances in Modeling Earth Systems* **13**, e2020MS002405 (2021).
321. Keisler, R. *Forecasting Global Weather with Graph Neural Networks* 2022.
322. Lam, R. *et al.* Learning skillful medium-range global weather forecasting. *Science* **0**, eadi2336 (2023).
323. Arcomano, T. *et al.* A Hybrid Approach to Atmospheric Modeling That Combines Machine Learning With a Physics-Based Numerical Model. *Journal of Advances in Modeling Earth Systems* **14**, e2021MS002712 (2022).
324. Taylor, J. & Feng, M. A deep learning model for forecasting global monthly mean sea surface temperature anomalies. *Frontiers in Climate* **4** (2022).
325. Nguyen, T., Brandstetter, J., Kapoor, A., Gupta, J. K. & Grover, A. *ClimaX: A foundation model for weather and climate* 2023.

326. Kashinath, K. *et al.* Physics-informed machine learning: case studies for weather and climate modelling. *Philosophical Transactions of the Royal Society A: Mathematical, Physical and Engineering Sciences* **379**, 20200093 (2021).
327. Cuomo, S. *et al.* *Scientific Machine Learning through Physics-Informed Neural Networks: Where we are and What's next* 2022.
328. Misyris, G. S., Venzke, A. & Chatzivasileiadis, S. *Physics-Informed Neural Networks for Power Systems in 2020 IEEE Power & Energy Society General Meeting (PESGM)* (2020), 1–5.
329. Cai, S., Mao, Z., Wang, Z., Yin, M. & Karniadakis, G. E. Physics-informed neural networks (PINNs) for fluid mechanics: a review. *Acta Mechanica Sinica* **37**, 1727–1738 (2021).
330. Yang, L., Zhang, D. & Karniadakis, G. E. Physics-Informed Generative Adversarial Networks for Stochastic Differential Equations. *SIAM Journal on Scientific Computing* **42**, A292–A317 (2020).
331. Wu, J.-L. *et al.* Enforcing statistical constraints in generative adversarial networks for modeling chaotic dynamical systems. *Journal of Computational Physics* **406**, 109209 (2020).
332. White, B. L., Singh, A. & Albert, A. Downscaling Numerical Weather Models with GANs. **2019**, GC43D–1357 (2019).
333. Hess, P., Drüke, M., Petri, S., Strnad, F. M. & Boers, N. Physically constrained generative adversarial networks for improving precipitation fields from Earth system models. *Nature Machine Intelligence* **4**, 828–839 (2022).
334. Bihlo, A. & Popovych, R. O. Physics-informed neural networks for the shallow-water equations on the sphere. *Journal of Computational Physics* **456**, 111024 (2022).
335. Yang, C., Yang, X. & Xiao, X. Data-driven projection method in fluid simulation. *Computer Animation and Virtual Worlds* **27**, 415–424 (2016).
336. Tompson, J., Schlachter, K., Sprechmann, P. & Perlin, K. *Accelerating Eulerian Fluid Simulation With Convolutional Networks in Proceedings of the 34th International Conference on Machine Learning (PMLR, 2017)*, 3424–3433.
337. Kochkov, D. *et al.* Machine learning accelerated computational fluid dynamics. *Proceedings of the National Academy of Sciences* **118**, e2101784118 (2021).
338. Lu, L., Jin, P., Pang, G., Zhang, Z. & Karniadakis, G. E. Learning nonlinear operators via DeepONet based on the universal approximation theorem of operators. *Nature Machine Intelligence* **3**, 218–229 (2021).
339. Watt-Meyer, O. *et al.* Correcting Weather and Climate Models by Machine Learning Nudged Historical Simulations. *Geophysical Research Letters* **48**, e2021GL092555 (2021).

340. Mitsui, T. & Boers, N. Seasonal prediction of Indian summer monsoon onset with echo state networks. *Environmental Research Letters* **16**, 074024 (2021).
341. Lim, B. & Zohren, S. Time-series forecasting with deep learning: a survey. *Philosophical Transactions of the Royal Society A: Mathematical, Physical and Engineering Sciences* **379**, 20200209 (2021).
342. Barrera-Animas, A. Y. *et al.* Rainfall prediction: A comparative analysis of modern machine learning algorithms for time-series forecasting. *Machine Learning with Applications* **7**, 100204 (2022).
343. Flora, M., Potvin, C., McGovern, A. & Handler, S. *Comparing Explanation Methods for Traditional Machine Learning Models Part 2: Quantifying Model Explainability Faithfulness and Improvements with Dimensionality Reduction* 2022.
344. Lopez-Gomez, I., McGovern, A., Agrawal, S. & Hickey, J. Global Extreme Heat Forecasting Using Neural Weather Models. *Artificial Intelligence for the Earth Systems* **2** (2023).
345. Suvorov, R. *et al.* *Resolution-robust Large Mask Inpainting with Fourier Convolutions* 2021.
346. Chi, L., Jiang, B. & Mu, Y. *Fast fourier convolution in Advances in neural information processing systems* (eds Larochelle, H., Ranzato, M., Hadsell, R., Balcan, M. & Lin, H.) **33** (Curran Associates, Inc., 2020), 4479–4488.
347. Yannic Kilcher. *Resolution-robust Large Mask Inpainting with Fourier Convolutions (w/ Author Interview)* 2021.
348. Ramachandran, P., Zoph, B. & Le, Q. V. *Searching for Activation Functions* 2017.
349. Ioffe, S. & Szegedy, C. *Batch Normalization: Accelerating Deep Network Training by Reducing Internal Covariate Shift* 2015.
350. Goodfellow, I. J. *et al.* *Generative Adversarial Networks* 2014.
351. Mescheder, L., Geiger, A. & Nowozin, S. *Which Training Methods for GANs do actually Converge?* 2018.
352. Nobre, C. A. & Borma, L. D. S. ‘Tipping points’ for the Amazon forest. *Current Opinion in Environmental Sustainability* **1**, 28–36 (2009).
353. Kopp, R. *et al.* in *Climate Science Special Report: Fourth National Climate Assessment* 411–429 (U.S. Global Change Research Program, Washington, DC, 2017).
354. Lovejoy, T. E. & Nobre, C. Amazon tipping point: Last chance for action. *Science Advances* (2019).
355. Parry, I. M., Ritchie, P. D. & Cox, P. M. Evidence of localised Amazon rainforest dieback in CMIP6 models. *Earth System Dynamics* **13**, 1667–1675 (2022).
356. Samanta, A., Ganguly, S., Vermote, E., Nemani, R. R. & Myneni, R. B. Why Is Remote Sensing of Amazon Forest Greenness So Challenging? *Earth Interactions* **16**, 1–14 (2012).

357. Hersbach, H. *et al.* The ERA5 global reanalysis. *Quarterly Journal of the Royal Meteorological Society* **146**, 1999–2049 (2020).
358. Schneider, U. *et al.* Evaluating the Hydrological Cycle over Land Using the Newly-Corrected Precipitation Climatology from the Global Precipitation Climatology Centre (GPCC). *Atmosphere 2017*, Vol. 8, Page 52 **8**, 52 (2017).
359. Adler, R. F. *et al.* The Global Precipitation Climatology Project (GPCP) Monthly Analysis (New Version 2.3) and a Review of 2017 Global Precipitation. *Atmosphere 2018*, Vol. 9, Page 138 **9**, 138 (2018).
360. Funk, C. C. *et al.* A quasi-global precipitation time series for drought monitoring. *Data Series* (2014).
361. Poveda, G., Jaramillo, L. & Vallejo, L. F. Seasonal precipitation patterns along pathways of South American low-level jets and aerial rivers. *Water Resources Research* (2014).
362. Boers, N. *et al.* The South American rainfall dipole: A complex network analysis of extreme events. *Geophysical Research Letters* **41**, 7397–7405 (2014).
363. Marengo, J. A., Jimenez, J. C., Espinoza, J. C., Cunha, A. P. & Aragão, L. E. Increased climate pressure on the agricultural frontier in the Eastern Amazonia–Cerrado transition zone. *Scientific Reports 2022 12:1* **12**, 1–10 (2022).
364. Nobre, C. A., Sellers, P. J. & Shukla, J. Amazonian Deforestation and Regional Climate Change. *Journal of Climate* **4**, 957–988 (1991).
365. Werth, D. The local and global effects of Amazon deforestation. *Journal of Geophysical Research* **107**, 8087 (2002).
366. Avissar, R. & Werth, D. Global Hydroclimatological Teleconnections Resulting from Tropical Deforestation. *Journal of Hydrometeorology* **6**, 134–145 (2005).
367. Robinson, A. *et al.* Description and validation of the ice-sheet model Yelmo (version 1.0). *Geoscientific Model Development* **13**, 2805–2823 (2020).
368. Cappelen, J. *Greenland-DMI historical climate data collection 1784-2019* tech. rep. (Danish Meteorological Institute, 2020).
369. Koenig, S. J. *et al.* Ice sheet model dependency of the simulated Greenland Ice Sheet in the mid-Pliocene. *Climate of the Past* **11**, 369–381 (2015).
370. Höning, D. *et al.* Multistability and Transient Response of the Greenland Ice Sheet to Anthropogenic CO₂ Emissions. *Geophysical Research Letters* **50**, e2022GL101827 (2023).
371. Sommers, A. N. *et al.* Retreat and Regrowth of the Greenland Ice Sheet During the Last Interglacial as Simulated by the CESM2-CISM2 Coupled Climate–Ice Sheet Model. *Paleoceanography and Paleoclimatology* **36**, e2021PA004272 (2021).
372. Muntjewerf, L. *et al.* Description and Demonstration of the Coupled Community Earth System Model v2 – Community Ice Sheet Model v2 (CESM2-CISM2). *Journal of Advances in Modeling Earth Systems* **13**, e2020MS002356 (2021).

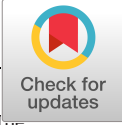
373. Morice, C. P., Kennedy, J. J., Rayner, N. A. & Jones, P. D. Quantifying uncertainties in global and regional temperature change using an ensemble of observational estimates: The HadCRUT4 data set: THE HADCRUT4 DATASET. *Journal of Geophysical Research: Atmospheres* **117**, n/a–n/a (2012).
374. Harris, I., Osborn, T. J., Jones, P. & Lister, D. Version 4 of the CRU TS monthly high-resolution gridded multivariate climate dataset. *Scientific Data* **7**, 109 (2020).
375. Vermote, E. & NOAA CDR Program. *NOAA Climate Data Record (CDR) of AVHRR Normalized Difference Vegetation Index (NDVI), Version 5* 2018.
376. Landy, J. C. *et al.* A year-round satellite sea-ice thickness record from CryoSat-2. *Nature* **609**, 517–522 (2022).
377. Dakos, V. *et al.* Slowing down as an early warning signal for abrupt climate change. *Proceedings of the National Academy of Sciences* **105**, 14308–14312 (2008).
378. Dakos, V. *et al.* Methods for Detecting Early Warnings of Critical Transitions in Time Series Illustrated Using Simulated Ecological Data. *PLOS ONE* **7**, e41010 (2012).
379. Slivinski, L. C. *et al.* Towards a more reliable historical reanalysis: Improvements for version 3 of the Twentieth Century Reanalysis system. *Quarterly Journal of the Royal Meteorological Society* **145**, 2876–2908 (2019).
380. Bell, B. *et al.* The ERA5 global reanalysis: Preliminary extension to 1950. *Quarterly Journal of the Royal Meteorological Society* **147**, 4186–4227 (2021).
381. (C3S), C. C. C. S. *Sea ice concentration daily gridded data from 1979 to present derived from satellite observations*
382. Hopcroft, P. O. & Valdes, P. J. Paleoclimate-conditioning reveals a North Africa land–atmosphere tipping point. *Proceedings of the National Academy of Sciences* **118**, e2108783118 (2021).
383. Hankel, C. & Tziperman, E. An approach for projecting the timing of abrupt winter Arctic sea ice loss. *Nonlinear Processes in Geophysics* **30**, 299–309 (2023).
384. Madsen, M. S. *et al.* The role of an interactive Greenland ice sheet in the coupled climate-ice sheet model EC-Earth-PISM. *Climate Dynamics* **59**, 1189–1211 (2022).
385. Wunderling, N. *et al.* Global warming overshoots increase risks of climate tipping cascades in a network model. *Nature Climate Change* **13**, 75–82 (2023).
386. Pfliederer, P., Schleussner, C.-F. & Sillmann, J. Limited reversal of regional climate signals in overshoot scenarios. *Environmental Research: Climate* **3**, 015005 (2024).

387. Lux, K., Ashwin, P., Wood, R. & Kuehn, C. Assessing the impact of parametric uncertainty on tipping points of the Atlantic meridional overturning circulation. *Environmental Research Letters* **17**, 075002 (2022).
388. Ragone, F., Wouters, J. & Bouchet, F. Computation of extreme heat waves in climate models using a large deviation algorithm. *Proceedings of the National Academy of Sciences* **115**, 24–29 (2018).



Paper I: The South American Monsoon System Approaches a Critical Transition

Bochow, N., Boers, N., The South American monsoon approaches a critical transition in response to deforestation. *Sci. Adv.* **9**, eadd9973 (2023).
<https://doi.org/10.1126/sciadv.add9973>



CLIMATOLOGY

The South American monsoon approaches a critical transition in response to deforestation

Nils Bochow^{1,2,3*} and Niklas Boers^{3,4,5}

The Amazon rainforest is threatened by land-use change and increasing drought and fire frequency. Studies suggest an abrupt dieback of large parts of the rainforest after partial forest loss, but the critical threshold, underlying mechanisms, and possible impacts of forest degradation on the monsoon circulation remain uncertain. Here, we use a nonlinear dynamical model of the moisture transport and recycling across the Amazon to identify several precursor signals for a critical transition in the coupled atmosphere-vegetation dynamics. Guided by our simulations, we reveal both statistical and physical precursor signals of an approaching critical transition in reanalysis and observational data. In accordance with our model results, we attribute these characteristic precursor signals to the nearing of a critical transition of the coupled Amazon atmosphere-vegetation system induced by forest loss due to deforestation, droughts, and fires. The transition would lead to substantially drier conditions, under which the rainforest could likely not be maintained.

INTRODUCTION

In combination with the impacts of anthropogenic climate change, regional land-use changes during the past decades have posed an unprecedented threat to the Amazon rainforest. Several studies suggest the existence of critical thresholds for an Amazon dieback and transition to savanna state, at global warming of 3° to 4°C on the one hand and deforestation of around 40% of the original rainforest area (1–8) on the other hand. Global warming has recently crossed 1°C above preindustrial levels, and more than 20% of the Brazilian Amazon rainforest area has already been cleared (9). Crossing the critical thresholds might induce an abrupt dieback of large parts of the rainforest, with severe ecological and climate impacts from regional to global scales.

The Amazon naturally provides many ecosystem and climate services (10) and is an essential component of the Earth's hydroclimate (11, 12). It constitutes the Earth's largest terrestrial carbon sink (13–15) and is essential for local and regional climate stability (16), with predicted decreases in precipitation and increases in air temperatures in South America in response to an Amazon dieback (5, 17–22). Besides the critical threshold in the vegetation system (3), a potential tipping point in the coupled atmosphere-vegetation dynamics of the South American monsoon system and the Amazon rainforest has been proposed, with serious implications for the monsoon circulation system when deforestation rates exceed 30 to 50% (5, 23).

Considering the potential consequences of an Amazon dieback, there is still a substantial lack of studies investigating potential precursor signals for critical transitions of the coupled vegetation-atmosphere system of tropical South America. There is growing empirical evidence of climatological and hydrological changes in Amazonia, such as rising air temperatures, extended dry seasons,

more frequent hydrological extreme events, particularly droughts, and increasing soil moisture stress. While previous droughts in the Amazon basin have partially been associated with changes in the regional circulation due to changes in the Hadley cell (24–27), the precise connection of all these changes with deforestation remains a largely open problem (22, 28–31).

On the basis of a space-for-time replacement, it has been shown that temporal autocorrelation of vegetation data [normalized difference vegetation index (NDVI)] scales negatively with mean annual precipitation in tropical forests, which suggests that rainforest vegetation is less resilient in more arid regions (32, 33). Furthermore, a loss of resilience of large parts of the rainforest over the past decades has been observed using remotely sensed vegetation optical depth data (34). Changes in the temporal autocorrelation can, under certain conditions, be interpreted as indicative of a loss of stability; however, such an analysis has not yet been performed for the coupled Amazon vegetation-atmosphere system.

Here, we show that observed changes in the hydrological cycle, as well as characteristic changes in well-established statistical indicators, might be first warning signals of a forthcoming regime shift.

For this purpose, we investigate several indicators that are associated with critical slowing down (CSD) when a system approaches a bifurcation-induced transition (35–38). When approaching the critical threshold, the restoring forces of the system diminish because the basin of attraction widens and thus the recovery rate after perturbations decreases and eventually approaches zero. Fluctuations increase and the state of the system resembles more and more its past states, and the resulting CSD can be traced, e.g., in terms of increasing variance and lag-one autocorrelation, which constitute the classical statistical precursor signals of critical transitions (36).

To understand where not only such statistical but also physical process-related precursor signals should be searched for, we first propose a nonlinear model of the moisture transport across South America, based on the fundamental moisture balance equations and coupled to the Amazon vegetation system. Guided by the results of our model simulations, we then conduct a thorough search for statistical and physical precursor signals in the ERA5 reanalysis data.

¹Department of Mathematics and Statistics, Faculty of Science and Technology, UiT The Arctic University of Norway, Tromsø, Norway. ²Physics of Ice, Climate and Earth, Niels Bohr Institute, University of Copenhagen, Copenhagen, Denmark. ³Potsdam Institute for Climate Impact Research, Potsdam, Germany. ⁴Earth System Modelling, School of Engineering and Design, Technical University of Munich, Munich, Germany. ⁵Department of Mathematics and Global Systems Institute, University of Exeter, Exeter, UK.

*Corresponding author. Email: nils.bochow@uit.no

We emphasize that the occurrence of characteristic changes in CSD indicators, such as rising lag-one autocorrelation or variance, on their own by no means implies the possibility or presence of a critical transition or of multistability in the system. After all, there may be many reasons why variance or lag-one autocorrelation might increase, also in systems that are monostable and thus cannot exhibit transitions between alternative states. The theory of CSD should only be applied for anticipating potential critical transitions if there are—a priori and independently from the CSD analysis—good reasons to assume that a given system under investigation has the potential for multistability. On the other hand, however, it should also be noted that, even if a system should not be assumed to exhibit multistability, CSD indicators may still be useful to quantify the resilience of the system (39).

In the case considered here, we will show that our model of the moisture transport and recycling over the Amazon suggests, in line with previous studies, that the coupled Amazon atmosphere-vegetation system exhibits the potential for bistability. In turn, the model results imply the potential for critical transitions between alternative states, due to positive feedbacks associated with the latent heating over the Amazon basin and the low-level circulation from the Atlantic Ocean to tropical South America (5). In particular, this is suggested independently from any CSD analysis or search for physical precursor signals. Under the a priori assumption of the possibility of alternative stable states as motivated by the modeling results, we then search for statistical CSD-based and physical precursor signals for transitions between the states.

Large parts of the Amazon rainforest experience strong seasonality in the rainfall rates. South of the Equator, the wet season retreat is marked by an abrupt precipitation decline during austral fall (March to May), while the wet season onset is characterized by a rapid increase in rainfall during austral spring (September to November). The wet season initiation has been associated with increased evapotranspiration and large-scale dynamic lifting due to cold-front incursions (40–42) and monsoon dynamics (43) a few months before the Intertropical Convergence Zone (ITCZ) migrates southward, and large amounts of moisture are transported from the tropical Atlantic Ocean to tropical South America. A delay of the wet season onset and increasing fire counts have been linked to changes in atmospheric circulation patterns toward conditions more characteristic for austral winter during the transition season (July to October) in the past decades (44). These changes are characterized by a strengthening South American low level jet, increased atmospheric subsidence over southern tropical South America, and fewer southerly cold-air incursions and anomalous convective activity over southern tropical South America (44).

Furthermore, it has been shown that the wet season onset is accelerated by atmospheric processes initiated by increased transpiration in the late dry season (45). The beginning of the wet season and the dry season length (DSL) are thus directly linked to the vegetation system. Moreover, convective latent heating over the Amazon basin strengthens the heating gradient between the Atlantic Ocean and the continent (Fig. 1). It has been shown that this enhances the easterly moisture inflow into South America by a factor of 2 to 3 during the wet season (46–48), establishing a positive feedback in the monsoonal circulation system.

To investigate the effects of deforestation and forest loss due to droughts and fires on the coupled vegetation-atmosphere system and particularly to provide guidance in the search for precursor

signals for a critical transition, we extend a recently introduced nonlinear model (5) that is based on the fundamental moisture balance equations for the moisture content in the soil and the atmosphere in dependence of precipitation, evapotranspiration, atmospheric advection, and the radiation budget. The model includes a nonlinear contribution representing the acceleration of low-level moisture flow caused by latent heating over the Amazon. Widespread deforestation and drought- or fire-induced forest dieback, via their effects on transpiration rates and radiation, have been shown to potentially trigger a collapse of the positive feedback related to convective latent heating, resulting in abrupt reductions in rainfall amounts after a critical deforestation threshold around 40% is crossed (5, 21, 23). This effect can already be observed in regions with high forest cover changes of 40 to 50%, with a growing tendency to become water limited due to decreased rainfall, increased potential evapotranspiration, and decreased actual evapotranspiration (49).

We extend the model by incorporating a mechanism for the vegetation response to changing precipitation, accounting for increased plant water stress with decreasing precipitation rates. Reduced rainfall rates over longer periods lead to a soil moisture deficit (SMD) and, ultimately, to increased tree mortality with threshold behavior (50–52). The seasonal cycle of the monsoon system is modeled as a periodically forced bistable system that annually oscillates between an on-state (wet season) and off-state (dry season) with a fold bifurcation-induced transition between on- and off-state (53).

Previous studies that investigated moisture recycling across the Amazon basin have not taken into account that changes of the forest functioning alter large-scale wind patterns although these are highly relevant for moisture recycling (54–58). In the used statistical models, the atmosphere in terms of low-level winds is constant by construction, and, therefore, the aforementioned feedbacks associated with circulation changes are suppressed. The novelty of our approach is to model the winds dynamically to account for these feedbacks between forest loss and alteration of atmospheric circulation patterns. We note that, while changes in the atmospheric circulation in tropical South America in the past decades have been identified, there remain many open questions regarding the links to anthropogenic forest loss (44).

Our model is mainly intended to provide guidance in the search for statistical and physical precursor signals in observation-based data, to find out whether the coupled Amazon vegetation-atmosphere system has been approaching a critical threshold. The model is not intended to obtain quantitatively realistic estimates of the consequences of deforestation, for example, in terms of the precise reductions of precipitation. Moreover, our model shall reveal mechanistic reasons for changes in observation-based data rather than to investigate the moisture recycling in Amazonia in detail. By construction, the abruptness of the transition might be overestimated by our model. For example, changes in surface roughness length in response to deforestation, which are ignored in our model, may have attenuating effects regarding the magnitude and the abruptness of the transition.

Previously proposed models (54, 56–58) are arithmetic models that compute the overall sum of ingoing and outgoing moisture, in contrast to our proposed model of dynamical differential equations that allow us to study the dynamical behavior of the system. The effects of changing temperature and atmospheric CO₂ level on the hydrological cycle in Amazonia remain still uncertain, and

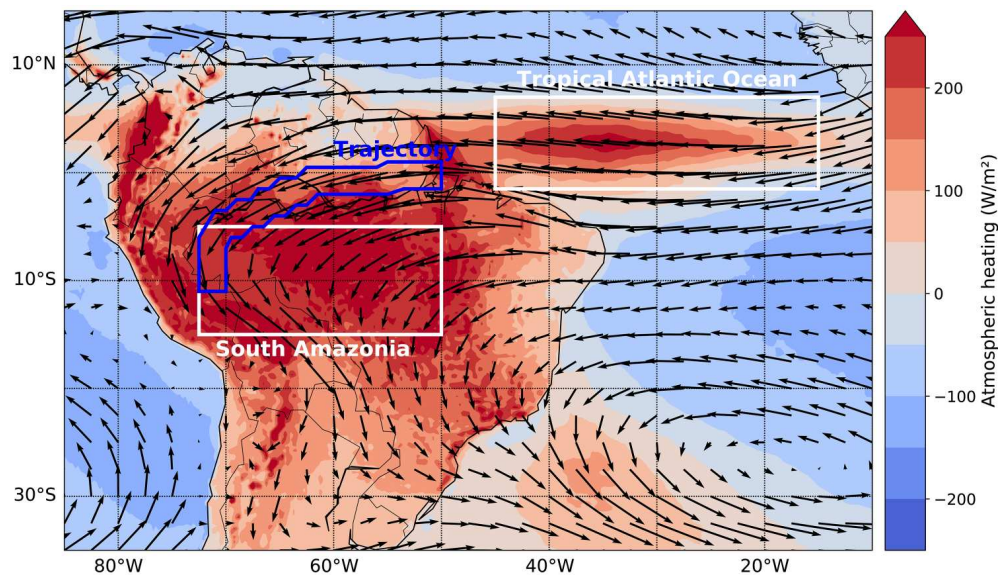


Fig. 1. Map of South America with wind fields and vertically integrated heating. Mean wind fields at the 750-hPa level and mean vertically integrated atmospheric heating, i.e., the sum of latent, sensitive, and radiative heating, for the wet season (December to January) from 1979 to 2019. The tropical Atlantic Ocean box and the southern Amazonian box used for our analysis are delineated in white, while the trajectory used for simulations is delineated in blue.

we do not consider them in our model. A detailed description of the extended model can be found in Materials and Methods.

RESULTS

To validate our model, we first compare the simulated spatiotemporal evolution of the model variables with corresponding time series from the ERA5 reanalysis (59). Across the 100 spatial boxes, we use for our model simulations, spanning the Amazon basin from east to west (Fig. 1), we find a very good agreement of the modeled observables with the corresponding reanalysis data in the wet season. We are also able to reproduce the seasonality, although there are expectable discrepancies between modeled variables and the reanalysis in the dry season (fig. S1).

To investigate the impacts of deforestation on the coupled vegetation-atmosphere system, we integrate our model with a gradually increasing number of deforested boxes. Note that deforestation here refers to either direct forest clearance or forest loss due to droughts or fires. Deforestation starts in the easternmost box and ends in the westernmost box. Deforestation is quantitatively implemented as a 40% decrease in the evapotranspiration and 40% increase in the sensible heat of the respective box, following results from field experiments and regional climate modeling experiments (60, 61). The precipitation recycling rate has been shown to gradually increase from the eastern to the western parts of Amazonia; it is largest in southwestern Amazonia, with more than 50% during the dry season and up to 40% during the wet season (61). We therefore use 40% as an annual mean along the trajectory.

We allow the system to adapt to the changing number of deforested boxes and reach its equilibrium for each number of deforested boxes, by integrating the model in hourly time steps over time spans of multiple decades. We find a steady but moderate decrease in the rainfall rates at the western boundaries of the Amazon as soon as deforestation in the eastern Amazon sets in. After exceeding a specific threshold in terms of deforested boxes, an abrupt rainfall

decline is apparent, which is associated with a bifurcation-induced critical transition in the underlying dynamics, resulting from the collapse of the latent-heat feedback. The system switches into a permanent dry season state and is not able to switch back into the annual wet season. This permanent dry season state is characterized by precipitation rates throughout the year similar to what is presently observed during the dry season. By including the vegetation's response to increasing water stress, the threshold is crossed considerably earlier, and the subsequent rainfall decline is more abrupt, compared to the original model without vegetation feedback (Fig. 2). This can be explained by the cascading effect introduced by the two-way coupling between the vegetation and the atmosphere (54, 56, 62). Although the critical forest loss threshold in our model (Fig. 2B) agrees with previous studies, we emphasize that our model is not intended to give quantitatively correct predictions of the critical deforestation level but rather to be used to infer what kind of precursor signals should be searched for in observation-based data to anticipate a critical transition of the couple Amazon atmosphere-vegetation system.

Before crossing the critical threshold, we observe prominent changes in several hydrological variables and statistical CSD indicators that may serve as precursor signals. Besides a decline in the precipitation P , we observe a nonlinear decline in the soil moisture S long before the critical transition (Fig. 3A). Furthermore, we find an increase in the DSL that is associated with a later onset of the wet season (Fig. 3B). The wet season initiation is hindered by reduced differential heating between the Atlantic Ocean and the South American continent due to the deforestation-induced decrease in the latent heating over Amazonia. The shortening of the wet season and the concomitant reduction of rainfall rates lead to increased plant water stress, which, in our simplified model, ultimately, triggers the dieback of the remaining rainforest further west. We refer to all the abovementioned pretransition changes in the hydrological cycle and atmospheric circulation as physical precursor signals because they are mechanistically associated with the

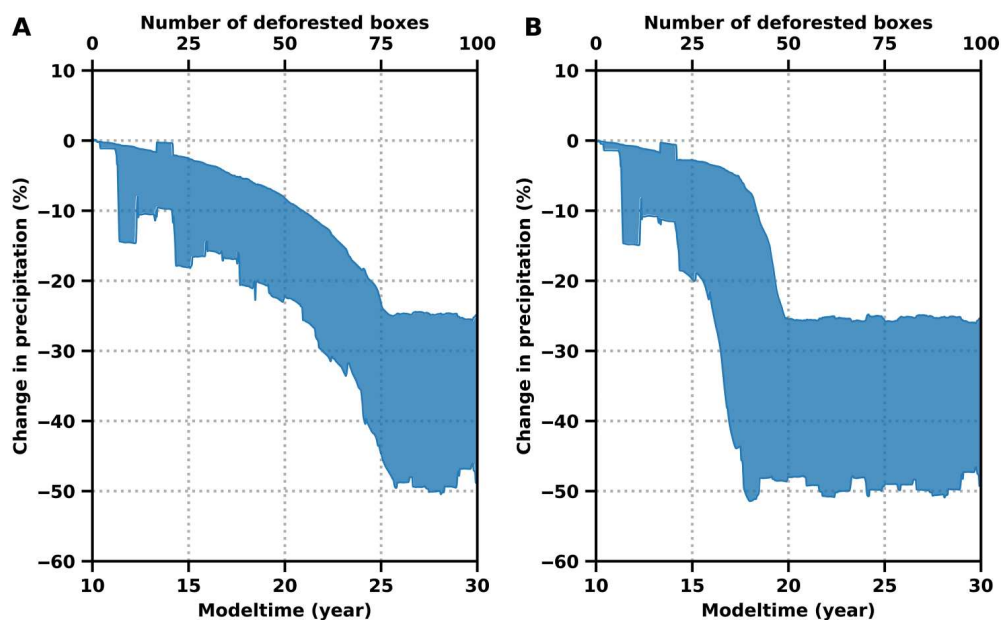


Fig. 2. Simulated precipitation rates without and with vegetation feedback after successive deforestation at the end of the trajectory. (A) Simulated annual mean precipitation rates, as functions of advancing deforestation at the end of the trajectory (box 90) for all possible choices of the different simulation parameters AF (amplification factor) and $\langle H \rangle^{AO}$ (see Materials and Methods) without vegetation feedback. The mean is calculated using a rolling window with size $w = 1$ year for every parameter configuration. Deforestation starts at year 10 in box 0 and subsequently proceeds westward, where it is completed at year 30 in box 100. The ranges of the different simulation parameters are $AF = 1.5$ to $AF = 3$, $\langle H \rangle^{AO}(t) = (80 \pm 40) \text{ W/m}^2$ to $\langle H \rangle^{AO}(t) = (140 \pm 40) \text{ W/m}^2$, with a step width of 0.25 for AF and 20 W/m^2 for $\langle H \rangle^{AO}(t)$. (B) Same as (A) but with vegetation feedback included, leading to early and more abrupt decline of P . Although the critical transition is in quantitative accordance with previous studies, we want to emphasize that our model is rather built to give guidance where to search for CSD to anticipate a forthcoming transition.

dynamics leading to the subsequent critical transition, as shown by our modeling results. We choose this term in contrast to the generic, statistical precursor signals associated with CSD preceding critical transitions. We further investigate these well-established indicators, given by the variance and the lag-one autocorrelation of the 5-day averaged modeled precipitation time series, with a deforestation rate of 0.5% per year within a rolling window of 150 years (Fig. 4). We calculate the Kendall rank correlation coefficient τ to measure the strength of the trends and generate surrogate data of the CSD indicators to test the significance of the inferred values of τ . The variance and lag-one autocorrelation show a clear positive trend ($\tau = 0.98$, $P < 10^{-4}$, and $\tau = 0.91$, $P < 10^{-4}$, respectively; see Fig. 4, C and D, and and fig. S2) and begin to increase long before the transition.

These results give guidance in where to search for precursor signals in the reanalysis and observational data. We analyze all abovementioned, physical and statistical, precursor signals in the evolution of hydrological variables from the ERA5 reanalysis data. We first analyze the soil moisture content and reveal a substantial decline not only in the Amazon basin but also further downstream of the low-level flow in the South American subtropics (Fig. 5A).

We proceed with analyzing the DSL from 1979 to 2019 in southern Amazonia (5°S to 15°S , 50°W to 70°W), using the daily averaged ERA5 reanalysis data using three different methods (see Materials and Methods). We find an extension of the dry season with all three methods, ranging from 1.25 to 2.7 pentads over the past 40 years (Fig. 5B). The main contribution to the lengthening of the dry season is a delayed onset of the wet season, while the wet season demise is relatively constant and only shows a slight tendency toward earlier days of the year (fig. S3). A spatial analysis reveals a

significant extension of the dry season primarily in southeastern Amazonia (fig. S4), where deforestation and drought- and fire-induced forest loss are most pronounced (63). The increasing DSL and delayed wet season onset in southern Amazonia revealed here corroborate the results of several earlier studies (25, 29, 44, 64–68). However, it should be noted the different studies do not necessarily agree on the exact spatial distribution of the observed changes.

As for our simulations, we also analyze the precipitation rates from 1979 to 2019 in the ERA5 data. We find an increase of both statistical indicators, variance and lag-one autocorrelation, in large parts of tropical South America (Fig. 6). The variance increases in most parts of Amazonia south of the Amazon River, while the lag-one autocorrelation shows the most pronounced increase in southwestern Amazonia and further to the south. We identify southwestern Amazonia as a region that shows a clear, simultaneous increase in both variance and lag-one autocorrelation, with $P < 0.1$ (figs. S5 and S6). Consequently, the variance and autocorrelation of the averaged precipitation time series in southwestern Amazonia show a clear increase (Fig. 6, C and D). The changes in lag-one autocorrelation and variance inferred here from the ERA5 reanalysis are consistent with corresponding results inferred from independent satellite- and gauge-based rainfall products (figs. S7, B to D, and S8, B to D). In particular, the trends in the autocorrelation show very similar spatial distributions across datasets. We note that increasing variance and particularly increasing lag-one autocorrelation can be observed along the aerial river that provides the main atmospheric moisture transport from the Amazon southward to the South American subtropics (69, 70), suggesting that the continental-scale circulation system is losing stability. According to our results, this loss of stability can be at least partly attributed to the

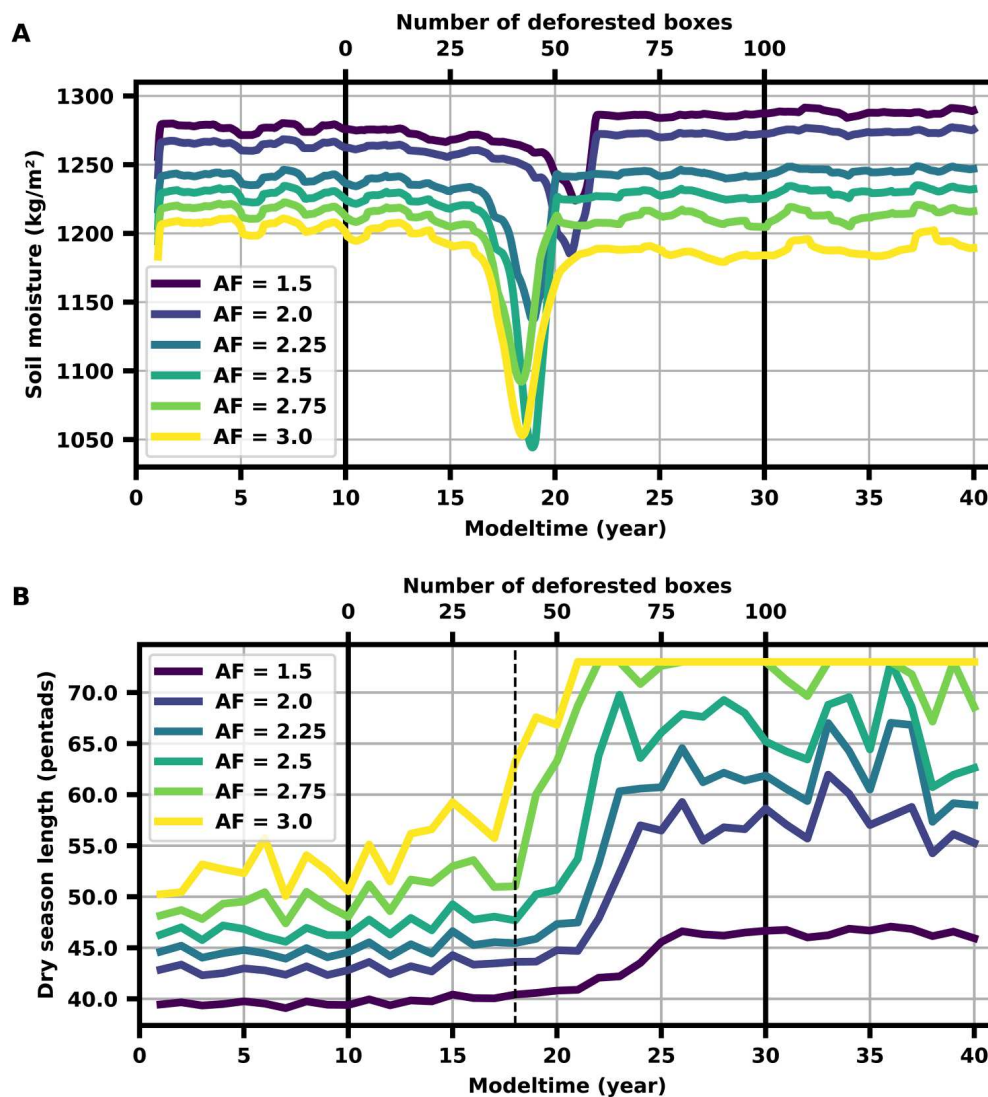


Fig. 3. Physical early-warning signals in simulated evolution of soil moisture and DSL in southern Amazonia. (A) Time-evolving yearly average of the simulated soil moisture (rolling window with width $w = 1$ year) for different AFs of the low-level moisture flow to South America, integrated SMD threshold = 450,000 kg h/m² and fixed ocean heating $\langle H \rangle^{AO}(t) = (120 \pm 20)$ (see Materials and Methods). Deforestation is initiated at year 10 (first solid black line) and completed at year 30 (second solid black line). Note that the soil moisture is the same long before and after the bifurcation-induced transition but declines strongly before the transition when the coupled system loses its prior equilibrium. The shortened wet season and the decreasing rainfall rates result in lower soil moisture levels, while the evapotranspiration rates stay at a high level and further deplete the soil during the dry season. This leads to an all-year-round decrease of the soil moisture and an increasing SMD before the dieback of the rainforest. It therefore serves as an efficient physical precursor for the transition. (B) Simulated DSL ($P < 180$ /month) with advancing deforestation for same simulation parameters as (A), at the end of the trajectory (box 90). Note the gradual increase of the DSL with an increasing fraction of deforested rainforest before the abrupt transition (dashed black line). For small AF, the switch into the wet season is still possible. However, the wet season length is strongly shortened and wet season precipitation is reduced. The DSL together with the wet season onset (see fig. S3) can, hence, serve as physical precursor signals.

impacts of changes in the Amazon vegetation system, including deforestation, drought-induced degradation, and forest fires.

DISCUSSION

The revealed changes in the ERA5 data show a substantial similarity to our model simulations for times before crossing the critical deforestation threshold. Alongside the statistical precursor signals, the observed decadal-scale decrease in soil moisture (Fig. 5A) together with the observed dry season prolongation (Fig. 5B), and especially the later wet season onset are consistent with the corresponding

transition precursor signals found in our simulations and thus suggest that the coupled atmosphere-vegetation system of the Amazon approaches the theoretically suggested tipping point. The increases in DSL and the later wet season onset in the ERA5 data are in good agreement with the results of previous studies (25, 29, 64–67).

While, in the ERA5 data, the extension of the dry season is mostly observable in the southeastern regions, where deforestation rates are strongest, a recent study (58) reports an intensification of the dry season mainly in central and southwestern Amazonia. However, it is concluded there that global climate change and

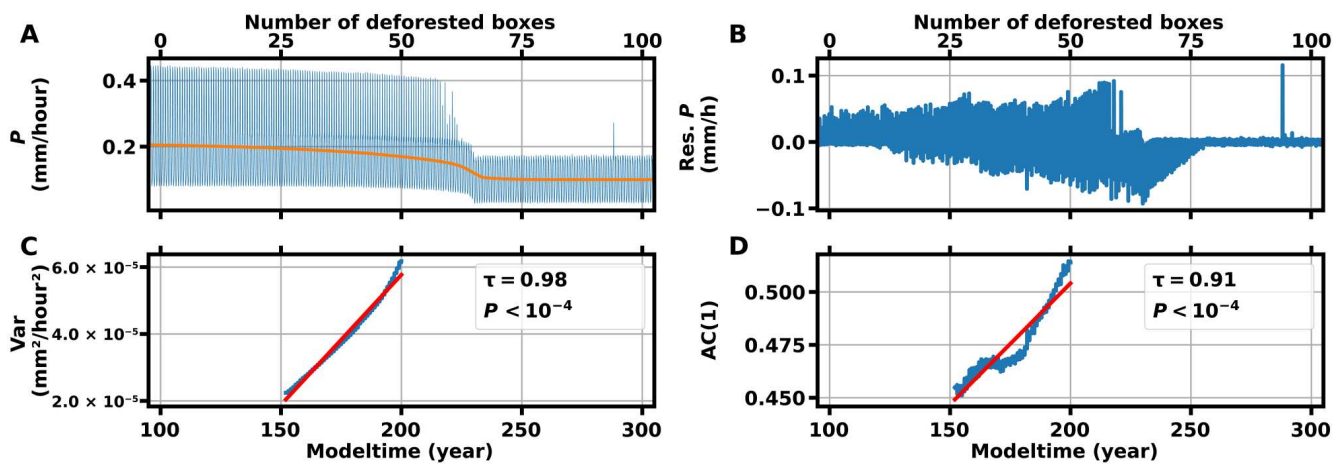


Fig. 4. Statistical precursor signals for simulated precipitation rates. (A) Five-day averaged simulated precipitation rates, as functions of advancing deforestation at the end of the trajectory (box 90). The nonlinear trend (orange) is obtained using a standard decomposition method (STL) (95) with a trend smoother length of 11 years and seasonal smoother length of 13 months. Deforestation starts at year 100 in box 0 and subsequently proceeds westward where it is completed at year 300 in box 100. Before crossing the tipping point, the wet season ($P \approx 0.4$) and dry season ($P \approx 0.15$) are apparent. The wet season rainfall rates show a steady decline with advancing deforestation. Flickering and increased variability in the wet season rainfall near the critical threshold can be observed. After exceeding the critical deforestation threshold, only the dry season state remains, with a small seasonal amplitude in the rainfall rates. The chosen simulation parameters are $AF = 3$, integrated SMD threshold = $20 \times 10^6 \text{ kg hour/m}^2$, and ocean heating $\langle H \rangle^{AO}(t) = (120 \pm 20) \text{ W/m}^2$. (B) Residual precipitation time series, obtained by subtracting the seasonal and nonlinear trend components from the original series. (C) Time-evolving endpoint variance computed in rolling window of width $w = 150$ years from year 0 (not shown) to year 200 of the detrended time series. Red line denotes the linear trend, and Kendall τ indicates the strength of the increase. (D) Same as (C) but for the lag-one autocorrelation [AC(1)].

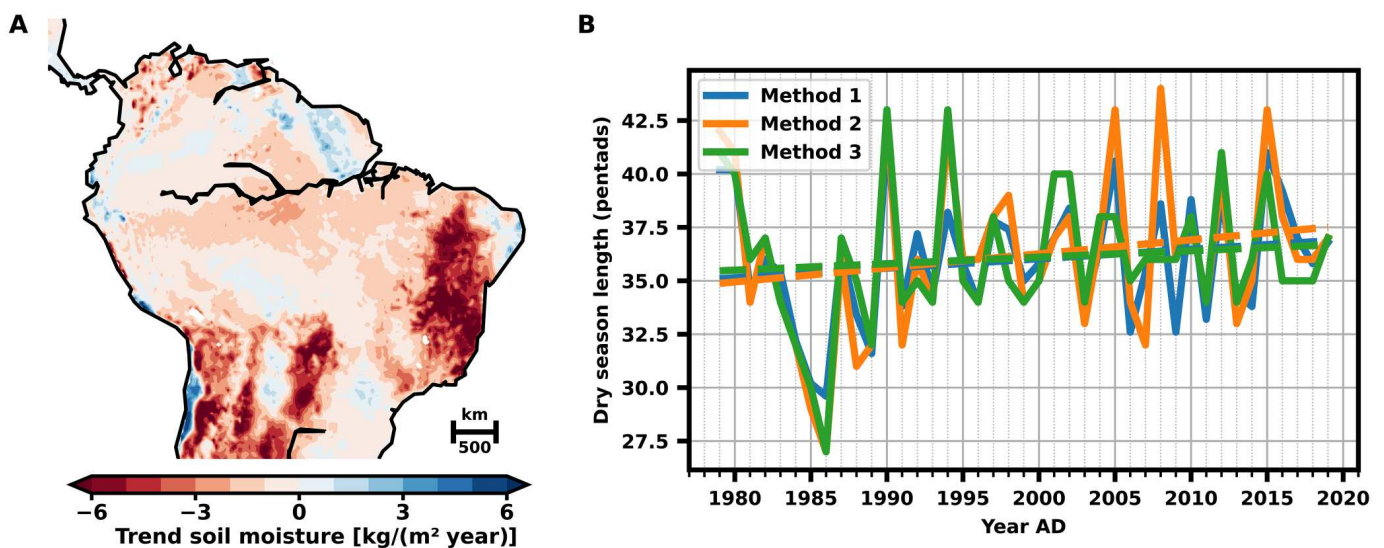


Fig. 5. Physical early-warning signals in ERA5 data: evolution of soil moisture and DSL in southern Amazonia. (A) Calculated linear trend in yearly averaged soil moisture from 1979 to 2019 in South America, determined from the ERA5 reanalysis for all available soil moisture layers. Most parts of tropical South America show a negative trend (red) in the soil moisture. (B) Observed DSL in southern Amazonia (5°S to 15°S , 50°W to 70°W) from 1979 to 2019, determined in three different ways (see Materials and Methods). Dashed lines denote the corresponding linear trends. We find a DSL increase of 4.4 (blue), 6.6 (orange), and 3.0 (green) pentad/century for the three different methods to determine the DSL, respectively. The data are taken from the ERA5 reanalysis (59). For a spatial analysis of the DSL, see fig. S4. AD, Anno Domini.

local deforestation effects are the main contributors, while, based on our model results, we additionally suspect circulation changes in response to deforestation in eastern Amazonia as cause for the observed increases of the DSL. In accordance with our results, trends in the atmospheric circulation in tropical South America over the past decades show a higher occurrence of wintertime circulation patterns and decrease of the frequency of circulation patterns characteristics for the transition season, as well as a weakening of the trade winds during and preceding droughts (27, 44). These

changes are characterized by increased southerly wind anomalies from the Amazon Basin toward Southeastern South America and intensified southerly cross-equatorial winds; both have been associated with a delayed onset of the monsoon (44). These changes in circulation patterns during the transition season have recently been associated with deforestation linked to the absence of deep convection over deforested regions before the wet season onset (42). Synoptic scale circulation changes, driven by continued extensive deforestation, could even lead to a delay in the onset of the wet

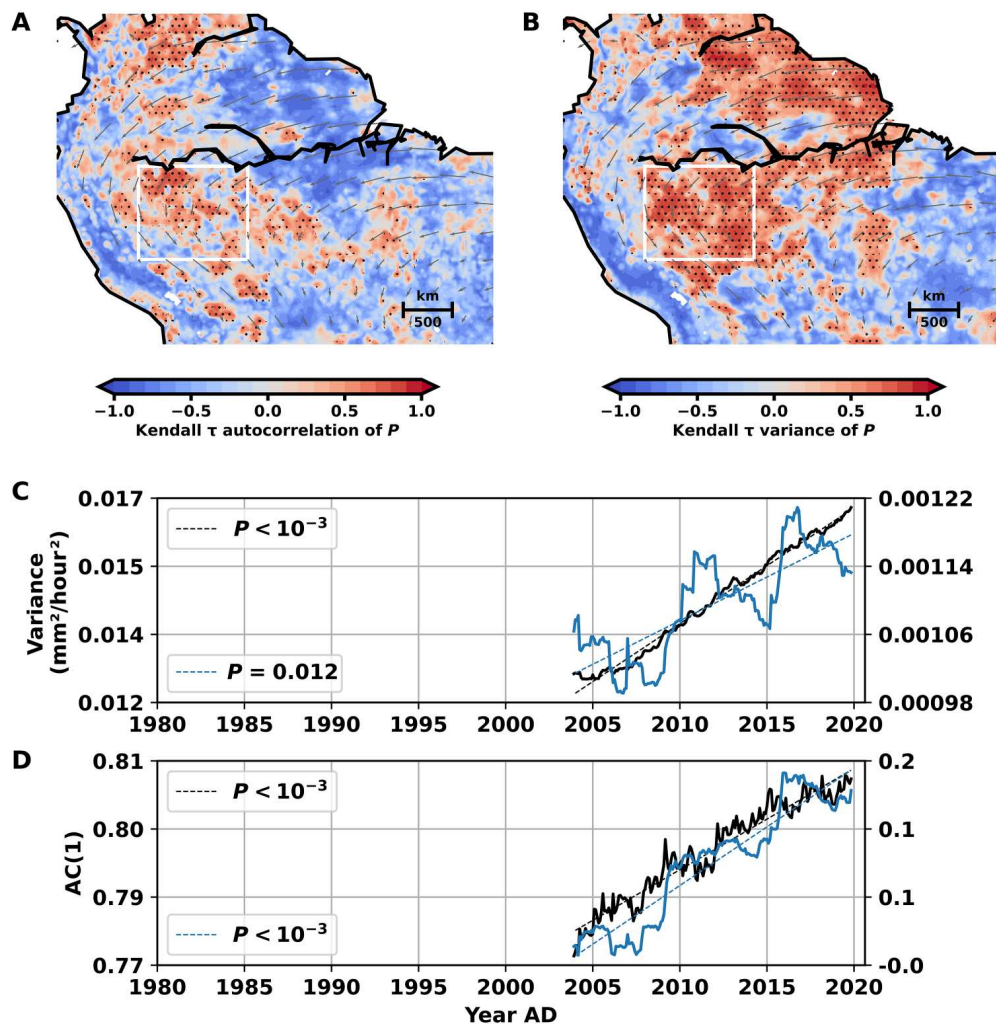


Fig. 6. Statistical early-warning signals in ERA5 data. Spatial patterns of Kendall τ for the (A) lag-one autocorrelation, and (B) variance of observed monthly averaged precipitation time series. CSD indicators are calculated for rolling windows of width $w = 20$ years. The trend is determined by Kendall τ of the respective indicator of the detrended and deseasoned precipitation time series at every site. Stippling marks regions with significantly increasing trends ($P < 0.05$; see Materials and Methods for details on the statistical test and fig. S6). Large parts of southwestern Amazonia show a simultaneous increase in variance and autocorrelation. Mean wet season wind fields (1979 to 2019) at 750 hPa are delineated in grey. The nonlinear trend of the underlying precipitation time series is removed via STL (95) with a trend smoother length of 5 years and seasonal smoother length of 13 months. The data are taken from the ERA5 reanalysis (59). In particular, the regions with high lag-one autocorrelation correspond well with the main atmospheric moisture transport routes in South America and particularly the aerial river across the Amazon to the subtropics. (C) Variance of the spatially averaged precipitation time series (black, left y axis) and variance of the spatially averaged, detrended, and deseasoned precipitation time series (blue, right y axis) for southwestern Amazonia from 1979 to 2019, calculated in a window $w = 25$ years [4°S to 12.5°S, 62.5°W to 72.5°W, white box in (A) and (B)]. Dashed lines denote linear regressions of the respective time series. For the detrending method, see Materials and Methods. (D) Same as (C) for autocorrelation at lag one [AC(1)]. See figs. S7 and S8 for corresponding results using alternative gauge- and satellite-based rainfall datasets.

season by more than a month (71). Wet season onset estimations based on outgoing longwave radiation support our findings of increasing DSL mainly in southeastern Amazonia and some parts of southwestern Amazonia (25, 44).

Previous modeling studies showed that extensive deforestation of the Amazon rainforest leads to changes in the energy balance of the whole Amazon basin and in the atmospheric circulation over tropical South America, which, in turn, leads to weakened moisture flux and precipitation in these regions (72). Deforestation leads to a local reduction of precipitation and evapotranspiration, as well as a decrease in average latent heat release that, in turn, weakens moisture convergence over western Amazonia (72). This leads, most

likely, to a prolongation of the dry season in these parts of South America.

In accordance with our model results, we propose the following chain of mechanisms in the coupled atmosphere-vegetation dynamics on the way to the deforestation-induced transition. The time needed to initiate the wet season prolongs as the atmospheric moisture and, hence, the average latent heat over the Amazon decreases with proceeding forest loss in the east. Large parts of Amazonia show a negative trend in atmospheric moisture content over the past decades (25). The heating gradient between the Atlantic Ocean and the continent weakens and impedes the annual transition into the wet season (44). Consistently, we observe increasing DSL and later wet season onset in the ERA5 data (Fig. 5B). The

shortened wet season and the decreasing rainfall rates result in lower soil moisture levels. Evapotranspiration rates, however, stay at a high level and further deplete the soil during the dry season. This leads to an all-year-round decrease of the soil moisture and an increasing SMD before the dieback of the rainforest. This increasing SMD can be clearly observed in the ERA5 data (Fig. 5A). After the dieback of the rainforest, the soil moisture approaches an alternative equilibrium consistent with the reduced precipitation and evapotranspiration of the savanna vegetation. At the critical point, the atmospheric moisture content does not suffice anymore to maintain precipitation and, thus, latent heating rates that could switch the system back into the annual wet season, resulting in a permanent dry season state. Consequently, this would result in a dieback of substantial parts of the rainforest.

We emphasize that the decreasing soil moisture that we observe in the ERA5 data is not simply a linear response to decreasing rainfall rates in Amazonia but rather a consequence of the changing hydrological budget of the coupled atmosphere-vegetation system. In general, the soil moisture shows a delayed response to reduced precipitable water and has been shown to be correlated to tropical Atlantic sea surface temperatures and reduced moisture inflow from the Atlantic and northern Amazonia (27). The precipitation rates in large parts of Amazonia do not consistently decrease with the negative trend in the soil moisture (fig. S9), and the links between soil moisture, precipitation, and other factors remain uncertain, especially in deforested areas (27).

It should also be noted that it is inherently hard to measure the soil moisture in the Amazon rainforest due to the high vegetation coverage that hinders satellite measurements. However, previous studies showed an agreement between satellite-based soil measurements and the ERA5 reanalysis in large parts of Brazil (27, 73). A recent soil moisture reconstruction study that combines satellite and tree ring measurements also supports the strong decline of the soil moisture in the Andes region in the past decades that is visible in the ERA5 data (74), increasing the general confidence in the ERA5 soil moisture product.

Similarly, quantifying rainfall in the Amazon region presents difficulties due to the scarcity of rain gauges (75). Rainfall products can differ substantially in South America on both spatial and temporal scales (76, 77). While the spatially averaged ERA5 precipitation rates in South America are in good agreement with the gauge-based rainfall product provided by the Global Precipitation Climatology Centre (GPCC) (78) after the year 1980, the ERA5 precipitation in tropical South America shows some deviation from GPCC (79, 80). To account for this uncertainty in the ERA5 precipitation, we repeat the statistical analysis for the three different satellite- and gauge-based rainfall products: Climate Hazards Group InfraRed Precipitation with Station data (CHIRPS) (81) and GPCC and Global Precipitation Climatology Project (GPCP) (82). While the four datasets not necessarily agree on the trend of rainfall over the past four decades (fig. S9), we find a strong agreement in the trends of the statistical CSD indicators (figs. S7 and S8).

The impacts of a weakened atmospheric circulation are expected to be greatest in the southwestern parts of the rainforest, due to the cascading effect of reduced moisture recycling over the basin. This implies that increasing deforestation rates in eastern Amazonia could lead to an extensive reduction of rainfall in remote parts of the rainforest (72). Large parts of the rainforest in southwestern Amazonia are still intact, which suggests that our findings of

changes in the large-scale precipitation patterns cannot be ascribed to local deforestation effects.

While the characteristic changes in our model simulations can by design be exclusively attributed to forest loss, this is not possible in observational or reanalysis data. Besides forest loss, several competing processes influence the climate in South America, such as El Niño events, sea surface temperature anomalies in the tropical Atlantic, and the consequences of global warming. For example, a poleward shift of the subtropical jets and equatorial contraction of the ITCZ is expected in a warmer climate, possibly leading to a delayed wet season onset and savanna expansion in the southern Amazon (83, 84). It has been shown that deforestation can enhance surface wind acceleration and increase the moisture inflow from the Atlantic and increase precipitation in intact regions of the rainforest due to decreased roughness length (85). While we do not account for this effect in our model, it could substantially increase the precipitation throughout the intact regions of the rainforest with further deforestation. Including this effect would potentially reduce the amplitude and abruptness of the transition shown in Fig. 2. Furthermore, an intensification of the Hadley and Walker cells, associated with anomalous sea surface temperatures in the tropical Pacific and north tropical Atlantic, as well as reduced moisture transport from the tropical Atlantic Ocean, has partially been linked to an increase of the frequency of dry days during the transition season in southern Amazonia over the past decades (24–26, 86).

Our model simulations imply that all four indicators will occur consistently before the critical transition, and, correspondingly, we reveal that all four of them occur consistently in the ERA5 data and in other observation datasets. It is unlikely that low-frequency natural variability such as the Atlantic multidecadal oscillation (AMO) and El Niño–Southern Oscillation (ENSO), possibly in conjunction with anthropogenic climate change, would lead to a similarly consistent occurrence of all four—in principle, independent—indicators. Moreover, we test the trends in the CSD indicators based on a phase surrogate test that preserves the variance and the autocorrelation structure of the original time series (fig. S6). In this sense, the detected trends are statistically significantly positive given the “natural variability” (in terms of variance and autocorrelation) and can thus not be explained by natural variability.

We showed that forest loss, caused by direct deforestation, droughts, and fires, might vastly contribute to a changing climate in Amazonia and could drive the coupled rainforest-monsoon circulation system past a tipping point. Recent changes in precipitation patterns, increasing DSL, reduced soil moisture, and more frequent extreme events might be much stronger linked to deforestation than previously assumed. The results presented here suggest an upcoming regime shift of the Amazon ecosystem if deforestation is not brought to a halt. We outline a detailed analysis of the observed changes in the hydrological variables that we identify with physical and statistical precursor signals, using high-resolution coupled vegetation-atmosphere models, as an urgent subject of future research.

MATERIALS AND METHODS

Model design

The main focus of the model is the relationship between a deforestation-induced decrease in the total surface heat flux and a positive feedback mechanism associated with the release of latent heat. To

investigate the consequences of deforestation, a nonlinear moisture transport model along a one-dimensional trajectory from the mouth of the Amazon River to the western boundary of the Amazon basin, following the low-level winds in the monsoon season, is constructed (see Fig. 1). The underlying equations are given by the moisture balance equations

$$\partial_t A = E - P - \nabla \cdot \mathbf{M} \quad (1)$$

$$\partial_t S = P - E - R \quad (2)$$

where A denotes the atmospheric moisture content, E is evapotranspiration, P is precipitation, S is the total soil moisture content, and R is the runoff. The term $\nabla \cdot \mathbf{M}$ denotes the divergence of vertically integrated moisture flow and is defined at each atmospheric layer λ as $\nabla \cdot \mathbf{M}^\lambda := A^\lambda \mathbf{W}^\lambda$, where \mathbf{W}^λ is the respective wind speed. The runoff R and the precipitation P are modeled as effective functions of S and A , respectively, with functional dependencies estimated from the ERA5 reanalysis. The evapotranspiration is obtained by sampling from a three-dimensional estimated probability density, dependent on the soil moisture S and the surface net solar radiation. The winds $\mathbf{W} = \mathbf{W}^T + \mathbf{W}^H$ are modeled in terms of a trade wind component \mathbf{W}^T and a convective latent-heating component \mathbf{W}^H . \mathbf{W}^H represents the amplification of wind speeds due to condensational heating in the wet season. Because this heating is dependent on precipitation and, hence, atmospheric moisture itself, the heating component introduces the nonlinearity to the model. The wind is modeled as

$$\mathbf{W}_i(t) = \mathbf{W}_i^T(t) + \mathbf{W}_i^H(t) \quad (3)$$

$$\mathbf{W}_i^T(t) = (w_0 - w_c) \left(1 + \frac{1}{1 + e^{w_1(t) \cdot i - w_2}} \right) + W_{i>70}^{\text{dry}}(t) \quad (4)$$

$$\mathbf{W}_i^H(t) = w_c L \pi(t) \left(1 + \frac{1}{1 + e^{w_1(t) \cdot i - w_2}} \right) \quad (5)$$

Here, $\pi(t)$ denotes the heating gradient between the Atlantic Ocean and the trajectory

$$\pi(t) = \langle H \rangle^{\text{trajectory}}(t) - \langle H \rangle^{\text{AO}}(t) \quad (6)$$

with $H = H^{\text{sensible}} + H^{\text{latent}} + H^{\text{rad}}$ and $\langle \cdot \rangle^R$ denoting the spatial average over the region R . The coefficients w_0 , $w_1(t)$, and w_2 are adjusted such that the modeled winds in the wet season match the observed wind speeds. Here, the parameters are chosen to be

$$w_0 = 16.5 \text{ km/hour} \quad (7)$$

$$w_1 = 0.6 - \left[0.03 \cdot \cos\left(\frac{2\pi}{8760} t - \pi\right) - 0.03 \right] \quad (8)$$

$$w_2 = 3.4 \quad (9)$$

The parameter w_c and w_0 determine the strengthening of the wind speeds and moisture inflow due to the latent heat release over the Amazon during the wet season. The amplification factor

(AF) of the winds is then given by

$$\text{AF} = \frac{w_0}{w_0 - w_c} \quad (10)$$

Varying w_c thus corresponds to controlling the strength of the heating-related feedback. The dimensionality factor L is defined as

$$L = \max \left\{ \frac{1}{\pi(t)} \right\} \quad (11)$$

and calculated for the undisturbed case, with no deforestation. In other words, L ensures that the amplification due to the heating winds is limited by AF. Only wind speeds at the 750-hPa level are considered because they are very similar to the mean wind speeds on the 700- to 900-hPa levels.

We integrate the discretized equations

$$A_i(t+1) = A_i(t) + E_i(t) - P_i(t) - \frac{W_i(t)A_i(t) - W_{i-1}(t)A_{i-1}(t)}{l} \quad (12)$$

$$S_i(t+1) = S_i(t) + P_i(t) - E_i(t) - R_i(t) \quad (13)$$

along the 100 boxes of the trajectory, in hourly steps. The subscript i denotes the respective spatial box, and $l = 30 \text{ km}$ is the length of a single box. The moisture divergence $\nabla \cdot \mathbf{M}$ is realized as forward difference quotient. Initial conditions are derived from the ERA5 reanalysis (59). We validate the model results against the ERA5 data (see fig. S1). For the investigation of precursor signals, we add white noise ($\sigma = 0.1$) to each $A_i(t)$ in Eq. 12.

Deforestation is simulated as a 40% reduction of the evapotranspiration E and a 40% increase in the sensible heat. However, the latent heat flux is two to four times higher than the sensible heat flux. This means that the reduction of E is the determining change. In addition to this ad hoc deforestation, a feedback mechanism between higher plant water stress and the vegetation is implemented. Less precipitation and longer dry seasons due to the weakening of the latent heat feedback lead to less soil moisture, which will eventually lead to increased tree mortality. Here, a simple threshold model is proposed. An integrated SMD is dynamically calculated, and, when the SMD exceeds a set threshold, this leads to deforestation of the box. For every box, the lowest soil moisture value before deforestation is set as a baseline. The integrated SMD is the sum of the soil values below the baseline. If the deficit exceeds the threshold, then the same consequences as in the case of manual deforestation occur.

Dry season length

There exist several methods to determine the onset and demise of the wet season in tropical regions. Here, we use three different methods to determine the DSL in the ERA5 data.

First, we calculate the climatological mean rainfall rate \bar{P} and the running 30-day mean precipitation rate \bar{P}_{30d} for all years. We identify all days where \bar{P}_{30d} is below the climatological mean and determine the longest sequence of consecutive dry days, ignoring wet spells (days with $\bar{P}_{30d} > \bar{P}$) shorter than 10 days. The longest sequence of dry days is the DSL of the respective year. The wet season retreat is the first day of the consecutive dry days and the onset date is the last day.

The second method is based on Liebmann *et al.* (87, 88). We calculate the 5-day mean precipitation for all years and determine the annual cumulative pentad rainfall anomaly $A(d)$ for every pentad d

$$A(d) = \sum_{j=0}^d (P_j - \bar{P})$$

with P_j as rainfall on pentad j and \bar{P} as climatological mean rainfall rate. The anomaly $A(d)$ increases when the pentad rainfall is above the climatological mean and decreases otherwise. The onset date of the wet season is then the maximum of $A(d)$, and the minimum of $A(d)$ denotes the end of the wet season. The difference between demise and onset yields the DSL.

The third method is a modification of Marengo *et al.* (29, 89). We calculate the 5-day mean precipitation for every year, \bar{P}_{5d} . The wet season demise is determined by the first date when \bar{P}_{5d} changes from above to below the climatological annual mean rain rate during six of the eight pentads. Vice versa, the wet season onset is the first pentad when \bar{P}_{5d} changes from below to above the climatological annual mean rain rate. If this criterion fails for a specific year, then the condition is relaxed to five of the eight pentads and, ultimately, to four of the eight pentads.

CSD and associated precursor signals

Several large-scale components of the Earth system are suspected to show abrupt shifts between different states when important control parameters, such as temperature or CO₂, approach critical thresholds, so-called tipping points (1). Key examples of such potential tipping elements are given by the Atlantic Meridional Overturning Circulation, the polar ice sheets, and the Amazon rainforest. While it is, in principle, hard to predict these abrupt shifts, various precursor signals that precede bifurcation-induced transitions in low-order random dynamical systems have been proposed (36, 90, 91). When the system approaches the critical threshold, the state of the system resembles more and more its past states, which is known as CSD. The restoring forces of the system diminish, and the rate of return to equilibrium after a perturbation approaches zero. This loss of resilience can be seen as a rise in the lag-one autocorrelation and variance of the fluctuations before crossing the tipping point (36, 92). Under the assumption that leading dynamical models of Earth system tipping elements can, to a first approximation, be represented by low-order random dynamical systems, the above motivates to search for precursor signals in the dynamics of tipping elements. Precursor signals related to CSD have been identified, for example, before collapses of the Atlantic Meridional Overturning Circulation in comprehensive model simulations (93, 94).

We calculate the variance and lag-one autocorrelation of the detrended time series within endpoint rolling windows half the size of the reanalysis time series ($w = 20$ years). For our model time series, we calculate the CSD indicators in a rolling window of size $w = 150$ years from year 0 to year 200 (Fig. 4).

We detrend the time series via seasonal trend decomposition (STL) based on locally estimated scatterplot smoothing (LOESS) (95) with the statsmodels Python package (96). The particular detrending parameters are given in the figure captions. The lag-one autocorrelation is computed directly as Pearson correlation coefficient between the time series and itself shifted by one time step. It should be noted that both variance and lag-one autocorrelation

have to increase (significantly) to conclude the proximity to a critical transition (90, 97).

Significance testing

To test the significance of our results, we test against the hypothesis that the trends in the CSD indicator time series are due to chance. By randomly shifting the phases in Fourier space, we generate $n = 10,000$ surrogates of the time series of the same length, which have no trend and preserve the variance and spectrum, and, hence, the autocorrelation function of the original time series (98–100). We calculate Kendall's τ for each generated surrogate time series and compare it with the Kendall τ of the original data. The fraction of cases where τ of the surrogates was equal or greater than the original τ gives the P value of our significance test, for a given τ value.

Sensitivity analysis

The following simulation parameters are varied to investigate the sensitivity of our results to these choices: the AF, the heating over the tropical Atlantic Ocean $\langle H \rangle^{\text{AO}}(t)$, the reduction of the evapotranspiration after deforestation ΔE , and the integrated SMD threshold. We find that our results are robust against reasonable variations in these parameters.

The consequences of deforestation depend on the values chosen for AF and $\langle H \rangle^{\text{AO}}(t)$. The AF determines the strength of the heating-related feedback; the higher the AF, the more severe the consequences. Nevertheless, for all AF within the bounds set by previous studies (46–48), we find an abrupt dieback of the rainforest (fig. S10).

A higher average heating over the Atlantic Ocean leads to a lower heating gradient between ocean and continent and, therefore, to an earlier breakdown of the heating-related feedback. We vary the spatial box used for averaging the atmospheric heating over the Atlantic by 1° to 2° in every direction and find $\langle H \rangle^{\text{AO}} = 80 \text{ W/m}^2$ to $\langle H \rangle^{\text{AO}} = 140 \text{ W/m}^2$ during the wet season (December to February) and $\langle H \rangle^{\text{AO}} = 30 \text{ W/m}^2$ to $\langle H \rangle^{\text{AO}} = 80 \text{ W/m}^2$ during the dry season (June to August), with an annual amplitude of 20 W/m² to 50 W/m². We use $\langle H \rangle^{\text{AO}} = 80 \text{ W/m}^2$, $\langle H \rangle^{\text{AO}} = 100 \text{ W/m}^2$, $\langle H \rangle^{\text{AO}} = 120 \text{ W/m}^2$, and $\langle H \rangle^{\text{AO}} = 140 \text{ W/m}^2$ for our simulations, each with an annual amplitude of 20 and 40 W/m². We show the precipitation rates for different AF and H^{AO} after successive deforestation in fig. S10. Although the position of the critical deforestation threshold and the abruptness of the transition depend on these choices, the results remain qualitatively unaltered.

The integrated SMD threshold is an artificial parameter that is chosen such that prolonged drought conditions over multiple years lead to degradation of the rainforest, which we quantitatively implement in the same way as deforestation. The specific choice for the SMD determines the timing of the rainforest dieback, but it has no influence on the severity of the rainfall decline (see fig. S11A). To investigate the statistical precursor signals and trends in the CSD indicators, we choose the SMD such that the dieback of the rainforest happens after 50% deforestation rate.

The reduction of the evapotranspiration ΔE is an essential parameter that determines the strength at which deforestation and vegetation degradation due to a persistent SMD affect the coupled hydrological cycle. The specific choice of the reduction, hence, influences the timing of the dieback. The higher ΔE , the lower the precipitation rates after deforestation and the earlier the dieback. Results from a field study suggest reductions of around 40% for

deforestation/degradation from closed rainforest to savanna, crop, or pasture (60). We show the influence of ΔE on the wet season precipitation for $\Delta E = 30$ to 50% for exemplary AF and $\langle H \rangle^{AO}(t)$ in fig. S11B. Qualitatively, the results are similar, however, with a rainforest dieback eventually occurring for all ΔE .

Supplementary Materials

This PDF file includes:

Figs. S1 to S11

REFERENCES AND NOTES

1. T. M. Lenton, H. Held, E. Kriegler, J. W. Hall, W. Lucht, S. Rahmstorf, H. J. Schellnhuber, Tipping elements in the Earth's climate system. *Proc. Natl. Acad. Sci. U.S.A.* **105**, 1786–1793 (2008).
2. C. A. Nobre, L. D. S. Borma, 'Tipping points' for the Amazon forest. *Curr. Opin. Environ. Sustain.* **1**, 28–36 (2009).
3. M. Hirota, M. Holmgren, E. H. Van Nes, M. Scheffer, Global resilience of tropical forest and savanna to critical transitions. *Science* **334**, 232–235 (2011).
4. R. Kopp, K. Hayhoe, D. R. Easterling, T. Hall, R. Horton, K. E. Kunkel, A. N. LeGrande, in *Climate Science Special Report: Fourth National Climate Assessment*, vol. 1 (U.S. Global Change Research Program, 2017), chap. 15, pp. 411–429.
5. N. Boers, N. Marwan, H. M. Barbosa, J. Kurths, A deforestation-induced tipping point for the South American monsoon system. *Sci. Rep.* **7**, 41489 (2017).
6. T. E. Lovejoy, C. Nobre, Amazon tipping point: Last chance for action. *Sci. Adv.* **5**, eaba2949 (2019).
7. D. I. A. McKay, A. Staal, J. F. Abrams, R. Winkelmann, B. Sakschewski, S. Loriani, I. Fetzer, S. E. Cornell, J. Rockström, T. M. Lenton, Exceeding 1.5°C global warming could trigger multiple climate tipping points. *Science* **377**, eabn7950 (2022).
8. I. M. Parry, P. D. Ritchie, P. M. Cox, Evidence of localised Amazon rainforest dieback in CMIP6 models. *Earth Syst. Dynam.* **13**, 1667–1675 (2022).
9. D. C. da Cruz, J. M. R. Benayas, G. C. Ferreira, S. R. Santos, G. Schwartz, An overview of forest loss and restoration in the Brazilian Amazon. *New For.* **52**, 1–6 (2021).
10. P. Verweij, S. Hess, *Keeping the Amazon Forests Standing: A Matter of Values* (World Wildlife Fund Zeist, 2009).
11. D. Werth, The local and global effects of Amazon deforestation. *J. Geophys. Res.* **107**, 8087 (2002).
12. R. Avissar, D. Werth, Global hydroclimatological teleconnections resulting from tropical deforestation. *J. Hydrometeorol.* **6**, 134–145 (2005).
13. Y. Pan, R. A. Birdsey, J. Fang, R. Houghton, P. E. Kauppi, W. A. Kurz, O. L. Phillips, A. Shvidenko, S. L. Lewis, J. G. Canadell, P. Ciais, R. B. Jackson, S. W. Pacala, A. D. McGuire, S. Piao, A. Rautiainen, S. Sitch, D. Hayes, A large and persistent carbon sink in the world's forests. *Science* **333**, 988–993 (2011).
14. E. A. Davidson, A. C. de Araújo, P. Artaxo, J. K. Balch, I. F. Brown, M. M. C. Bustamante, M. T. Coe, R. S. DeFries, M. Keller, M. Longo, J. W. Munger, W. Schroeder, B. S. Soares-Filho, C. M. Souza, S. C. Wofsy, The Amazon basin in transition. *Nature* **481**, 321–328 (2012).
15. E. Rödig, M. Cuntz, A. Rammig, R. Fischer, F. Taubert, A. Huth, The importance of forest structure for carbon fluxes of the Amazon rainforest. *Environ. Res. Lett.* **13**, 054013 (2018).
16. C. A. Nobre, P. J. Sellers, J. Shukla, Amazonian deforestation and regional climate change. *J. Climate* **4**, 957–988 (1991).
17. J. A. Marengo, C. A. Nobre, G. Sampaio, L. F. Salazar, L. S. Borma, in *Tropical Rainforest Responses to Climatic Change* (Springer Berlin Heidelberg, 2011), pp. 259–283.
18. D. Lawrence, K. Vandecar, Erratum: Effects of tropical deforestation on climate and agriculture. *Nat. Clim. Chang.* **5**, 174 (2015).
19. D. V. Spracklen, L. Garcia-Carreras, The impact of Amazonian deforestation on Amazon basin rainfall. *Geophys. Res. Lett.* **42**, 9546–9552 (2015).
20. C. A. Nobre, G. Sampaio, L. S. Borma, J. C. Castilla-Rubio, J. S. Silva, M. Cardoso, Land-use and climate change risks in the Amazon and the need of a novel sustainable development paradigm. *Proc. Natl. Acad. Sci. U.S.A.* **113**, 10759–10768 (2016).
21. T. E. Lovejoy, C. Nobre, Amazon tipping point. *Sci. Adv.* **4**, eaat2340 (2018).
22. C. Smith, J. C. Baker, D. V. Spracklen, Tropical deforestation causes large reductions in observed precipitation. *Nature*, 270–275 (2023).
23. G. Sampaio, C. Nobre, M. H. Costa, P. Satyamurty, B. S. Soares-Filho, M. Cardoso, Regional climate change over eastern Amazonia caused by pasture and soybean cropland expansion. *Geophys. Res. Lett.* **34**, 1–7 (2007).
24. J. C. Espinoza, J. Ronchail, J. A. Marengo, H. Segura, Contrasting North-South changes in Amazon wet-day and dry-day frequency and related atmospheric features (1981–2017). *Clim. Dynam.* **52**, 5413–5430 (2019).
25. J. A. Marengo, J. C. Jimenez, J. C. Espinoza, A. P. Cunha, L. E. Aragão, Increased climate pressure on the agricultural frontier in the Eastern Amazonia-Cerrado transition zone. *Sci. Rep.* **12**, 457 (2022).
26. V. B. Rao, S. H. Franchito, M. B. Rosa, D. Govardhan, S. N. Figueroa, V. S. L. Bhargavi, In a changing climate Hadley cell induces a record flood in amazon and another recorded drought across South Brazil in 2021. *Nat. Hazards* **114**, 1549–1561 (2022).
27. P. A. Arias, J. A. Martínez, J. D. Mejía, M. J. Pazos, J. C. Espinoza, S. Wongchuig-Correa, Changes in normalized difference vegetation index in the Orinoco and Amazon River Basins: Links to tropical atlantic surface temperatures. *J. Climate* **33**, 8537–8559 (2020).
28. C. T. Almeida, J. F. Oliveira-Júnior, R. C. Delgado, P. Cubo, M. C. Ramos, Spatiotemporal rainfall and temperature trends throughout the Brazilian Legal Amazon, 1973–2013. *Int. J. Climatol.* **37**, 2013–2026 (2017).
29. R. Fu, L. Yin, W. Li, P. A. Arias, R. E. Dickinson, L. Huang, S. Chakraborty, K. Fernandes, B. Liebmann, R. Fisher, R. B. Myneni, Increased dry-season length over southern Amazonia in recent decades and its implication for future climate projection. *Proc. Natl. Acad. Sci. U.S.A.* **110**, 18110–18115 (2013).
30. J. A. Marengo, J. Tomasella, L. M. Alves, W. R. Soares, D. A. Rodriguez, The drought of 2010 in the context of historical droughts in the Amazon region. *Geophys. Res. Lett.* **38**, 1–5 (2011).
31. J. A. Marengo, C. M. Souza Jr., K. Thonicke, C. Burton, K. Halladay, R. A. Betts, L. M. Alves, W. R. Soares, Changes in climate and land use over the Amazon Region: Current and future variability and trends. *Front. Earth Sci.* **6**, 228 (2018).
32. J. Verbesselt, N. Umlauf, M. Hirota, M. Holmgren, E. H. van Nes, M. Herold, A. Zeileis, M. Scheffer, Remotely sensed resilience of tropical forests. *Nat. Clim. Chang.* **6**, 1028–1031 (2016).
33. T. Smith, N. Boers, Global vegetation resilience linked to water availability and variability. *Nat. Commun.* **14**, 498 (2023).
34. C. A. Boulton, T. M. Lenton, N. Boers, Pronounced loss of Amazon rainforest resilience since the early 2000s. *Nat. Clim. Chang.* **12**, 271–278 (2022).
35. V. Dakos, M. Scheffer, E. H. van Nes, V. Brovkin, V. Petoukhov, H. Held, Slowing down as an early warning signal for abrupt climate change. *Proc. Natl. Acad. Sci. U.S.A.* **105**, 14308–14312 (2008).
36. M. Scheffer, J. Bascompte, W. A. Brock, V. Brovkin, S. R. Carpenter, V. Dakos, H. Held, E. H. van Nes, M. Rietkerk, G. Sugihara, Early-warning signals for critical transitions. *Nature* **461**, 53–59 (2009).
37. S. R. Carpenter, W. A. Brock, Rising variance: A leading indicator of ecological transition. *Ecol. Lett.* **9**, 311–318 (2006).
38. N. Boers, M. Ghil, T. F. Stocker, Theoretical and paleoclimatic evidence for abrupt transitions in the Earth system. *Environ. Res. Lett.* **17**, 093006 (2022).
39. T. Smith, D. Traxl, N. Boers, Empirical evidence for recent global shifts in vegetation resilience. *Nat. Clim. Chang.* **12**, 477–484 (2022).
40. W. Li, R. Fu, Transition of the large-scale atmospheric and land surface conditions from the dry to the wet season over Amazonia as diagnosed by the ECMWF re-analysis. *J. Climate* **17**, 2637–2651 (2004).
41. W. Li, R. Fu, Influence of cold air intrusions on the wet season onset over Amazonia. *J. Climate* **19**, 257–275 (2006).
42. J. P. Sierra, J. C. Espinoza, C. Junquas, S. Wongchuig, J. Polcher, V. Moron, L. Fita, P. A. Arias, A. Schrapfner, R. Pennel, Impacts of land-surface heterogeneities and amazonian deforestation on the wet season onset in southern amazon. *Climate Dynam.* 10.1007/s00382-023-06835-2, (2023).
43. J. Zhou, K.-M. Lau, Does a Monsoon climate exist over South America? *J. Climate* **11**, 1020–1040 (1998).
44. J. C. Espinoza, P. A. Arias, V. Moron, C. Junquas, H. Segura, J. P. Sierra-Pérez, S. Wongchuig, T. Condom, Recent changes in the atmospheric circulation patterns during the dry-to-wet transition season in South Tropical South America (1979–2020): Impacts on precipitation and fire season. *J. Climate* **34**, 9025–9042 (2021).
45. J. S. Wright, R. Fu, J. R. Worden, S. Chakraborty, N. E. Clinton, C. Risi, Y. Sun, L. Yin, Rainforest-initiated wet season onset over the southern Amazon. *Proc. Natl. Acad. Sci. U.S.A.* **114**, 8481–8486 (2017).
46. B. J. Hoskins, M. J. Rodwell, A model of the Asian summer monsoon. Part I: The global scale. *J. Atmos. Sci.* **52**, 1329–1340 (1995).
47. F. Jin, B. J. Hoskins, The direct response to tropical heating in a baroclinic atmosphere. *J. Atmos. Sci.* **52**, 307–319 (1995).
48. M. J. Rodwell, B. J. Hoskins, Subtropical anticyclones and summer monsoons. *J. Climate* **14**, 3192–3211 (2001).

49. S. Wongchuig, J. C. Espinoza, T. Condom, H. Segura, J. Ronchail, P. A. Arias, C. Junquas, A. Rabatel, T. Lebel, A regional view of the linkages between hydro-climatic changes and deforestation in the Southern Amazon. *Int. J. Climatol.* **42**, 3757–3775 (2022).
50. Y. Malhi, L. E. O. C. Aragão, D. Galbraith, C. Huntingford, R. Fisher, P. Zelazowski, S. Sitch, C. McSweeney, P. Meir, Exploring the likelihood and mechanism of a climate-change-induced dieback of the Amazon rainforest. *Proc. Natl. Acad. Sci. U.S.A.* **106**, 20610–20615 (2009).
51. O. L. Phillips, G. van der Heijden, S. L. Lewis, G. López-González, L. E. O. C. Aragão, J. Lloyd, Y. Malhi, A. Monteagudo, S. Almeida, E. A. Dávila, I. Amaral, S. Andelman, A. Andrade, L. Arroyo, G. Aymard, T. R. Baker, L. Blanc, D. Bonal, Á. C. A. de Oliveira, K. J. Chao, N. D. Cardozo, L. da Costa, T. R. Feldpausch, J. B. Fisher, N. M. Fyllas, M. A. Freitas, D. Galbraith, E. Gloor, N. Higuchi, E. Honorio, E. Jiménez, H. Keeling, T. J. Killeen, J. C. Lovett, P. Meir, C. Mendoza, A. Morel, P. N. Vargas, S. Patiño, K. S. H. Peh, A. P. Cruz, A. Prieto, C. A. Quesada, F. Ramírez, H. Ramírez, A. Rudas, R. Salamão, M. Schwarz, J. Silva, M. Silveira, J. W. Ferry Slik, B. Sonké, A. S. Thomas, J. Stropp, J. R. D. Taplin, R. Vásquez, E. Vilanova, Drought-mortality relationships for tropical forests. *New Phytol.* **187**, 631–646 (2010).
52. P. Meir, T. E. Wood, D. R. Galbraith, P. M. Brando, A. C. L. da Costa, L. Rowland, L. V. Ferreira, Threshold responses to soil moisture deficit by trees and soil in tropical rain forests: Insights from field experiments. *Bioscience* **65**, 882–892 (2015).
53. S. Bathiany, N. Scheffer, E. H. Van Nes, M. S. Williamson, T. M. Lenton, Abrupt climate change in an oscillating world. *Sci. Rep.* **8**, 5040 (2018).
54. D. C. Zemp, C. F. Schleussner, H. M. J. Barbosa, R. J. van der Ent, J. F. Donges, J. Heinke, G. Sampaio, A. Rammig, On the importance of cascading moisture recycling in South America. *Atmos. Chem. Phys.* **14**, 13337–13359 (2014).
55. A. D. Nobre, “The future climate of Amazonia scientific assessment report” (Tech. Rep., Articulación Regional Amazónica, 2014).
56. D. C. Zemp, C.-F. Schleussner, H. M. J. Barbosa, M. Hirota, V. Montade, G. Sampaio, A. Staal, L. Wang-Erlandsson, A. Rammig, Self-amplified Amazon forest loss due to vegetation-atmosphere feedbacks. *Nat. Commun.* **8**, 14681 (2017).
57. A. Staal, O. A. Tuinenburg, J. H. C. Bosmans, M. Holmgren, E. H. van Nes, N. Scheffer, D. C. Zemp, S. C. Dekker, Forest-rainfall cascades buffer against drought across the Amazon. *Nat. Clim. Chang.* **8**, 539–543 (2018).
58. A. Staal, B. M. Flores, A. P. D. Aguiar, J. H. C. Bosmans, I. Fetzer, O. A. Tuinenburg, Feedback between drought and deforestation in the Amazon. *Environ. Res. Lett.* **15**, 044024 (2020).
59. H. Hersbach, B. Bell, P. Berrisford, S. Hirahara, A. Horányi, J. Muñoz-Sabater, J. Nicolas, C. Peubey, R. Radu, D. Schepers, A. Simmons, C. Soci, S. Abdalla, X. Abellan, G. Balsamo, P. Bechtold, G. Biavati, J. Bidlot, M. Bonavita, G. Chiara, P. Dahlgren, D. Dee, M. Diamantakis, R. Dragani, J. Flemming, R. Forbes, M. Fuentes, A. Geer, L. Haimberger, S. Healy, R. J. Hogan, E. Hólm, M. Janisková, S. Keeley, P. Laloyaux, P. Lopez, C. Lupu, G. Radnoti, P. Rosnay, I. Rozum, F. Vamborg, S. Villaume, J. N. Thépaut, The ERA5 global reanalysis. *Q. J. Roy. Meteorol. Soc.* **146**, 1999–2049 (2020).
60. C. von Randow, A. O. Manzi, B. Kruijt, P. J. de Oliveira, F. B. Zanchi, R. L. Silva, M. G. Hodnett, J. H. C. Gash, J. A. Elbers, M. J. Waterloo, F. L. Cardoso, P. Kabat, Comparative measurements and seasonal variations in energy and carbon exchange over forest and pasture in South West Amazonia. *Theor. Appl. Climatol.* **78**, 5–26 (2004).
61. F. Dominguez, J. Eiras-Barca, Z. Yang, D. Bock, R. Nieto, L. Gimeno, Amazonian moisture recycling revisited using WRF with water vapor tracers. *J. Geophys. Res. Atmos.* **127**, e2021JD035259 (2022).
62. D. V. Spracklen, S. R. Arnold, C. M. Taylor, Observations of increased tropical rainfall preceded by air passage over forests. *Nature* **489**, 282–285 (2012).
63. Instituto Nacional de Pesquisas Espaciais, “Terrabrisilis/Prodes” (Tech. Rep., Instituto Nacional de Pesquisas Espaciais and National Institute for Space Research, 2020).
64. J. Agudelo, P. A. Arias, S. C. Vieira, J. A. Martínez, Influence of longer dry seasons in the Southern Amazon on patterns of water vapor transport over northern South America and the Caribbean. *Clim. Dynam.* **52**, 2647–2665 (2019).
65. A. T. Leite-Filho, V. Y. Sousa Pontes, M. H. Costa, Effects of deforestation on the onset of the rainy season and the duration of dry spells in Southern Amazonia. *J. Geophys. Res. Atmos.* **124**, 5268–5281 (2019).
66. A. T. Leite-Filho, M. H. Costa, R. Fu, The southern Amazon rainy season: The role of deforestation and its interactions with large-scale mechanisms. *Int. J. Climatol.* **40**, 2328–2341 (2020).
67. M. Ruiz-Vásquez, P. A. Arias, J. A. Martínez, J. C. Espinoza, Effects of Amazon basin deforestation on regional atmospheric circulation and water vapor transport towards tropical South America. *Clim. Dynam.* **54**, 4169–4189 (2020).
68. I. C. Correa, P. A. Arias, M. Rojas, Evaluation of multiple indices of the South American monsoon. *Int. J. Climatol.* **41**, E2801–E2819 (2021).
69. G. Poveda, L. Jaramillo, L. F. Vallejo, Seasonal precipitation patterns along pathways of South American low-level jets and aerial rivers. *Water Resour. Res.* **50**, 98–118 (2014).
70. N. Boers, A. Rheinwalt, B. Bookhagen, H. M. J. Barbosa, N. Marwan, J. Marengo, J. Kurths, The South American rainfall dipole: A complex network analysis of extreme events. *Geophys. Res. Lett.* **41**, 7397–7405 (2014).
71. L. F. S. Commar, G. M. Abrahão, M. H. Costa, A possible deforestation-induced synoptic-scale circulation that delays the rainy season onset in Amazonia. *Environ. Res. Lett.* **18**, 044041 (2023).
72. J. P. Sierra, C. Junquas, J. C. Espinoza, H. Segura, T. Condom, M. Andrade, J. Molina-Carpio, L. Ticona, V. Mardoñez, L. Blacutt, J. Polcher, A. Rabatel, J. E. Sicart, Deforestation impacts on Amazon-Andes hydroclimatic connectivity. *Clim. Dynam.* **58**, 2609–2636 (2021).
73. J. C. A. Baker, D. Castilho de Souza, P. Y. Kubota, W. Buermann, C. A. S. Coelho, M. B. Andrews, M. Gloor, L. Garcia-Carreras, S. N. Figueroa, D. V. Spracklen, An assessment of land-atmosphere interactions over south America using satellites, reanalysis, and two global climate models. *J. Hydrometeorol.* **22**, 905–922 (2021).
74. A. González-Reyes, A. Venegas-González, A. Muñoz, I. Schneider, The first soil moisture reconstruction in the Mediterranean Chilean Andes region developed by tree rings and satellite observations to inform climate change impacts in South America. *EGUGA 10.5194/egusphere-egu21-13831*, (2021).
75. L. A. Blacutt, D. L. Herdies, L. G. G. de Gonçalves, D. A. Vila, M. Andrade, Precipitation comparison for the CFSR, MERRA, TRMM3B42 and Combined Scheme datasets in Bolivia. *Atmos. Res.* **163**, 117–131 (2015).
76. S. Golian, M. Javadian, A. Behrang, On the use of satellite, gauge, and reanalysis precipitation products for drought studies. *Environ. Res. Lett.* **14**, 075005 (2019).
77. P. Papastefanou, C. S. Zang, Z. Angelov, A. A. de Castro, J. C. Jimenez, L. F. C. de Rezende, R. C. Ruscica, B. Sakschewski, A. A. Sörensson, K. Thonicke, C. Vera, N. Viovy, C. von Randow, A. Rammig, Recent extreme drought events in the Amazon rainforest: Assessment of different precipitation and evapotranspiration datasets and drought indicators. *Biogeosciences* **19**, 3843–3861 (2022).
78. U. Schneider, P. Finger, A. Meyer-Christoffer, E. Rustemeier, M. Ziese, A. Becker, Evaluating the hydrological cycle over land using the newly-corrected precipitation climatology from the global precipitation climatology centre (GPCC). *Atmosphere* **8**, 52 (2017).
79. B. Bell, H. Hersbach, A. Simmons, P. Berrisford, P. Dahlgren, A. Horányi, J. Muñoz-Sabater, J. Nicolas, R. Radu, D. Schepers, C. Soci, S. Villaume, J. R. Bidlot, L. Haimberger, J. Woollen, C. Buontempo, J.-N. Thépaut, The ERA5 global reanalysis: Preliminary extension to 1950. *Q. J. Roy. Meteorol. Soc.* **147**, 4186–4227 (2021).
80. D. A. Lavers, A. Simmons, F. Vamborg, M. J. Rodwell, An evaluation of ERA5 precipitation for climate monitoring. *Q. J. Roy. Meteorol. Soc.* **148**, 3152–3165 (2022).
81. C. C. Funk, P. J. Peterson, M. F. Landsfeld, D. H. Pedreros, J. P. Verdin, J. D. Rowland, B. E. Romero, G. J. Husak, J. C. Michaelsen, A. P. Verdin, A quasi-global precipitation time series for drought monitoring. *Data Series 10.3133/ds832*, (2014).
82. R. F. Adler, M. R. P. Sapiano, G. J. Huffman, J.-J. Wang, G. Gu, D. Bolvin, L. Chiu, U. Schneider, A. Becker, E. Nelkin, P. Xie, R. Ferraro, D.-B. Shin, The global precipitation climatology project (GPCP) monthly analysis (New Version 2.3) and a review of 2017 global precipitation. *Atmosphere* **9**, 138 (2018).
83. P. A. Arias, R. Fu, C. Vera, M. Rojas, A correlated shortening of the North and South American monsoon seasons in the past few decades. *Clim. Dynam.* **45**, 3183–3203 (2015).
84. C. Häggi, C. M. Chiessi, U. Merkel, S. Mulitza, M. Prange, M. Schulz, E. Scheffuß, Response of the Amazon rainforest to late Pleistocene climate variability. *Earth Planet. Sci. Lett.* **479**, 50–59 (2017).
85. J. Eiras-Barca, F. Dominguez, Z. Yang, D. Chug, R. Nieto, L. Gimeno, G. Miguez-Macho, Changes in South American hydroclimate under projected Amazonian deforestation. *Ann. N. Y. Acad. Sci.* **1472**, 104–122 (2020).
86. J. C. Espinoza, H. Segura, J. Ronchail, G. Drapeau, O. Gutierrez-Cori, Evolution of wet-day and dry-day frequency in the western Amazon basin: Relationship with atmospheric circulation and impacts on vegetation. *Water Resour. Res.* **52**, 8546–8560 (2016).
87. B. Liebmann, I. Bladé, G. N. Kiladis, L. M. V. Carvalho, G. B. Senay, D. Allured, S. Leroux, C. Funk, Seasonality of African precipitation from 1996 to 2009. *J. Climate* **25**, 4304–4322 (2012).
88. Y. Jiang, L. Zhou, C. J. Tucker, A. Raghavendra, W. Hua, Y. Y. Liu, J. Joiner, Widespread increase of boreal summer dry season length over the Congo rainforest. *Nat. Clim. Change* **9**, 617–622 (2019).
89. J. A. Marengo, B. Liebmann, V. E. Kousky, N. P. Filizola, I. C. Wainer, Onset and end of the rainy season in the Brazilian Amazon Basin. *J. Climate* **14**, 833–852 (2001).
90. V. Guttal, C. Jayaprakash, Changing skewness: An early warning signal of regime shifts in ecosystems. *Ecol. Lett.* **11**, 450–460 (2008).
91. S. Kéfi, V. Guttal, W. A. Brock, S. R. Carpenter, A. M. Ellison, V. N. Livina, D. A. Seekell, M. Scheffer, E. H. van Nes, V. Dakos, Early warning signals of ecological transitions: Methods for spatial patterns. *PLOS ONE* **9**, e92097 (2014).

92. V. Dakos, E. H. van Nes, M. Scheffer, Flickering as an early warning signal. *Theor. Ecol.* **6**, 309–317 (2013).
93. T. M. Lenton, R. J. Myerscough, R. Marsh, V. N. Livina, A. R. Price, S. J. Cox; the GENIE Team, Using GENIE to study a tipping point in the climate system. *Philos. Trans. R. Soc. A Math. Phys. Eng. Sci.* **367**, 871–884 (2009).
94. C. A. Boulton, L. C. Allison, T. M. Lenton, Early warning signals of atlantic meridional overturning circulation collapse in a fully coupled climate model. *Nat. Commun.* **5**, 5752 (2014).
95. R. Cleveland, W. Cleveland, J. McRae, I. Terpenning, STL: Seasonal-trend decomposition procedure based on LOESS. *J. Off. Stat.* **6**, 3–73 (1990).
96. S. Seabold, J. Perktold, paper presented at Proceedings of the 9th Python in Science Conference, Austin, TX, 28 June to 3 July 2010.
97. P. D. Ditlevsen, S. J. Johnsen, Tipping points: Early warning and wishful thinking. *Geophys. Res. Lett.* **37** 10.1029/2010GL044486, (2010).
98. J. Theiler, S. Eubank, A. Longtin, B. Galdrikian, J. Doyne Farmer, Testing for nonlinearity in time series: The method of surrogate data. *Physica D. Nonlinear Phenom.* **58**, 77–94 (1992).
99. M. Rypdal, Early-warning signals for the onsets of Greenland interstadials and the younger dryas-preboreal transition. *J. Climate* **29**, 4047–4056 (2016).
100. N. Boers, Early-warning signals for Dansgaard-Oeschger events in a high-resolution ice core record. *Nat. Commun.* **9**, 2556 (2018).

Acknowledgments

Funding: N.Boe. acknowledges funding by the Volkswagen Foundation. This is TiPES contribution #111; the TiPES (Tipping Points in the Earth System) project has received funding from the European Union's Horizon 2020 research and innovation program under grant agreement no. 820970. N.Boe. acknowledges further funding by the European Union's Horizon 2020 research and innovation programme under the Marie Skłodowska-Curie grant agreement no. 956170. **Author contributions:** N.Boe. conceived the study. N.Boc. performed the analysis. Both authors discussed and interpreted results. N.Boc. wrote the paper with contributions from N.Boe. **Competing interests:** The authors declare that they have no competing interests. **Data and materials availability:** All data needed to evaluate the conclusions in the paper are present in the paper and/or the Supplementary Materials. The meteorological data are publicly available. The ERA5 reanalysis (59) can be downloaded from <https://cds.climate.copernicus.eu/>. The CHIRPS precipitation dataset (81) can be downloaded from www.chc.ucsb.edu/data/chirps. The GPCC precipitation dataset is available at www.psl.noaa.gov/data/gridded/data/gpcc.html (78). The GPCP dataset is available at <https://psl.noaa.gov/data/gridded/data/gpcp.html> (82). All code used for the analysis and the model is available on Zenodo at www.doi.org/10.5281/zenodo.8121629 and on GitHub at <https://github.com/NilsBochow/SAMS-critical-transition>.

Submitted 23 July 2022

Accepted 21 July 2023

Published 4 October 2023

10.1126/sciadv.add9973

Supplementary Materials for

The South American monsoon approaches a critical transition in response to deforestation

Nils Bochow and Niklas Boers

Corresponding author: Nils Bochow, [nils.bochow@uit.no](mailto:nil.bochow@uit.no)

Sci. Adv. **9**, eadd9973 (2023)
DOI: 10.1126/sciadv.add9973

This PDF file includes:

Figs. S1 to S11

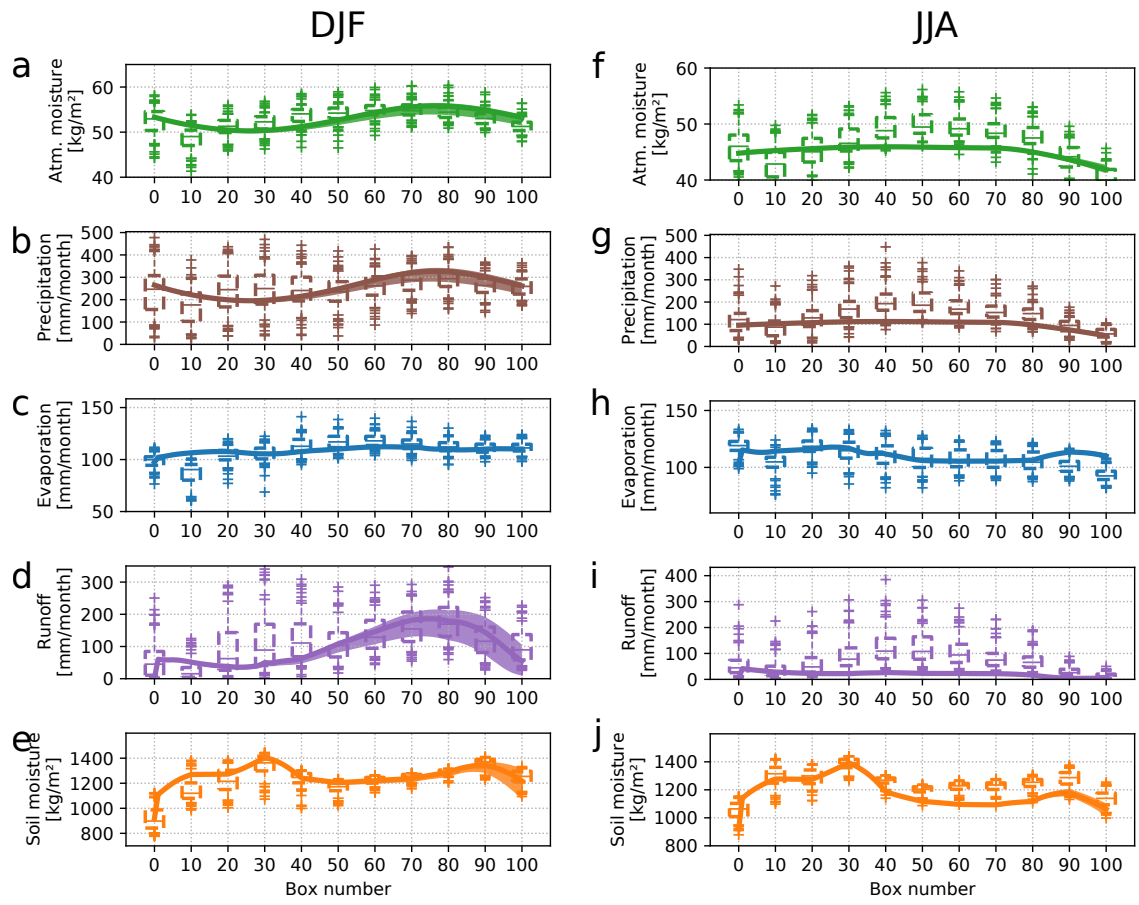


Figure S1: Comparison between model results and reanalysis. Comparison between ERA5 reanalysis (box plots dashed with whiskers at 5th and 95th percentile) and model results (solid lines, filled area) for all atmospheric variables of the model, along the trajectory of 100 boxes. Results are shown for the wet season (DJF, a-e) and for the dry season (JJA, f-j). Filled areas indicate the range of values for all choices of the different simulation parameters AF and $\langle H \rangle^{AO}$. Solid line denotes mean value. Note that we use all available soil moisture layers in ERA5 with a total depth of 2.89 m.

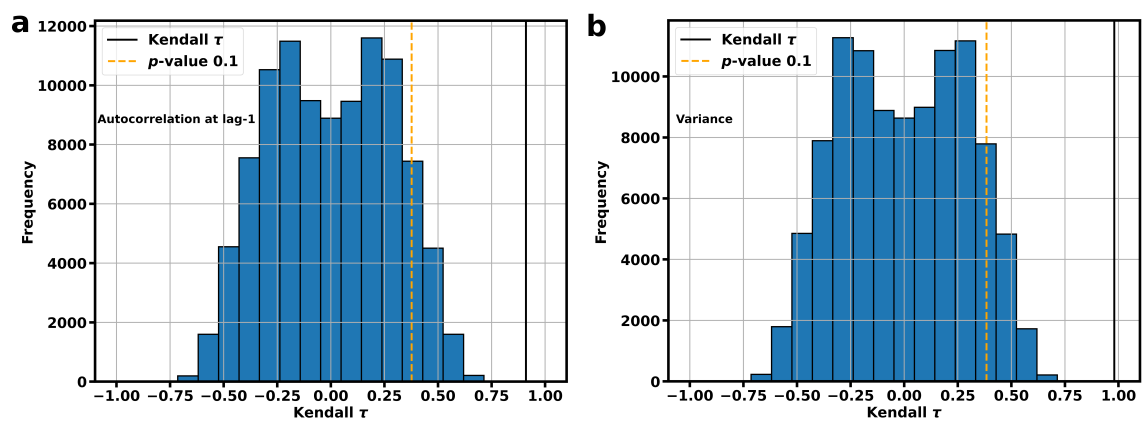


Figure S2: Histogram of Kendall τ derived from 100,000 surrogate time series of lag-one autocorrelation and variance of the modelled precipitation rates. (a) Histogram of lag-one autocorrelation from surrogate time series generated by phase randomisation (see Methods). The dashed orange line denotes the threshold corresponding to a p -value of $p = 0.1$, and the black line denotes Kendall τ derived from the original modelled time series series (see Fig. 4 a). (b) Same as (a) but for variance.

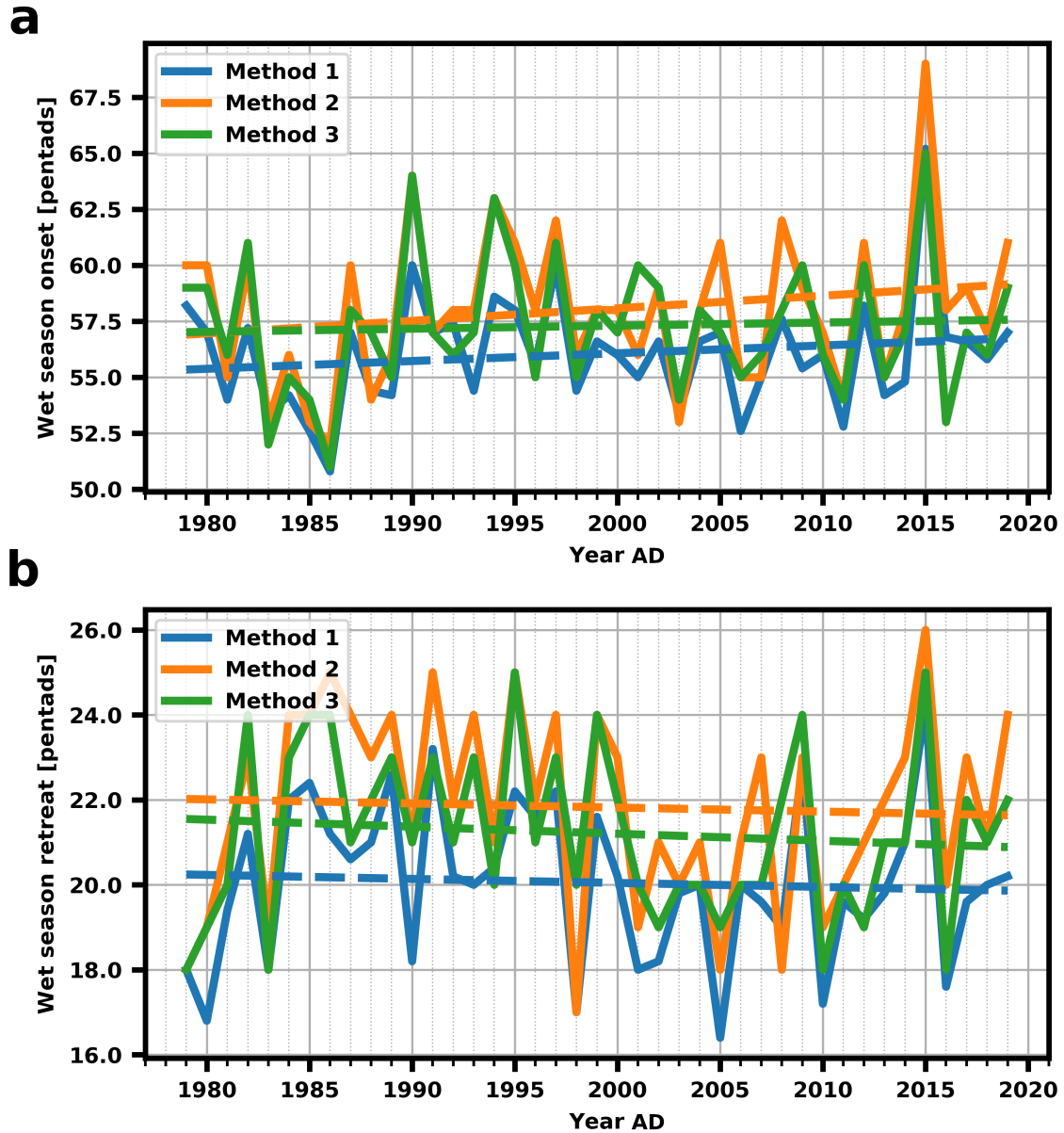


Figure S3: Wet season onset and retreat date in southern Amazonia. (a) Wet season onset date in southern Amazonia ($5 - 15^{\circ}\text{S}$, $50^{\circ} - 70^{\circ}\text{W}$) from 1979-2019 for the three different methods used (see methods). Dashed lines denote the corresponding linear trends. We find an increase of 3.5 (blue), 5.6 (orange) and 1.4 *pentad/century* (green) for the three methods, respectively. (b) Same as (a) but for the wet season retreat date. We find a decrease of -0.9 (blue), -1.0 (orange), and -1.6 *pentad/century* (green) of the retreat date. Data is taken from the ERA5 reanalysis (58). The wet season hence tends to initiate later and end earlier, consistently with an increase in DSL.

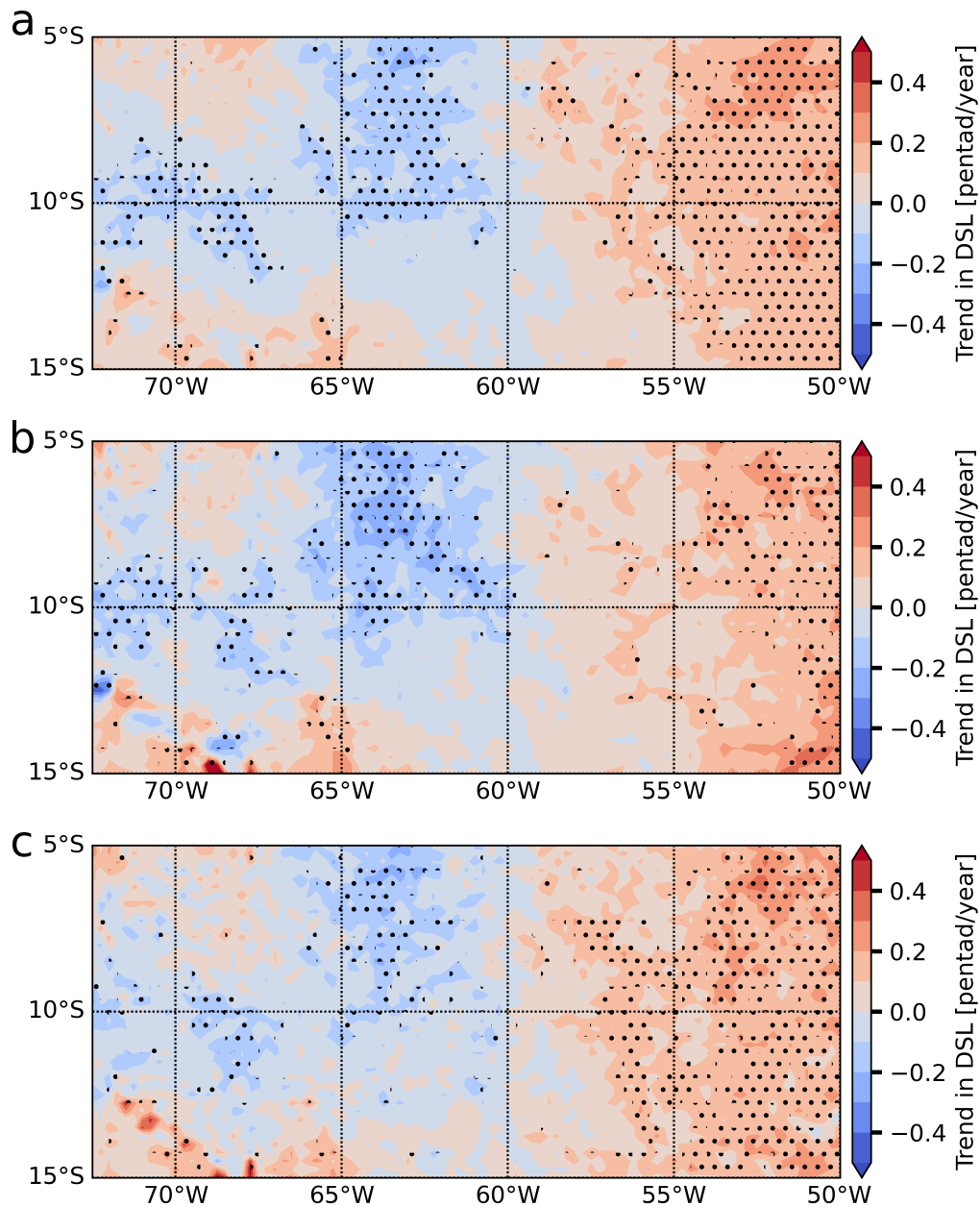


Figure S4: Map of trends in dry season length for the southern Amazon in ERA5. Calculated linear trend in the dry season length from 1979-2019 in southern Amazonia, based on the ERA5 reanalysis, using the three different methods used (see methods). Areas with p -value < 0.05 are hatched. (a) Dry season length calculated with method 1, (b) Calculated with method 2, (c) calculated with Method 3. All three methods show the same spatial pattern.

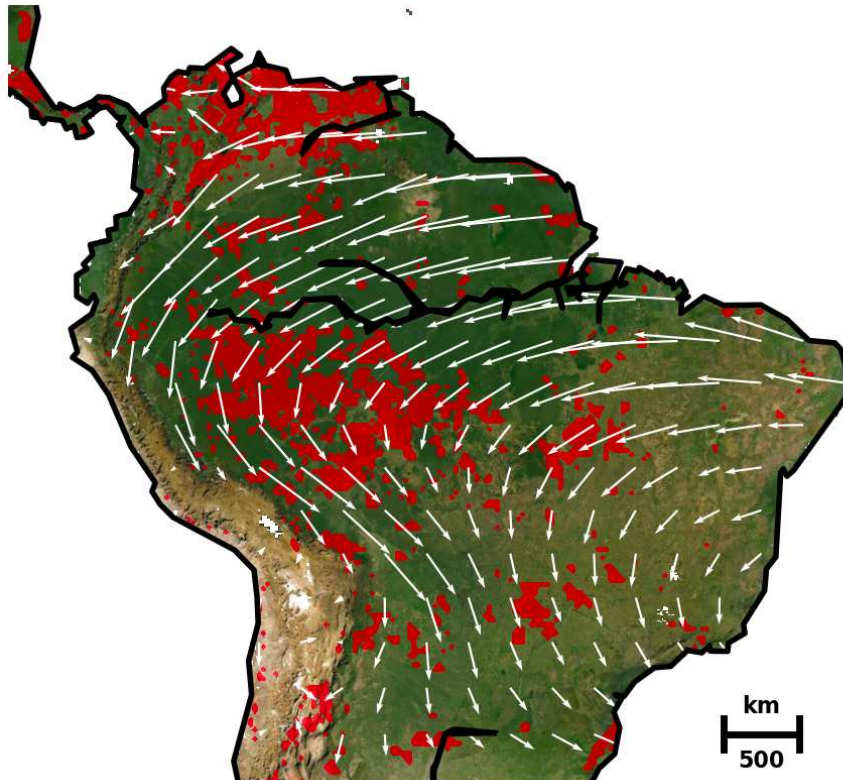


Figure S5: Regions with simultaneous increase in variance and autocorrelation in ERA5. The red areas denote regions where variance and autocorrelation in ERA5 precipitation rates increase. See Fig. 6 and method section for methods.

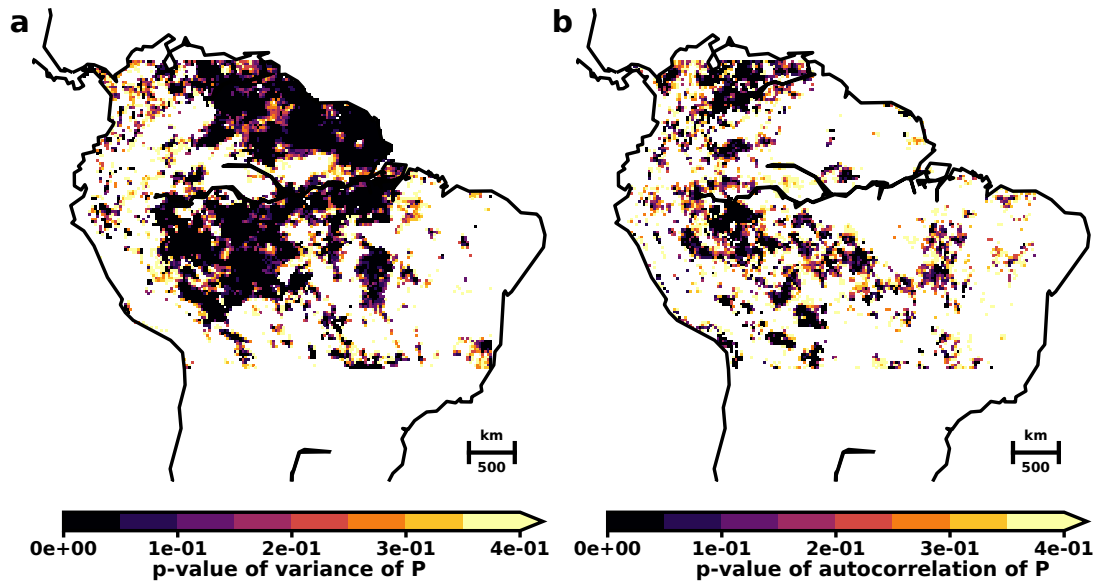


Figure S6: Map of p -values estimated from distribution of Kendall τ derived from 10000 surrogate data sets of autocorrelation and variance in southwestern Amazonia in ERA5. (a) Map of the p -values for our phase-surrogate test to determine the significance of the trend in the lag-one autocorrelation in the precipitation rates in northern South America. The p -values are only shown for regions with positive trend in the autocorrelation. White areas denote regions with negative trends. (b) Same as (a) but for the variance. It can be inferred that the increases in both variance and lag-one autocorrelation in southwestern Amazonia are mostly significant.

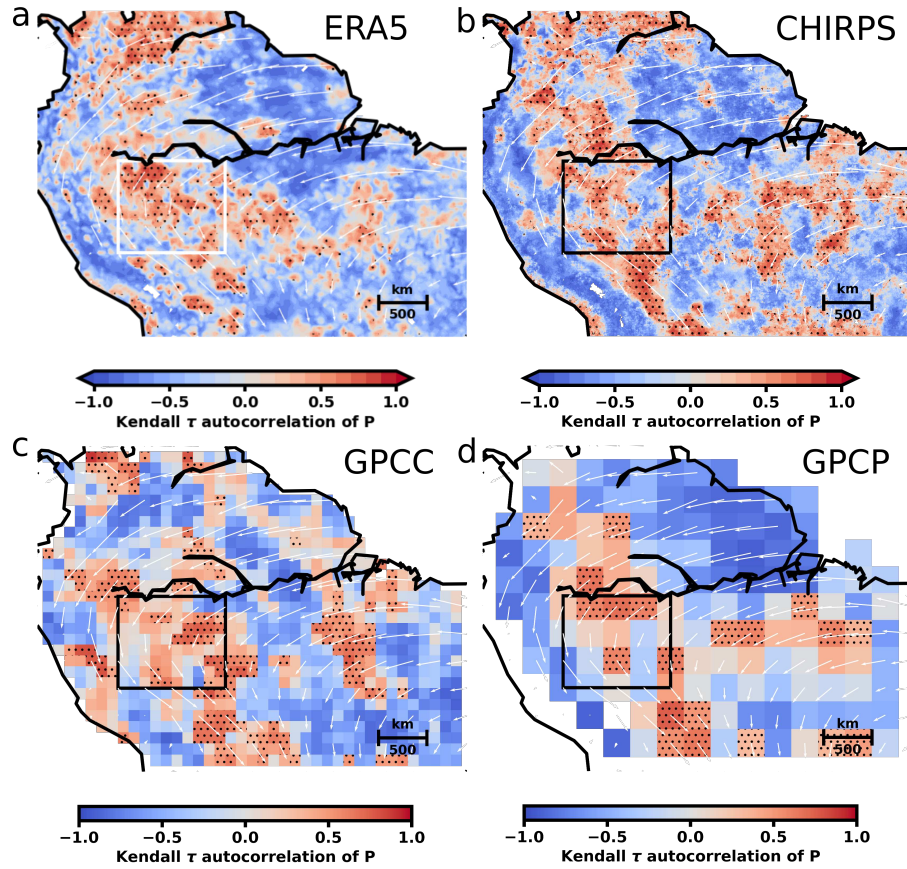


Figure S7: Temporal lag-one autocorrelation in different precipitation data sets. Spatial patterns of Kendall τ for the lag-one autocorrelation of observed monthly averaged precipitation time series for different precipitation data sets. The autocorrelation is calculated for rolling windows of width $w = 20$ years. The trend is determined by Kendall τ of the respective indicator of the detrended and de-seasoned precipitation time series at every site. Stippling marks regions with significantly increasing trends ($p < 0.05$, see Methods for details on the statistical test). Mean wet season wind fields (1979-2019) at 750 hPa are delineated in white. The non-linear trend of the underlying precipitation time series is removed via STL (85) with a trend smoother length of 5 years and seasonal smoother length of 13 months. **(a)** For ERA5 precipitation (1979-2019). This subpanel is identical with Fig. 6a. **(b)** CHIRPS (1981-2022) (79) **(c)** GPCC (1982-2020) (76) **(d)** GPCP (1979-2022) (80).

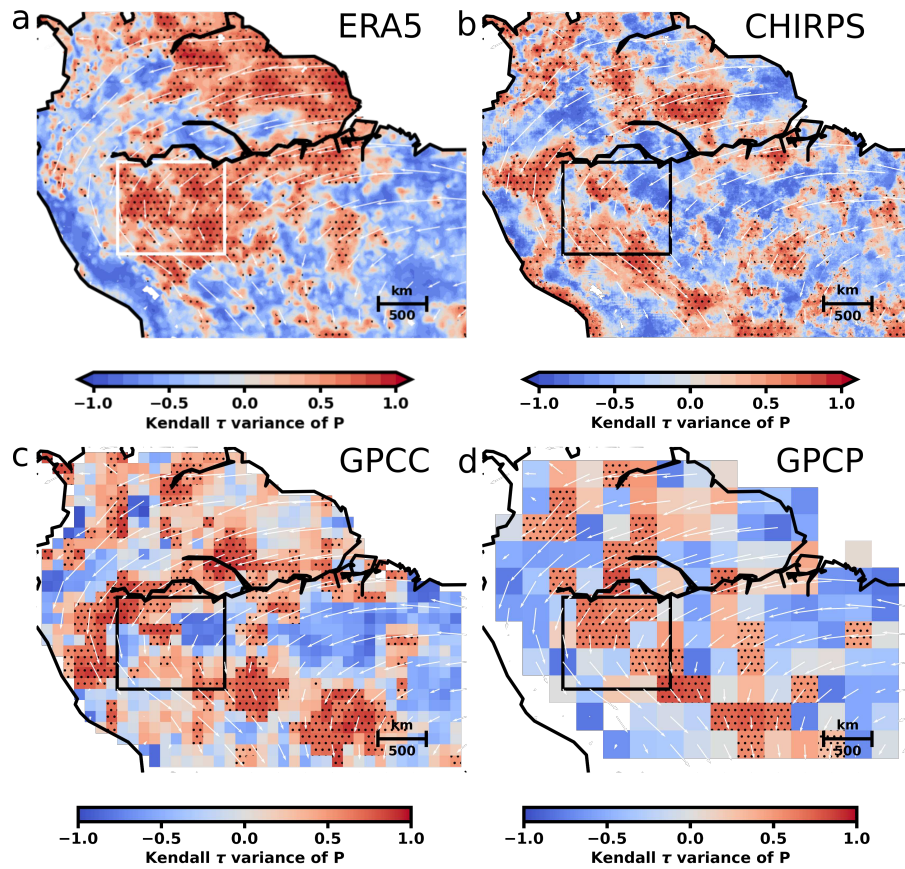


Figure S8: Temporal variance in different precipitation data sets. Spatial patterns of Kendall τ for the variance of observed monthly averaged precipitation time series for different precipitation data sets. The variance is calculated for rolling windows of width $w = 20$ years. The trend is determined by Kendall τ of the respective indicator of the detrended and de-seasoned precipitation time series at every site. Stippling marks regions with significantly increasing trends ($p < 0.05$, see Methods for details on the statistical test). Mean wet season wind fields (1979-2019) at 750 hPa are delineated in white. The non-linear trend of the underlying precipitation time series is removed via STL (85) with a trend smoother length of 5 years and seasonal smoother length of 13 months. **(a)** For ERA5 precipitation (1979-2019). This subpanel is identical with Fig. 6b. **(b)** CHIRPS (1981-2022) (79) **(c)** GPCC (1982-2020) (76) **(d)** GPCP (1979-2022) (80).

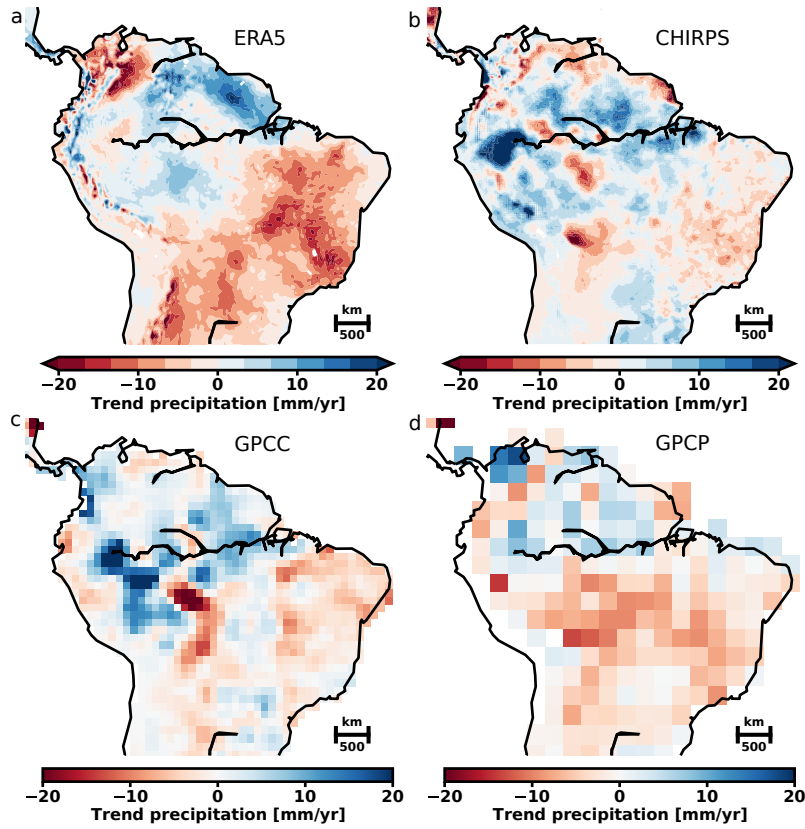


Figure S9: Trends in precipitation rates in South America obtained from different precipitation data sets. (a) Calculated linear trend in yearly averaged precipitation rates from 1979-2019 in South America, determined from the ERA5 reanalysis. Large parts of the Amazon rainforest show a positive trend (blue) in the precipitation rates. This suggests that the observed decreasing soil moisture is not a linear response to the precipitation rates but rather a response to changes of the hydrological budget of the coupled atmosphere-vegetation system in ERA5. (b) Same as (a) but for the CHIRPS dataset from (1981-2022). (c) GPCP (1982-2020) (d) GPC (1979-2022).

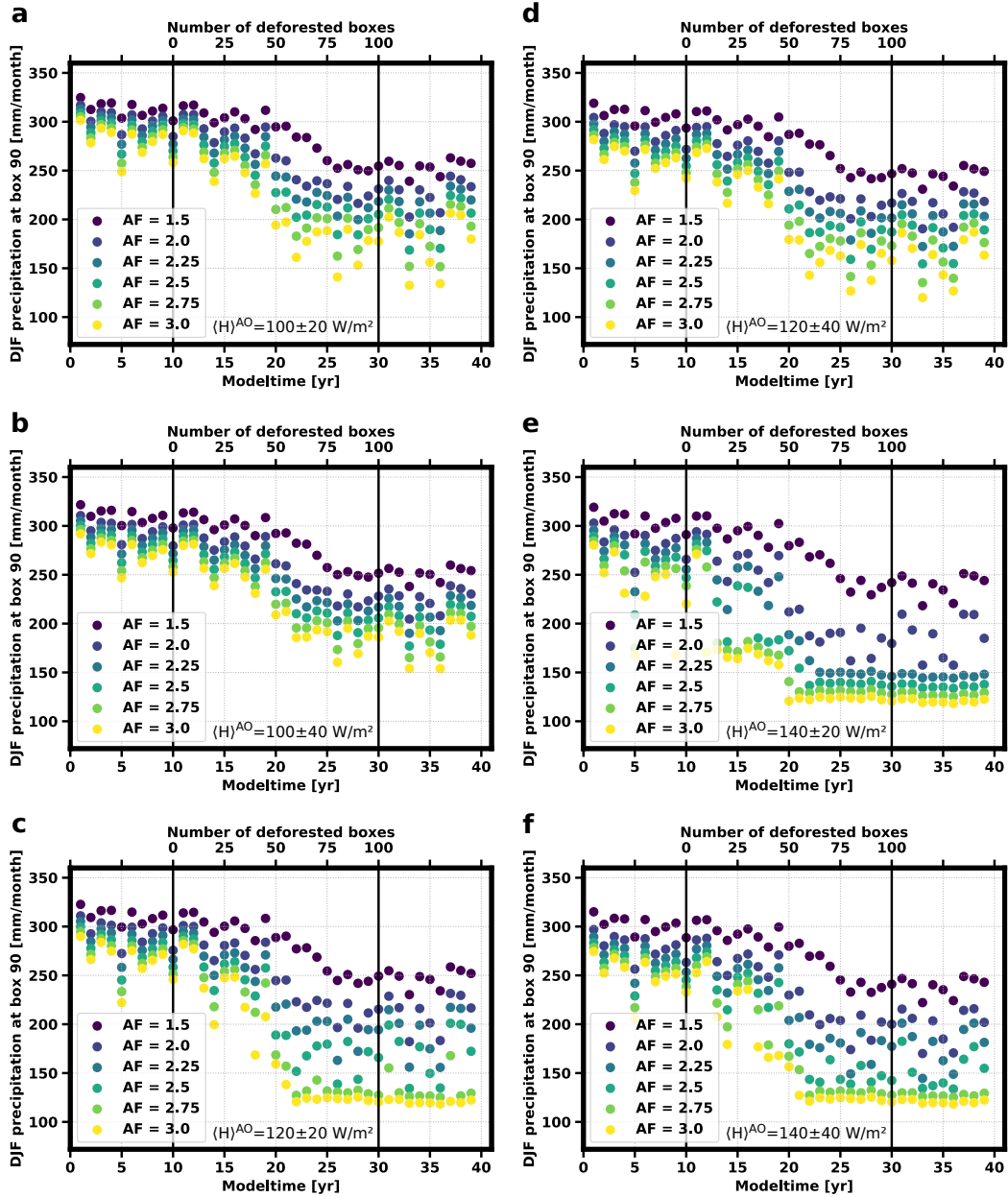


Figure S10: Simulated wet season precipitation for different amplification factors and atmospheric heating over the Atlantic, after successive deforestation. We show the wet season precipitation P_{DjF} in box 90 for all amplification factors AF and a selection of investigated atmospheric heating values over the Atlantic ocean $\langle H \rangle^{\text{AO}}$, with successive deforestation. Deforestation is initiated at year 10 and is completed at year 30. All simulations show a dieback of the rainforest prior to 50% deforestation. For lower values of AF and $\langle H \rangle^{\text{AO}}$ there is still an annual transition into the wet season (a, b, d) after complete rainforest loss. For high AF and $\langle H \rangle^{\text{AO}}$ we find a permanent dry season state after rainforest dieback (c,e,f). It should be noted that the amplification factor is most realistically between 2-3 (45–47).

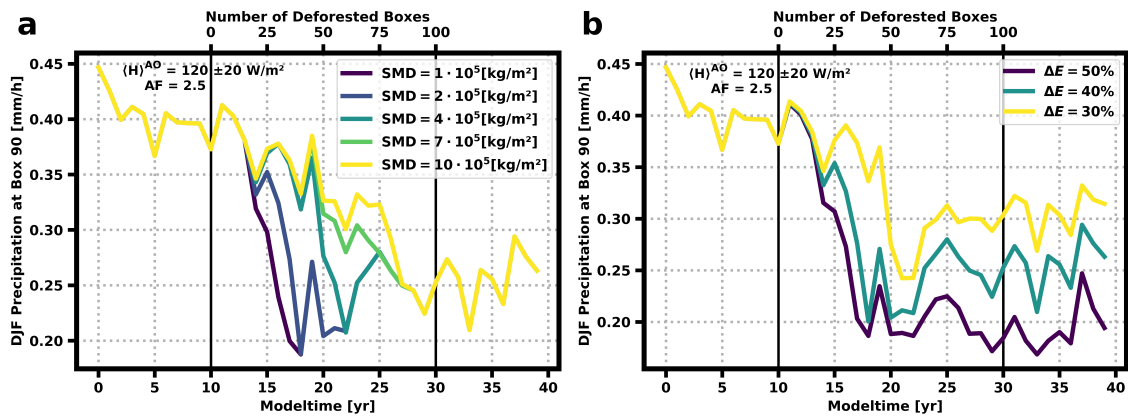


Figure S11: Simulated wet season precipitation for different soil moisture deficit thresholds and reductions of the evapotranspiration after successive deforestation. (a) Wet season precipitation P_{DJF} in box 90 for different values of the soil moisture deficit threshold SMD after successive deforestation. The atmospheric heating over the Atlantic ocean $\langle H \rangle^{AO} = (120 \pm 20) \text{ W/m}^2$ and the amplification factor $AF = 2.5$ are fixed. Deforestation is initiated at year 10 and is completed at year 30. All simulations show dieback of the rainforest prior to 50% deforestation. (b) Same as (a) but for different values of the reduction of the evapotranspiration after deforestation ΔE .



Paper II: Overshooting the Critical Threshold for the Greenland Ice Sheet

Bochow, N., Poltronieri, A., Robinson, A., Montoya, M., Rypdal, M., Boers, N.
Overshooting the critical threshold for the Greenland ice sheet. *Nature* **622**,
528–536 (2023). <https://doi.org/10.1038/s41586-023-06503-9>

Overshooting the critical threshold for the Greenland ice sheet


<https://doi.org/10.1038/s41586-023-06503-9>

Received: 20 January 2023

Accepted: 28 July 2023

Published online: 18 October 2023

Open access

 Check for updates

Nils Bochow^{1,2,3✉}, Anna Poltronieri¹, Alexander Robinson^{3,4,5}, Marisa Montoya^{5,6}, Martin Rypdal¹ & Niklas Boers^{3,7,8}

Melting of the Greenland ice sheet (GrIS) in response to anthropogenic global warming poses a severe threat in terms of global sea-level rise (SLR)¹. Modelling and palaeoclimate evidence suggest that rapidly increasing temperatures in the Arctic can trigger positive feedback mechanisms for the GrIS, leading to self-sustained melting^{2–4}, and the GrIS has been shown to permit several stable states⁵. Critical transitions are expected when the global mean temperature (GMT) crosses specific thresholds, with substantial hysteresis between the stable states⁶. Here we use two independent ice-sheet models to investigate the impact of different overshoot scenarios with varying peak and convergence temperatures for a broad range of warming and subsequent cooling rates. Our results show that the maximum GMT and the time span of overshooting given GMT targets are critical in determining GrIS stability. We find a threshold GMT between 1.7 °C and 2.3 °C above preindustrial levels for an abrupt ice-sheet loss. GrIS loss can be substantially mitigated, even for maximum GMTs of 6 °C or more above preindustrial levels, if the GMT is subsequently reduced to less than 1.5 °C above preindustrial levels within a few centuries. However, our results also show that even temporarily overshooting the temperature threshold, without a transition to a new ice-sheet state, still leads to a peak in SLR of up to several metres.

Melting of the GrIS has contributed more than 20% to the observed SLR since AD 2002 (ref. 7). Modelling results indicate that the GrIS exhibits several stable states, with critical transitions between them when the GMT exceeds a critical threshold^{4,6,8}. With further global warming, a partial to complete loss of the ice sheet is expected, implying an increase of the global sea level by up to 7 m (refs. 3,9). The land-ice contribution to SLR until the year AD 2100 is expected to be in the range of several decimetres, with the GrIS being one of the main contributors^{10–12}. As well as the direct impacts on coastal ecosystems and populations, the North Atlantic freshening resulting from a melting GrIS might contribute to a weakening or even destabilization of the Atlantic Meridional Overturning Circulation (AMOC), which would have global-scale impacts, including disruptions of the African and Asian monsoon systems^{13–16}.

In recent decades, meltwater runoff from the GrIS has accelerated relative to global surface temperatures¹⁷ and there are precursor signals of an impending critical transition detectable in ice cores from the central-western GrIS¹⁸. There is, therefore, a need to explore the future trajectories of the GrIS under different emission scenarios. Furthermore, it is important to understand what is required to prevent a runaway effect. The so-far insufficient efforts to reduce global emissions make it necessary to investigate scenarios in which we do not achieve current warming targets, such as those defined in the Paris Agreement, by the end of the twenty-first century^{19–21}. Different options to remove CO₂ from the atmosphere, including carbon

capture and storage technologies and large-scale reforestation, could make it possible to maintain such temperature goals in the long term, even if a temporary overshoot occurs²². These subsequent efforts to reduce GMTs after AD 2100 could have a substantial mitigating effect because many of the large-scale components of the climate system change slowly compared with the current rate of global warming. In the following, we refer to temporary exceedances of temperature targets or critical temperature thresholds as overshoots and to the equilibrium temperatures that will be reached in the long term as convergence temperatures.

Owing to the effect of inertia, crossing a critical threshold in a dynamical system with several stable states does not necessarily imply that a transition to an alternative state is realized. It is possible to temporarily overshoot the tipping threshold of a system without triggering a transition to a new system state²³. Thus, the temperature threshold of the GrIS could be surpassed without committing to total mass loss, if later on, yet within a specific time frame, actions are taken that reduce the temperature back under the critical threshold.

The overshoot phenomenon is particularly relevant for the GrIS because the timescales for mass loss are long compared with changes in anthropogenic greenhouse emissions. The separation of timescales could make it possible to reverse ice loss if global surface temperatures decrease sufficiently quickly after an initial overshoot. However, because of the complexity of the ice sheet and the various physical

¹Department of Mathematics and Statistics, UiT – The Arctic University of Norway, Tromsø, Norway. ²Physics of Ice, Climate and Earth, Niels Bohr Institute, University of Copenhagen, Copenhagen, Denmark. ³Potsdam Institute for Climate Impact Research, Potsdam, Germany. ⁴Alfred-Wegener-Institut, Helmholtz-Zentrum für Polar- und Meeresforschung, Potsdam, Germany. ⁵Department of Earth Science and Astrophysics, Complutense University of Madrid, Madrid, Spain. ⁶Instituto de Geociencias, CSIC-UCM, Madrid, Spain. ⁷Earth System Modelling, School of Engineering & Design, Technical University of Munich, Munich, Germany. ⁸Department of Mathematics and Global Systems Institute, University of Exeter, Exeter, UK. ✉e-mail: nils.bochow@uit.no

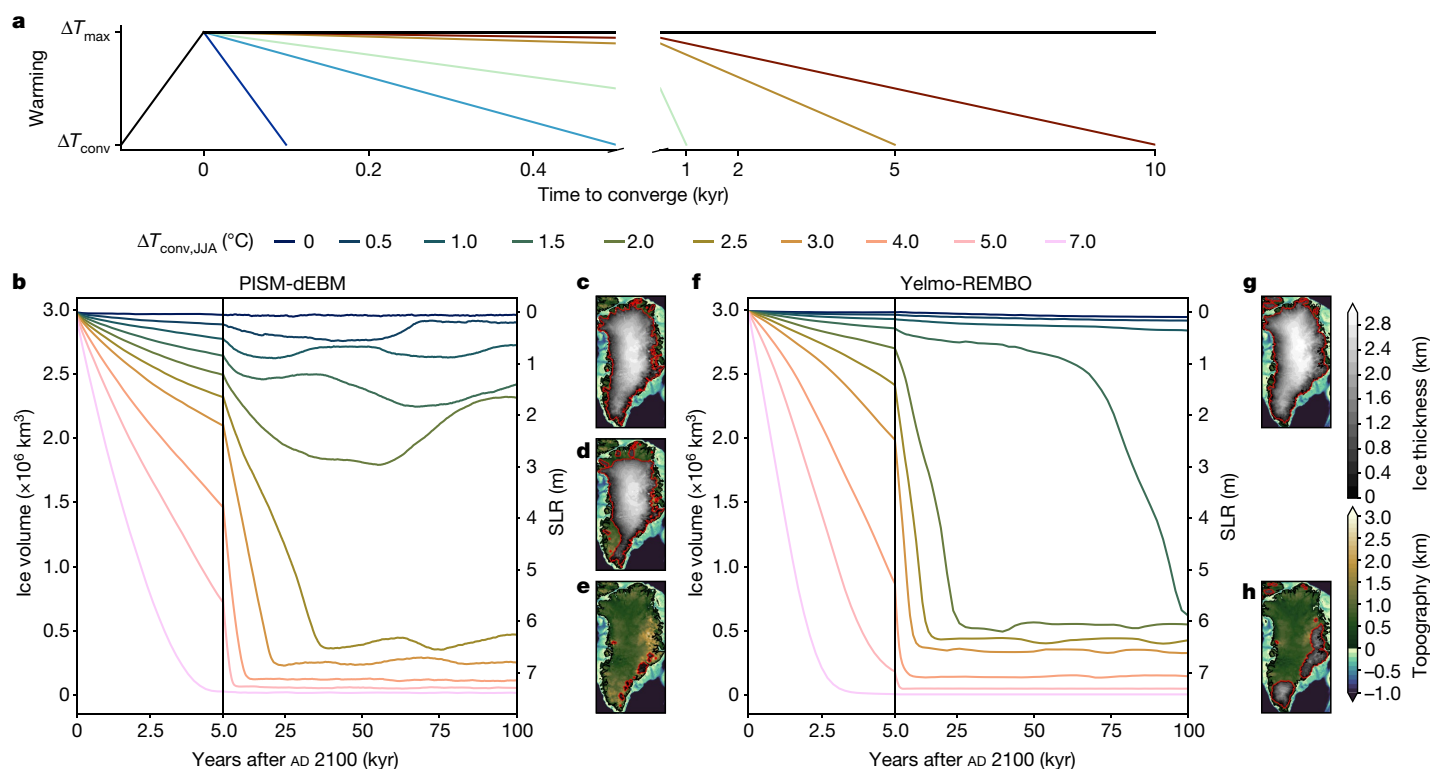


Fig. 1 | Time series of ice volume and spatial extents of the GrIS for warming scenarios without mitigation. **a**, Sketch of applied warming and cooling scenarios in this study. The warming period lasts for 100 years, followed by varying cooling phases. The black line corresponds to scenarios without mitigation as shown in this figure. **b**, Evolution of total GrIS ice volume simulated by PISM-dEBM, without reversal of the temperature anomalies (black line in panel **a**), for different temperature anomalies between $\Delta T_{\text{JJA}} = 0^\circ\text{C}$ and 7.0°C above present. The warming period lasts for 100 years until year AD 2100 and temperatures are kept constant afterwards. Three qualitatively different regimes are noticeable: (1) present-day configuration with fully extended ice sheet or only slightly reduced volume; (2) intermediate state with around 75%

of present-day ice volume; and (3) basically ice-free states. The vertical black line at 5 kyr denotes a change of the x-axis scaling for visual clarity. We normalize the ice volumes to the observed present-day values (see Methods sections ‘PISM-dEBM’ and ‘Yelmo-REMBO’). **c**, Ice thickness of present-day ice-sheet configuration in PISM-dEBM. The ice sheet is fully extended. **d**, Same as **c** but the intermediate state for $\Delta T_{\text{conv,JJA}} = 2.0^\circ\text{C}$, after 100,000 years with PISM-dEBM. The southwestern part of the ice sheet is fully retracted. **e**, Same as **c** but for the ice-free state with PISM-dEBM. **f,g,h**, Same as **b,c,e**, respectively, but for Yelmo-REMBO. Only two regimes can be identified: (1) present-day configuration; and (2) near-ice-free states. The maps were made with the Python package cartopy⁵² and Natural Earth.

processes that play a role, including ice flow and surface processes, it is intrinsically challenging to determine the temperature thresholds and required cooling rates that will prevent a substantial loss of the GrIS.

In this modelling study, we identify safe operating spaces by analysing the behaviour of the GrIS under different warming projections that exceed the presumed critical threshold, but in which the temperature is subsequently reduced. We explore the influence of realistic greenhouse gas emission and corresponding warming scenarios for the twenty-first century in accordance with the most recent Intergovernmental Panel on Climate Change report¹. Subsequently, we apply different idealized carbon-removal scenarios that lead to a temperature decrease on time-scales varying from one hundred to tens of thousands of years (Fig. 1a).

We investigate the behaviour of the GrIS using two independent, state-of-the-art ice-sheet models: a new version of the Parallel Ice Sheet Model (PISM) with a modified version of the diurnal Energy Balance Model (dEBM-simple) for the surface mass balance^{24,25} and the ice-sheet model Yelmo²⁶ coupled to the Regional Energy-Moisture Balance Orographic (REMBO) model²⁷. Both approaches have been extensively tested and validated and have been used to simulate the past, present-day and future evolution of ice sheets^{10,11,25,28–32}.

We force the two models, PISM-dEBM-simple (hereafter PISM-dEBM) and Yelmo-REMBO, by a prescribed change in regional summer temperature relative to present day and apply a scaling factor of 1.61 between regional winter and summer surface temperature to obtain the temperature forcing over the seasonal cycle. This forcing can then

be translated into GMT above preindustrial through a linear scaling that accounts for higher warming rates in the Arctic region relative to the global mean (see Methods section ‘Climate forcing’).

In a first set of experiments, we force the models with a prescribed linear summer (June, July, August (JJA)) temperature increase from year AD 2000 (present day) to AD 2100 to a maximum summer temperature anomaly of $\Delta T_{\text{max,JJA}}$ (Fig. 1a). Thereafter, we linearly decrease the temperature between AD 2100 and AD 2200 back to different convergence temperature anomalies between $\Delta T_{\text{conv,JJA}} = 0^\circ\text{C}$ and 4.0°C above present day (that is, $\Delta T_{\text{conv,GMT}} = 0.5^\circ\text{C}$ and 3.9°C convergence GMT above preindustrial (see Methods section ‘Climate forcing’)). We keep the prescribed temperature anomaly constant after AD 2200 and run the models for another 100 kyr to study the long-term evolution of the ice sheet for each peak warming scenario. In a second set of experiments, we investigate the timescale dependence of the GrIS response following the cooling. After the initial temperature increase until AD 2100, we vary the convergence time (Δt_{conv}), that is, the time needed to reach the convergence temperature, with Δt_{conv} spanning from 100 years to several millennia for various convergence temperatures. We then investigate the behaviour of the GrIS for these different cooling scenarios.

Evolution without long-term temperature reductions

When kept constant after year AD 2100, the temperature increase during the twenty-first century leads to at least some further melting of

the GrIS for every prescribed positive temperature anomaly (Fig. 1b,f). However, the melt is moderate for temperature anomalies smaller than 1.0 °C for both models. In the long term, the runs with PISM-dEBM show that there is a substantial ice-volume loss of more than 20% for $\Delta T_{\text{JJA}} > 1.0$ °C and more than 80% loss for $\Delta T_{\text{JJA}} > 2.2$ °C (Fig. 1b). In runs with Yelmo-REMBO, a temperature anomaly $\Delta T_{\text{JJA}} > 1.4$ °C leads to a complete melting of the ice sheet (Fig. 1f). Yelmo-REMBO only has two stable ice-sheet states: a close to present-day state and a near-ice-free state (Fig. 1g,h). For PISM-dEBM, there is an extra regime; several intermediate states with around 50–90% of current GrIS ice volume are accessible (Fig. 1c–e). The spatial extent of the different ice-sheet states is in accordance with earlier work^{3,5,33}.

The intermediate states in the runs with PISM-dEBM show a gradual and eventual complete retreat of the southwestern part of the ice sheet (Extended Data Fig. 1). Simultaneously, there is a retreat of the ice sheet in the northern part of the GrIS, yet the southwestern part is the most sensitive to warming. For a warming $\Delta T_{\text{JJA}} > 2.2$ °C the remaining GrIS is lost abruptly. The ice sheet fluctuates on a decamillennial timescale for some configurations and does not reach a steady state. For a warming of $\Delta T_{\text{JJA}} = 2.0$ °C, the ice sheet recovers back to approximately 75% of the present-day ice-sheet volume after an initial loss of 40% of the ice-sheet volume (Fig. 1d). The recovery is a result of the glacial isostatic adjustment³⁴. The uplift of the bedrock counteracts the melt-elevation feedback and leads to colder temperatures, which allow the ice sheet to partially regrow³⁴. Although the same simulations with Yelmo-REMBO do not show any stable intermediate states, the ice sheet does show the same spatial sensitivity to warming, with an initial retreat of the southwestern GrIS followed by a retreat of the northern part of the ice sheet (Extended Data Fig. 2). For the most extreme warming scenario of $\Delta T_{\text{JJA}} = 7.0$ °C, the ice sheet is lost in less than 5,000 years in both models.

Short-term overshoots

A reduction in temperature from AD 2100 to AD 2200 leads to a mitigation of the ice loss, depending on the convergence temperature reached (Fig. 2). Regardless of the peak temperature in AD 2100, a convergence temperature increase of 1.5 °C GMT above preindustrial ($\Delta T_{\text{JJA}} = 1.3$ °C) by AD 2200 or lower leads to a stable ice sheet, with the equivalent of less than 1 m long-term SLR contribution in simulations with both models (Fig. 2a,b). However, the maximum interim SLR contribution with PISM-dEBM slightly exceeds 1 m for 1.5 °C GMT above preindustrial (Extended Data Fig. 3). For convergence temperatures $\Delta T_{\text{JJA}} > 2.2$ °C for PISM-dEBM and $\Delta T_{\text{JJA}} > 1.4$ °C for Yelmo-REMBO, the ice sheet is completely lost, regardless of the overshoot temperature in the year AD 2100. The safe zone is sharply separated from the transition area, which is visible as an abrupt transition in the cross-sections of the stability diagram (Fig. 2c,d). Although the ice sheet shows a more gradual loss before the critical threshold with PISM-dEBM (Fig. 2c), the ice loss is more abrupt with Yelmo-REMBO and the SLR contribution is less than 1 m before the critical threshold is crossed (Fig. 2d). Regardless of the model, the ice-sheet equilibrium only depends on the absolute temperature increase by AD 2200, that is, the convergence temperature anomaly, and not the peak value at AD 2100. This can be explained by the slow response timescale of the ice sheet to the temperature change.

For low convergence temperature anomalies, the ice-sheet volume barely changes in simulations with either model. For high warming, the equilibration time is very slow, on the timescale of decamillennia. For intermediate warming levels, the ice sheet does not reach a classical equilibrium in simulations with PISM-dEBM but fluctuates on decamillennial timescales. This is particularly true for the intermediate states close to the threshold of $\Delta T_{\text{JJA}} = 2.2$ °C, which are not in equilibrium after even 100 kyr (triangle symbols in Fig. 2a). Likewise, the simulations with Yelmo-REMBO forced with $\Delta T_{\text{conv,JJA}} = 1.5$ °C are not yet in equilibrium after 100 kyr and eventually evolve further towards the ice-free state (Fig. 2b,d).

Long-term overshoots

To investigate the timescale dependence of the overshoot of the temperature threshold, we decrease the temperature after AD 2100 to different convergence temperatures ranging from $\Delta T_{\text{JJA}} = 0$ °C to 4.0 °C and vary the convergence time to reach the respective convergence temperature from 100 years to several millennia (Fig. 1a). All scenarios considered show a loss of ice volume. As expected, the longer the convergence time and the higher the overshoot temperature, the larger the ice loss. However, there are important dependencies of the ice-sheet evolution (and thus maximum SLR contributions) on the exact convergence times and temperatures (Fig. 3). For a convergence time of 1,000 years, the maximum SLR contribution is similar to the equilibrium and maximum SLR contributions for a 100-year convergence time (Fig. 2 and Extended Data Figs. 3 and 4a,b), implying that the maximum ice loss is reached after the warming and cooling phase. However, an overshoot temperature of $\Delta T_{\text{max,JJA}} > 6.0$ °C leads to a greater maximum SLR contribution than at equilibrium (Extended Data Figs. 3 and 4a,b). Even for a convergence temperature of $\Delta T_{\text{conv,JJA}} = 0$ °C, the maximum SLR contribution exceeds 1 m for the highest overshoot temperature in both models (Fig. 3a,b). For a convergence time of 10,000 years, there is a strong dependence of the maximum SLR contribution on the overshoot temperature (Fig. 3c,d). Both models exceed 1 m SLR contribution for an overshoot temperature $\Delta T_{\text{max,JJA}} > 2.5$ °C in the year AD 2100, given a convergence temperature of $\Delta T_{\text{conv,JJA}} = 0$ °C. For an overshoot temperature of $\Delta T_{\text{max,JJA}} > 6.0$ °C with a subsequent return to present-day conditions, the simulated SLR contribution is at least 5 m with PISM-dEBM and 7 m with Yelmo-REMBO.

For a convergence temperature of $\Delta T_{\text{conv,JJA}} = 0$ °C, we find that, for all scenarios, the ice sheet eventually returns to values close to the present-day ice volume in both models (Fig. 4). For the short-term overshoots ($\Delta t_{\text{conv}} < 500$ years), the models show very similar SLR contributions and the maximum ice-volume loss before ice-sheet regrowth is in the range of 50 cm SLR equivalent (Fig. 4a,b). For a convergence time of 1,000 years, the SLR contribution is less than 1.25 m with either model, followed by a recovery to the present-day ice sheet. For convergence times of more than 5,000 years, a complete loss of the ice sheet can occur before recovery, with a SLR contribution of 7 m (Fig. 4c,d). Although Yelmo-REMBO shows a complete loss of the ice sheet, before regrowth, for the highest overshoot temperatures and a convergence time of 5,000 years, PISM-dEBM only shows a complete loss, before recovery, for a convergence time of 10,000 years, regardless of the convergence temperature (Fig. 5a,b).

For higher convergence temperatures, the GrIS does not necessarily return to its present-day ice volume, highlighting the potential practical irreversibility caused by the hysteresis of the ice sheet (Fig. 5c,d). With PISM-dEBM, the ice sheet approaches the intermediate states noted above. The ice-volume loss at equilibrium gradually increases with increasing convergence temperature, reaching up to 25% of the present-day ice volume for a convergence temperature of $\Delta T_{\text{conv,JJA}} = 2.2$ °C. However, with PISM-dEBM, the ice sheet always recovers to the equivalent equilibrium, as for a simple ramp-up simulation (which we will refer to as the reference simulation hereafter; black lines in Fig. 5) for a given temperature anomaly. In simulations with Yelmo-REMBO, the ice sheet does not always regrow to the same ice volume corresponding to the reference simulation (Fig. 5d). Close to the threshold, the ice sheet shows a dependence on the convergence time. A convergence time greater than 5,000 years, combined with a high overshoot temperature, prevents regrowth of the ice sheet even below the critical threshold (Extended Data Fig. 4d). For a convergence temperature of $\Delta T_{\text{conv,JJA}} = 0.5$ °C and long convergence times, the ice sheet regrows to an intermediate state with around 2 m SLR contribution after a complete loss (Fig. 5d).

For all scenarios, the maximum SLR contribution strongly depends on the maximum temperature, the convergence temperature and the

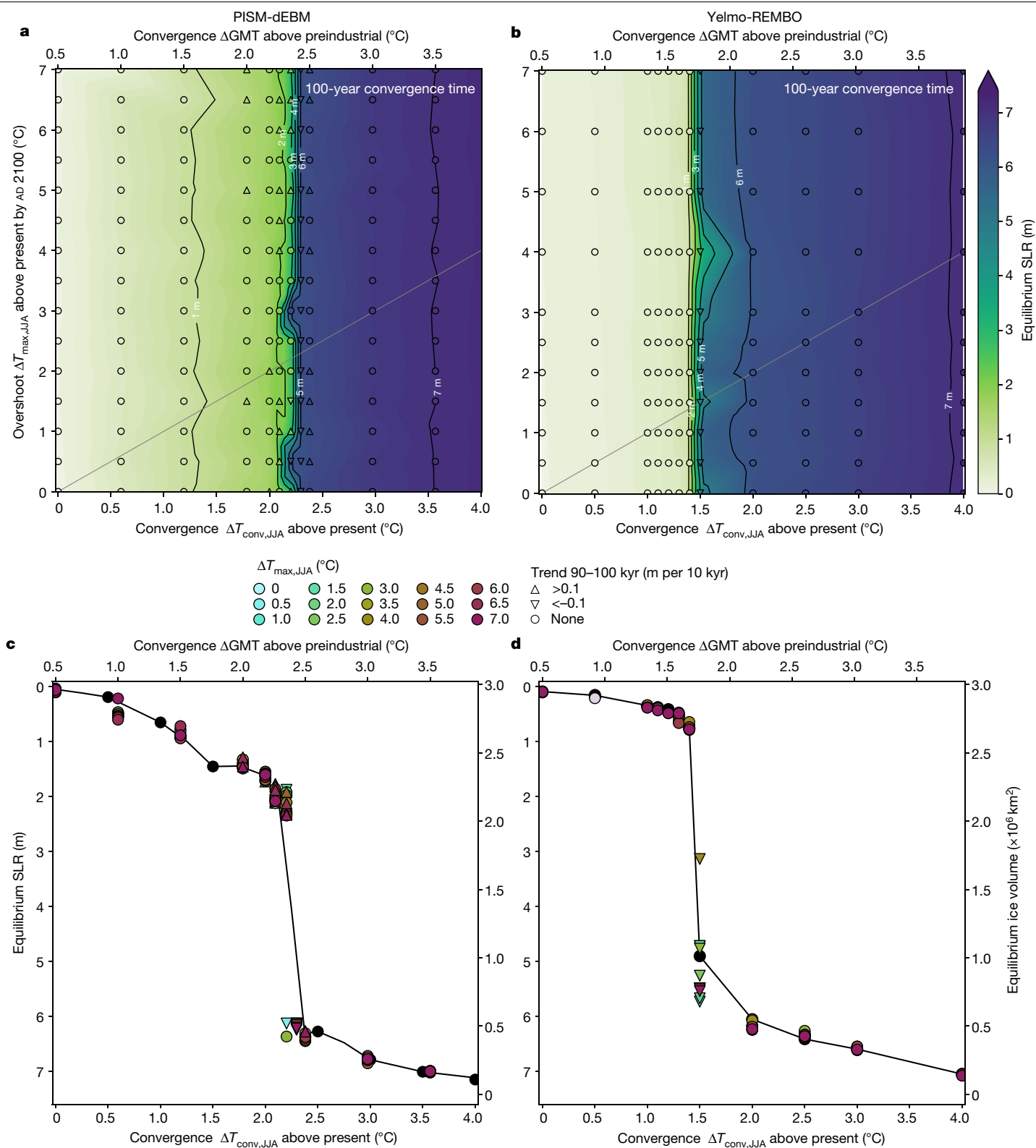


Fig. 2 | Stability diagram of the GrIS after warming and subsequent cooling. **a**, Stability diagram of the GrIS for PISM-dEBM. Different warming rates are applied for 100 years, followed by various cooling rates for another 100 years. The temperature is kept constant afterwards for another 100 kyr. White regions indicate a present-day-like ice sheet, green–blue regions mark intermediate states and purple corresponds to the ice-free state. The grey line corresponds to the warming rates at which the overshoot temperature equals the convergence temperature (that is, no mitigation; the time series of simulations along the grey line is depicted in Fig. 1). Below the grey line,

the overshoot temperature in year AD 2100 is smaller than the convergence temperature in AD 2200. Corresponding time series of every simulation are shown in Extended Data Fig. 5. **b**, Same as **a** but for Yelmo-REMBO. **c**, Cross-sections of the stability diagram for all applied overshoot temperatures indicated on the y axis of **a**. A sharp decrease of the ice volume can be inferred for $\Delta T_{conv,JJA}$ above $2.2^{\circ}C$ in all cross-sections, resulting in several intermediate and ice-free GrIS states. **d**, Same as **c** but for Yelmo-REMBO, for which the critical temperature is around $\Delta T_{conv,JJA} = 1.4^{\circ}C$. The triangles mark simulations that have still not converged during the time span from 90 kyr to 100 kyr (see legend).

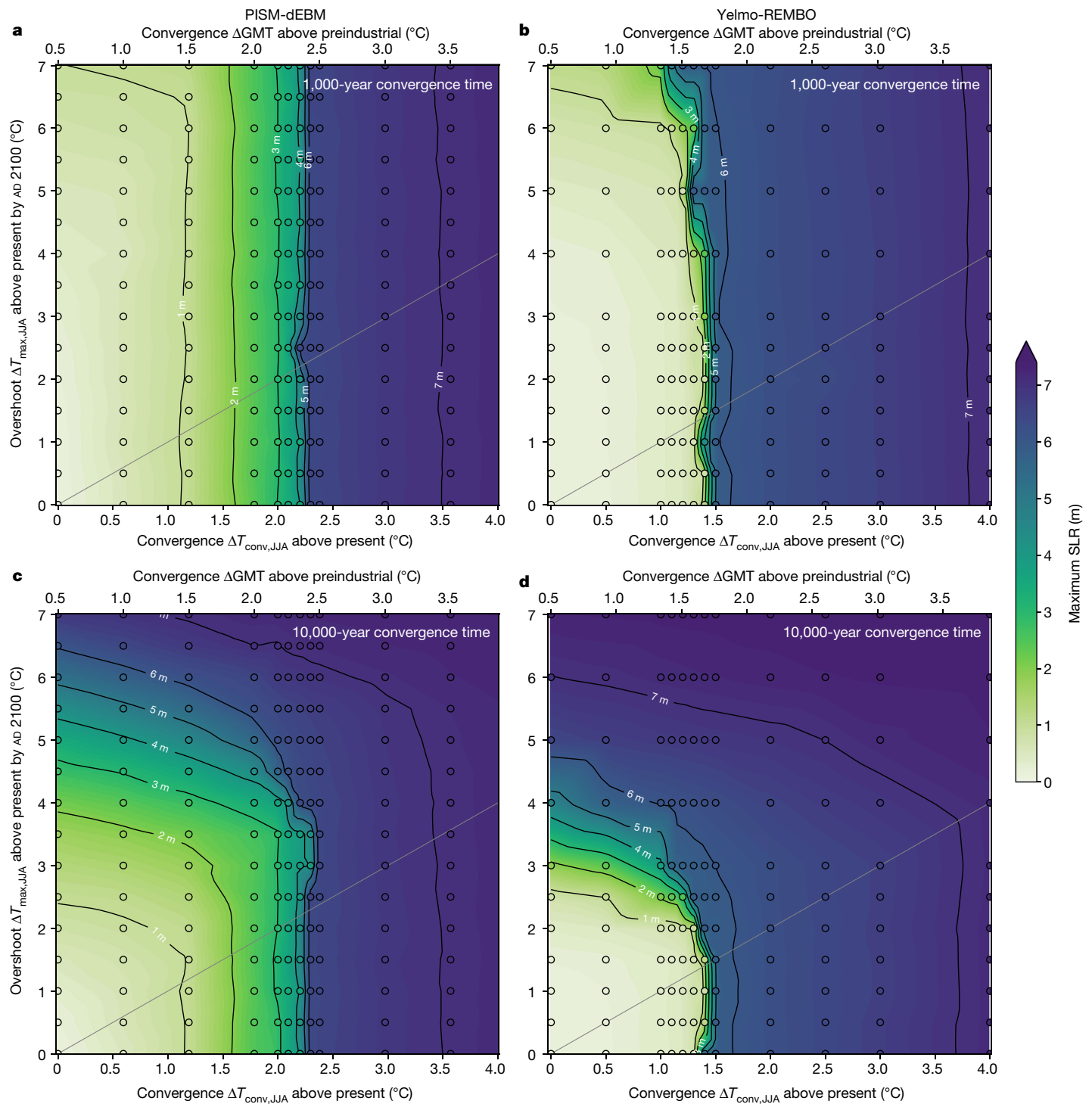


Fig. 3 | Maximum SLR contribution of the GrIS after warming and subsequent cooling for two different convergence times. **a**, Maximum SLR contribution of the GrIS for PISM-dEBM, for 1,000 years convergence time. Different warming rates are applied for 100 years, followed by various cooling rates for a convergence time of 1,000 years. The temperature is kept constant afterwards for another 100 kyr. **b**, Same as **a** but for Yelmo-REMBO. **c,d**, Same as

a,b, respectively, but for a convergence time of 10,000 years. The maximum SLR contribution shows a clear dependence on the overshoot temperature. White regions indicate a present-day-like ice sheet, green–blue regions mark intermediate states and purple corresponds to the near-ice-free state. The grey lines correspond to the scenarios for which the overshoot temperature equals the convergence temperature.

convergence time (Fig. 5). Generally, the larger the maximum temperature, the convergence time and the convergence temperature, the larger the maximum SLR contribution. The longer the convergence times, the stronger the dependence of the maximum SLR contribution on the overshoot temperature (Fig. 6). Our key result is that, regardless of the model used, it is possible to define safe and unsafe scenarios dependent on a chosen target maximum SLR contribution.

For example, we find that a convergence time shorter than 1,000 years with a convergence temperature around $\Delta T_{\text{conv,JJA}} = 0^\circ\text{C}$ keeps the GrIS SLR contribution below 2 m for all overshoot temperatures (Fig. 6) with both models. For overshoot temperatures below the critical threshold, the maximum SLR contribution is weakly dependent on the convergence time, which is not surprising given that the maximum SLR contribution for a given maximum temperature anomaly

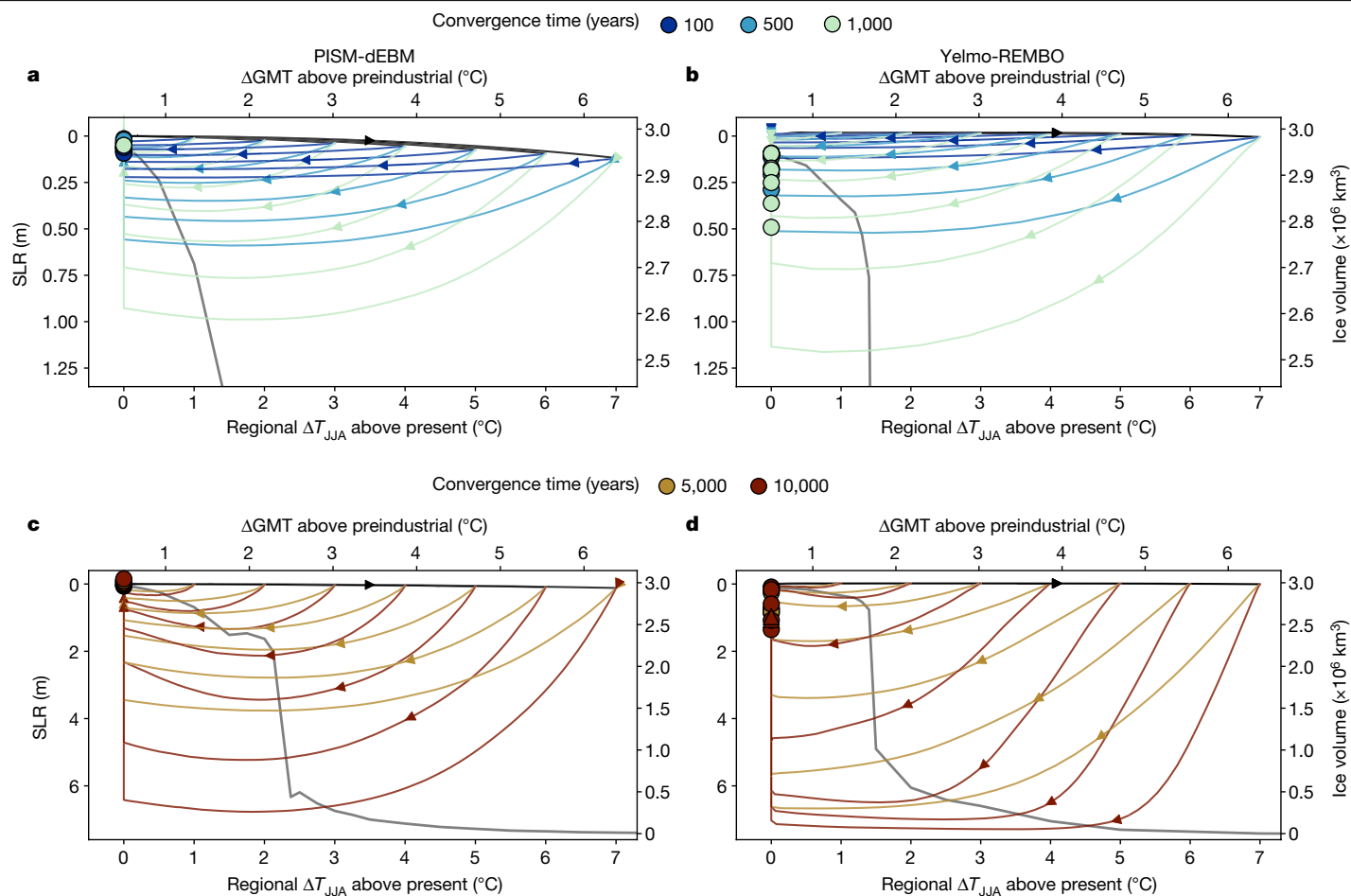


Fig. 4 | Trajectories of overshoot scenarios converging to a regional summer temperature of 0°C above present (0.5°C GMT above preindustrial level) for various peak warmings and convergence times. a, Trajectories of ice-sheet volume for PISM-dEBM for convergence times of 100, 500 and 1,000 years. All three scenarios show an ice loss that reaches its maximum during the cooling phase. The apparent jump of the end states (dots) at $\Delta T_{JJA} = 0^\circ\text{C}$ corresponds to a recovery of the ice sheet after the cooling phase. The end states are defined as the mean ice volume after 90–100 kyr. The thick

dark grey line corresponds to the equilibrium states for the applied temperature anomaly, showing that the actual, realistic trajectories are strongly out of equilibrium. **b,** Same as **a** but for the ice-sheet model Yelmo-REMBO. **c, d,** Same as **a, b**, respectively, but for convergence times of 5,000 and 10,000 years. For all scenarios, both models show a recovery to close to the present-day ice sheet. The maximum SLR contribution is reached during the cooling phase, highlighting the importance of considering long-term committed SLR in climate negotiations.

is generally equal to or lower than the equilibrium SLR contribution of that forcing value (Fig. 3).

Discussion

We use two different state-of-the-art ice-sheet-modelling approaches, with varying complexity, and show that the results obtained from both approaches are consistent, despite the fact that the feedbacks captured by the models differ to some extent. We use a recently published version of PISM that is driven at the surface by the dEBM (PISM-dEBM) to capture surface albedo feedbacks. This improves on the more conventional positive degree-day parameterization, which might fail for past and future climate conditions^{35–39}. Increased surface melt reduces reflectivity of the ice-sheet surface and hence leads to an increase in the melt rates, which is captured by the dEBM. Although the extra atmospheric warming that can result from reducing albedo is not captured by this model setup, Yelmo-REMBO includes this feedback as the atmosphere is dynamically coupled to the snowpack energy balance. Possible negative atmospheric feedbacks that have been shown to potentially decelerate the ice loss are also not included in PISM-dEBM. It has been shown that changes in cloud cover, circulation patterns and precipitation lead to increased accumulation in the high-altitude, cold interior of the ice sheet and can increase the critical temperature threshold⁵. However,

Yelmo-REMBO includes a dynamic albedo simple atmosphere that produces increased precipitation following the retreating ice-sheet margin and therefore captures the negative feedbacks at least to some degree. Nevertheless, we propose to extend the work presented here to a setup with a fully coupled, comprehensive atmosphere general circulation model as an interesting follow-up study.

It has recently been shown that, to some extent, glacial isostatic adjustment can counteract the positive feedbacks that are believed to cause a hysteresis of the GrIS with global warming, such as the melt-elevation feedback and albedo feedback³⁴. However, the timescale of this feedback is still debated^{40,41} and is often neglected on sub-millennial timescales³. The fluctuations of the ice sheet on a decamillennial timescale simulated by PISM-dEBM are believed to be the consequence of an interplay between bedrock uplift and melt-elevation feedback^{34,42}. We find that the intermediate GrIS states found with PISM-dEBM are at least partially caused by the interplay between the glacial isostatic adjustment and melt-elevation feedback and we find fewer intermediate states without bedrock uplifting (Extended Data Fig. 6e). Palaeoclimatic simulations of the Pliocene GrIS show similar intermediate states as seen with PISM-dEBM⁴². By strong contrast, however, Yelmo-REMBO uses the same Earth deformation model and we do not observe similar oscillations with this model. This may point to a different balance between positive feedbacks (largely

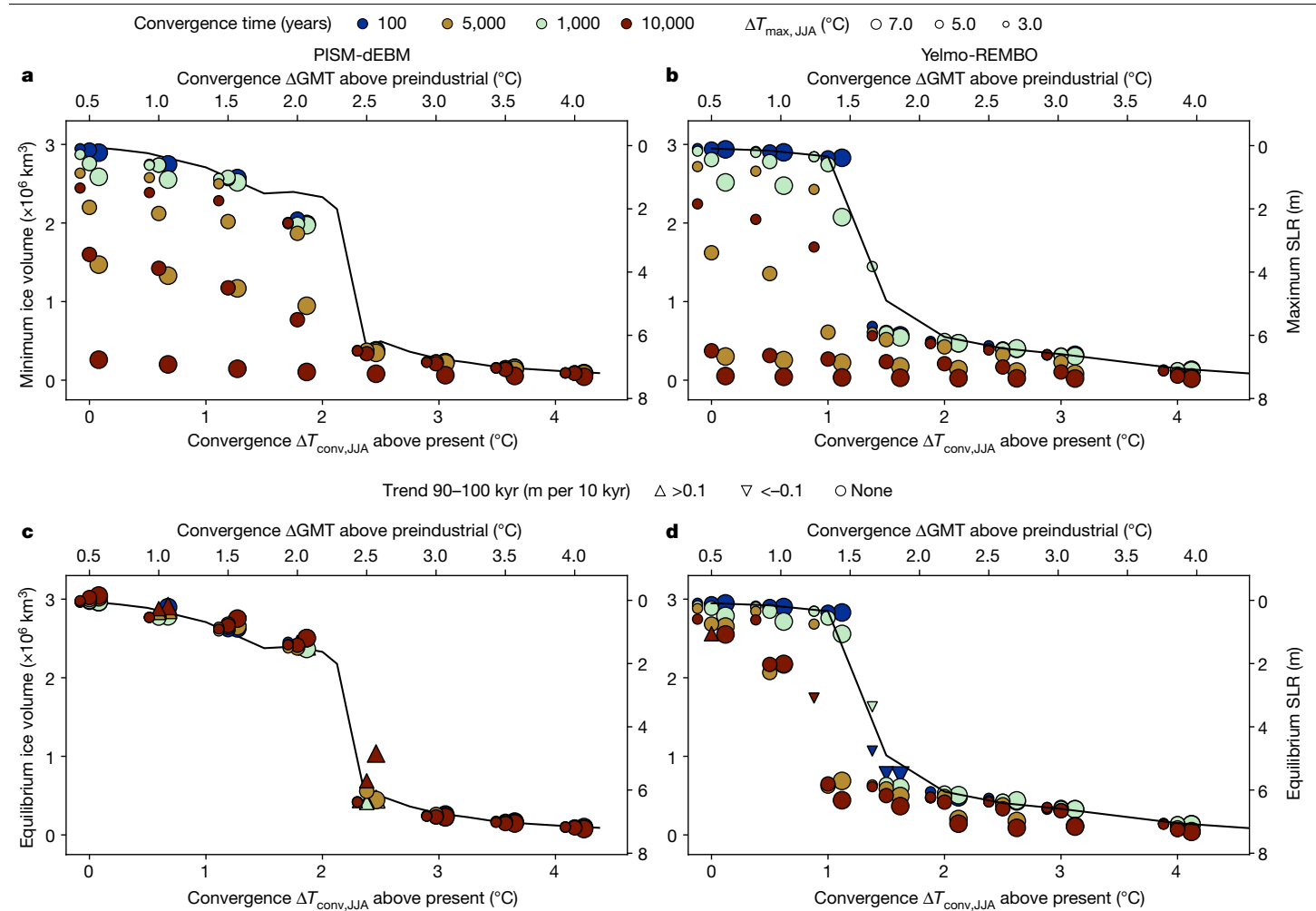


Fig. 5 | Minimum and equilibrium ice volume for different overshoot scenarios. **a**, Minimum ice volume and maximum SLR contribution for different convergence temperatures ($\Delta T_{\text{conv,JJA}}$) between 0 °C and 4.0 °C above present, overshoot temperatures between $\Delta T_{\text{max,JJA}} = 3.0$ °C and 7.0 °C and convergence times between 100 and 10,000 years for PISM-dEBM. For higher overshoot temperatures and longer convergence times, the minimum ice volume is lower. A convergence time of 10,000 years leads to a complete, temporary loss of the GrIS for all overshoot temperatures. The black line corresponds to the equilibrium reference simulation without any

temperature decrease. **b**, Same as **a** but for Yelmo-REMBO. The behaviour is similar to PISM-dEBM except for the fact that a complete temporary GrIS loss is already possible for shorter convergence times of 5,000 years. **c,d**, Same as **a,b**, respectively, but for the ice volume after 90–100 kyr. The triangles denote simulations that still show a trend after 100 kyr. The ice sheet regrows to the reference simulation in all cases with PISM-dEBM but not with Yelmo-REMBO. The latter shows a temperature range of roughly 0.5 °C below the critical threshold, which shows irreversibility after a complete loss of the GrIS.

at the surface) and the glacial isostatic rebound and should certainly be studied with more models in future work.

Our temperature thresholds are in accordance with previous work^{4,6,8,43–45} and agree with the general consensus that limiting global warming below the range of 1.5–2.5 °C above preindustrial levels can prevent the most severe consequences^{6,8}. However, we do not aim to give a precise threshold value for the safe zone but rather to show that it is possible to mitigate a critical loss of the GrIS and the associated SLR contribution if efforts are made to (1) prevent extreme warming by AD 2100 and (2) reduce the temperature after a reasonable time, that is, centuries. Failing in either of these efforts can result in large SLR contributions from the GrIS even for convergence temperatures of between 0 and 1.5 °C above preindustrial.

Notably, in the warming-only experiments, we find that several intermediate stable states of the GrIS are accessible with PISM-dEBM as temperatures increase before the remaining ice sheet is lost abruptly, but not with Yelmo-REMBO. This seems, therefore, to be a model-dependent behaviour that is a result of applying different ice dynamics, climatic forcing and interactions within the system. It is clear that the existence of the intermediate states facilitates reversibility of

the ice loss before the final threshold is crossed with PISM-dEBM. In previous studies that investigate the short-term response of the GrIS to global warming, it has been shown that future projections can differ substantially across models^{10,11}. Yet, we find qualitatively remarkably similar behaviour with both models used here. A coordinated model intercomparison following an experimental setup such as the one used here would help to constrain the uncertainty in potential critical thresholds and the long-term future ice-sheet evolution.

Our simulations are restricted to horizontal resolutions of 16–20 km, which means that small-scale processes are not well represented. The choice of this resolution was because of computational constraints and the large number of simulations. However, we are mostly interested in the large-scale evolution of the GrIS on decamillennial timescales. Previous work has shown that the chosen resolutions give similar results to higher-spatial-resolution simulations³, so we expect that our conclusions are robust. Nonetheless, this should be a target for future work.

Long-term climate projections for Greenland remain uncertain, as most Earth-system-model simulations typically end by the year AD 2100 (ref. 46). Although we based our estimate of Arctic amplification on Coupled Model Intercomparison Project (CMIP) Phase 6 (CMIP6)

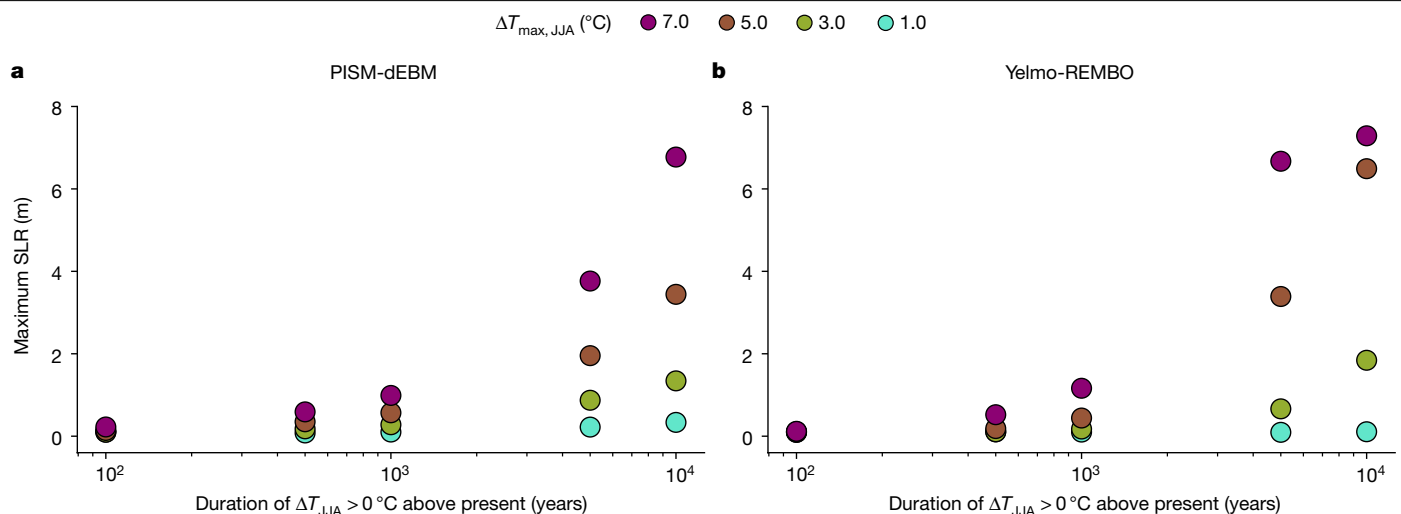


Fig. 6 | Maximum SLR contribution for different overshoot scenarios with a convergence GMT of 0.5 °C above preindustrial (corresponding to $\Delta T_{\text{JJA}} = 0$ °C above present). **a**, Maximum SLR contribution for four different overshoot temperatures and convergence times, up to 10,000 years. **b**, Same as **a** but for Yelmo-REMBO. On timescales of less than 1,000 years,

the models show a maximum SLR contribution of less than 2 m for all overshoot temperatures. An overshoot temperature of less than 3 °C prevents a SLR contribution of more than 2 m. On long timescales, Yelmo-REMBO shows a slightly higher SLR contribution for high overshoot temperatures than PISM-dEBM.

models, there is considerable uncertainty about the extent of future warming in the Arctic. Recently, it has been shown that the Arctic warms four times faster than the global average and thus substantially exceeds previous estimates and projections from climate models⁴⁷. Arctic amplification of this magnitude would reduce the safe space for the GrIS substantially. However, surface temperatures around Greenland might not increase that severely in the future^{47,48}. On multimillennial timescales, there may be substantial changes in global climate, atmosphere and ocean circulation that are hard to quantify today. For example, a weakening AMOC leads to decreasing Greenland temperatures^{13,49}, which could help to restabilize the ice sheet. However, at the same time, a weakening of the AMOC is expected to decrease precipitation over Greenland^{13,49}, which could lead to the opposite effect and destabilize the GrIS even more. These further interactions should be tackled in the future by Earth system models with interactive ice-sheet components.

The potential irreversibility of a loss of the GrIS is an important concern^{8,50}. Our results show that mitigation of an ice-sheet loss is possible if temperatures are reduced relatively quickly after a temporary overshoot. We find several stable intermediate ice-sheet configurations with PISM-dEBM that return to the present-day state if the climate returns to present-day conditions. However, if longer time spans are needed to cool down to a relatively safe convergence GMT of, for example, 1.0 °C, the SLR contribution from the GrIS can still exceed several metres for thousands of years. With Yelmo-REMBO, there is a temperature range of 0.5 °C below the threshold that shows irreversibility; even if the convergence temperature is below the critical threshold after an initial overshoot, the GrIS does not regrow. This emphasizes the risk of an irreversible ice-sheet loss for long-term overshoot scenarios. Moreover, total runoff amounts would still be substantial even for a reversible ice-sheet loss, with possibly severe consequences for the AMOC⁵¹. Remarkably, the timescale of ice loss relative to their respective thresholds agrees very well across the two models used here. It should be emphasized nevertheless that quantitative differences between the two ice-sheet models are present and should be investigated in the future.

We find a threshold for an abrupt, complete loss of the GrIS around 2.3 °C GMT above preindustrial level with PISM-dEBM and 1.7 °C GMT above preindustrial level with Yelmo-REMBO, which is in agreement with previously reported critical temperatures for the GrIS^{4,6,43–45}. We show that a transition to an ice-free GrIS state can be avoided in

scenarios that overshoot this critical temperature threshold, as long as the temperature anomaly is subsequently reduced sufficiently quickly. Our results highlight the critical role of warming and cooling rates as well as the maximum and convergence temperatures. In our simulations, southwestern Greenland is most sensitive to temperature changes and primarily determines the spatial extent of the potential intermediate states. However, even without an irreversible transition to a new stable ice-sheet state, the intermediate SLR contribution from the GrIS can exceed several metres, depending on the warming and cooling rate, as well on as the convergence temperature.

Online content

Any methods, additional references, Nature Portfolio reporting summaries, source data, extended data, supplementary information, acknowledgements, peer review information; details of author contributions and competing interests; and statements of data and code availability are available at <https://doi.org/10.1038/s41586-023-06503-9>.

1. IPCC: Summary for Policymakers. In *Climate Change 2021: Mitigation of Climate Change* (eds Allan, R. P. et al.) (Cambridge Univ. Press, 2021).
2. Levermann, A. & Winkelmann, R. A simple equation for the melt elevation feedback of ice sheets. *Cryosphere* **10**, 1799–1807 (2016).
3. Aschwanden, A. et al. Contribution of the Greenland Ice Sheet to sea level over the next millennium. *Sci. Adv.* **5**, eaav9396 (2019).
4. Pattyn, F. et al. The Greenland and Antarctic ice sheets under 1.5 °C global warming. *Nat. Clim. Change* **8**, 1053–1061 (2018).
5. Gregory, J. M., George, S. E. & Smith, R. S. Large and irreversible future decline of the Greenland ice sheet. *Cryosphere* **14**, 4299–4322 (2020).
6. Robinson, A., Calov, R. & Ganopolski, A. Multistability and critical thresholds of the Greenland ice sheet. *Nat. Clim. Change* **2**, 429–432 (2012).
7. Rietbroek, R., Brunnabend, S.-E., Kusche, J., Schröter, J. & Dahle, C. Revisiting the contemporary sea-level budget on global and regional scales. *Proc. Natl Acad. Sci. USA* **113**, 1504–1509 (2016).
8. Armstrong McKay, D. I. et al. Exceeding 1.5°C global warming could trigger multiple climate tipping points. *Science* **377**, eabn7950 (2022).
9. Gregory, J. M., Huybrechts, P. & Raper, S. C. B. Threatened loss of the Greenland ice-sheet. *Nature* **428**, 616–616 (2004).
10. Goelzer, H. et al. The future sea-level contribution of the Greenland ice sheet: a multi-model ensemble study of ISMIP6. *Cryosphere* **14**, 3071–3096 (2020).
11. Seroussi, H. et al. ISMIP6 Antarctica: a multi-model ensemble of the Antarctic ice sheet evolution over the 21st century. *Cryosphere* **14**, 3033–3070 (2020).
12. Edwards, T. L. et al. Projected land ice contributions to twenty-first-century sea level rise. *Nature* **593**, 74–82 (2021).
13. Jackson, L. C. et al. Global and European climate impacts of a slowdown of the AMOC in a high resolution GCM. *Clim. Dyn.* **45**, 3299–3316 (2015).

14. Caesar, L., Rahmstorf, S., Robinson, A., Feulner, G. & Saba, V. Observed fingerprint of a weakening Atlantic Ocean overturning circulation. *Nature* **556**, 191–196 (2018).
15. Boers, N. Observation-based early-warning signals for a collapse of the Atlantic Meridional Overturning Circulation. *Nat. Clim. Change* **11**, 680–688 (2021).
16. Boers, N., Ghil, M. & Stocker, T. F. Theoretical and paleoclimatic evidence for abrupt transitions in the Earth system. *Environ. Res. Lett.* **17**, 093006 (2022).
17. Trusel, L. D. et al. Nonlinear rise in Greenland runoff in response to post-industrial Arctic warming. *Nature* **564**, 104–108 (2018).
18. Boers, N. & Rypdal, M. Critical slowing down suggests that the western Greenland Ice Sheet is close to a tipping point. *Proc. Natl Acad. Sci. USA* **118**, e2024192118 (2021).
19. Rogelj, J. et al. Energy system transformations for limiting end-of-century warming to below 1.5 °C. *Nat. Clim. Change* **5**, 519–527 (2015).
20. Raftery, A. E., Zimmer, A., Frierson, D. M. W., Startz, R. & Liu, P. Less than 2 °C warming by 2100 unlikely. *Nat. Clim. Change* **7**, 637–641 (2017).
21. Tong, D. et al. Committed emissions from existing energy infrastructure jeopardize 1.5 °C climate target. *Nature* **572**, 373–377 (2019).
22. Azar, C., Johansson, D. J. A. & Mattsson, N. Meeting global temperature targets—the role of bioenergy with carbon capture and storage. *Environ. Res. Lett.* **8**, 034004 (2013).
23. Ritchie, P. D. L., Clarke, J. J., Cox, P. M. & Huntingford, C. Overshooting tipping point thresholds in a changing climate. *Nature* **592**, 517–523 (2021).
24. Winkelmann, R. et al. The Potsdam Parallel Ice Sheet Model (PISM-PIK) – part 1: model description. *Cryosphere* **5**, 715–726 (2011).
25. Zeitz, M., Reese, R., Beckmann, J., Krebs-Kanzow, U. & Winkelmann, R. Impact of the melt–albedo feedback on the future evolution of the Greenland Ice Sheet with PISM-dEBM-simple. *Cryosphere* **15**, 5739–5764 (2021).
26. Robinson, A. et al. Description and validation of the ice-sheet model Yelmo (version 1.0). *Geosci. Model Dev.* **13**, 2805–2823 (2020).
27. Robinson, A., Calov, R. & Ganopolski, A. An efficient regional energy-moisture balance model for simulation of the Greenland Ice Sheet response to climate change. *Cryosphere* **4**, 129–144 (2010).
28. Tabone, I., Blasco, J., Robinson, A., Alvarez-Solas, J. & Montoya, M. The sensitivity of the Greenland Ice Sheet to glacial–interglacial oceanic forcing. *Clim. Past* **14**, 455–472 (2018).
29. Blasco, J., Tabone, I., Alvarez-Solas, J., Robinson, A. & Montoya, M. The Antarctic Ice Sheet response to glacial millennial-scale variability. *Clim. Past* **15**, 121–133 (2019).
30. Garbe, J., Albrecht, T., Levermann, A., Donges, J. F. & Winkelmann, R. The hysteresis of the Antarctic Ice Sheet. *Nature* **585**, 538–544 (2020).
31. Albrecht, T., Winkelmann, R. & Levermann, A. Glacial-cycle simulations of the Antarctic Ice Sheet with the Parallel Ice Sheet Model (PISM) – part 2: parameter ensemble analysis. *Cryosphere* **14**, 633–656 (2020).
32. Garbe, J., Zeitz, M., Krebs-Kanzow, U. & Winkelmann, R. The evolution of future Antarctic surface melt using PISM-dEBM-simple. *Cryosphere Discuss.* <https://doi.org/10.5194/tc-2022-249> (2023).
33. Solgaard, A. M. & Langen, P. L. Multistability of the Greenland ice sheet and the effects of an adaptive mass balance formulation. *Clim. Dyn.* **39**, 1599–1612 (2012).
34. Zeitz, M., Haacker, J. M., Donges, J. F., Albrecht, T. & Winkelmann, R. Dynamic regimes of the Greenland Ice Sheet emerging from interacting melt-elevation and glacial isostatic adjustment feedbacks. *Earth Syst. Dyn.* **13**, 1077–1096 (2022).
35. Bougamont, M. et al. Impact of model physics on estimating the surface mass balance of the Greenland ice sheet. *Geophys. Res. Lett.* **34**, L17501 (2007).
36. Bauer, E. & Ganopolski, A. Comparison of surface mass balance of ice sheets simulated by positive-degree-day method and energy balance approach. *Clim. Past* **13**, 819–832 (2017).
37. Krebs-Kanzow, U., Gierz, P. & Lohmann, G. Brief communication: an ice surface melt scheme including the diurnal cycle of solar radiation. *Cryosphere* **12**, 3923–3930 (2018).
38. Rückamp, M., Falk, U., Frieler, K., Lange, S. & Humbert, A. The effect of overshooting 1.5 °C global warming on the mass loss of the Greenland ice sheet. *Earth Syst. Dyn.* **9**, 1169–1189 (2018).
39. Krebs-Kanzow, U. et al. The diurnal Energy Balance Model (dEBM): a convenient surface mass balance solution for ice sheets in Earth system modeling. *Cryosphere* **15**, 2295–2313 (2021).
40. Barletta, V. R. et al. Observed rapid bedrock uplift in Amundsen Sea Embayment promotes ice-sheet stability. *Science* **360**, 1335–1339 (2018).
41. Whitehouse, P. L., Gomez, N., King, M. A. & Wiens, D. A. Solid Earth change and the evolution of the Antarctic Ice Sheet. *Nat. Commun.* **10**, 503 (2019).
42. Koenig, S. J. et al. Ice sheet model dependency of the simulated Greenland Ice Sheet in the mid-Pliocene. *Clim. Past* **11**, 369–381 (2015).
43. Van Breedam, J., Goelzer, H. & Huybrechts, P. Semi-equilibrated global sea-level change projections for the next 10 000 years. *Earth Syst. Dyn.* **11**, 953–976 (2020).
44. Noël, B., van Kampenhout, L., Lenaerts, J. T. M., van de Berg, W. J. & van den Broeke, M. R. A 21st century warming threshold for sustained Greenland ice sheet mass loss. *Geophys. Res. Lett.* **48**, e2020GL090471 (2021).
45. Höning, D. et al. Multistability and transient response of the Greenland ice sheet to anthropogenic CO₂ emissions. *Geophys. Res. Lett.* **50**, e2022GL101827 (2023).
46. Eyring, V. et al. Overview of the Coupled Model Intercomparison Project Phase 6 (CMIP6) experimental design and organization. *Geosci. Model Dev.* **9**, 1937–1958 (2016).
47. Rantanen, M. et al. The Arctic has warmed nearly four times faster than the globe since 1979. *Commun. Earth Environ.* **3**, 168 (2022).
48. Nowicki, S. et al. Experimental protocol for sea level projections from ISMIP6 stand-alone ice sheet models. *Cryosphere* **14**, 2331–2368 (2020).
49. Liu, W., Fedorov, A. V., Xie, S.-P. & Hu, S. Climate impacts of a weakened Atlantic Meridional Overturning Circulation in a warming climate. *Sci. Adv.* **6**, eaaz4876 (2020).
50. Sommers, A. N. et al. Retreat and regrowth of the Greenland Ice Sheet during the Last Interglacial as simulated by the CESM2-CISM2 coupled climate–ice sheet model. *Paleoceanogr. Paleoclimatol.* **36**, e2021PA004272 (2021).
51. Jackson, L. C. et al. Understanding AMOC stability: the North Atlantic Hosing Model Intercomparison Project. *Geosci. Model Dev.* **16**, 1975–1995 (2023).
52. *Cartopy: A Cartographic Python Library with a Matplotlib Interface* (Met Office, Cartopy, 2010); <https://scitools.org.uk/cartopy>

Publisher's note Springer Nature remains neutral with regard to jurisdictional claims in published maps and institutional affiliations.



Open Access This article is licensed under a Creative Commons Attribution 4.0 International License, which permits use, sharing, adaptation, distribution and reproduction in any medium or format, as long as you give appropriate credit to the original author(s) and the source, provide a link to the Creative Commons licence, and indicate if changes were made. The images or other third party material in this article are included in the article's Creative Commons licence, unless indicated otherwise in a credit line to the material. If material is not included in the article's Creative Commons licence and your intended use is not permitted by statutory regulation or exceeds the permitted use, you will need to obtain permission directly from the copyright holder. To view a copy of this licence, visit <http://creativecommons.org/licenses/by/4.0/>.

© The Author(s) 2023, corrected publication 2023

Methods

PISM-dEBM-simple

We use the open-source, state-of-the-art PISM version v1.2-41-g53a9818 with the dEBM-simple surface mass balance module and parameterized climate forcing. PISM is a three-dimensional, thermomechanically coupled ice-sheet/ice-shelf model that combines the shallow-ice approximation (SIA) and shallow-shelf approximation (SSA) of the non-Newtonian Stokes model. This hybrid SSA + SIA approach permits modelling of the whole domain from the ice-sheet flow zone with grounded ice to the ice-shelf flow zones in an appropriate manner²⁴. The ice rheology is based on the Glen–Paterson–Budd–Lliboutry–Duval flow law⁵³ with an exponent of $n = 3$ with the enhancement factors $E_{SSA} = 1$ and $E_{SIA} = 3$ for the SSA and SIA flow, respectively.

We use a pseudo-plastic sliding law⁵⁴ of the form

$$\boldsymbol{\tau}_b = -\tau_c \frac{\mathbf{u}}{u_0^q |\mathbf{u}|^{1-q}},$$

with the basal shear stress $\boldsymbol{\tau}_b$, basal sliding velocity \mathbf{u} , yield stress τ_c and a threshold velocity u_0 . We chose $q = 0.5$ and a threshold velocity of $u_0 = 100 \text{ m year}^{-1}$ for our simulations.

The yield stress is determined by the Mohr–Coulomb criterion⁵⁵

$$\tau_c = c_0 + (\tan\phi) N_{\text{till}}$$

that connects the effective pressure N_{till} , a material property field ϕ (till friction angle) and the till cohesion c_0 . The effective pressure N_{till} is determined by the subglacial hydrology model, the till friction angle ϕ is a piecewise linear function of bed elevation⁵⁶ and the till cohesion c_0 is set to 0.

We model the deformation of the Earth owing to the changes in the ice load using the Lingle–Clark model^{57,58}. The model is described by a purely elastic lithosphere with a flexural rigidity of $5 \times 10^{24} \text{ N m}^{-1}$ and the upper mantle is represented as a three-dimensional viscous half-space with a viscosity of $10^{21} \text{ Pa s}^{-1}$. The model uses a time-dependent partial differential equation that generalizes and improves on the standard elastic plate lithosphere model (ELRA)⁵⁸.

To calculate the surface mass balance, we use a recently developed dEBM-simple²⁵. The dEBM-simple is a modified version of the earlier introduced full dEBM^{37,39}. We use the standard parameters used by Zeitz et al.²⁵, except for the coefficients c_1 and c_2 , which calibrate the energy balance of the snowpack in the melt equation. These we set to $c_1 = 20 \text{ W m}^{-2} \text{ K}$ and $c_2 = -50 \text{ W m}^{-2}$, based on an optimization of the product of temporal and spatial root-mean-square error of the surface mass balance with regards to the MARv3.12 regional climate model surface mass balance from 1980 to 2000 (ref. 59). We keep the orbital parameters fixed to the present-day values²⁵. The transmissivity of the atmosphere is given by a linear function and assumed not to change in future climate. For an extensive description of the dEBM and the implementation in PISM, see refs. 25,37,39.

The present-day near-surface temperature and precipitation rates are given by climatological means (monthly 1980–2000) from the regional climate model MARv3.12 (ref. 59). We apply an elevation-dependent correction of the surface temperature and precipitation, imposing a lapse rate of $\Gamma = 6 \text{ K km}^{-1}$. The precipitation P changes 3.6% per degree of temperature change. The change of precipitation with increasing temperature is derived from a linear fit of the mean annual precipitation against surface air temperature from 37 CMIP6 SSP585 runs (Extended Data Table 2). We use the default spatiotemporal constant ocean boundary conditions with a constant sub-shelf melt rate of 0.05 m year^{-1} .

Our simulations are initialized from a reference equilibrium state of the GrIS that resembles the present-day configuration. We show the ice-surface elevation and ice-surface velocity deviation from observational data in Extended Data Fig. 7. To obtain our reference

state, we bootstrap the ice-sheet model from present-day conditions, including ice thickness and bedrock elevation, taken from BedMachine v5 (refs. 56,60), and basal heat flux⁶¹, as well as climatological mean (monthly 1980–2000) surface temperature and precipitation taken from the regional climate model MARv3.12 (ref. 59). We run the model until an equilibrium state is reached, but for at least 50,000 years. All simulations were performed on a regular rectangular grid with a horizontal resolution of 20 km and an equally spaced grid in the vertical direction with a resolution of 40 m.

We normalize the ice volume such that the initial volume corresponds to the observed ice volume of 7.42 m sea-level equivalent in all plots⁵⁶.

Yelmo-REMBO

The ice-sheet model Yelmo²⁶ resolves ice dynamics by means of the higher-order DIVA solver⁶². Thermodynamics are linked to dynamics by means of effective viscosity, which is determined with a Glen's flow law formulation ($n = 3$) and enhancement factors in the shearing, streaming and floating regimes of 3, 1 and 0.7, respectively. The basal friction is determined with a regularized Coulomb law⁶³ of the form

$$\boldsymbol{\tau}_b = -c_b \left(\frac{|\mathbf{u}_b|}{|\mathbf{u}_b| + u_0} \right)^q \frac{\mathbf{u}_b}{|\mathbf{u}_b|},$$

with $u_0 = 100 \text{ m year}^{-1}$ and $q = 0.2$. $c_b = c_0 + (\tan\phi) N_{\text{till}}$ is the basal yield stress (Pa), in which N_{till} is the effective pressure at the base and ϕ represents the material strength of the bed as a till friction angle. As in PISM, $c_0 = 0$ and ϕ is set as a piecewise linear function of bedrock elevation with $\phi_{\text{min}} = 0.5^\circ$ at bedrock elevations at or below -700 m and $\phi_{\text{max}} = 40^\circ$ at or above 700 m . Effective pressure at the base of the ice sheet is modelled following ref. 64. When ice is frozen at the base, then the effective pressure equals the overburden pressure ($N_{\text{till}} = \rho g H$), and when a saturated water layer is present for temperate ice, the effective pressure reduces to 2% of the overburden pressure value. To determine the basal water layer thickness, basal hydrology is resolved locally (no horizontal transport), depending on water production from melting/freezing the base of the ice sheet and a constant till drainage rate of 1 mm year^{-1} . The water layer is limited to 2 m, at which point the till below the ice sheet is considered saturated. Geothermal heat flux is imposed using the reconstruction in ref. 61. Glacial isostatic adjustment of the bedrock is determined using the Lingle–Clark model, as with PISM, and the same parameter values are used. Yelmo is run at 16-km horizontal resolution, with ten terrain-following coordinates in the vertical dimension. The ice-sheet model is coupled bidirectionally to the regional climate model REMBO²⁷. REMBO is a two-dimensional energy–moisture balance model in the atmosphere. At the ice-sheet surface, the snowpack is modelled as a single layer. The surface energy balance is approximated through the insolation–temperature melt equation, which accounts for changes in insolation and temperature, as well as surface albedo, but ignores other components. The snowpack and atmosphere evolves with a daily time step over the year and provides the mean annual surface temperature and surface mass balance to the ice-sheet model. At the domain boundaries, the climatological near-surface temperature is imposed, along with desired temperature anomalies. REMBO resolves the snowpack and surface energy balance on the ice-sheet-model grid and resolves the atmospheric dynamics at 120-km resolution. To reduce biases in the simulated present-day ice sheet, an extra 4 m year^{-1} of melt is included in the surface mass balance for areas in which there is no ice present in Greenland today. A simple oceanic anomaly method is used to determine the basal mass balance for marine ice at the grounding line: $\dot{b} = \dot{b}_{\text{ref}} + \kappa \Delta T_{\text{ocn}}$, in which $\kappa = 10 \text{ m year}^{-1} \text{ K}^{-1}$ and $\dot{b}_{\text{ref}} = -1 \text{ m year}^{-1}$ and $\Delta T_{\text{ocn}} = 0.25 T_{2\text{m,ann}}$.

Yelmo-REMBO is initialized with the present-day topography and ice-sheet thickness and a semi-analytical solution for the ice-temperature profile at each grid point. The model is then run for 25 kyr to equilibrate the ice sheet with the climatic forcing from REMBO.

Article

This is not long enough to reach full thermodynamic equilibrium, but the ice sheet becomes stable by this point with a well-defined thermodynamic distribution. As with PISM-dEBM, we normalize the ice volume such that the initial volume corresponds to the observed ice volume of 7.42 m sea-level equivalent in all plots⁵⁵.

Climate forcing

The Arctic region is experiencing the most rapid regional warming around the globe^{65–67}. To translate the increase in GMT to the warming rate of Greenland and vice versa, we fit the historical (1850–2014) and SSP585 (2015–2100) global mean surface temperature to the mean surface temperature anomaly around Greenland for summer (JJA) from the first available run of the 37 different CMIP6 models to get a scaling factor between regional temperature and GMT increase⁴⁶ (Extended Data Table 1). We derive the relationship

$$\Delta\text{GMT}_{\text{p1}} = f \times \Delta T_{\text{JJA}} + 0.5 \text{ } ^\circ\text{C} \quad (1)$$

between GMT above preindustrial $\Delta\text{GMT}_{\text{p1}}$ and regional summer temperature increase ΔT_{JJA} above present. The factor 0.5 °C is the increase of GMT in the reference period for our initial ice sheet states (1980–2000) compared with preindustrial levels (1850–1900) and is derived from HadCRUT5 observational data⁶⁸. The factor $f = \frac{1}{1.19} \text{ } ^\circ\text{C}^{-1}$ is the best estimate of the scaling factor between regional Greenland summer temperature and GMT derived from the CMIP6 SSP585 scenarios (Extended Data Table 1)

For the future scenarios, we apply a spatially constant temperature anomaly with a temperature-dependent seasonal amplitude. We use the scaling factor of 1.61 between regional winter and summer temperature (Extended Data Table 1). We model the difference in the scaling factor between the seasons as a cosine function with a period of 1 year. We fit observational surface temperature in southwestern Greenland for winter and summer from 1850 to 2019 against summer and winter GMT and find consistent scaling factors^{68,69} (Extended Data Fig. 8).

Structural and parametric uncertainties

We address both possible structural and parametric uncertainties of our results. Here structural uncertainties are those associated with the model mechanisms and the structure of the model, whereas parametric uncertainties refer to those that are because of incomplete knowledge of the optimal values for the parameters of a given model.

We account for structural uncertainties by carrying out our experiments with two independent ice-sheet models, PISM-dEBM and Yelmo-REMBO. We show all our results obtained with both models side by side in the figures and conclude that our results are remarkably robust for both models; they are thus unlikely to be affected by structural uncertainties in general, although important differences do arise in the details.

Also, we investigate the parametric uncertainties potentially associated with our results by performing further sensitivity analyses with PISM-dEBM, varying critical parameters that influence the ice dynamics, surface mass balance and further climatic factors (Extended Data Fig. 6). Specifically, we vary the pseudo-plastic sliding exponent, the SSA enhancement factor, the parameter for the bed viscosity, the SIA enhancement factor, the grid resolution, the melt equation parameterization and the precipitation–temperature scaling. Furthermore, we show results without the Earth deformation model.

Although the exact ice-volume loss differs slightly for each combination of the parameters, the qualitative behaviour remains the same. Only the simulation without an Earth deformation model shows a qualitatively different behaviour without a recovery of the ice sheet after an initial loss for some temperature anomalies. This is because of the missing glacial isostatic adjustment. The critical threshold of the ice sheet is not greatly influenced by the ice dynamics parameterization. The melt equation parameterization and

precipitation scaling influence the critical temperature threshold to some extent, yet within the range set by the two independent models. However, the qualitative behaviour does not change and a recovery after an initial loss is seen for all combinations for small temperature anomalies.

It should be noted that, in both models, the ice-sheet response is very sensitive when temperatures are close to the critical thresholds. For example, two simulations with PISM-dEBM show an ice-free state at the temperature of $\Delta T_{\text{JJA}} = 2.2 \text{ } ^\circ\text{C}$, although the other simulations show a recovery to a mostly glaciated Greenland (Fig. 2a). Similar behaviour can be observed for Yelmo-REMBO, for which one of the simulations shows delayed ice loss when forced with the threshold temperature $\Delta T_{\text{JJA}} = 1.5 \text{ } ^\circ\text{C}$, but it eventually transitions to the ice-free state. We attribute this to computational errors that can influence the simulations for temperatures very close to the threshold temperature.

Data availability

The CMIP6 data are freely distributed and available at <https://esgf-node.llnl.gov/search/cmip6/> (ref. 46). The BedMachine v5 data are available at <https://nsidc.org/data/IDBMG4/versions/5> (refs. 56,60). The output of the regional climate model MARv3.12 is available at <ftp://ftp.climato.be/fettweis/MARv3.12/Greenland/> (ref. 59). The observational temperature HadCRUT5 is available at <https://www.metoffice.gov.uk/hadobs/hadcrut5/> (ref. 68). The observational ice-sheet velocity MEaSUREs is available at <https://nsidc.org/data/NSIDC-0670/versions/1> (refs. 70,71). The datasets generated and analysed during the current study are available on Zenodo at <https://doi.org/10.5281/zenodo.8155423>.

Code availability

PISM is open source and freely distributed on GitHub <https://github.com/pism/pism>. The ice-sheet model Yelmo is open source and freely distributed on GitHub <https://github.com/palma-ice/yelmo>. The code for analysis and plotting of the model output, as well as an example script of how to run PISM-dEBM, is available in the same Zenodo repository as the model output at <https://doi.org/10.5281/zenodo.8155423>.

- Llibouty, L. & Duval, P. Various isotropic and anisotropic ices found in glaciers and polar ice caps and their corresponding rheologies. *Int. J. Rock Mech. Min. Sci. Geomech. Abstr.* **22**, 198 (1985).
- Schoof, C. & Hindmarsh, R. C. A. Thin-film flows with wall slip: an asymptotic analysis of higher order glacier flow models. *Q. J. Mech. Appl. Math.* **63**, 73–114 (2010).
- Cuffey, K. M. & Paterson, W. S. B. *The Physics of Glaciers* 4th edn (Academic, 2010).
- Morlighem, M. et al. BedMachine v3: complete bed topography and ocean bathymetry mapping of Greenland from multibeam echo sounding combined with mass conservation. *Geophys. Res. Lett.* **44**, 11,051–11,061 (2017).
- Lingle, C. S. & Clark, J. A. A numerical model of interactions between a marine ice sheet and the solid earth: application to a West Antarctic ice stream. *J. Geophys. Res. Oceans* **90**, 1100–1114 (1985).
- Bueler, E., Lingle, C. S. & Brown, J. Fast computation of a viscoelastic deformable Earth model for ice-sheet simulations. *Ann. Glaciol.* **46**, 97–105 (2007).
- Fettweis, X. et al. Reconstructions of the 1900–2015 Greenland ice sheet surface mass balance using the regional climate MAR model. *Cryosphere* **11**, 1015–1033 (2017).
- Morlighem, M. et al. *IceBridge BedMachine Greenland Version 5* (NSIDC, 2022); <https://nsidc.org/data/IDBMG4/versions/5>
- Shapiro, N. M. & Ritzwoller, M. H. Inferring surface heat flux distributions guided by a global seismic model: particular application to Antarctica. *Earth Planet. Sci. Lett.* **223**, 213–224 (2004).
- Robinson, A., Goldberg, D. & Lipscomb, W. H. A comparison of the stability and performance of depth-integrated ice-dynamics solvers. *Cryosphere* **16**, 689–709 (2022).
- Joughin, I., Smith, B. E. & Schoof, C. G. Regularized Coulomb friction laws for ice sheet sliding: application to Pine Island Glacier, Antarctica. *Geophys. Res. Lett.* **46**, 4764–4771 (2019).
- Bueler, E. & van Pelt, W. Mass-conserving subglacial hydrology in the Parallel Ice Sheet Model version 0.6. *Geosci. Model Dev.* **8**, 1613–1635 (2015).
- Serreze, M. C. & Francis, J. A. The Arctic amplification debate. *Clim. Change* **76**, 241–264 (2006).
- Serreze, M. C., Barrett, A. P., Stroeve, J. C., Kindig, D. N. & Holland, M. M. The emergence of surface-based Arctic amplification. *Cryosphere* **3**, 11–19 (2009).
- Screen, J. A. & Simmonds, I. The central role of diminishing sea ice in recent Arctic temperature amplification. *Nature* **464**, 1334–1337 (2010).

68. Morice, C. P. et al. An updated assessment of near-surface temperature change from 1850: the HadCRUT5 data set. *J. Geophys. Res. Atmos.* **126**, e2019JD032361 (2021).
69. Cappelen, J. Greenland - DMI historical climate data collection 1784-2019. Technical report of the Danish Meteorological Institute (2020).
70. Joughin, I., Smith, B. & Howat, I. *MEaSUREs Multi-year Greenland Ice Sheet Velocity Mosaic Version 1* (NSIDC, 2016); <https://nsidc.org/data/NSIDC-0670/versions/1>
71. Joughin, I., Smith, B. E. & Howat, I. M. A complete map of Greenland ice velocity derived from satellite data collected over 20 years. *J. Glaciol.* **64**, 1–11 (2018).
72. Crameri, F., Shephard, G. E. & Heron, P. J. The misuse of colour in science communication. *Nat. Commun.* **11**, 5444 (2020).

Acknowledgements This is TIPES contribution #209; the TIPES ('Tipping Points in the Earth System') project has received funding from the European Union's Horizon 2020 research and innovation programme under grant agreement no. 820970. This work was supported by the UiT Aurora Centre Program, UiT The Arctic University of Norway (2020) and the Research Council of Norway (project number 314570). The simulations with PISM-dEBM were performed on the Fram supercomputer provided by Sigma2 - the National Infrastructure for High Performance Computing and Data Storage in Norway under the projects NN8008K and NN9348K. N.Boe. acknowledges further funding by the Volkswagen Foundation and the European Union's Horizon 2020 research and innovation programme under the Marie Skłodowska-Curie grant agreement no. 956170, as well as from the German Federal Ministry

of Education and Research under grant no. 01LS2001A. A.R. received funding from the European Union (ERC, FORCLIMA, 101044247). Development of PISM is supported by NSF grants PLR-1644277 and PLR-1914668 and NASA grants NNX17AG65G and 20-CRYO2020-0052. We thank M. Zeitz for her comments on PISM-dEBM that resolved computational problems. Some of the plots are made using scientific colour maps by Crameri et al.⁷².

Author contributions N.Boe. conceived the study. N.Boc. and N.Boe. designed the study. A.R. performed the experiments with Yelmo-REMO. N.Boc. performed the experiments with PISM-dEBM and analysed the output data. A.P. assembled and analysed CMIP6 data and wrote parts of the extended data. N.Boc., N.Boe., A.R., M.M. and M.R. discussed and interpreted results. N.Boc. wrote the paper, with contributions from N.Boe., A.R., M.M. and M.R.

Competing interests The authors declare no competing interests.

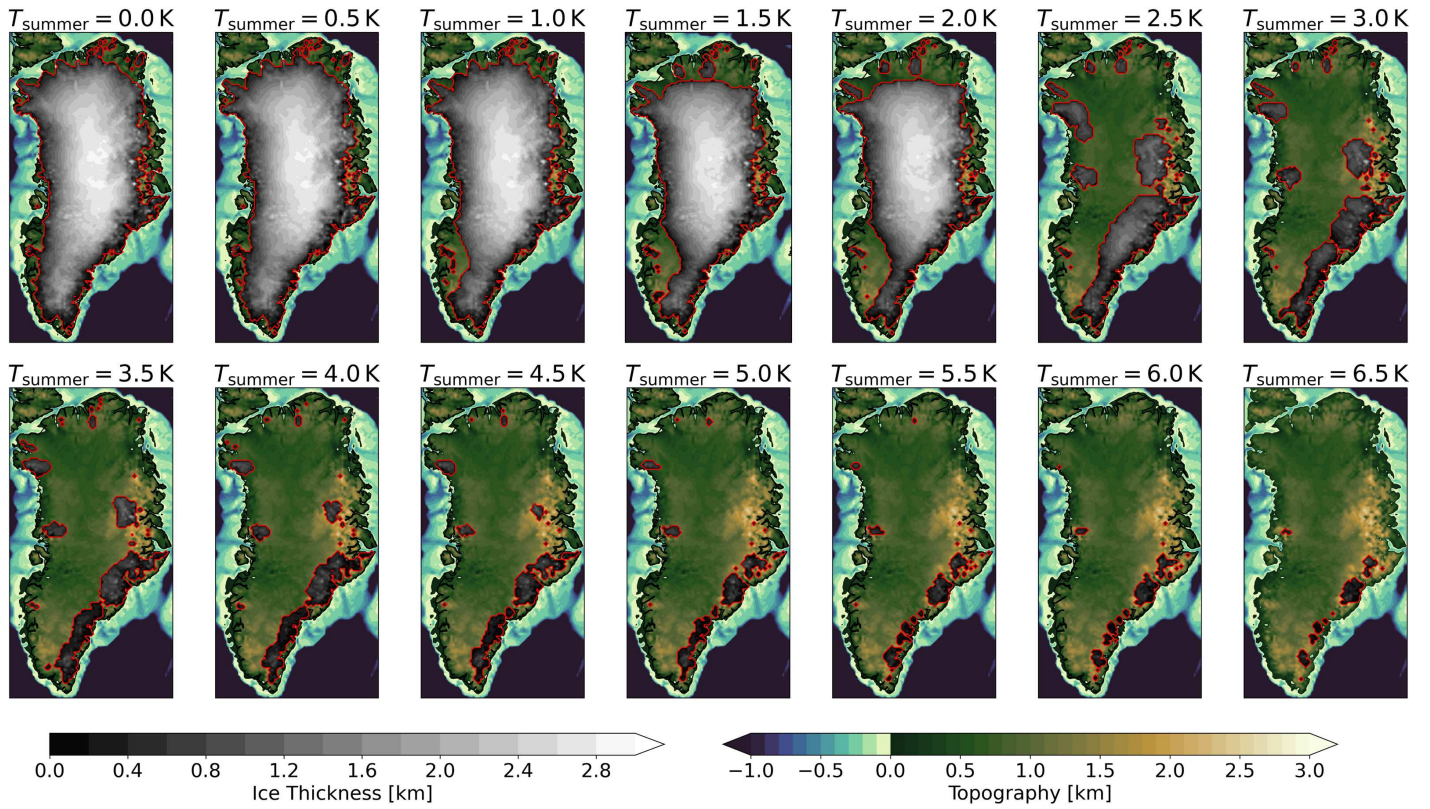
Additional information

Supplementary information The online version contains supplementary material available at <https://doi.org/10.1038/s41586-023-06503-9>.

Correspondence and requests for materials should be addressed to Nils Bochow.

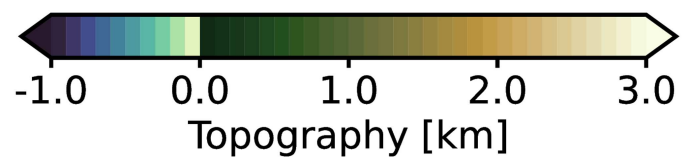
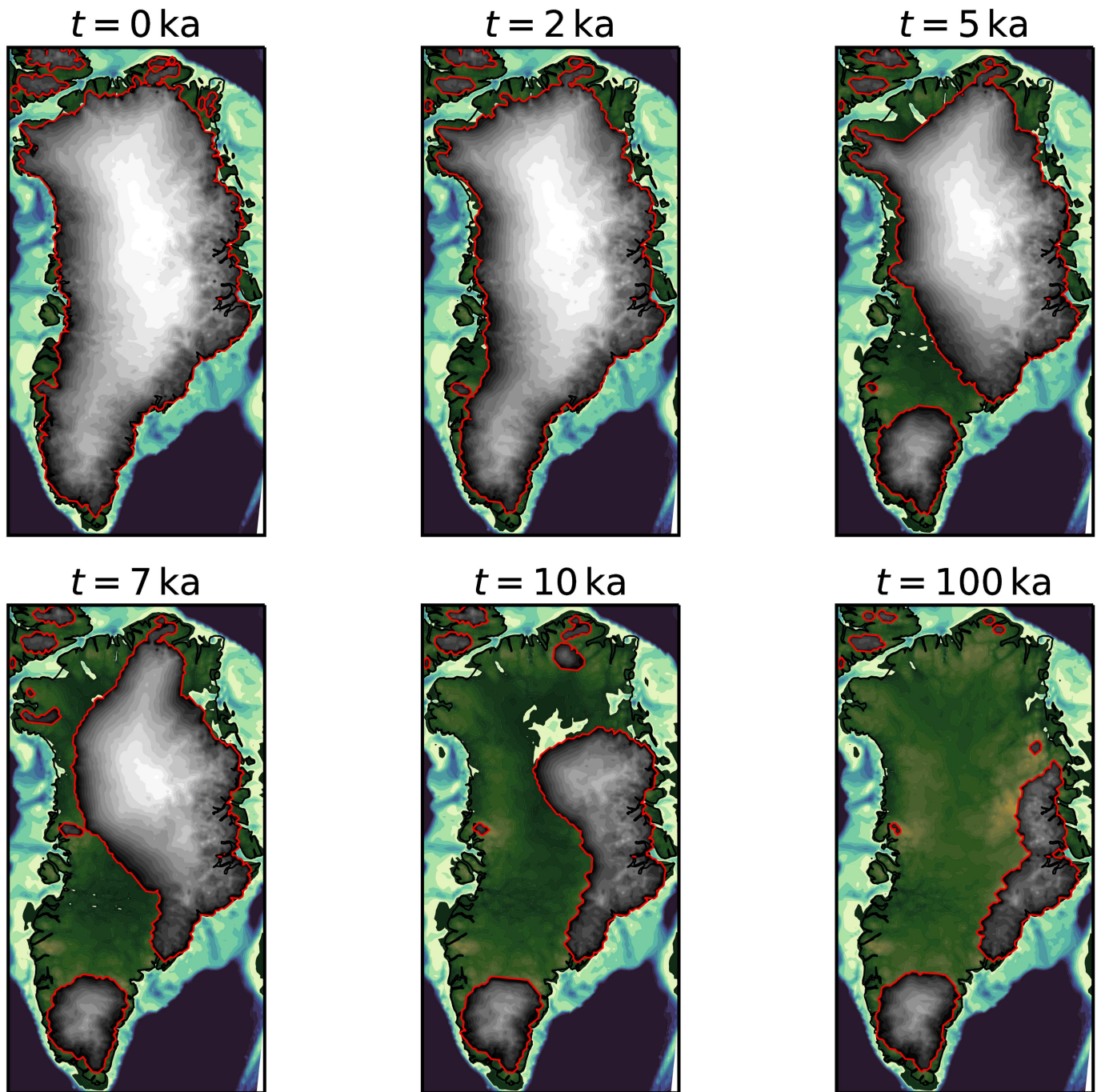
Peer review information *Nature* thanks Anna Von der Heydt and the other, anonymous, reviewer(s) for their contribution to the peer review of this work. Peer reviewer reports are available.

Reprints and permissions information is available at <http://www.nature.com/reprints>.



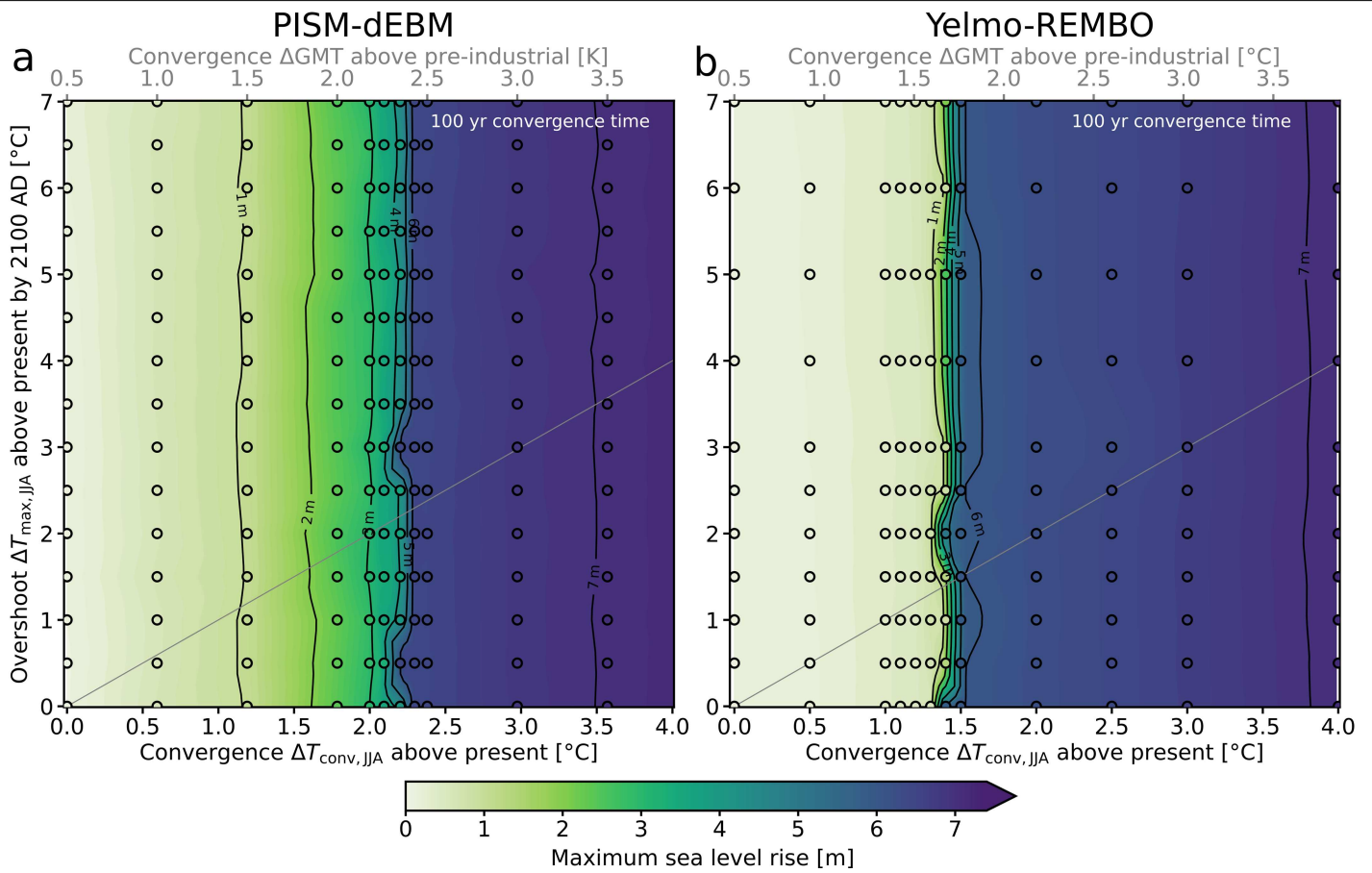
Extended Data Fig. 1 | Spatial maps of the GrIS after 100 kyr for warming scenarios without mitigation for PISM-dEBM. Equilibrium states of the GrIS for regional summer warming convergence temperatures between 0 °C and 6.5 °C. The warming period lasts for 100 years and the temperature remains constant afterwards. Several different states can be distinguished: present-day configuration with fully extended ice sheet, several intermediate states with

around 50–90% of the present-day ice volume for warming levels between 0 °C and 2.0 °C and an ice-free state. The ice-sheet extent is denoted by a red outline. The spatial configurations correspond to the end states in Fig. 1 and Extended Data Fig. 5. The maps were made with the Python package cartopy⁵² and Natural Earth.



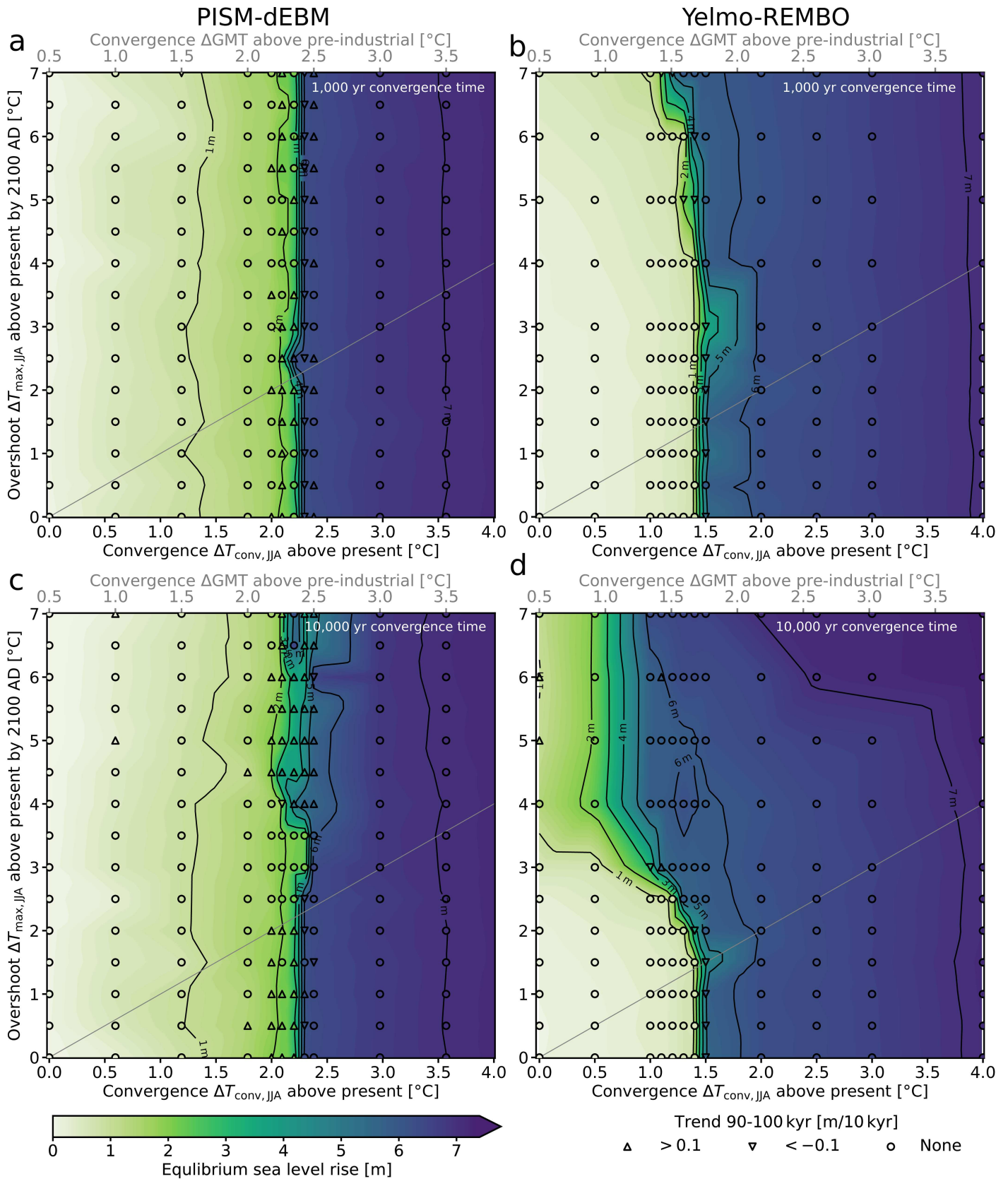
Extended Data Fig. 2 | Spatial evolution of the GrIS for $\Delta T_{\text{conv, JJA}} = 3.0^\circ\text{C}$ in Yelmo-REMO. Exemplary transient snapshots of the GrIS for a regional summer warming convergence temperature of 3.0°C . The warming period lasts for 100 years and the temperature remains constant afterwards.

The ice-sheet extent is denoted by a red outline. Southwestern Greenland shows the highest sensitivity to warming, followed by the northern part of Greenland. After 10,000 years, most of the ice sheet has melted. The maps were made with the Python package cartopy⁵³ and Natural Earth.



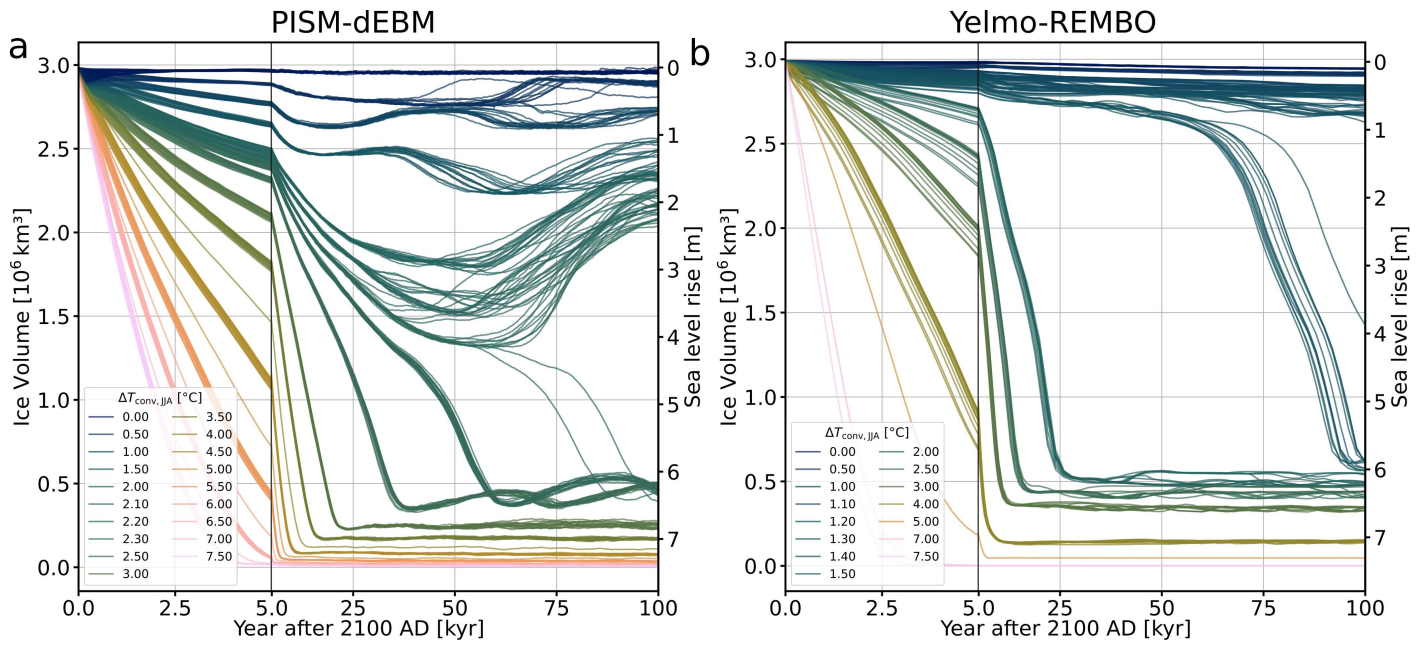
Extended Data Fig. 3 | Maximum SLR contribution of the GrIS after warming and subsequent cooling for 100 years convergence time. a, Evolution of ice volume of the whole GrIS for regional summer temperature changes between 0 °C and 7.0 °C above present for PISM-dEBM. The warming period lasts for 100 years, with subsequent cooling for another 100 years to the convergence temperature. Three different states can be distinguished: present-day configuration with fully extended ice sheet, intermediate state with around

60% of the present-day ice volume and an ice-free state. The semi-stable state recovers close to present-day ice-sheet volume after 100 kyr owing to glacial isostatic adjustment. Some runs show oscillatory behaviour on the timescale of several 10 kyr. The corresponding spatial maps are shown in Fig. 1 and Extended Data Fig. 1 and the resulting stability diagram is shown in Fig. 2. **b,** Same as **a** but for Yelmo-REMBO. Only two states are found; present-day and a near-ice-free state.



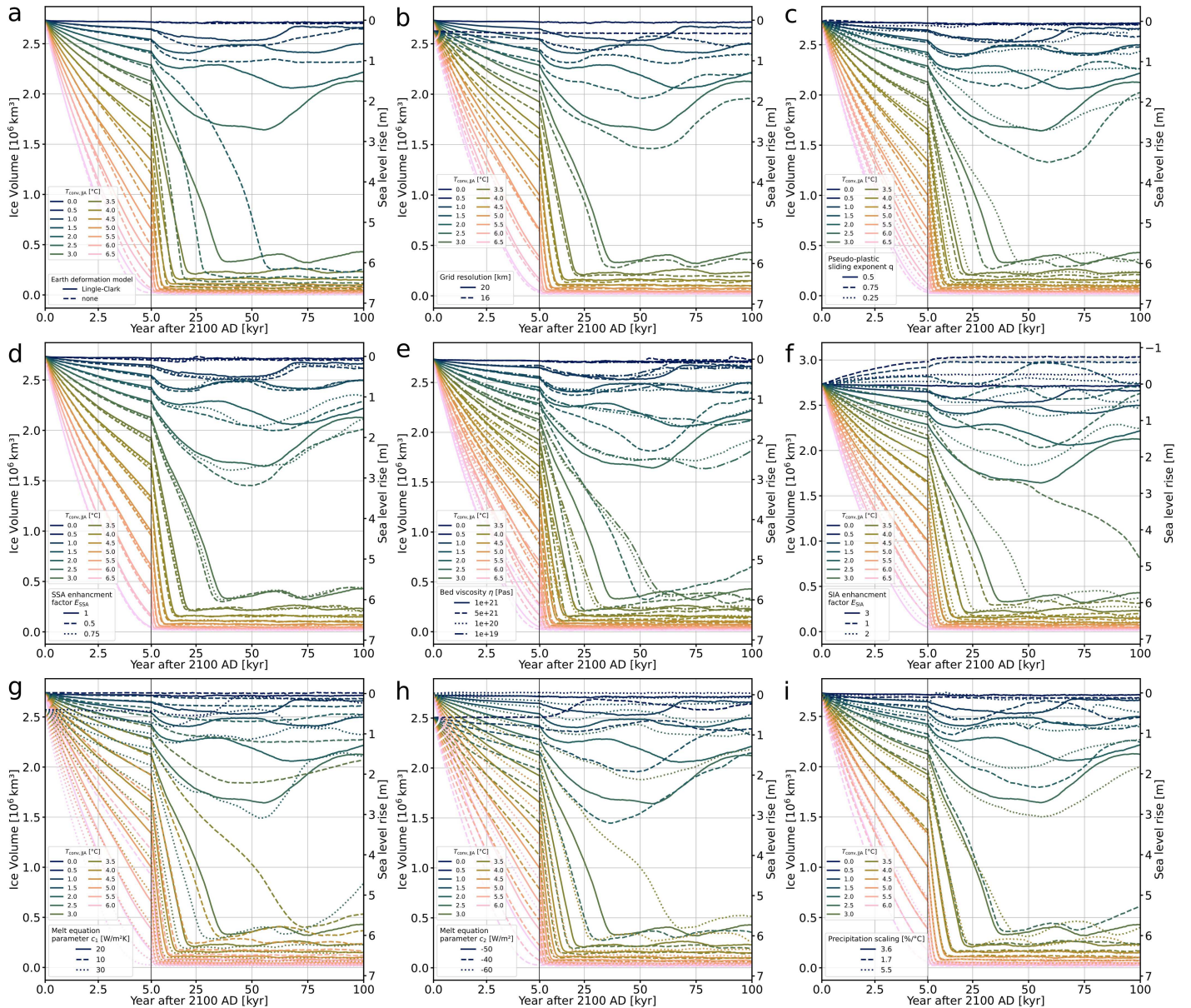
Extended Data Fig. 4 | Equilibrium SLR contribution of the GrIS after warming and subsequent cooling for convergence times of 1,000 and 10,000 years. **a.** Stability diagram of the GrIS with PISM-dEBM. Different warming rates are applied for 100 years, followed by various cooling rates for another 1,000 years. The temperature is kept constant afterwards for another 100 kyr. White regions indicate a present-day-like ice sheet, green–blue regions mark intermediate states and purple corresponds to the ice-free state.

The grey line corresponds to the scenarios for which the overshoot temperature equals the convergence temperature. Below the grey line, the overshoot temperature in the year 2100 AD is smaller than the convergence temperature in 2200 AD. **b.** Same as **a** but for Yelmo-REMBO. **c,d.** Same as **a,b**, respectively, but for a convergence time of 10,000 years. The equilibrium states show a dependence on the overshoot temperature close to the threshold temperature.



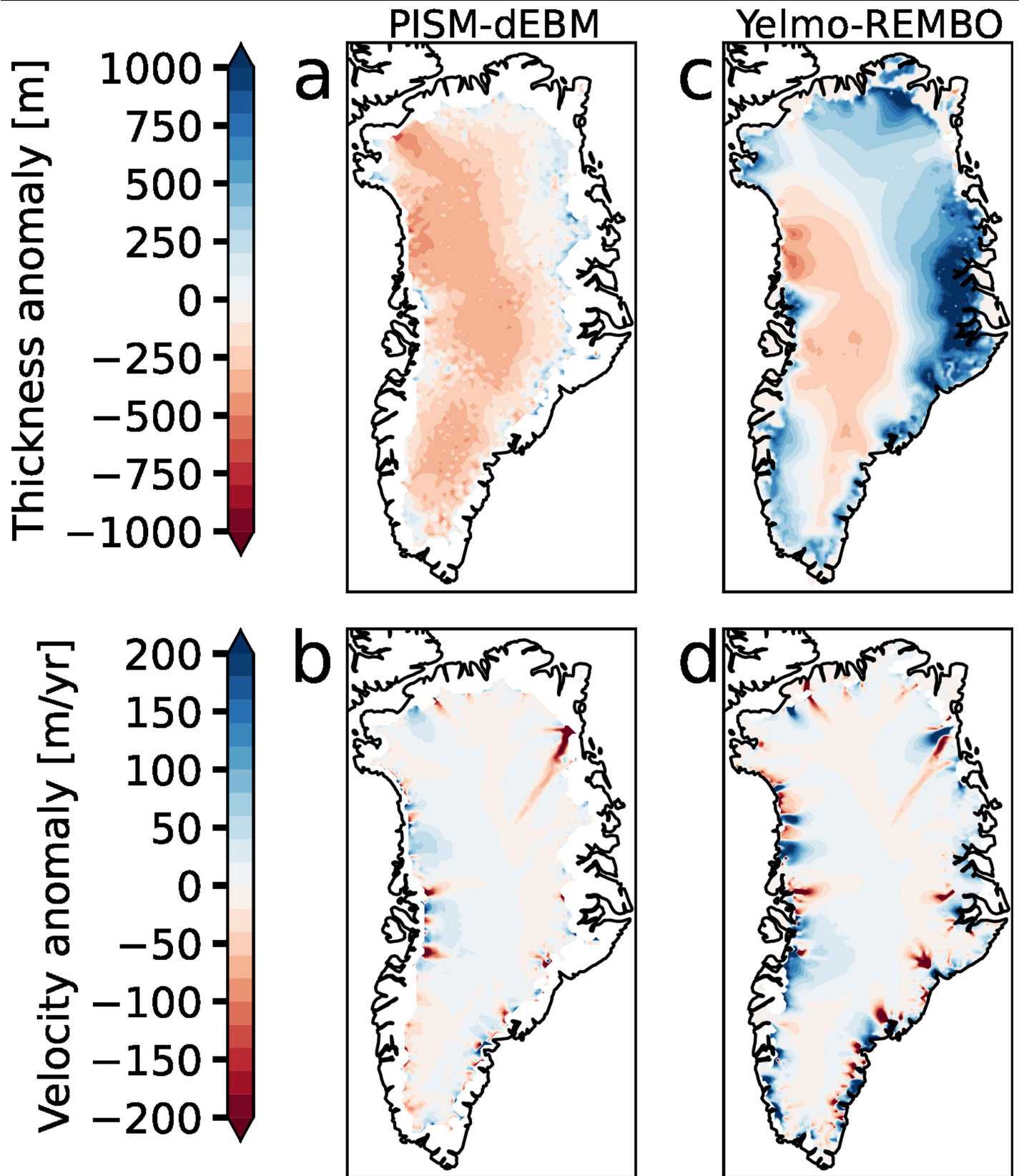
Extended Data Fig. 5 | Extended time series of ice volume for warming scenarios with mitigation. a, Evolution of ice volume of the whole GrIS for regional summer temperature changes between 0 °C and 7.5 °C above present for PISM-dEBM. The warming period lasts for 100 years, followed by cooling for another 100 years to the convergence temperature. Three different states are distinguishable: present-day configuration with fully extended ice sheet, intermediate state with around 60% of the present-day ice volume and an

ice-free state. The semi-stable state recovers close to the present-day ice-sheet volume after 100 kyr owing to glacial isostatic adjustment. Some runs show oscillatory behaviour on the timescale of several 10 kyr. The corresponding spatial maps are shown in Fig. 1 and Extended Data Fig. 1 and the resulting stability diagram is shown in Fig. 2. **b,** Same as **a** but for Yelmo-REMBO. Only two states are distinguishable; present-day and a near-ice-free state.



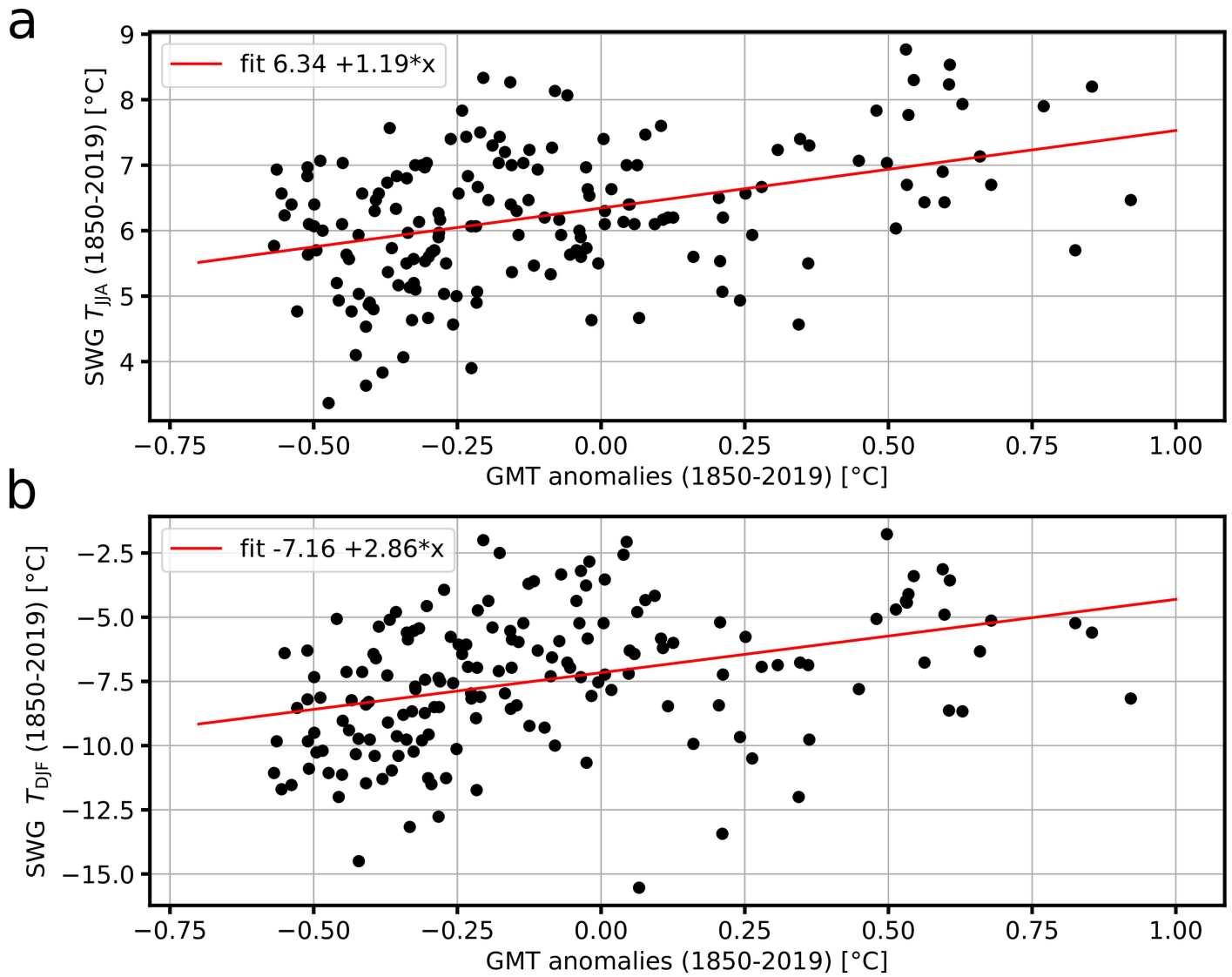
Extended Data Fig. 6 | Sensitivity of long-term evolution under warming to model parameter variation. Evolution of total GrIS ice volume simulated by PISM-dEBM, for which the temperature anomalies are not reversed for different temperature anomalies between $\Delta T_{JJA} = 0^\circ\text{C}$ and 6.5°C above present with variations of important model parameters. The dashed lines correspond to simulations with changes in the parameters compared with the reference parameters. There is no further spin-up of the initial state to account for the parameter changes except for **b**. **a**, Evolution of total GrIS ice volume for regional summer temperature changes between 0°C and 6.5°C above present with and without an Earth deformation model. The solid line corresponds to

the reference simulation, as we use it in the main text. **b-f**, Same as **a** but for the tested model parameter variation (dashed lines) in comparison with the reference simulation. **b**, Grid resolution. **c**, Pseudo-plastic sliding exponent. **d**, Enhancement factor for the SSA velocities. **e**, Half-space (mantle) viscosity. **f**, Flow enhancement factor for SIA. **g**, Melt equation parameter c_1 (see Methods section 'PISM-dEBM'). **h**, Melt equation parameter c_2 . **i**, Precipitation scaling. Although the exact ice-volume loss differs for the different parameter choices, the qualitative behaviour is the same. Only the simulations without bed deformation model show a qualitatively different behaviour without a recovery after an initial ice loss for temperature anomalies between 1.0 and 2.0°C .



Extended Data Fig. 7 | Difference between observed and simulated initial-state ice thickness and velocity in PISM-dEBM and Yelmo-REMBO. **a**, Difference between simulated initial state and observed ice thickness (BedMachine v5 (refs. 56,60)) with PISM-dEBM. Blue and red areas denote regions in which the simulation overestimates and underestimates the thickness, respectively. The root-mean-square error is 260 m. Observational

data were regridded to a 20-km grid to ensure comparability. **b**, Same as **a** but for the ice sheet velocity (MEaSURES v1 (refs. 70,71)). The root-mean-square error is 60 m year⁻¹. **c,d**, Same as **a,b**, respectively, but for Yelmo-REMBO. The root-mean-square error of the ice thickness is 399 m. The root-mean-square error of the velocity is 83 m year⁻¹. The maps were made with the Python package cartopy⁵² and Natural Earth.



Extended Data Fig. 8 | Fit of historical air surface temperature in southwestern Greenland against GMT. a. Linear fit of summer surface air temperature T_{JJA} in southwestern Greenland (SWG)⁶⁹ against global mean surface air temperature anomalies for 1850–2019. The GMTs are taken from

HadCRUT5 (ref. 68). The scaling factors agree in their uncertainty with the CMIP6-derived scaling factors. **b.** Same as **a** but for winter surface air temperature T_{DJF} in SWG against GMT.

Article

Extended Data Table 1 | Scaling factors between regional winter surface temperature in Greenland and regional summer temperatures and between regional summer surface temperature and global mean surface temperature

Model name	Historical		SSP585	
	DJF/JJA	JJA/GMT	DJF/JJA	JJA/GMT
ACCESS-CM2	1.24314	1.55784	1.68832	1.10120
ACCESS-ESM1-5	1.73007	1.76506	2.02724	1.04376
AWI-CM-1-1-MR	1.32796	1.25945	1.82360	0.99303
BCC-CSM2-MR	1.29499	0.90418	2.26547	0.84801
CAMS-CSM1-0	2.15478	0.63802	2.21623	0.67288
CanESM5	1.76195	1.16298	2.02841	1.08541
CESM2	1.21479	1.62255	1.39828	0.91612
CESM2-WACCM	1.22269	1.51080	1.59764	1.00008
CIESM	0.59212	0.52382	1.17684	1.85676
CMCC-CM2-SR5	1.00370	1.37371	1.27209	1.55352
CMCC-ESM2	1.06552	1.39911	1.45985	1.60628
CNRM-CM6-1	1.34151	2.86455	1.40100	1.26130
CNRM-CM6-1-HR	1.26669	1.25802	1.60006	1.17709
CNRM-ESM2-1	1.01460	2.55458	1.36261	1.18301
EC-Earth3	1.73116	2.64813	1.04662	1.56726
EC-Earth3-CC	1.96319	3.34523	1.06750	1.89909
EC-Earth3-Veg	1.73052	2.97792	1.09530	1.70582
EC-Earth3-Veg-LR	1.53602	3.20890	1.08838	1.83091
FGOALS-f3-L	1.53602	0.88812	2.55654	0.99939
FGOALS-g3	0.67795	1.14430	1.70377	0.79942
FIO-ESM-2-0	1.12462	1.34199	1.51423	1.37146
GFDL-ESM4	0.59354	0.83519	1.16744	0.97431
HadGEM3-GC31-LL	0.88461	1.22988	1.39971	1.30237
HadGEM3-GC31-MM	0.83721	1.44161	1.28213	1.24049
INM-CM4-8	1.20071	0.86486	2.30557	1.12200
INM-CM5-0	0.76044	1.27254	1.84016	1.06189
IPSL-CM6A-LR	1.65678	1.46502	1.44866	1.36732
KIOST-ESM	0.97104	0.91166	1.53603	0.72659
MIROC6	0.85111	0.72640	1.97290	1.20458
MIROC-ES2L	1.15751	0.72640	1.94393	1.04821
MPI-ESM1-2-HR	1.43216	1.32521	1.80874	1.03589
MPI-ESM1-2-LR	1.33128	1.30071	1.51064	1.02537
MRI-ESM2-0	0.65250	1.21552	1.65335	0.87347
NESM3	1.43084	1.56126	1.78717	1.17106
NorESM2-LM	0.76920	0.63713	1.61181	1.16325
NorESM2-MM	0.92682	1.11325	1.48325	0.95163
UKESM1-0-LL	1.43775	1.93959	1.37611	1.37244
Mean	1.23408	1.48748	1.60858	1.19223
SD	0.39992	0.72539	0.37444	0.31023

List of the 37 CMIP6 models⁴⁶ used for the scaling-factor comparison. The second and fourth columns show the scaling factor between the mean winter surface temperature in Greenland and the mean summer surface temperature in Greenland, respectively, for historical and SSP585 runs. The third and fifth columns show the scaling factor between regional summer surface temperature in Greenland and global mean surface temperature.

Extended Data Table 2 | Scaling factor of annual mean precipitation in Greenland against mean summer surface temperature in Greenland for SSP585 runs

Model name	SSP585 scaling factor [%]
ACCESS-CM2	4.26337
ACCESS-ESM1-5	4.30279
AWI-CM-1-1-MR	4.43382
BCC-CSM2-MR	3.35385
CAMS-CSM1-0	6.30719
CanESM5	7.62772
CESM2	0.41463
CESM2-WACCM	1.16871
CIESM	2.77636
CMCC-CM2-SR5	3.52098
CMCC-ESM2	4.40673
CNRM-CM6-1	3.03457
CNRM-CM6-1-HR	4.58830
CNRM-ESM2-1	2.12144
EC-Earth3	2.77394
EC-Earth3-CC	3.41980
EC-Earth3-Veg	3.23276
EC-Earth3-Veg-LR	3.21419
FGOALS-f3-L	7.25859
FGOALS-g3	0.69556
FIO-ESM-2-0	2.53140
GFDL-ESM4	1.80231
HadGEM3-GC31-LL	3.08538
HadGEM3-GC31-MM	3.12996
INM-CM4-8	6.86774
INM-CM5-0	5.58120
IPSL-CM6A-LR	4.62000
KIOST-ESM	2.61953
MIROC6	3.34743
MIROC-ES2L	4.89060
MPI-ESM1-2-HR	3.06237
MPI-ESM1-2-LR	6.28110
MRI-ESM2-0	0.62048
NESM3	6.08938
NorESM2-LM	0.87454
NorESM2-MM	0.55605
UKESM1-0-LL	3.69790
Mean	3.58305
SD	1.91032

List of the 37 CMIP6 models⁴⁶ used for the comparison. The second column shows the percentage change of the mean annual precipitation in Greenland for changing mean summer surface temperature in Greenland for SSP585.



Paper III: Reconstruction of Climate Fields Using Deep Learning

Bochow, N., Poltronieri, M., Rypdal, M., Boers, N. Reconstructing historical climate fields with deep learning. arXiv: 2311.18348 [physics.geo-ph]. <https://doi.org/10.48550/arXiv.2311.18348>

Reconstructing Historical Climate Fields With Deep Learning

Nils Bochow^{1,2,3*}, Anna Poltronieri¹, Martin Rypdal¹,
Niklas Boers^{3,4,5}

¹Department of Mathematics and Statistics, UiT - The Arctic
University of Norway, Tromsø, Norway.

²Physics of Ice, Climate and Earth, Niels Bohr Institute, University of
Copenhagen, Copenhagen, Denmark.

³Potsdam Institute for Climate Impact Research, Potsdam, Germany.

⁴Earth System Modelling, School of Engineering & Design, Technical
University of Munich, Munich, Germany.

⁵Department of Mathematics and Global Systems Institute, University
of Exeter, Exeter, UK.

*Corresponding author(s). E-mail(s): nils.bochow@uit.no;

Abstract

Historical records of climate fields are often sparse due to missing measurements, especially before the introduction of large-scale satellite missions. Several statistical and model-based methods have been introduced to fill gaps and reconstruct historical records. Here, we employ a recently introduced deep-learning approach based on Fourier convolutions, trained on numerical climate model output, to reconstruct historical climate fields. Using this approach we are able to realistically reconstruct large and irregular areas of missing data, as well as reconstruct known historical events such as strong El Niño and La Niña with very little given information. Our method outperforms the widely used statistical kriging method as well as other recent machine learning approaches. The model generalizes to higher resolutions than the ones it was trained on and can be used on a variety of climate fields. Moreover, it allows inpainting of masks never seen before during the model training.

Introduction

Observational climate data is typically sparse before systematic observations such as buoys, ship measurements, or satellite measurements were introduced. Generally, the further back in time we go, the fewer observations are available [1]. Temperature and precipitation records are the best-observed climate fields in the recent past and reach back until the 19th century, but measurements are still sparse and rely heavily on interpolation especially for earlier parts of the records [2, 3]. Even more severely, for many important climate variables, such as sea-ice thickness or vegetation indices, no measurements exist at all before the introduction of large-scale satellite missions. The corresponding time series often span a few decades or even only years [e.g., 4, 5]. The low spatial and temporal resolution introduces large uncertainties and limits our understanding of important climatic processes [1, 2, 6].

Several approaches and methods to produce historical climate fields based on the available observations have been developed in the past. One approach is to run state-of-the-art weather models with observations and past weather forecasts to produce reanalysis products that provide a complete picture of the past weather and climate for the last decades [7, 8]. While reanalyses are successful in providing spatiotemporally continuous and consistent data, they often struggle with specific regions and variables and inherit biases the employed numerical models suffer from [8, 9].

An alternative approach is to use statistical methods to reconstruct missing information. In this regard, kriging or Gaussian process regression is widely used in the geosciences [10–12]. However, statistical methods typically do not include knowledge of the temporal and spatial patterns of the underlying climatic fields and therefore fail to reconstruct these patterns, especially for large missing areas.

In recent years, machine learning (ML) has become widely used in geoscience and climate science, with the promise of better performance than statistical methods while still providing easy usability and, to some extent, knowledge of the underlying physical processes [13, 14]. The applications of machine learning in climate science are vast and range from classical time series forecasting [15–17], down-scaling and post-processing of numerical models [18, 19], to time series reconstruction [13, 20]. Furthermore, there is a substantial ongoing effort to combine traditional numerical Earth system models with machine learning methods to leverage the advantages of both approaches [14, 21–28].

In this study, we consider the reconstruction of spatial climate fields as an image inpainting problem. Inpainting images based on given information is a classical problem in computer vision and many approaches have been proposed in recent years [29–31]. We apply the recently introduced state-of-the-art deep learning approach *Resolution-robust Large Mask Inpainting with Fourier Convolutions* (LaMa) [32] to reconstruct different climate fields with a focus on surface temperature records. We train our model on numerical climate model output from the Coupled Model Intercomparison Project to reconstruct the missing measurements in observational data. Our method is able to reconstruct climate fields with very sparse information and highly irregular missing data. We show that our approach outperforms kriging and other machine learning methods. Moreover, it is able to inpaint different data sets than the ones it was trained on, and can be used on a variety of structurally different climatic fields at varying resolutions.

The surface temperature is one of the most important climate variables, as a direct measure of climate change. Global instrumental temperature records reach back to the mid-19th century [2] with local observations reaching back as far as the mid-17th century [33]. However, on average, less than 30% of Earth’s surface before the year 1900 AD have measurements in the state-of-the-art observational data set HadCRUT4 (Fig. 1a). This is similar for other widely used long-term temperature data. Therefore, surface temperature records serve as perfect proof-of-concept application for the image inpainting task in climate science.

Results

To inpaint the temperature records, we train our model on the historical surface temperatures from the Coupled Model Intercomparison Project 5 (CMIP5) ensemble (1850–2012 AD); see Methods. We follow a previously introduced mask generation approach [13] and mask the training data with the missing masks derived from the observational gaps in the temperature data set HadCRUT4 [2] during training.

First, we evaluate the model on the same held-out CMIP5 member as in [13] to directly compare with their inpainting approach, which is based on partial convolutions (PConv). In a second step, we evaluate the trained model on each HadCRUT4 mask for 2251 randomly held-out months of the CMIP5 ensemble. This gives a total of 4,641,750 combinations of images and masks. As a baseline comparison, we compare

our results with statistical kriging. Subsequently, we reconstruct the HadCRUT4 data and show examples of other applications.

Comparison with related work

In order for our method to be directly comparable to the previously introduced PConv method [13], we evaluate LaMa on the same held-out CMIP5 ensemble member. We mask the held-out 145th CMIP5 member with the corresponding HadCRUT4 masks for each month over the time span 1870-2005 AD to have the same temporal range as Kadow et al. [13] (Fig. 2a,b). We reconstruct the held-out CMIP5 member over the whole time span with LaMa and kriging and compare it with the PConv approach, as well as an additional reanalysis product (Fig. 2). In the following, we refer to the square root of the spatially weighted average of the squared differences between the ground truth and the inpainted image as the spatial RMSE. Additionally, we define the site-wise RMSE as the RMSE at each site, averaged over the time dimension. The mean site-wise RMSE is the spatially weighted average of the site-wise RMSE in all grid cells. Hence, the main difference between the two main evaluation metrics that we focus on is the order of averaging in time and space. In each time step, we exclude the grid cells that have known values for the calculations of the RMSE.

Our model is able to realistically reconstruct the spatial patterns and amplitude of the surface temperature. An exemplary spatial reconstruction for February 1870 for all methods, i.e. LaMa, kriging, and PConv [13], is shown in Fig. 2. There is high agreement between the reconstructed temperature fields and the ground truth. While the tropical and sub-tropical regions show strong similarities between ground truth and reconstruction, the polar regions show the strongest deviation from the ground truth for all methods (Fig. 3, Tab. 1).

All machine learning methods show an improvement compared to kriging in terms of the mean site-wise and mean spatial RMSE (Fig. 3, Tab. 1). LaMa outperforms all other methods with a 15% lower mean site-wise RMSE than the reference PConv method (Fig. 3e, Tab. 1). LaMa shows the largest improvement in the northern hemisphere, especially in North America and Asia, but also in the subtropical southern hemisphere and in west Antarctica compared to kriging (green regions in Fig. 3d). LaMa and the PConv method show a lower site-wise RMSE in 79% and 71% of the grid cells compared to kriging, respectively. For all methods, the temporally averaged site-wise RMSE is largest in the Arctic and Antarctic region. Interestingly, the PConv approach shows a slightly worse performance in the northern and southern

Pacific than kriging in terms of the site-wise RMSE (Fig. 3e), while LaMa shows better performance in this region. Both ML methods show considerably worse performance in East Antarctica and slightly worse performance in the Indian Ocean than kriging. Note that East Antarctica is in the west in the projection shown in the maps here. The weaker performance in the aforementioned regions is likely a result of the high-temperature variation in these regions. Kriging, by definition, produces a smooth temperature field that might be closer to the ground truth for highly temporally variable regions. Especially for Antarctica the reconstructed temperature fields via kriging are very homogeneous due to the distance of known measurements, while the machine learning approaches inpaint a highly variable Antarctica as learned from the CMIP5 data (Fig. 2). This suggests that the available temperature information fed into the networks is not sufficient to successfully infer the temperature patterns in Antarctica.

In 78% of the grid cells, LaMa shows a lower site-wise RMSE than the reconstruction based on PConv (Fig. 3f). LaMa is also able to reconstruct the GMT time series reasonably and closely follows the ground truth (Fig. S1). LaMa shows comparable performance to the PConv method [13] with slightly worse RMSE of the yearly GMT, but lower spatial RMSE and higher correlation between the yearly GMT time series than PConv and kriging (Fig. S1).

Evaluation on CMIP5

In addition to the evaluation on the single held-out CMIP5 ensemble member, we evaluate the model on 2251 held-out months of the entire CMIP5 ensemble against all 2064 HadCRUT4 masks. We calculate the spatial and site-wise ensemble RMSE of the infilled evaluation temperature data and compare it with kriging (Fig. 4). Here, *ensemble mean* refers to the mean over all months of the 2251 CMIP5 ensemble members, and *temporal mean* refers to a mean over the masks, which corresponds to the temporal dimension of the HadCRUT4 records.

LaMa has a temporal ensemble mean of the spatial RMSE of 1.02 K and the reconstructed images via kriging have a mean spatial RMSE of 1.23 K (Fig. 4d). The ensemble mean of the site-wise RMSE shows a similar behavior (Fig. 4a,b,c). LaMa shows a more than 20% smaller mean site-wise RMSE than kriging (Fig. 4a,b,c) but shows a higher spatial RMSE than kriging for very large masks (> 80%). Otherwise, LaMa consistently outperforms kriging for all masks.

The spatial RMSE of the infilled images via kriging and LaMa depends on the ratio of missing values and shows a decrease around mask number 1200-1300, which

corresponds to the year 1950-1960 AD (Fig. 4d). This is due to the introduction of large-scale observational instruments and therefore greater coverage of temperature observations. Both methods show a seasonal dependency of the spatial RMSE (Fig. 4d) due to a difference in the seasonal global temperature coverage, mostly in the polar regions. The summer months in the polar regions have a greater coverage than the winter months. This leads to a higher spatial RMSE for the austral winter than in the boreal winter when observations in Antarctica are sparse, since Antarctica is the region with the largest uncertainty.

The spatial patterns of the site-wise RMSE are similar to the site-wise RMSE of the single member test set, with the maximum RMSE close to the poles and a minimum in the tropical and subtropical regions (Fig. 4a,b). Especially, the RMSE in the northern hemisphere is notably smaller for LaMa than for kriging.

HadCRUT4

After demonstrating that LaMa is able to reconstruct spatial and temporal patterns of the CMIP5 temperatures, we apply the trained network to the HadCRUT4 observational data. We show that our method is able to accurately reconstruct the spatial and temporal patterns of the HadCRUT4 data set. As there is no control data for the reconstructed temperature observations, we first compare with reconstructed HadCRUT4 temperatures via kriging [6] and also analyze spatial patterns in the reconstruction, focusing on known historical events.

We take a spatially weighted mean to obtain the temporal time series of the global mean temperatures for all methods. The reconstructed yearly GMTs show a strong correlation (Pearson correlation coefficient $r > 0.99$) and the same trend as the masked HadCRUT4 temperature time series for all methods (Fig. 5). LaMa shows a lower GMT for the mid-19th century relative to the masked mean and the temperature reconstructed via kriging or PConv. The main contributor is a slightly colder Antarctica in LaMa’s temperature reconstruction compared to the other methods (Fig. 5e,f). There is no a priori reason to believe that the global mean time series reconstructed by LaMa is unreasonable.

Due to the nature of the data, there is no ground truth that we can compare our reconstructions to. Hence, we compare the reconstructed temperature fields to well-known historical events such as strong El Niño episodes. The El Niño in the year 1877/1878 AD is known to have been extraordinarily strong and is linked to famines around the globe [34, 35]. However, historical temperature records for these years

are sparse. LaMa is able to reproduce the warm Pacific Ocean based on the sparse records, whereas kriging is not able to reconstruct the spatial patterns of the temperature anomaly (Fig. S2). The reconstruction based on partial convolutions, PConv (Fig. S2e), also shows a warm Pacific but with a smaller spatial extent. We also show an opposite example of a strong La Niña year with a cold Pacific for February 1917 AD [36, 37] (Fig. S3). Kriging does not reconstruct the same spatial extent of the cold Pacific compared to LaMa, which shows a strongly anomalous cold Pacific (Fig. S3). Statistical interpolation tends to inpaint large missing areas with values close to zero (e.g., Fig. S2). However, even for these anomalous historical events, it is still hard to verify the validity of the reconstructed temperature anomalies. We compare our exemplary reconstructions visually with the 20CRv3.SI reanalysis [38] (Fig. S2f & S3f). The machine learning reconstructions for the two exemplary months show a strong similarity with the reanalysis, while the kriging reanalysis does not show the same spatial patterns. This suggests that LaMa is indeed able to capture the dynamics underlying the global temperature fields. However, the temperature anomalies in Antarctica, in particular, show different spatial patterns across the different reconstructions and temperature products.

Beyond HadCRUT4

LaMa is able to generalize to higher resolutions than the ones it is trained on and is not restricted to temperature fields. We inpaint the 90x90 pixel Berkeley Earth Surface Temperatures (BEST) [39] using the LaMa model trained on the 72x72 pixel CMIP5 images (Fig. S4). We also show an exemplary reconstruction of sea ice concentration to show the application to a structurally different climatic field (Fig. S5).

We do not modify the trained model before evaluating on the BEST temperature records. We transform the BEST temperature records to 90x90 pixel images with the same procedure as before, which corresponds to a 156.25% higher resolution than the images we trained the model on. LaMa, trained solely on the HadCRUT4 masks, shows visible artifacts in the inpainted spatial fields, especially at the edges of the gaps (not shown here), and is therefore not suitable for reconstructions on unseen masks. This problem can easily be facilitated by employing a different mask generation algorithm during training. By generating random masks during training on the fly, using a previously proposed mask generation algorithm [32], LaMa generalizes to different masks than the ones seen during training. In the following, we call LaMa with randomly generated masks during the training *LaMa random*. We show that LaMa random is able

to inpaint the missing areas in the BEST record without any strong artifacts (Fig. S4). LaMa random is therefore better suited for generalization tasks when the final mask shapes for inference are not known during the training.

It should be noted that the very low resolution we use for the training images limits the application to higher resolutions. However, it has been shown that LaMa can generalize to resolutions up to four times higher than those it is trained on [32]. Hence, a significantly stronger upsampling than from CMIP5 (72x72 pixels) to BEST (90x90 pixels) should be possible.

To show the applicability to a different climate field, we train LaMa on the daily sea ice concentration from 1979-2022, taken from the ERA5 reanalysis [8, 40] with a resolution of 180x1440 px (northern hemisphere). This gives a total of 15,450 monthly fields, where we hold out 1,054 random months for evaluation and 1,043 random months for validation. Even for this relatively small training sample, LaMa is able to reconstruct the spatial extent and concentration of the sea ice reasonably well (Fig. S5). LaMa learns the continent distribution during training and correctly predicts the extent of the sea ice, given very little information of the unmasked areas (Fig. S5a,d). LaMa correctly reconstructs the seasonality of the sea ice concentration with a maximum in winter (Fig. S5a) and a minimum in summer (Fig. S5d). The largest deviations from the ground truth are generally at the edges of the sea ice, while the central Arctic shows the lowest error (Fig. S5c). This exemplary case of the sea ice concentration shows that LaMa can be applied to a variety of structurally different climate fields.

Conclusions

Reconstruction of historical observations is an active and important research field in climate science with vast implications for the present climate, short- and long-term future projections, and climate change attribution. Previously used methods often struggle with large irregular gaps in climate fields or with resolving spatial patterns. We show that LaMa is able to realistically reconstruct global temperature records across different data sets and resolutions. LaMa clearly outperforms the widely used kriging with a 21.0% smaller spatially averaged site-wise RMSE (Tab. 1). Furthermore, our method outperforms a previously proposed deep learning method based on partial convolutions [13]. In terms of the spatially averaged site-wise RMSE, LaMa outperforms PConv by 13.5% (Tab. 1), and 78% of the grid cells show a lower site-wise RMSE on the test set (Fig. 3f).

We train the model on very low-resolution images (72x72 pixel), which makes it difficult to resolve global teleconnections. Nonetheless, our model is able to realistically reconstruct spatial temperature patterns on a global level. Training on high-resolution images is limited by the available GPU infrastructure. However, due to the ability of LaMa to train on lower-resolution images than the ones it is evaluated on, this problem can be mitigated. While the training of the model can take several wall time days, depending on the training size, the evaluation is done in the order of minutes. It is hence much faster than gap-filling with dynamical models and still faster than statistical methods.

While LaMa can generalize to data different from its training set, the masks derived from BEST appear to be too dissimilar from the HadCRUT4 masks, which LaMa was trained on, to yield sensible reconstructions. We find that randomly generated masks during training ensure applicability on masks never seen during training, but on the HadCRUT4-derived masks LaMa almost consistently outperforms LaMa random in terms of the error metrics (Fig. S6). We note, however, that an improved random mask generation during training could potentially further improve LaMa random. Furthermore, we show that LaMa can be applied to a variety of structurally very different climate fields (Fig. S5).

The global time series reconstructed by LaMa shows slightly lower GMT until the year 1880 AD. With LaMa we find a GMT of 1.09°C above pre-industrial level (1850-1900) for the period 2010-2020, while the best estimate based on the masked HadCRUT4 data set gives a warming level of 1.00°C for the same period. This is mostly due to a colder southern hemisphere, especially in the Antarctic region, reconstructed by LaMa. Due to the sparse observations at the poles, it is difficult to validate the plausibility of the reconstructed temperatures in these areas. While the colder Antarctica reconstructed by LaMa is a priori not implausible, we attribute a possible underestimation of Antarctic temperatures to two reasons. Firstly, the variability of the surface temperature in Antarctica across the CMIP5 ensemble is large [41]. For a similar global surface temperature distribution, the temperatures in Antarctica might differ vastly between the single ensemble members. This makes it hard for the machine learning model to learn useful spatial connections that lead to reasonable Antarctic temperature predictions. Secondly, the inpainting problem turns into an outpainting problem for the polar regions, which is inherently harder. There are almost no known measurements for any time step in close proximity to Antarctica. While LaMa is able to extrapolate the polar regions reasonably well, the performance is worse than in

the non-polar regions (Fig. 3). However, the left and right edges of the images, corresponding to the prime meridian, do not necessarily show a higher RMSE than other regions (Fig. 3), which suggests that this is not the main reason.

For a masking ratio of more than 80%, LaMa shows a higher mean site-wise RMSE on the testing set than the other methods (Fig. 4d). This is due to artifacts with unusually high temperatures in western Antarctica (bottom right corner of the image) for some of the CMIP5 ensemble members. Similarly to Kadow et al. [13], we attribute this to effects at the edges of the images, as mentioned above. LaMa random does not exhibit these artifacts, which suggests that a more sophisticated mask generation during training could resolve these issues. We do not observe any artifacts in the other reconstructed data sets.

Convolutional neural networks (CNN) are generally not able to capture the spherical geometry of the Earth well, which can lead to the aforementioned artifacts at the edges. Graph neural networks or spherical convolutions could facilitate this problem [13, 42, 43]. The rising popularity of generative models makes it a promising alternative to CNN-based models for the reconstruction of climate fields. Especially, recently introduced diffusion models [e.g., 44, 45] show promising performance on image inpainting tasks. Furthermore, by using video-inpainting techniques [46] rather than image-inpainting, the temporal dimension of the data could directly be taken into account. However, little work has been done so far in that direction and the physical plausibility of such models remains uncertain.

Reconstructions via deep learning can aid in understanding past and present changes in the Earth system. By learning the spatiotemporal patterns of the underlying climate fields, LaMa is able to realistically reconstruct a variety of observables with varying resolutions. Our easy-to-use deep learning model clearly outperforms previous methods and therefore serves as an alternative to conventional methods used in the geosciences.

Methods

Resolution-robust Large Mask Inpainting with Fourier Convolutions (LaMa)

We utilize the recently introduced LaMa model [32] that builds on Fourier convolutions for reconstructing missing image regions. LaMa is a feed-forward ResNet-like inpainting network with a multi-component loss. LaMa has been shown to outperform other machine learning methods such as AOT GAN [47], GCPR [48], or latent diffusion models [32, 49, 50], and is able to inpaint large missing areas with a high receptive field. LaMa is able to inpaint high-resolution images even if trained on lower-resolution images. We extend and modify the model to allow drawing of pre-generated masks from HDF5 files during training and evaluation, as well as to enable training and evaluation on rectangular images. LaMa outperforms the method based on partial convolutions [13] in terms of spatial metrics and shows comparable performance on a temporal mean global scale. For the full description of the network architecture we refer to the original paper [32].

Training procedure and preprocessing

We train the model on the monthly surface temperature (tas) of 239,616 CMIP5 ensemble members following [13]. For the training and evaluation, we transform the temperature records into 72x72 px greyscale png-images with three identical RGB channels. We normalize the images with respect to the maximum and minimum values in the full CMIP5 set such that the maximum temperature corresponds to 255 and the minimum value to 0. Therefore, the maximum resolution of the reconstruction is given by $\frac{|\mathbf{u}_{\max}|+|\mathbf{u}_{\min}|}{256}$ with \mathbf{u} as the climatic field of interest. For our monthly mean temperature reconstruction, this leads to an effective maximum resolution of approximately 0.19°C. We convert the floats to integers during the transformation of the temperature records to images by truncation. In the following, we take the transformed temperature records as ground truth when we refer to the metrics of our machine learning model. For simplicity, we only plot the non-transformed HadCRUT4 temperature time series and add the difference between the HadCRUT4 masked temperature records and the transformed HadCRUT4 temperature records when we plot the reconstructed LaMa temperature time series.

We hold out 27,702 images for validation and 2,250 images for evaluation. Furthermore, we hold out one CMIP5 ensemble member from training for comparison

with the approach by [13]. We use two different mask-generation methods during the training. For the first approach, we train the model on randomly drawn masks derived from the HadCRUT4 [2] missing masks. In the following, we name this model *LaMa*. Our second approach generates random masks following the approach of [32] during training, hereafter *LaMa random*. We train both models on two NVidia Tesla V100 GPUs with a maximum of 60 epochs with a batch size of 100. We choose the training checkpoint with the lowest error metrics on the evaluation data set for each model. Therefore, we use the 57th checkpoint for *LaMa random* and the 60th checkpoint for *LaMa fixed*. For the full training parameters, we refer to the configuration files in the GitHub repository.

We use the software package PyKriging [51] for reconstructing the temperature records via kriging.

Declarations

Data availability The HadCRUT4 data [2] is available at <https://www.metoffice.gov.uk/hadobs/hadcrut4/>. The NOAA/CIRES/DOE 20th Century Reanalysis (V3) data is provided by the NOAA PSL, Boulder, Colorado, USA, and is available at their website at https://psl.noaa.gov/data/gridded/data.20thC_ReanV3.html [38]. The BEST data set is freely available at <https://berkeleyearth.org/data/> [39]. The sea ice concentration data is available at <https://cds.climate.copernicus.eu/cdsapp#!/dataset/satellite-sea-ice-concentration>.

Code availability The original LaMa model is available on GitHub at <https://github.com/advimman/lama>. Our modified version is available at https://github.com/NilsBochow/lama_reconstruction.

Author contributions N.Bow. and N.Boe. conceived and designed the study. N.Bow. carried out the computations and analyzed the results. All authors discussed the results. N.Bow. wrote the paper with contributions from all authors.

Competing interests The authors declare no competing interests.

Acknowledgments This is TiPES contribution #XX. The TiPES (“Tipping Points in the Earth System”) project has received funding from the European Union’s Horizon 2020 research and innovation program under grant agreement No 820970. N.Boe. acknowledges further funding by Volkswagen foundation and the European Union’s Horizon 2020 research and innovation program under the Marie Skłodowska-Curie grant agreement No. 956170, as well as from the Federal Ministry of Education and Research under grant No. 01LS2001A. This work was supported by the UiT Aurora Centre Program, UiT The Arctic University of Norway (2020), and the Research Council of Norway (project number 314570). Parts of the computations were performed on resources provided by Sigma2 - the National Infrastructure for High Performance Computing and Data Storage in Norway under the project nn8008k. Support for the Twentieth Century Reanalysis Project version 3 data set is provided by the U.S. Department of Energy, Office of Science Biological and Environmental Research (BER), by the National Oceanic and Atmospheric Administration Climate Program Office, and by the NOAA Earth System Research Laboratory Physical Sciences Laboratory. The authors gratefully acknowledge the European Regional Development Fund (ERDF), the German Federal Ministry of Education and Research and the Land Brandenburg for supporting this project by

providing resources on the high performance computer system at the Potsdam Institute for Climate Impact Research. Some of the figures are made with color maps by Cramer et al. [52]. We thank R. Suvorov for answering technical questions regarding their LaMa model, J. Meuer for providing the CMIP5 training and validation data and C. Kadow for providing the output of their model.

References

- [1] Ben-Yami, M., Skiba, V., Bathiany, S. & Boers, N. Uncertainties in critical slowing down indicators of observation-based fingerprints of the Atlantic Overturning Circulation (2023). URL <http://arxiv.org/abs/2303.06448>. ArXiv:2303.06448 [physics].
- [2] Morice, C. P., Kennedy, J. J., Rayner, N. A. & Jones, P. D. Quantifying uncertainties in global and regional temperature change using an ensemble of observational estimates: The HadCRUT4 data set: THE HADCRUT4 DATASET. *Journal of Geophysical Research: Atmospheres* **117**, n/a–n/a (2012). URL <http://doi.wiley.com/10.1029/2011JD017187>.
- [3] Harris, I., Osborn, T. J., Jones, P. & Lister, D. Version 4 of the CRU TS monthly high-resolution gridded multivariate climate dataset. *Scientific Data* **7**, 109 (2020). URL <https://www.nature.com/articles/s41597-020-0453-3>. Number: 1 Publisher: Nature Publishing Group.
- [4] Vermote, E. & NOAA CDR Program. NOAA Climate Data Record (CDR) of AVHRR Normalized Difference Vegetation Index (NDVI), Version 5 (2018). URL <https://www.ncei.noaa.gov/metadata/geoportal/rest/metadata/item/gov.noaa.ncdc:C01558/html>.
- [5] Landy, J. C. *et al.* A year-round satellite sea-ice thickness record from CryoSat-2. *Nature* **609**, 517–522 (2022). URL <https://www.nature.com/articles/s41586-022-05058-5>. Number: 7927 Publisher: Nature Publishing Group.
- [6] Cowtan, K. & Way, R. G. Coverage bias in the HadCRUT4 temperature series and its impact on recent temperature trends. *Quarterly Journal of the Royal Meteorological Society* **140**, 1935–1944 (2014). URL <https://onlinelibrary.wiley.com/doi/abs/10.1002/qj.2297>. [_eprint: https://onlinelibrary.wiley.com/doi/pdf/10.1002/qj.2297](https://onlinelibrary.wiley.com/doi/pdf/10.1002/qj.2297).
- [7] Kalnay, E. *et al.* The NCEP/NCAR 40-Year Reanalysis Project. *Bulletin of the American Meteorological Society* **77**, 437–472 (1996). URL https://journals.ametsoc.org/view/journals/bams/77/3/1520-0477_1996_077_0437_tnyrp_2_0_co_2.xml. Publisher: American Meteorological Society Section: Bulletin of the American Meteorological Society.

- [8] Bell, B. *et al.* The ERA5 global reanalysis: Preliminary extension to 1950. *Quarterly Journal of the Royal Meteorological Society* **147**, 4186–4227 (2021). URL <https://onlinelibrary.wiley.com/doi/abs/10.1002/qj.4174>. eprint: <https://onlinelibrary.wiley.com/doi/pdf/10.1002/qj.4174>.
- [9] Slivinski, L. C. *et al.* An Evaluation of the Performance of the Twentieth Century Reanalysis Version 3. *Journal of Climate* **34**, 1417–1438 (2021). URL <https://journals.ametsoc.org/view/journals/clim/34/4/JCLI-D-20-0505.1.xml>. Publisher: American Meteorological Society Section: Journal of Climate.
- [10] Berezowski, T. *et al.* CPLFD-GDPT5: High-resolution gridded daily precipitation and temperature data set for two largest Polish river basins. *Earth System Science Data* **8**, 127–139 (2016). URL <https://essd.copernicus.org/articles/8/127/2016/>. Publisher: Copernicus GmbH.
- [11] Sekulić, A., Kilibarda, M., Protić, D., Tadić, M. P. & Bajat, B. Spatio-temporal regression kriging model of mean daily temperature for Croatia. *Theoretical and Applied Climatology* **140**, 101–114 (2020). URL <https://doi.org/10.1007/s00704-019-03077-3>.
- [12] Belkhir, L., Tiri, A. & Mouni, L. Spatial distribution of the groundwater quality using kriging and Co-kriging interpolations. *Groundwater for Sustainable Development* **11**, 100473 (2020). URL <https://www.sciencedirect.com/science/article/pii/S2352801X20300461>.
- [13] Kadow, C., Hall, D. M. & Ulbrich, U. Artificial intelligence reconstructs missing climate information. *Nature Geoscience* **13**, 408–413 (2020). URL <https://www.nature.com/articles/s41561-020-0582-5>. Number: 6 Publisher: Nature Publishing Group.
- [14] Irrgang, C. *et al.* Towards neural Earth system modelling by integrating artificial intelligence in Earth system science. *Nature Machine Intelligence* **3**, 667–674 (2021). URL <https://www.nature.com/articles/s42256-021-00374-3>. Number: 8 Publisher: Nature Publishing Group.
- [15] Mitsui, T. & Boers, N. Seasonal prediction of Indian summer monsoon onset with echo state networks. *Environmental Research Letters* **16**, 074024 (2021). URL <https://dx.doi.org/10.1088/1748-9326/ac0acb>. Publisher: IOP Publishing.

- [16] Lim, B. & Zohren, S. Time-series forecasting with deep learning: a survey. *Philosophical Transactions of the Royal Society A: Mathematical, Physical and Engineering Sciences* **379**, 20200209 (2021). URL <https://royalsocietypublishing.org/doi/full/10.1098/rsta.2020.0209>. Publisher: Royal Society.
- [17] Lam, R. *et al.* Learning skillful medium-range global weather forecasting. *Science* **0**, eadi2336 (2023). URL <https://www.science.org/doi/10.1126/science.adi2336>. Publisher: American Association for the Advancement of Science.
- [18] Grattarola, D. & Vandergheynst, P. Generalised Implicit Neural Representations (2022). URL <http://arxiv.org/abs/2205.15674>. ArXiv:2205.15674 [cs, eess].
- [19] Hess, P., Druke, M., Petri, S., Strnad, F. M. & Boers, N. Physically constrained generative adversarial networks for improving precipitation fields from Earth system models. *Nature Machine Intelligence* **4**, 828–839 (2022). URL <https://www.nature.com/articles/s42256-022-00540-1>. Number: 10 Publisher: Nature Publishing Group.
- [20] Huang, Y., Yang, L. & Fu, Z. Reconstructing coupled time series in climate systems using three kinds of machine-learning methods. *Earth System Dynamics* **11**, 835–853 (2020). URL <https://esd.copernicus.org/articles/11/835/2020/>. Publisher: Copernicus GmbH.
- [21] Monteleoni, C., Schmidt, G. A. & McQuade, S. Climate Informatics: Accelerating Discovering in Climate Science with Machine Learning. *Computing in Science & Engineering* **15**, 32–40 (2013). Conference Name: Computing in Science & Engineering.
- [22] Reichstein, M. *et al.* Deep learning and process understanding for data-driven Earth system science. *Nature* **566**, 195–204 (2019). URL <https://www.nature.com/articles/s41586-019-0912-1>. Number: 7743 Publisher: Nature Publishing Group.
- [23] Yuval, J., O’Gorman, P. A. & Hill, C. N. Use of Neural Networks for Stable, Accurate and Physically Consistent Parameterization of Subgrid Atmospheric Processes With Good Performance at Reduced Precision. *Geophysical Research Letters* **48**, e2020GL091363 (2021). URL <https://onlinelibrary.wiley.com/doi/abs/10.1029/2020GL091363>. _eprint:

<https://onlinelibrary.wiley.com/doi/pdf/10.1029/2020GL091363>.

- [24] Zhu, Y. *et al.* Physics-informed deep-learning parameterization of ocean vertical mixing improves climate simulations. *National Science Review* **9**, nwac044 (2022). URL <https://doi.org/10.1093/nsr/nwac044>.
- [25] Gelbrecht, M., White, A., Bathiany, S. & Boers, N. Differentiable programming for Earth system modeling. *Geoscientific Model Development* **16**, 3123–3135 (2023). URL <https://gmd.copernicus.org/articles/16/3123/2023/>. Publisher: Copernicus GmbH.
- [26] Schneider, T. *et al.* Harnessing AI and computing to advance climate modelling and prediction. *Nature Climate Change* **13**, 887–889 (2023). URL <https://www.nature.com/articles/s41558-023-01769-3>. Number: 9 Publisher: Nature Publishing Group.
- [27] de Burgh-Day, C. O. & Leeuwenburg, T. Machine learning for numerical weather and climate modelling: a review. *Geoscientific Model Development* **16**, 6433–6477 (2023). URL <https://gmd.copernicus.org/articles/16/6433/2023/>. Publisher: Copernicus GmbH.
- [28] Kochkov, D. *et al.* Neural General Circulation Models (2023). URL <http://arxiv.org/abs/2311.07222>. ArXiv:2311.07222 [physics].
- [29] Qin, Z., Zeng, Q., Zong, Y. & Xu, F. Image inpainting based on deep learning: A review. *Displays* **69**, 102028 (2021). URL <https://www.sciencedirect.com/science/article/pii/S0141938221000391>.
- [30] Zhang, X. *et al.* DE-GAN: Domain Embedded GAN for High Quality Face Image Inpainting. *Pattern Recognition* **124**, 108415 (2022). URL <https://www.sciencedirect.com/science/article/pii/S0031320321005914>.
- [31] Chen, Y., Xia, R., Zou, K. & Yang, K. RNON: image inpainting via repair network and optimization network. *International Journal of Machine Learning and Cybernetics* **14**, 2945–2961 (2023). URL <https://doi.org/10.1007/s13042-023-01811-y>.
- [32] Suvorov, R. *et al.* Resolution-robust Large Mask Inpainting with Fourier Convolutions (2021). URL <http://arxiv.org/abs/2109.07161>. ArXiv:2109.07161 [cs,

- eess].
- [33] Parker, D. E., Legg, T. P. & Folland, C. K. A new daily central England temperature series, 1772–1991. *International Journal of Climatology* **12**, 317–342 (1992). URL <https://onlinelibrary.wiley.com/doi/abs/10.1002/joc.3370120402>. _eprint: <https://onlinelibrary.wiley.com/doi/pdf/10.1002/joc.3370120402>.
- [34] Davis, M. *Late Victorian holocausts: El Niño famines and the making of the third world* (Verso Books, 2002).
- [35] Huang, B., L'Heureux, M., Hu, Z.-Z., Yin, X. & Zhang, H.-M. How Significant Was the 1877/78 El Niño? *Journal of Climate* **33**, 4853–4869 (2020). URL <https://journals.ametsoc.org/view/journals/clim/33/11/jcli-d-19-0650.1.xml>. Publisher: American Meteorological Society Section: Journal of Climate.
- [36] Giese, B. S. & Ray, S. El Niño variability in simple ocean data assimilation (SODA), 1871–2008. *Journal of Geophysical Research: Oceans* **116** (2011). URL <https://onlinelibrary.wiley.com/doi/abs/10.1029/2010JC006695>. _eprint: <https://onlinelibrary.wiley.com/doi/pdf/10.1029/2010JC006695>.
- [37] Voskresenskaya, E., Marchukova, O. & Marine Hydrophysical Institute, Russian Academy of Sciences. Qualitative classification of the La Niña events. *Physical Oceanography* (2015). URL <http://physical-oceanography.ru/repository/2015/3/2.html>.
- [38] Slivinski, L. C. *et al.* Towards a more reliable historical reanalysis: Improvements for version 3 of the Twentieth Century Reanalysis system. *Quarterly Journal of the Royal Meteorological Society* **145**, 2876–2908 (2019). URL <https://onlinelibrary.wiley.com/doi/abs/10.1002/qj.3598>. _eprint: <https://onlinelibrary.wiley.com/doi/pdf/10.1002/qj.3598>.
- [39] Rohde, R. A. & Hausfather, Z. The Berkeley Earth Land/Ocean Temperature Record. *Earth System Science Data* **12**, 3469–3479 (2020). URL <https://essd.copernicus.org/articles/12/3469/2020/>. Publisher: Copernicus GmbH.
- [40] (C3S), C. C. C. S. Sea ice concentration daily gridded data from 1979 to present derived from satellite observations. URL <https://cds.climate.copernicus.eu/cdsapp#!/dataset/satellite-sea-ice-concentration?tab=overview>.

- [41] Tang, M. S. Y., Chenoli, S. N., Samah, A. A. & Hai, O. S. An assessment of historical Antarctic precipitation and temperature trend using CMIP5 models and reanalysis datasets. *Polar Science* **15**, 1–12 (2018). URL <https://www.sciencedirect.com/science/article/pii/S1873965217300981>.
- [42] Keisler, R. Forecasting Global Weather with Graph Neural Networks (2022). URL <http://arxiv.org/abs/2202.07575>. ArXiv:2202.07575 [physics].
- [43] Scher, S. & Messori, G. Physics-inspired adaptations to low-parameter neural network weather forecasts systems (2023). URL <http://arxiv.org/abs/2008.13524>. ArXiv:2008.13524 [physics].
- [44] Lugmayr, A. *et al.* RePaint: Inpainting using Denoising Diffusion Probabilistic Models (2022). URL <http://arxiv.org/abs/2201.09865>. ArXiv:2201.09865 [cs].
- [45] Wei, C. *et al.* Diffusion Models as Masked Autoencoders (2023). URL <http://arxiv.org/abs/2304.03283>. ArXiv:2304.03283 [cs].
- [46] Höppe, T., Mehrjou, A., Bauer, S., Nielsen, D. & Dittadi, A. Diffusion Models for Video Prediction and Infilling (2022). URL <http://arxiv.org/abs/2206.07696>. ArXiv:2206.07696 [cs, stat].
- [47] Zeng, Y., Fu, J., Chao, H. & Guo, B. Aggregated Contextual Transformations for High-Resolution Image Inpainting (2021). URL <http://arxiv.org/abs/2104.01431>. ArXiv:2104.01431 [cs].
- [48] Hukkelås, H., Lindseth, F. & Mester, R. Image Inpainting with Learnable Feature Imputation (2020). URL <http://arxiv.org/abs/2011.01077>. ArXiv:2011.01077 [cs, eess].
- [49] Rombach, R., Blattmann, A., Lorenz, D., Esser, P. & Ommer, B. High-Resolution Image Synthesis with Latent Diffusion Models (2022). URL <http://arxiv.org/abs/2112.10752>. ArXiv:2112.10752 [cs].
- [50] Kulshreshtha, P., Pugh, B. & Jiddi, S. Feature Refinement to Improve High Resolution Image Inpainting (2022). URL <http://arxiv.org/abs/2206.13644>. ArXiv:2206.13644 [cs, eess].

- [51] Murphy, B., Yurchak, R. & Müller, S. GeoStat-Framework/PyKrige: v1.7.0 (2022). URL <https://zenodo.org/record/7008206>. Language: eng.
- [52] Crameri, F., Shephard, G. E. & Heron, P. J. The misuse of colour in science communication. *Nature Communications* **11**, 5444 (2020). URL <https://www.nature.com/articles/s41467-020-19160-7>. Number: 1 Publisher: Nature Publishing Group.

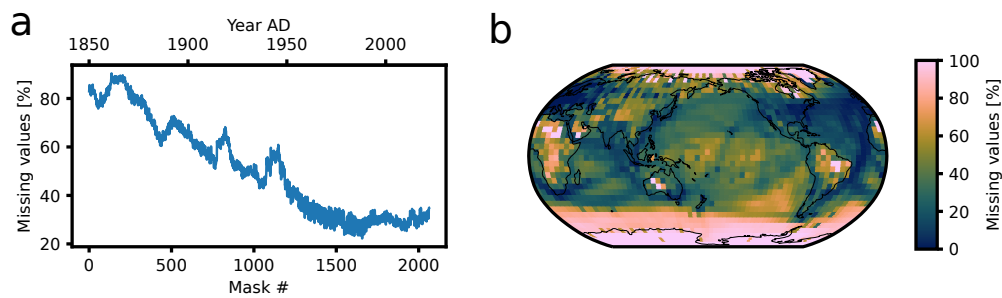


Fig. 1 Spatial map and temporal time series of missing observations in HadCRUT4. (a) Time series of the missing value ratio on the grid cell level in HadCRUT4 for the whole Earth. There is a steady increase in the observational temperature coverage with some exceptions such as the two world wars. (b) Spatial missing ratio in HadCRUT4 over the whole time span from 1850-2022. The polar regions show the lowest coverage of temperature records.

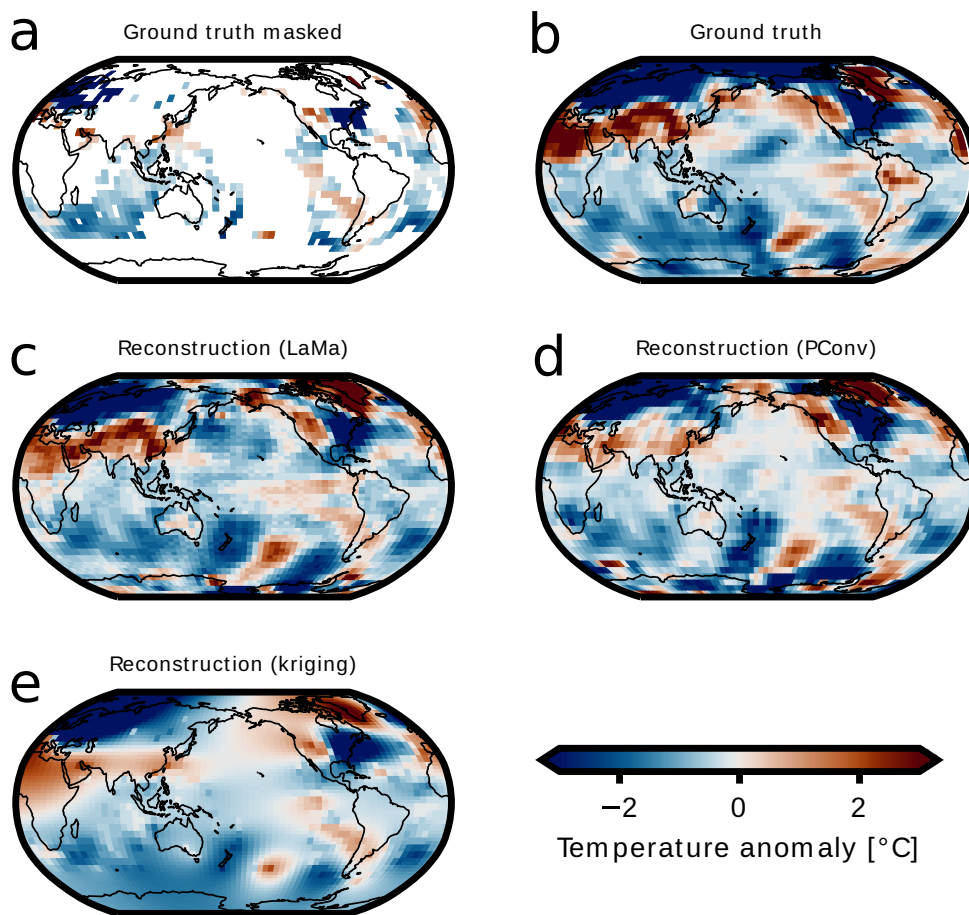


Fig. 2 Exemplary reconstructed CMIP5 temperatures for all methods. (a) Masked ground truth for February 1870 derived from a held-out CMIP5 member, masked with the corresponding HadCRUT4 mask for this date. White areas denote masked regions. (b) Ground truth without masking. (c) Infilled temperatures via LaMa. The spatial patterns are very similar to the ground truth. (d,e) Same as (c) but for PConv [13] and kriging, respectively. While the spatial patterns reconstructed by the deep learning methods are very similar to the ground truth, some regions show the opposite trend in the temperature e.g., northern South America.

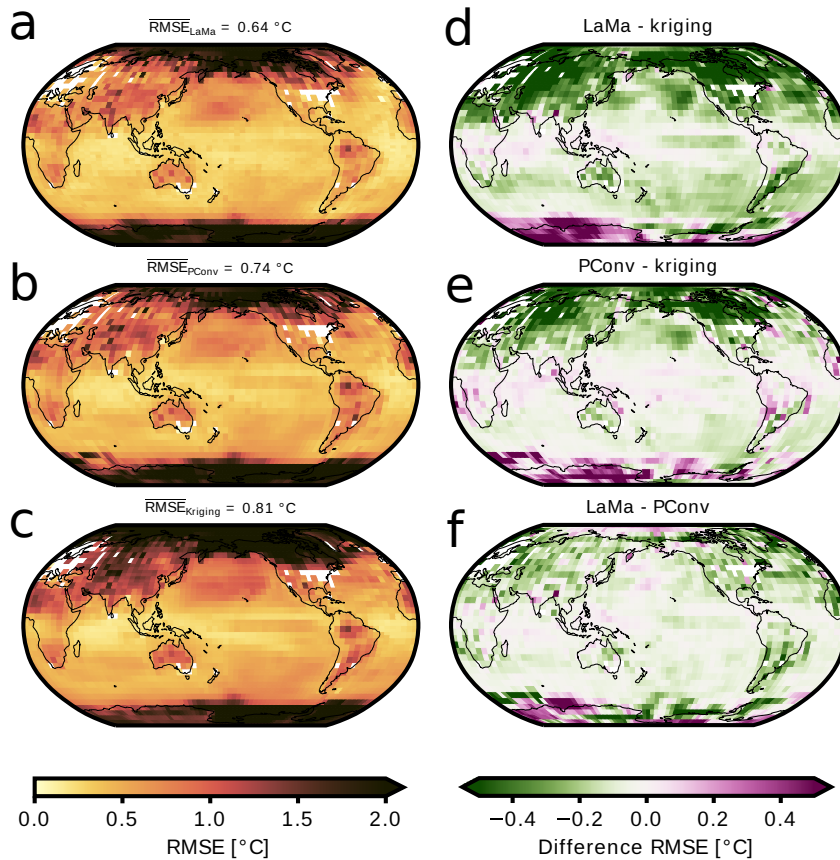


Fig. 3 Average site-wise root-mean-square error and comparison between methods for single held-out CMIP5 member. (a) Temporally averaged RMSE at each site for inpainted CMIP5 held-out member using LaMa fixed. The white areas denote the regions with available temperature records for the whole time span 1870-2005 AD. The spatially weighted average of the site-wise RMSE is 0.64°C . The polar regions, especially Antarctica, show the greatest RMSE, while the tropical and subtropical regions show the smallest RMSE. (b, c) Same as (a) but for PConv [13] and kriging. Both machine learning methods show a smaller mean RMSE than kriging. Especially in the northern hemisphere the RMSE is smaller. (c) Difference between temporally averaged RMSE at each site for LaMa and kriging. Green areas denote regions where the RMSE of LaMa is smaller than that of the baseline kriging method. Purple areas denote greater RMSE than for kriging. LaMa fixed shows a lower RMSE than kriging in 79% of the grid cells. (d) Same as (c) but for PConv [13]. PConv shows in 71% of the grid cells a smaller RMSE than kriging. (e) Comparison between LaMa and PConv. Green areas denote regions where the RMSE of LaMa is smaller than of the PConv method. LaMa shows a lower RMSE than PConv in 78% of all grid cells.

Table 1 Comparison between all methods in terms of the RMSE. Spatially weighted average of the site-wise RMSE and average spatial RMSE for both LaMa methods, PConv, and kriging for the single CMIP5 ensemble member. The improvement compared to kriging is denoted in the parentheses. LaMa shows considerable improvement in comparison with the other methods. LaMa random outperforms kriging and has a similar performance as PConv.

Model	spatially averaged site-wise RMSE [°C]	temporally averaged spatial RMSE [°C]
LaMa	0.64 (21.0%)	0.99 (16.8%)
LaMa random	0.74 (8.6%)	1.10 (7.6%)
PConv	0.74 (8.6%)	1.08 (9.2%)
Kriging	0.81	1.19

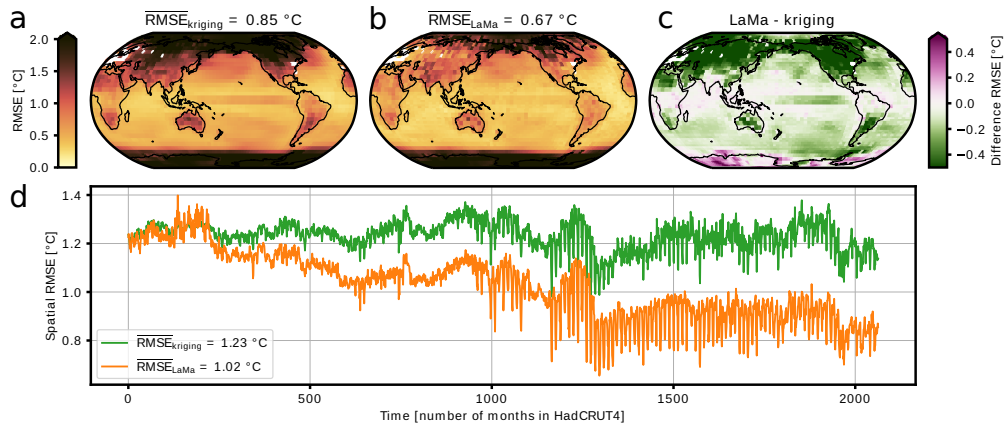


Fig. 4 Error statistics on the held-out CMIP5 members for each HadCRUT4 mask. (a) Average site-wise RMSE for kriging on the randomly held-out 2251 months from the CMIP5 ensemble. We calculate the site-wise RMSE for every combination of HadCRUT4 masks from 1850 to 2021 AD and month. The spatially weighted average of the site-wise RMSE is 0.85°C . The polar regions show the largest RMSE, while the tropics and subtropical oceans show the lowest RMSE. White grid cells denote regions where temperature observations are available for the whole time span. (b) Same as (a) but for LaMa. The site-wise RMSE is lower in most grid cells than for kriging. Especially, in the northern hemisphere there is a strong improvement compared to kriging. LaMa outperforms kriging in terms of the spatially averaged site-wise RMSE. (c) Difference between temporally averaged RMSE at each site for LaMa and kriging. Green areas denote regions where the RMSE of LaMa is smaller than that of the baseline kriging method. Purple areas denote greater RMSE than for kriging. (d) Spatial RMSE for both methods and all HadCRUT4 masks, which are ordered in time; note that generally the size of the masks in terms of the number of missing data declines over time. LaMa outperforms kriging almost consistently for all masks. LaMa shows a higher RMSE than kriging for very large masked areas ($\geq 80\%$) but outperforms kriging otherwise. Especially for small masks, the average spatial RMSE is substantially lower for LaMa than for kriging.

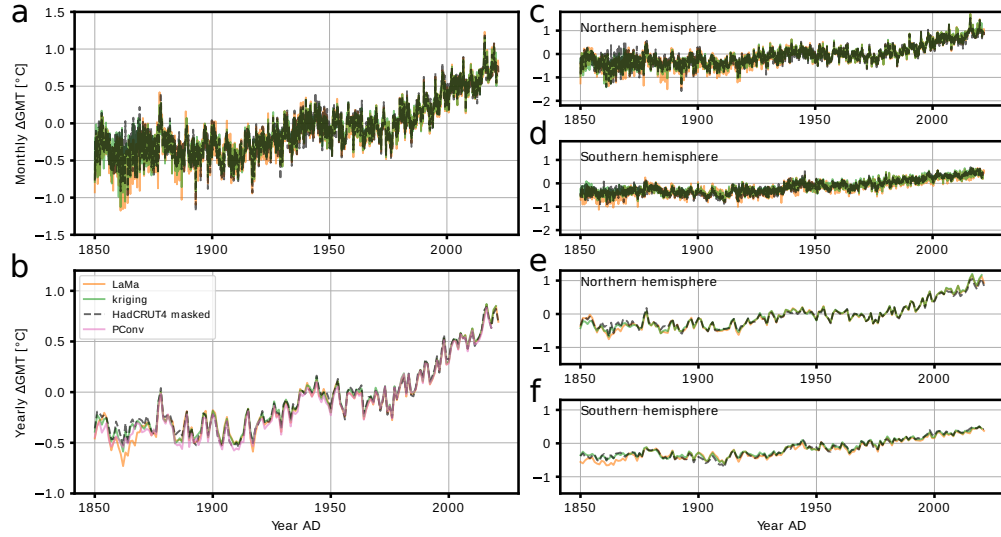


Fig. 5 Reconstructed HadCRUT4 global mean temperature time series. (a) Monthly HadCRUT4 timeseries from 1850 to 2022. The reconstructions from LaMa and kriging as well as the mean of the masked HadCRUT4 records are shown. The dashed black curve is the spatially averaged GMT derived from the incomplete HadCRUT4 observations. (b) Same as a but for the yearly averaged GMT. Additionally, we show the reconstruction based on the PConv method. The Pearson correlation between the masked time series, i.e., yearly GMT and LaMa is $r_{\text{LaMa}} = 0.99$, for kriging $r_{\text{kriging}} = 0.99$ and $r_{\text{PConv}} = 0.99$. (c,d) Same as a but for the Northern and Southern hemisphere, respectively. (e,f) Same as c,d but for the yearly time series.

Supplementary Information

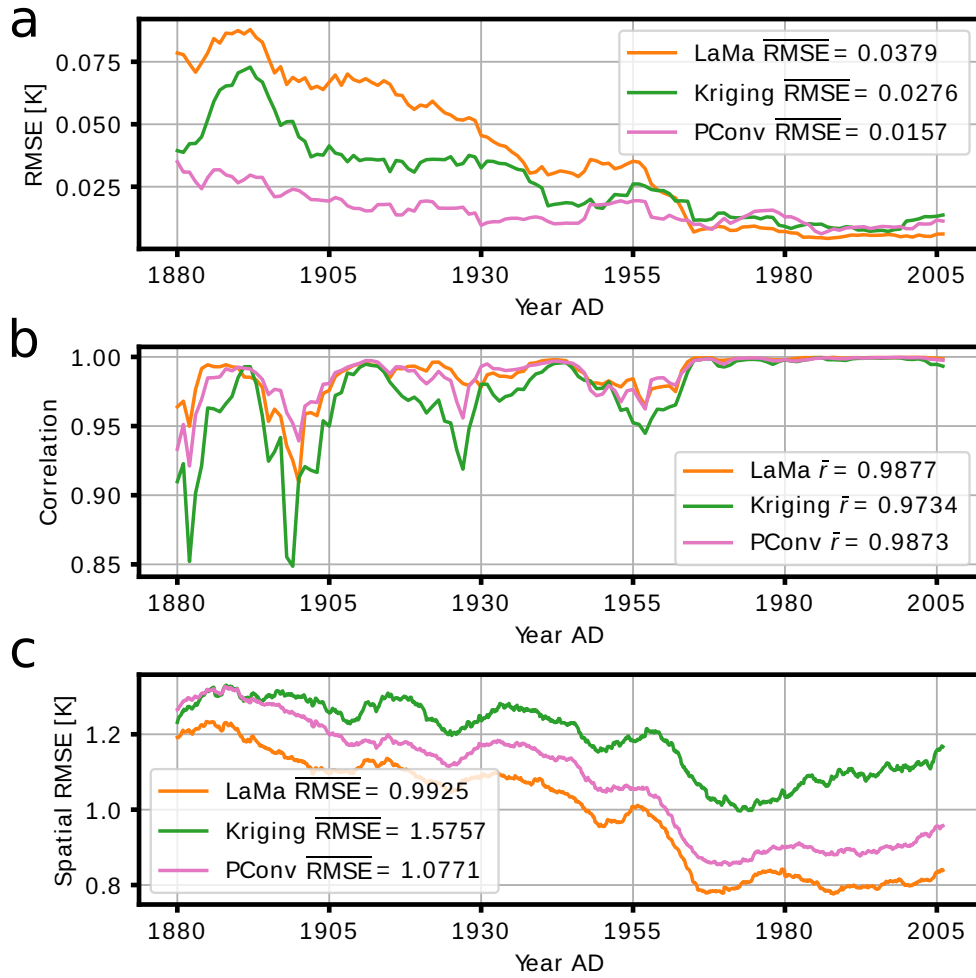


Fig. S1 Comparison with reconstruction method via PConv and kriging for held-out CMIP5 member. (a) Root-mean-squared error between infilled yearly time series for LaMa, kriging and PConv [13] and the held out CMIP5 member (ground truth) in a rolling window with size $w = 10$ years (1870-2005 AD). The mean RMSEs over the whole time period are denoted in the legend. (b) Same as (a) but for correlation between yearly temperature time series. (c) Weighted spatial root-mean-squared error of monthly temperature fields in a rolling window with window size $w = 10$ years.

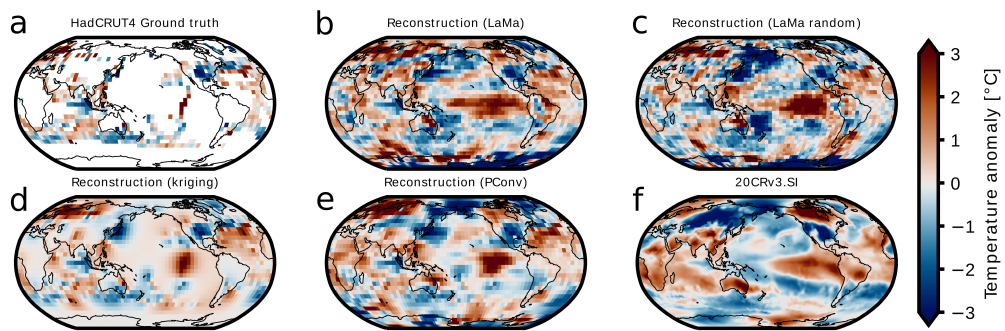


Fig. S2 Reconstructed HadCRUT4 temperature field for November 1877. (a) Original HadCRUT4 temperature anomaly records. This also corresponds to the input into the trained model. (b) Reconstructed temperature anomalies with LaMa. The strong El Niño is clearly visible in the Pacific. (c) Same but for LaMa random. The spatial extent of the El Niño is clearly visible. (d) Reconstructed temperatures via PConv [13]. (e) Reconstructed temperatures via kriging [6]. The method fails to reconstruct the spatial extent of the El Niño. (f) Temperature anomalies taken from 20CRv3.SI reanalysis.

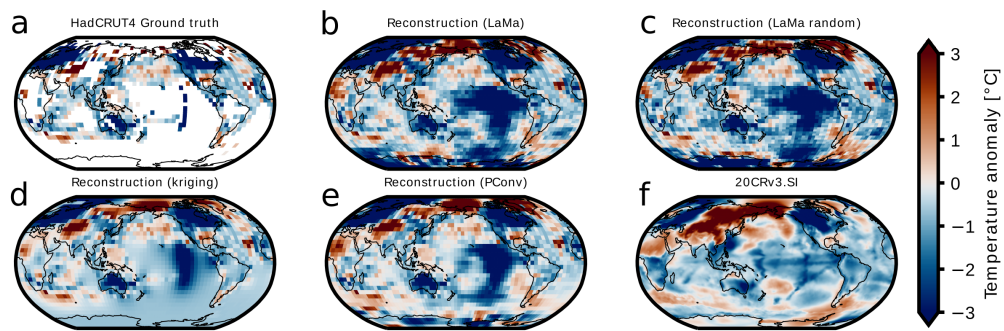


Fig. S3 Reconstructed HadCRUT4 temperature fields for February 1917. (a) Original HadCRUT4 temperature anomaly records. This also corresponds to the input into the trained model. (b) Reconstructed temperature anomalies with LaMa. The strong La Niña is clearly visible in the Pacific. (c) Same but for LaMa random. The spatial extent of the La Niña is clearly visible. (d) Reconstructed temperatures via PConv [13]. (e) Reconstructed temperatures via kriging [6]. The method fails to reconstruct the spatial extent of the La Niña. (f) Temperature anomalies taken from 20CRv3.SI reanalysis.

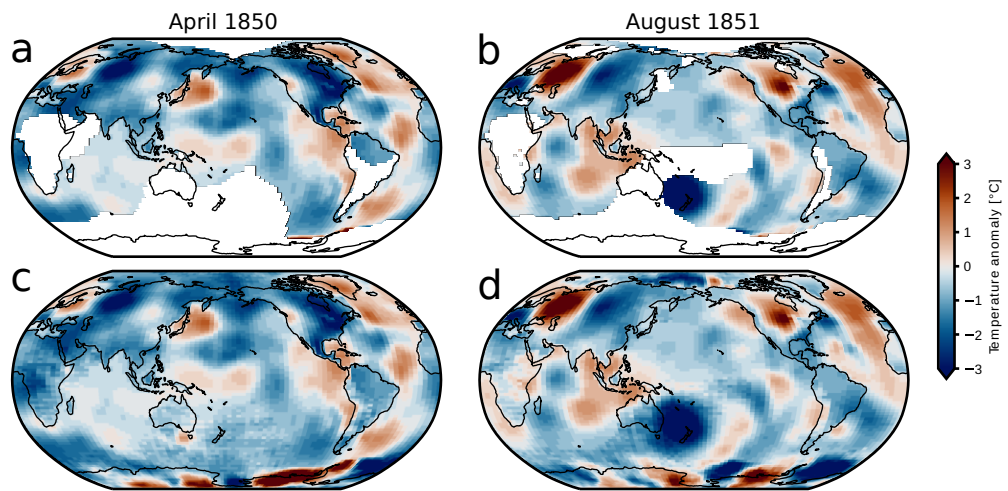


Fig. S4 Reconstruction of two exemplary months for higher resolution BEST data set. (a) Reconstruction of BEST [39] (90x90 px resolution) for April 1850 using LaMa random trained on CMIP5 (72x72 px resolution). (b) Same as (a) but for August 1851. (c,d) Same as (a,b) but for not inpainted temperature records, respectively.

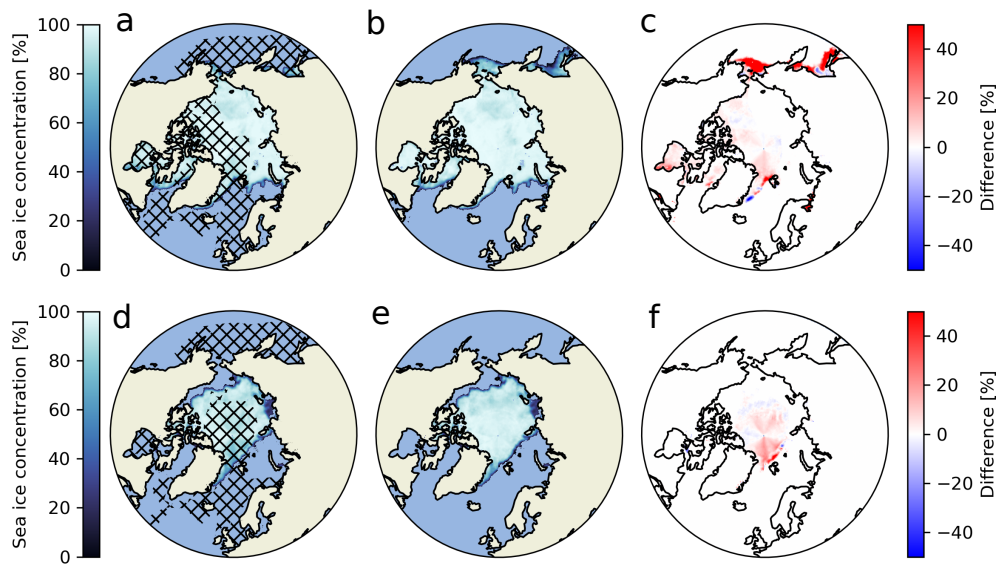


Fig. S5 Exemplary reconstruction of sea ice concentration for two different months in ERA5. (a) Ground truth of sea ice concentration for held-out December 14, 1979 taken from ERA5 reanalysis [40]. Hatched area denote regions that are masked for reconstruction. We use LaMa fixed trained on daily sea ice concentration from 1979 to 2022 taken from ERA5 for the reconstruction. (b) Reconstructed sea ice concentration via LaMa fixed. The model is able to reconstruct the spatial extent and concentration of the sea ice reasonably well. (c) Absolute difference between the ground truth and the reconstructed sea ice concentration. Red areas denote overestimated sea ice concentration by the reconstruction, while blue regions denote underestimated sea ice concentration. (d,e,f) Same as a, b, c but for September 16, 1979, respectively.

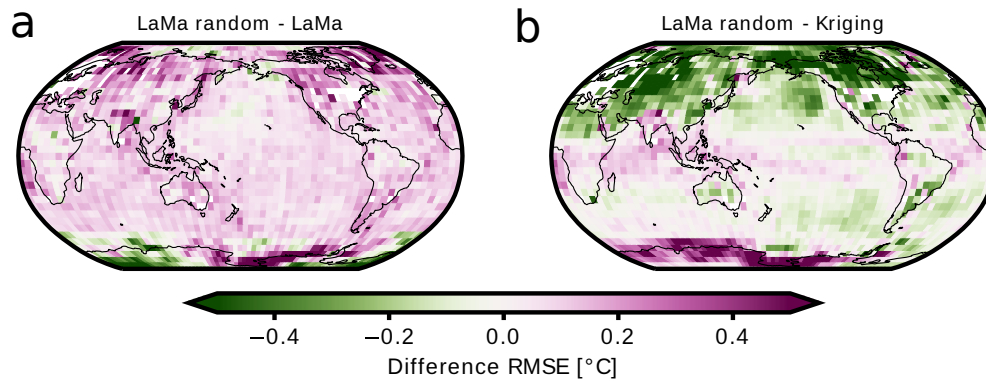


Fig. S6 Difference in site-wise RMSE between LaMa random and LaMa/Kriging. (a) Difference between temporally averaged RMSE at each site between LaMa random and LaMa for held-out CMIP5 member. The white areas denote the regions with available temperature records for the whole time span 1870-2005 AD. Purple areas denote regions where the RMSE of LaMa random is greater than of LaMa. Green areas denote where the RMSE of LaMa random is smaller than for LaMa. LaMa shows a lower RMSE than LaMa random in 82% of the grid cells. (b) Same as a but for the difference between LaMa random and kriging. LaMa random shows a lower site-wise RMSE than kriging in 65% of the grid cells (green areas).

